Functional Analysis of Protein S-Palmitoylation Enzymes

by

Dahvid Davda

A dissertation submitted in partial fulfillment
of the requirements for the degree of
Doctor of Philosophy
(Chemical Biology)
in the University of Michigan
2015

Doctoral Committee:

Assistant Professor Brent R. Martin, Chair
Professor Carol A. Fierke
Professor Kristina I. Håkansson
Associate Professor Zaneta Nikolovska-Coleska

Dedication

I dedicate this work to my long-time academic mentor and dear friend Dr. Tracy Simpson, who inspired me to study the life sciences.

Acknowledgements

Throughout this thesis work and my entire graduate career I have shared the comfort and had the support and encouragement of many people, to whom I am truly grateful. I will mention a few individuals here, but my apologies go out in advance to anyone who I may inadvertently missed.

First and foremost, I must thank my thesis advisor, Dr. Brent Martin, for his incredible support, endless guidance and valuable instruction that were essential to my progress over the years. He has taught me many scientific lessons, the most important of which is how to be a rigorous scientist. In addition, Brent has introduced me to many exciting topics and techniques such as mass spectrometry-based proteomics and protein palmitoylation in general. His investment in me is thus greatly appreciated.

I would like thank Dr. Carol Fierke for taking time to meet and mentor me in the field of protein lipidation. In addition, I wish to sincerely express my gratitude to all of my thesis committee members; in particular, I would like to acknowledge Dr. Kicki Håkansson and Dr. Zaneta Nikolovska-Colesca for upholding high-standards, recommending great experimental ideas and providing their priceless scientific point of view during all of these investigations.

Special thanks go out to all Martin lab, Fierke lab and Mapp lab members, past and present, for their support, constructive discussions, helpful feedback and reagents, including those I took without their knowledge, but made sure to give back right away when they found out. While in the lab, I am thankful to have had the opportunity to mentor a handful of both graduate and undergraduate students. To the current and future members of the Martin lab, I wish you the best of luck with your investigations.

Among others, extra thanks to Dr. Ruma Banerjee and her lab members for teaching me my first steady-state enzyme velocity assays among many other

experiments. Also, thanks to Dr. Neil Marsh and his lab members for teaching me fundamental concepts in enzymology.

I must acknowledge and express appreciation for the monetary contributions that I received from the University of Michigan's Rackham school of graduate studies; I have been awarded both a merit fellowship and a pre-doctoral fellowship. Without their financial support, this project would physically not have been possible.

My graduate career has been a great journey and I have had the pleasure of meeting many wonderful people along the way. I want to especially thank Andrea, Mike, Aliyah and Eric from the Fierke lab, Remy from the Kopleman lab and Max from the Garcia lab for sharing many excellent experiences and sometimes providing a non-scientific social atmosphere.

I would like to thank my siblings, Lucas, Elazar, Simy and Tatiana for providing me much necessary comfort, and most importantly for discussions regarding the 'big picture' of my scientific studies. Thank you for being there for me. To my parents, Itzchak and Sultana Rivka, thank you for being supportive of me during this stage of my life and all those leading up to it.

Lastly, to my wife Jeannie, there are no words that I can use to describe the gratitude and appreciation I have for you. I know I would not have been able to accomplish this feat without your invaluable help, nourishment and love. I am deeply and forever indebted to you. Thank you for your companionship during this adventure; looking forward to many more.

Preface

The work herein includes both unpublished material and published research work carried out under the guidance and instruction of my thesis chair Dr. Brent R. Martin. The following describes the scientific journals to which this dissertation work was or will be submitted to in the future. Chapter 1 contains intellectual work that was contributed by me and Dr. Brent R. Martin and was published as a review for Medicinal Chemistry Communications on December of 2013. Chapter 2 consists of studies completed primarily by me and was published in ACS Chemical Biology on July of 2013. The majority of the intellectual and physical work included in Chapter 3 was contributed by me, Dr. Kristin Labby, Dr. Jeannie Hernandez and Dr. Jaimeen Majmudar. This study will be submitted in a future manuscript to Chemistry & Biology. Chapter 4 incorporates work that was accomplished by me and Dr. Jeannie Hernandez, and will be submitted to Molecular Cell as a primary research article. Appendix A contains the complete published data set for the proteomic analysis described in Chapter 2. Appendix B contains the complete unpublished data set for the proteomic analysis described in Chapter 4. The beginning of each research chapter details individuals and their contributions to the particular study, such as experiments that were conducted or intellectual input that was provided, because their efforts were critical to the success of these projects.

Table of Contents

List of Figures

List of Tables

List of Equations

List of Appendices

List of Abbreviations, Acronyms and Symbols

% v/v - Percent volume
% w/v - Percent weight per volume
16:0 - Palmitic acid
17ODYA - 17-Octadecynoic acid
2BP - 2-Bromopalmitate
2BPN3 - 16-Azido-2-bromopalmitate
2IA - Iodoacetamide
^{3}H - Tritium
Ab - Antibody
ABHD - Alpha, beta hydrolase
Ac - Acetyl
ADH - Alcohol dehydrogenase
Alk - Alkynyl
APT - Acyl-protein thioesterase
BPM - Biotin polyethylene glycol maleimide
CoA - Coenzyme A
CRAF - Raf-1 proto-oncogene, serine/threonine kinase
DHHC - Aspartate-histidine-histidine-cysteine containing motif or enzyme
EC_{50} - Half maximal stimulatory concentration
ECAD - Epithelial cadherin
EGFR - Epidermal growth factor receptor
ERBIN - Erbb2 interacting protein
ERK - Extracellular regulated MAP kinase
F127 - Pluronic F127, a.k.a. Poloxamer 407
FP-Biotin - Fluorophosphonate biotin
FP-PEG-Rh - Fluorophosphonate polyethylene glycol rhodamine
FP-Rh - Fluorophosphonate rhodamine
FRAP - Fluorescence recovery after photobleaching
g - Grams
GAPDH - Glyceraldehyde-3-phosphate dehydrogenase
$G_{\alpha,i}$ - Gaunine nucleotide -binding protein G(i) subunit alpha
h - Hours
HEPES - 4-(2-hydroxyethyl)-1-piperazineethanesulfonic acid
IB - Immunoblot
IC_{50} - Half maximal inhibitory concentration
K_i - Equilibrium inhibitory constant
K_m - Substrate concentration at half maximal enzyme velocity

k_{obs} - the observed rate constant associated with the apparent order and molecularity of a given reaction
k_{off} - the dissociation rate constant of a first-order unimolecular reaction
L - Liters
LCFA - Long-chain fatty acid
LPA - Lysophosphatidic acid
LPC - Lysophosphatidyl choline
LPE - Lysophosphatidyl ethanolamine
LPI - Lysophosphatidyl inositol
LYPLA - Lysophospholipase
M - Molarity
MAPK - Mitogen activated protein kinase
MEK - Mitogen-activated protein kinase kinase
min - Minutes
mol - Moles
NaCl - Sodium chloride
NEM - N-ethylmaleimide
NH2OH - Hydroxylamine
Palm - Palmitic acid
PAT - Protein acyltransferase
PBS - Phosphate buffered saline
Ph - Phenyl
Ras - Ras sarcoma virus oncogene
RCF - Relative centrifugal force
Res-*O*-Ac - Resorufin O-Acetate
rhEGF- Recombinant human epidermal growth factor
s - Seconds
Scrib - Scribble planar cell polarity protein
SDS - Sodium dodecyl sulfate, a.k.a. Sodium lauryl sulfate
SDS-PAGE - Sodium dodecyl sulfate polyacrylamide gel electrophoresis
TCEP - Tris(2-carboxyethyl)phosphine
Tris - tris(hydroxymethyl)aminomethane
TUBA - Tubulin alpha subunit
Tween20 - Polysorbate 20
TX100 - Triton X-100

Abstract

Protein S-palmitoylation is a dynamic, hydrophobic, post-translational modification of cysteine residues that is required for the spatiotemporal organization of hundreds of proteins. In turn, protein palmitoylation contributes to the composition of cellular membrane environments and plays fundamental roles in cancer, neurological disorders and many other human diseases. Despite its central function in human pathology, still, little is known about the enzymes that catalyze the addition (protein S-acyl transferases) and removal (S-acyl protein thioesterases) of this modification. The two enzyme families, DHHCs and LYPLAs, are thought to make up the so-called dynamic palmitoylation machinery in which dual action of acyltransferases and thioesterases promote proper membrane targeting for an expanding list of dynamically palmitoylated proteins. Indeed, a steady growth in studies of these enzymes is beginning to shed light on their biological functions, revealing that the interplay between these opposing catalysts may be more complex than previously thought. More specific tools for these enzymes can therefore provide a more complete molecular description of dynamic palmitoylation events and its regulation in various biological settings.

The work presented in this thesis explores the chemical mechanisms and physiological roles of DHHCs and LYPLAs by developing, characterizing and employing novel tools for their study in the context of cancer biology. In the second chapter, the cellular targets of a widely-used, mechanism-based protein acyltransferase inhibitor are profiled and analyzed. In the third chapter, a mechanistic description of divergent thioesterase active-site ligand specificities is presented using both a structural and a kinetic approach. In the third chapter, novel acyl-protein thioesterase inhibitors are applied to define their roles in organizing cell junctions and suppressing metastatic transformation. One of the fundamental goals in this thesis is to address the limitations of current chemical tools of protein palmitoylation and provide a framework for the development of selective pharmacological agents to accelerate the study of this

modification. From a physiological standpoint, this work offers novel insights into the *in vivo* functions of palmitoyl transferases and de-palmitoylases, highlighting the intricacies of the regulatory system governing the palmitoylation state of a given protein.

Chapter 1:
Review of Protein *S*-Palmitoylation, Associated Enzymes, Substrates and Physiological Roles

1.1 General introduction

Many soluble proteins must temporarily associate with the membrane phase to perform various biological tasks, such as signaling[1] and trafficking[2]. To engage the lipid bilayer, these peripheral membrane proteins make use of a number of targeting mechanisms including: non-covalent interactions with membrane-resident proteins[3,4], membrane-binding domains that rely on electrostatic[5,6] and polar[7,8] lipid head-group interactions, and specialized auxiliary groups deriving from posttranslational modifications (PTMs) of particular protein side chains. The last process, termed protein lipidation, involves the installment of lipid moieties that mediate direct interactions with hydrophobic membrane constituents[9–12] (Table 1). A diverse range of lipid molecules are coupled to proteins and these may be classified into two main categories based on the "destination" to which the protein is targeted. Lipid anchors such as *O*-cholesteroyl, *O*- and *N*- acyl groups, and glycosylphosphatidylinositol (GPI) linkers are used to orient secreted polypeptides destined to the extracellular face of cells[9,13–17]. These secretory-related modifications are beyond the scope of the research and discussion presented in this work; therefore, their details will not be discussed further and the reader is referred to reviews on these topics elsewhere [18–25]. As for intracellular dwelling proteins, there are three types of lipidation events utilized for tethering proteins toward the cytoplasmic face of cells, namely prenylation, *N*-myristoylation and *S*-palmitoylation[26–35]. While palmitoylation is the focal point of the studies herein, it frequently occurs in proximity to *N*-myristoylated and prenylated sites[36–39]. For this reason, these modifications will be discussed in short within the context of protein palmitoylation.

Modification	Subtitutent	Protein Linkage	Site of Modification	Installing Enzymes
S-Acylation‡	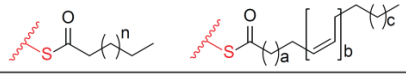	Thioester	Cysteine	DHHCs
N-Myristoylation%	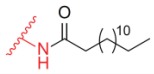	Amide	|$M_{terminal}$|**G**XXXXS/T••• Lysine	NMTs Unknown
Prenylation*	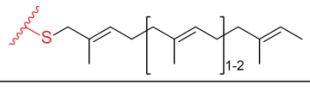	Thioether	•••**C**|aa$X_{terminal}$| •••**C**X**C**$_{terminal}$, •••**CC**$X_{terminal}$	FTase GGTaseI GGTaseII
Cholesteroylation∞	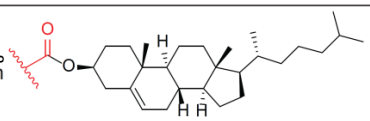	Ester	•••**G**|CF•••|	Autocatalytic
O-Acylation†		Ester	G$_{terminal}$S**S**FLSP••• •••CKCHGa**S**GSCXaKTCW•••	GOAT Porcn
N-Palmitoylation#	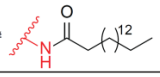	Amide	**C**$_{terminal}$••• (for Hh) |$M_{terminal}$|**G**C••• (for Gαs)	Hhat Unknown
Glycophosphatidyl inositol (GPI) Linker§	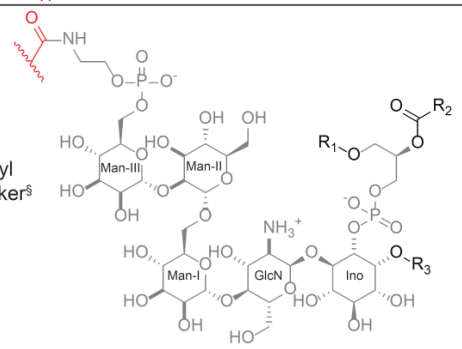	Amide	•••s**s**$^{\omega}$|ss•••|	GPI-Transamidase

Table 1 Known lipid-based protein modifications that occur in cells. The top three entries in this table are lipid modifications that occur in the cytoplasm, while the bottom four entries detail modifications that take place in the lumen of the secretory pathway. In the 'Substituent' column, protein-derived chemical moieties are colored in red. In the 'Site of Modification' column, uppercase single letter abbreviations are used in the conventional way to denote the corresponding amino acid residues, except for lowercase letters where 'a' stands for a hydrophobic residue and 's' for a small side chain residue. The lipid attachment site is highlighted by the bold underlined letter, centered three dots stands for the rest of the amino acid sequence, and vertical bars signify a sequence that is removed prior or after installment of the lipid group.

‡ Studies have shown that, in addition to palmitate (C16:0), other fatty acids are found to be thioacylated onto proteins.[40,41] These include acyl chain lengths between 14 and 22 carbons which may have varying degrees of unsaturation (e.g. C20:4).[42–45]

% Although *N*-Myristoyltransferases (NMTs) acylate N-terminal glycine residues cotranslationally[13], a few proteins are known to be modified by fatty acyl groups on the ε-amino of lysine, although the mechanism and function of this modification are unclear[46,47].

* Prenylation sites of farnesyltransferase (FTase) and geranylgeranyltransferase-I (GGTase-I) are typified by the CaaX motif, whereas GGTase-II features a broader scope of substrate sequences.[48,49]

∞Hedgehog (Hh) proteins are the only known targets of this intein-mediated autocatalytic modification.[23,50]

† Ghrelin is the only protein known to be *S*-octanoylated by Ghrelin *O*-acyltransferase (GOAT).[51] Wnt proteins are the only examples of Porcupine (Porcn)-catalyzed *O*-acylation with the long-chain, unsaturated fatty acid palmitoleate.[52] The sequence displayed in the 'Site of Modification' column is putative based on the high sequence homology in vicinity of Wnt-3a acylation site.[5317]

N-palmitoylation is featured in Hh proteins and it occurs when an N-terminal cysteine is thioacylated and subsequently undergoes intramolecular rearranges into a stable amide bond.[37]The process by which certain G_{α} subunits are N-palmitoylated at their glycine residue is unknown.[54]

§ Once fully synthesized, the GPI moiety is typically attached towards a pro-protein's C-terminus via an internal proteolytic cleavage followed by a transamidation reaction.[22,55] The R groups represent variable acyl chains that have been reported.[56] For simplicity, various reported modification of the oligosaccharide have been omitted.

1.2 The Physicochemical Nature and Biological Implications of Protein *S*-Palmitoylation

Protein *S*-palmitoylation broadly refers to the modification of the cysteine thiol side chain by activated fatty acids which results in a protein with a thioester-linked fatty acyl group (Figure 1-1). The particular chemical transformation taking place is a thioacylation reaction although it is typically dubbed as *S*-palmitoylation to reflect that most proteins display the saturated, sixteen carbon (C16:0) fatty acid, palmitate[3]. Nevertheless, a variety of long-chain fatty acids (LCFAs), with different chain lengths and degrees of unsaturation, have been reported to thioacylate proteins *in vivo*, these include arachidonate (C20:4), palmitoleate (C16:1), stearate (C18:0) and oleate (C18:1)[40,42,45,57–59]. This is in stark contrast to most other lipid modification events which primarily result in the installment of only one or two different types of lipid molecules as documented so far (Table 1). Many efforts have been made to explain the observed diversity of linked fatty acids, with some maintaining that it could be indicative of the spontaneous reaction occurring in cells as it could parallel the cellular distributions of activated LCFAs[60,61]. Others suggest that putative installing enzymes may exhibit broad acyl substrate specificities.[62] However, to date, no satisfactory explanation has been offered.

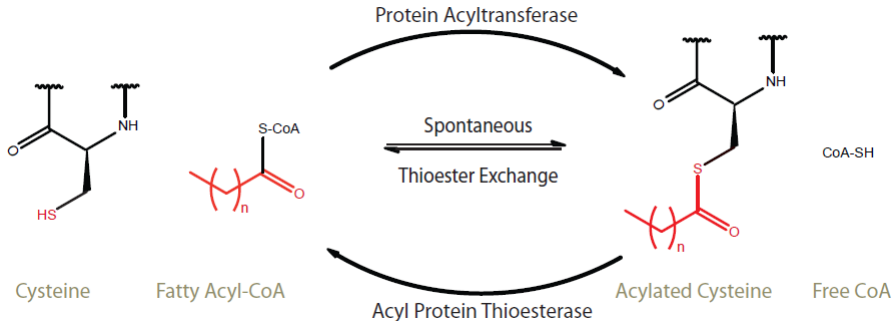

Figure 1-1 The dynamic nature of protein S-palmitoylation. In this reaction, protein cysteine residues are acylated by activated fatty acids in the form of acyl-CoAs resulting in the release of a proton and free CoA molecule. Unlike other lipid-based PTMs, palmitoylation is reversible on the time-scale of the protein and this is due to the labile nature of the scissile bond. This feature allows for both spontaneous and enzyme-catalyzed modes of thioester hydrolysis, that latter of which lends itself to a number of regulatory mechanisms. Nevertheless, some proteins remain stably palmitoylated while others cycle rapidly.

Akin to other forms of protein lipidation, palmitoylation promotes stable membrane association of otherwise soluble proteins[31,63]. As shall be discussed in greater detail, cytosolic proteins typically achieve transient membrane associations

before they can be thioacylated by the palmitoylation machinery.[36,64] Once palmitoylated though, the protein exhibits increased membrane affinity and may result, in certain circumstances, in virtually permanent membrane attachment known as kinetic membrane trapping.[65] This occurs because the protein, which is already weakly attracted to the membrane via some other mechanism, is now further equipped with a hydrophobic 'handle' that directly partitions into the lipid bilayer of the membrane, thus preventing the 'doubly-anchored' protein from fully dissociating[66]. In addition, a single protein may contain a number of palmitoylation sites[67,68], which tend to cluster near each other, making the protein even more lipophilic[65,69]. Interestingly, both the occurrence of multiple palmitoylation sites and the identities of the attached fatty acids have shown to impact a protein's membrane localization by targeting it to specific intracellular compartments[64,70–75] or segregating it into ordered lipid-microdomains such as lipid rafts[66,76–78].

Although the anchoring functionality is commonly provided by all protein lipid modification, it is unique in *S*-Acylation because the lipid attachment is intrinsically unstable and therefore reversible[37,79] which may obviate the need for devoted PTM 'erasers'. Other lipid-based PTMs are characterized by chemically-resistant linkages such as the amide bond of an *N*-myristoylated glycine and the thioether bond of a prenylated cysteine (Table 1). In contrast, a typical unactivated thioester bond stores enough chemical potential such that its free energy of hydrolysis (ΔG ~ 30 kJ/mol) is on par with that of the energetic phosphoric acid anhydride containing metabolite adenosine triphosphate (ATP).[80,81] Indeed, the energy stored in thioester hydrolysis is ordinarily harnessed in a variety of anabolic and catabolic reactions[82–84]. Although highly reactive towards nucleophiles, thioesters are kinetically stable in neutral pH-buffered solutions[85] suggesting that cellular *S*-deacylation would require specific enzymatic action. Though some S-acyl linkages have shown to be exceptionally stable[86–88], the labile nature of the thioester bond guarantees a 'deadline' for the many fatty thioacyl linkages[31,32,89–92]; in turn, *S*-palmitoylation gives rise to the dynamic membrane engagement that is necessary for subcellular trafficking, protein stability and activity of numerous proteins.[37,93,94]

Protein *S*-acylation was first observed over 35 years ago in viral envelope glycoproteins[43,95–97] and since then, has shown to be far-reaching having been ascribed to a growing list of diverse integral and peripherally associated membrane proteins including cytoskeletal elements, soluble enzymes, signal transducers, scaffolds, receptors, ion channels and cell adhesion molecules.[32,36,98–104] In light of this staggering diversity, no consensus amino acid sequence has been found to target proteins to *S*-acylation, although some general commonalities exist. Palmitoylation sites are frequently observed at either the terminal ends of proteins, within cysteine-rich domains or at juxtamembrane segments such as polybasic regions and transmembrane domains.[9,35,64,105] In addition, terminal protein palmitoylation sites often neighbor other stably linked lipid modifications such as N-terminal myristoyl and C-terminal prenyl groups[94]. Thus, the lack of an apparent consensus site would suggest that either non-specific thioacylating enzymes exist or that protein palmitoylation proceeds via nonenzymatic mechanisms.

Considerable efforts have been directed at delineating the *in vivo* mechanism by which fatty acyl groups install onto proteins. For a long time, *S*-acylation was thought to occur strictly via nonenzymatic means. Small molecule thiols are known to exchange with existing thioesters in a trans-esterification reaction called autoacylation[80], however, the physiological extent of this reactivity was unknown. To this end, short peptides from the lipidated termini of several palmitoylated proteins were shown to thioacylate *in vitro* when presented with lipid vesicles and metabolic acyl donors such as acyl-coenzyme A (acyl-CoA) species[79,106–108]. Autoacylation strongly depended on the presence of a lipid bilayer as well as the lipophilicity of the peptide which, in this experiment, was conferred by prior lipid installment. This was reasonable because acyl-CoAs are amphiphilic compounds[109] and like other detergents, would preferentially partition into the lipid vesicle therefore necessitating the peptide to engage the membrane before it can react with it. Later it was shown that the rate of *in vitro* autoacylation also correlated with sequence context surrounding the cysteine residue, with hydrophobic and basic residues accelerating the reaction. Again, this reactivity was justified since autoacylation is highly dependent on the deprotonated state of the thiol (i.e. thiolate), which basic residues are expected to promote by lowering the thiol's pK_a value[110,111]. Finally, a

number of full-length proteins, were reported to autoacylate *in vitro* when presented with palmitoyl-CoA (palm-CoA)[59,62], in particular myristoylated $G_{i\alpha}$ subunits which undergo near-stoichiometric conversion[112]. Overall, these studies contended that the impact of a particular sequence context on its degree of autoacylation implied that for some cysteines, the *S*-acylation site is intrinsically encoded and hence did not require enzymatic activity.

A number of seminal findings have since challenged the notion of physiologically-relevant autocatalytic palmitoylation events[113,114]. Namely, acyl-CoA binding proteins (ACBPs) were shown to inhibit the autoacylation reaction in a dose-dependent fashion. (ref) This was conceivable as cellular ACBPs bind tightly to and sequester activated fatty acids to prevent unwanted hydrolysis. Importantly, estimated cellular concentrations of all reactants suggested that the rate of *in vivo* autoacylation was negligible and could not account for the exceptionally fast palmitoylation rates observed for a number of signaling protein in cells[86,115]. Furthermore, the catalytic activities of later described thioacylating enzymes, which will be expounded upon in following subchapters, were shown to be largely unaffected by physiological concentrations of ACBPs.[113] Taken together, these experiments argued that poor availability of acyl-CoA donors would limit the extent of spontaneous *S*-acylation *in vivo* and suggested that instead, most palmitoylation events were likely to be driven by specific enzymes. Clearly, more precise and accurate tools for measuring the endogenous distribution and cellular levels of ACBPs, acyl-CoAs, acylated proteins and their non-acylated counterparts will be indispensible in aiding our understanding of spontaneous and enzymatic acylation events.

1.3 Tools and Techniques for Studying Protein S-Palmitoylation

This subchapter describe some of the most prevailing approaches that investigators currently use for the study of protein palmitoylation. The basic principles and specific details of each method are discussed succinctly. The primary objective of this portion is to highlight the benefits and limitations associated with each technique and offer potential improvements which may increase the reproducibility and reliability of a particular method.

Metabolic labeling by radiolabeled palmitate isotopes. Metabolic labeling with the radioactive tritiated fatty acid analog, [^{3}H]-palmitate, represents the most traditional method for detecting S-palmitoylation events and accurately quantifying the palmitoylated levels of a given protein.[116,117] In this experiment, cell cultures expressing the desired protein are treated with [^{3}H]-palmitate for a duration that depends on the turnover rate of the protein or its attached fatty acid. During this pulse period, the tracer, which is near identical to the naturally-occurring palmitate, is metabolically incorporated into endogenous sites of palmitoylation, resulting in radioactive proteins which can be detected by standard autoradiography techniques[118]. Alternatively, a chase period can be invoked to observe dynamic palmitoylation turnover. During this time, proteins overwhelmed with saturating concentrations of palmitate to facilitate the exchange of their tracer which results in decreased of metabolic labeling over time (Figure 1-2).

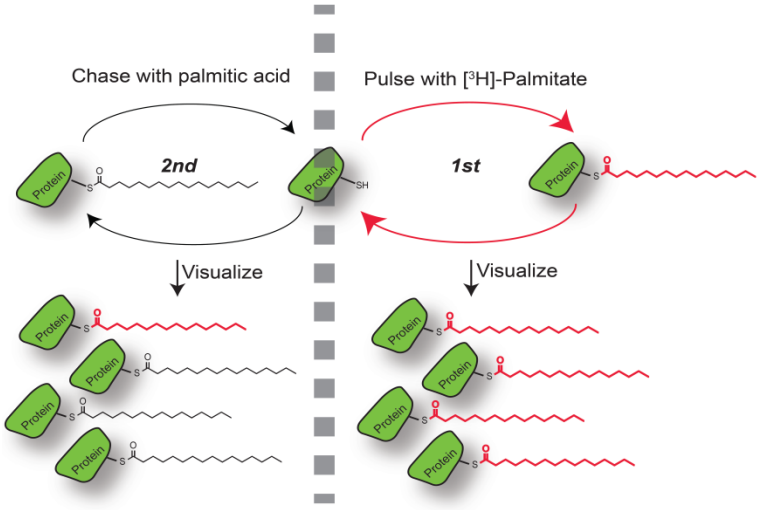

Figure 1-2 Monitoring dynamic palmitoylation turnover via the pulse-chase method.

Although regarded as the least invasive of all approaches, metabolic radiolabeling suffers from a number of drawbacks, some of which are shared with other metabolic incorporation techniques simply due to the nature of the experiment. First, metabolic methods in general, relay heavily on the incorporation efficiency of a given protein, which may be very low for both stably

palmitoylated proteins and long-lived palmitoylated proteins. Furthermore, metabolic methods require that the cells be 'flooded' with non-physiological concentrations of a single fatty acid variant which has shown to exert pleiotropic effects throughout metabolism[119–122]. Most importantly, due to its weak radioactive signal, this tritiated palmitate labeling requires extended X-ray film exposures lasting weeks to months, which historically impeded the study of this important posttranslational modification. Some have circumvented this issue by employing the radioactive iodinated fatty acid analog ω-[^{125}I]-palmitate to yield brighter signals resulting in reduced exposure times compared to fluorography with ^{3}H.[123] However, many have refrained from conducting experiments with this potent γ-particle emitting isotopologue due to serious health concerns.

Metabolic labeling by alkynylated palmitate analogs. A new approach to study protein palmitoylation uses a commercially available fatty acid analog, 17-octadecynoic acid (17ODYA)[10,124]. After brief metabolic labeling, cell lysates are reacted with azide-modified reporter tags, such as biotin-azide or rhodamine-azide, using the biocompatible click chemistry reaction (Figure 1-3). This simple approach forms a covalent linkage by the formation of a triazole, linking both reporter and metabolically labeled protein[92,125]. This method allows for reproducible labeling and identification of hundreds of palmitoylated proteins by in-gel fluorescence, as well as the capacity to measure their stability and turnover using traditional pulse-chase methods[86]. As oppose to radiolabel experiments, shorter experiment times may be exercised, and biotin attachment enables the selective enrichment of modified proteins for both detection (immunoblot) and enrichment (pulldown). The major disadvantage of this technique is the alkyne functionality of 17ODYA which makes this fatty acid distinct from all others, possibly restricting the range of incorporated proteins.

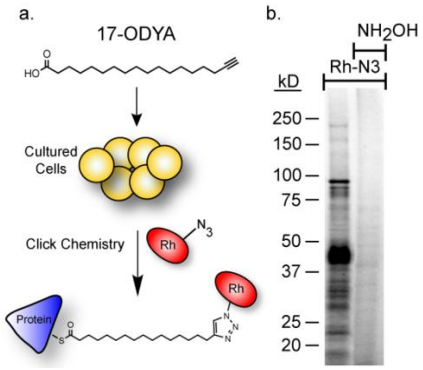

Figure 1-3 Protein palmitoylation detection via 17ODYA labeling. (a) Metabolic bioorthogonal strategy for detecting endogenously palmitoylated proteins with click chemistry. (b) Fluorescence gel-based analysis of palmitoylated proteins before and after thioester hydrolysis with hydroxylamine.

This metabolic labeling approach has been used in chemo-proteomic platforms for studying the global dynamics of protein palmitoylation[86,126]. Stable isotope labeling with amino acids in cell culture (SILAC) methods were employed to generate isotopically distinct (i.e. “light” vs. “heavy”) peptides for comparative quantitative mass spectrometry-based proteomic analysis. Dynamically palmitoylated proteins were then tracked by combining a pulse of 17-ODYA with a chase of excess palmitic acid (Figure 1-4).

Figure 1-4 Monitoring palmitoylation turnover via 17ODYA-enriched SILAC proteomics.

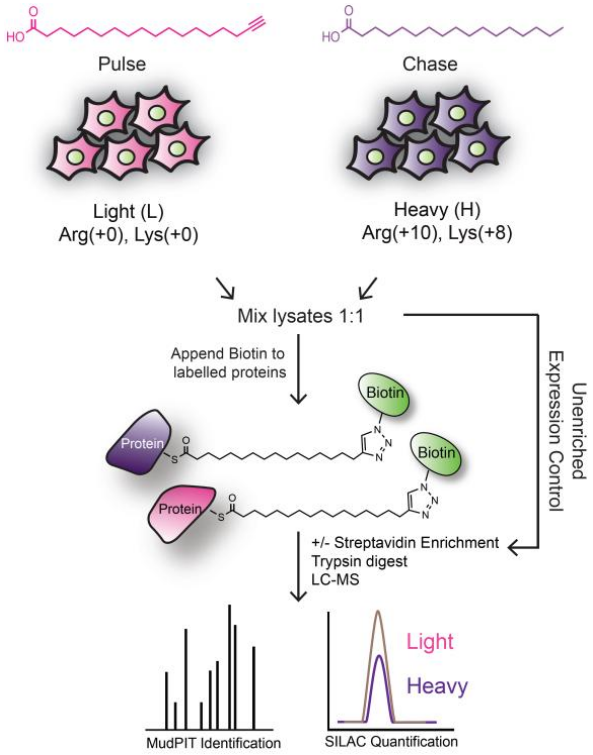

In a separate pulse-chase experiment, the isotopic pairs were treated after the initial 17ODYA pulse with the broad-spectrum lipase inhibitor hexadecylfluoro-phosphate (HDFP) or vehicle for 4 hours. After lysis and click chemistry-mediated ligation to biotin-azide, samples were enriched by streptavidin pull-down, combined, and digested with trypsin. Quantitative analysis was then performed using a high-resolution mass spectrometer. These experiments identified palmitoylation events which were stabilized by lipase inhibition, and those events for which rapid turnover is independent of inhibitor treatment (Figure 1-5).

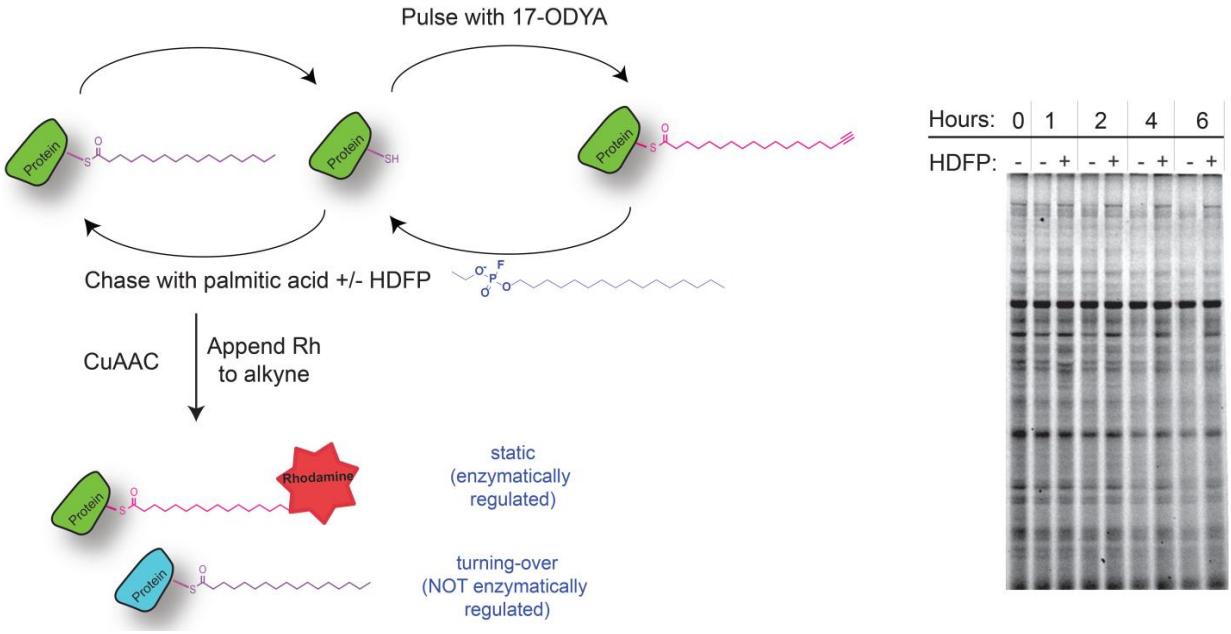

Figure 1-5 17ODYA pulse-chase experiments in the presence of HDFP identify enzyme-mediated depalmitoylation events.

Functional group exchange techniques. The labile nature of S-acylation remains one of the major obstacles that hamper the study of this modification. Acyl group exchange methods such as the well know acyl-biotin exchange (ABE) protocol[127,128] are novel enrichment strategies that have been used to selectively exchange native *S*-acyl groups with other stably attached functionalities such as the biotin affinity group in ABE[91]. In general, free cysteine thiols are first alkylated with a capping agent such the α,ß-unsaturated imide *N*-ethylmaleimide (NEM), and then half of the sample is treated briefly with the nucleophilic hydroxylamine (NH_2OH) reagent which, under the right conditions, selectively hydrolyzes thioester linked groups. The newly liberated thiols are then reacted with another alkylating agent coupled to an affinity tag like biotin. Stable biotinylated protein are then enriched with an appropriate affinity resin (e.g. streptavidin agarose) and can be detected by immunoblot or mass spectrometric platforms (Figure 1-6). Aside from the protocol being lengthy and often requiring larger amounts of protein, ABE, if not performed right, may suffer from both false positive and false negative results. False positives may occur either due to incomplete preliminary alkylation, enrichments of other short chain thioesterified modifications, and other non-specific reactivities which alkylating agents may exhibit, such NEM;'s reaction with

lysine side chains[129]. False negatives on the other hand, are mainly caused by the loss of thioester linkage before it can be selectively cleaved with NH_2OH.

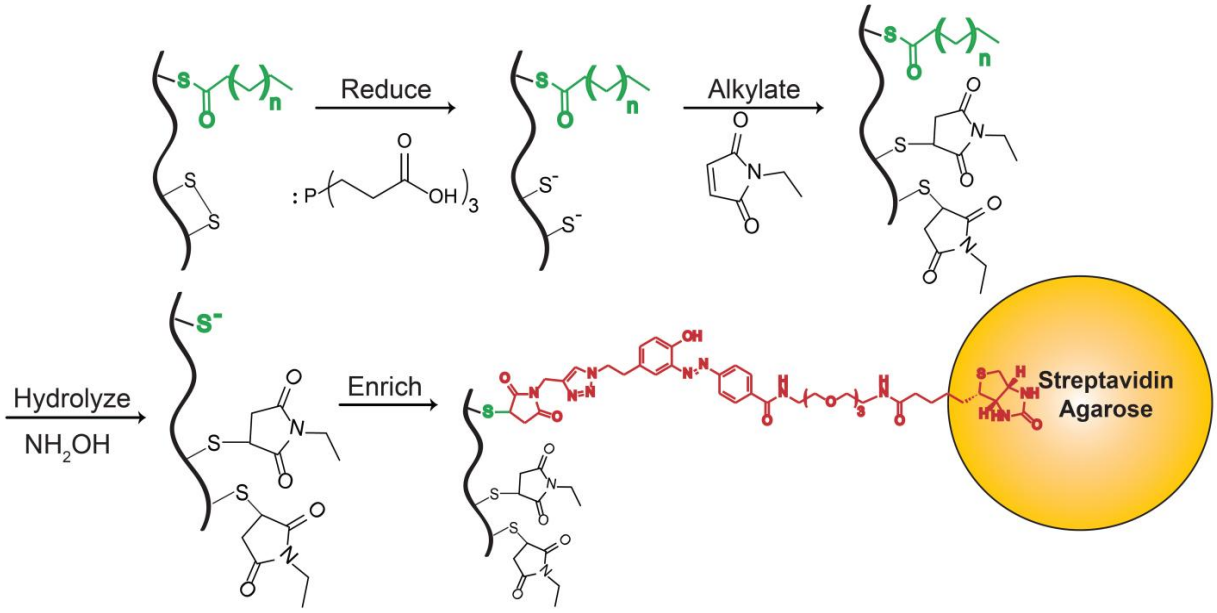

Figure 1-6 Acyl biotin exchange protocol resulting in enriched thioacylated proteins. Free thiols are typically reduced with a non-sulfur reducing agent such as tris-(2-carboxyethyl)phosphine to liberate disulfide which may interfere with subsquent steps. See main text for procedural details.

The major improvement offered by acyl exchange techniques is its ability to convert an otherwise fleeting linkage into a stable one, and in turn yield more reproducible experimental results. Given that any number of functional groups could, in theory, be exchanged with a thioester, an approach which exchanges thioesters with a molecule of a few kilodalton (kDa) mass may be used to measure the stoichiometry about the palmitoylation site. In principle, the typical ABE protocol would be followed until the final biotinylation step, which could be replaced with an alkylation reaction to a small protein (~10 kDa). This way, when the proteins are separated by SDS-PAGE and probed by western blots, the observed mobility shift can be used to calculated the fractions of the proteins that are acylated. Indeed, this type of methodology has been applied successfully to other challenging PTMs[130] and therefore should be feasible for *S*-acylation as well.

In conclusion all current detection techniques for thioacylation suffer from a common handicap: inability to reveal or decipher the chemical identity of the attached *S*-acyl group. Metabolic labeling methods only allow for the examination of proteins that

are willing to incorporate the tracer, some of which may not normally do so, thus acylated proteins featuring other acyl groups other than palmitate are excluded from further studies. Acyl exchange methods feature a different problem which technically speaking, does not exclude diverse thioacylated species from the analysis per se; instead, the chemical exchange of the acyl group, which is central to the success of this method, destroys the native acylation site essentially preventing one from investigating the endogenous acyl species. Thus, there are currently no *S*-acylation detection techniques that can be utilize for the study of variable-chain thioacylation events other than palmitoylation. Indeed better techniques will be necessary for characterizing the physiological roles and biophysical behavior of different *S*-acyl forms of a given protein.

In vivo localization techniques. Fluorescence microscopy experiments are the most routinely used means for assaying the subcellular localization and trafficking of palmitoylated proteins.[131–134] There are two general types of fluorescent experiments which differ by the genetic origin of the protein to be studied. Endogenous palmitoylated proteins can be typically monitored by end-point immunofluorescent experiments, in which cells must be fixed prior to probing the desired proteins with immunologically-based stains such as antibodies raised against the palmitoylated proteins.[135] The major obstacle associated with immunology-based methods is that the antibody cannot typically distinguish between the unmodified protein and its acylated counterpart, and therefore supplementary confirmation of the protein's palmitoylation state must be employed. A recent chemical biology strategy has circumvented this issue by coupling antibodies which detect either the target protein or the latent *O*-palmitoylation reporter fatty ω-alkynyl analog.[136] A signal is thus detected only when the target protein has its acyl group reporter installed. Indeed, these and other innovative approaches will accelerate cell biology studies of protein fatty *S*-acylation.

Exogenously expressed palmitoylated proteins are frequently used when the localization of mutant variants are to be assayed. A variety of fluorescence microscopy techniques are available for probing the dynamic localization behavior of a target protein, many of which rely on fusing the target protein to a genetically-encoded epitope tag. The green fluorescent protein (GFP), or its engineered variants, is by far the most featured tags, as it is amenable to diverse experimental conditions.[137] GFP tagging has

been used for obtaining both steady-state and transient localization information for many palmitoylated protein.[138–143] Whereas steady-state subcellular localization can be viewed with standard epifluorescent or confocal microscopes , a protein's three-dimensional diffusion characteristics have be monitored by fluorescence recovery after photobleaching experiments[144–147]. In these experiments, a certain region of interest such as a segment of the plasma membrane, is illuminated with a high-intensity laser and the fluorescence of the residing GFP-tagged protein is quenched. The dynamics of the surrounding fluorescing probes can now be monitored as they diffuse throughout the sample and 'fill in' the non-fluorescent patch. A recent study has used this technique to assay the contribution of protein palmitoylation to the membrane attachment of the axonal survivor factor NMNAT2.[148] In conclusion, like in most other fluorescence microscopy techniques, one should employ both positive and negative palmitoylation controls as these tools cannot differentiate between the palmitoylation states of the target protein.

1.4 Functions of Protein *S*-Acyltransferases

The current prevailing view in the palmitoylation field is that protein acylation events are principally mediated by a family of protein acyltransferases (PATs) in a context-specific manner.[36,37,79] These membrane bound enzymes, termed DHHCs, have been shown to specifically palmitoylate proteins using acyl-CoAs as lipid donors[140]. Despite their importance in a range of cellular processes and implication in human diseases[50,75,149–151], the mechanism, regulation, substrate specificities and physiological roles of many PATs remain undefined.

PATs were first discovered via elegant genetic and biochemical studies in yeast[152–154]. This fundamental finding led to the discovery of orthologous acyltransferases across all eukaryotic kingdoms implying that protein palmitoylation was catalyzed by devoted enzymes. As mentioned in an earlier chapter, some have speculated that the natural diversity of fatty acids incorporated into thioacylated proteins could be attributed to the broad acylCoA specificities of the corresponding PATs[155]. Indeed, the heterodimeric yeast PAT, Erf2/Erf4 and the human PAT DHHC2 both displays wide lipid substrate specificity seeing that they catalyzed comparable thioacylation reactions employing a variety of acylCoA chain lengths with different unsaturation degrees.[41,156] Furthermore, it was later confirmed that PATs showed exclusive preference to using metabolic acylCoAs as their acyl donors. Most importantly, PAT-mediated reactions were largely resistant to ACBPs which sharply contrasted with autoacylation's reported ACBP sensitivity[113]; Altogether, these results suggested that in cells, PATs had high affinity toward acylCoAs, and along with the discovery of endogenous PAT substrates[157], it was clear that enzymes mediated a majority of protein *S*-acylation events *in vivo*.

Soon after, It was realized, again in yeast, that PATs shared a central domain which genomic databases indicated was conserved in all eukaryotic genomes.[158,159] These PATs constitute a phylogenetic family of polytopic transmembrane proteins, all of which share a highly conserved cysteine rich domain (CRD) with a consensus *aspartate-histidine-histidine-cysteine* (DHHC) signature motif in its center (Figure 1-7).[160] At least twenty-three members of PAT DHHC enzymes are present in mammals, with most containing additional protein interaction motifs including *S*RC *h*omology *3*

(SH3) domains, *P*SD95-*D*LG1-*Z*O1 (PDZ) binding motifs, and ankyrin repeats. These auxiliary domains are thought to serve as key protein-protein interaction modules that direct PAT protein substrate selectivity (Figure 1-7), however, they could potentially serve other functions independent of acyltransferase activity[62,159,161–163]. To this end, human DHHC5 has shown to interact with the neuronal scaffolding protein, post synaptic density 95 (PSD95) but did not catalyze its acylation[163], whereas DHHC5 palmitoylation activity on Grip1b depended on PDZ domain interactions with the enzyme[162]. These conflicting results demonstrate that PATs can employ their interaction domains for additional functions outside of protein acylation.

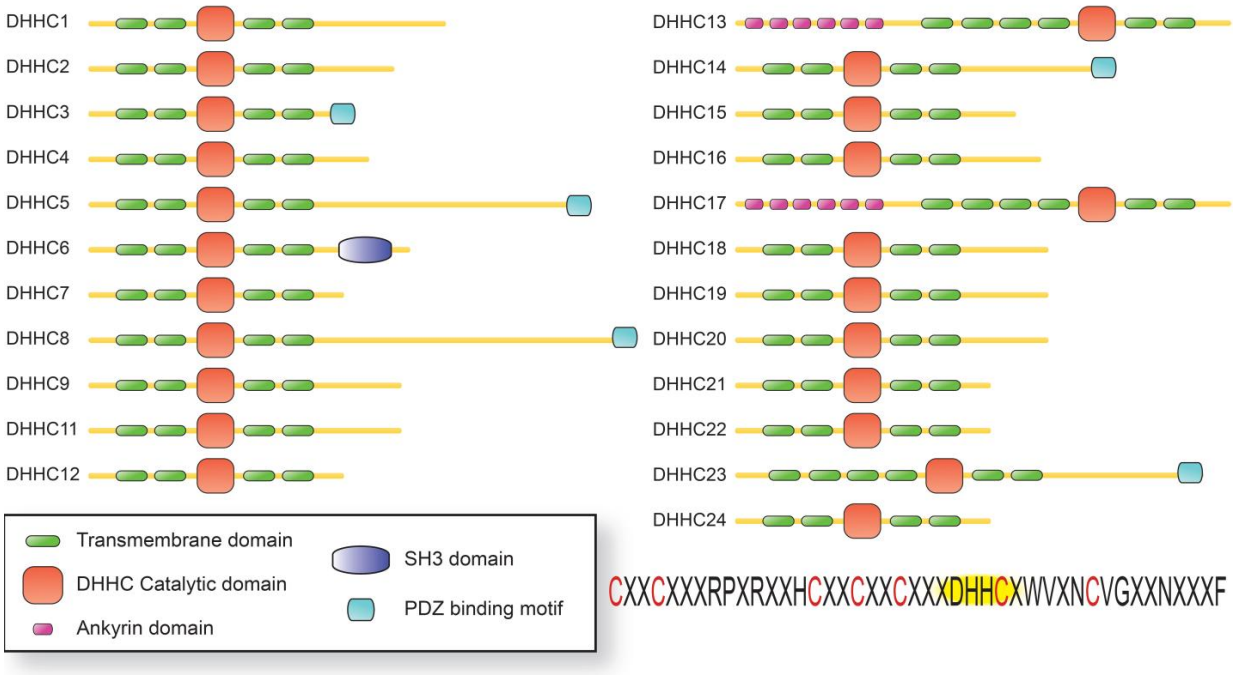

Figure 1-7 The modular architecture of human DHHC protein S-acyl transferases. Although there are no available crystal structures for PATs, they have been mainly characterized by their respective primary sequences which feature a the DHHC-CRD pictured at the bottom left and a variety of known protein-protein interaction motifs that are thought to guide substrate specificity and cellular functions.

Current attempts at annotating DHHC protein substrates typically rely on over-expression studies to ascertain which DHHCs lead to an increase in acylation levels of a given palmitoylated protein[164,165]. Thus, it generally appears that DHHC enzymes may share a large collection of protein substrates. In spite of being a thorough analysis of PAT activities, these types of experiments do not provide an answer as to which DHHC is the physiologically responsible acyltransferase. Instead, these heterologous studies may be skewed towards the activity of highly expressible enzymes and exclude PATs

which necessitate additional cofactors for activity, like the yeast Erf2/Erf4 enzyme[166]. Therefore, over-expression studies ought to be validated by subsequent genetic knockdown of DHHCs in question. In this regard, individual members have been suggested to differ in substrate specificity which may be a function of the distinct intracellular localizations found for different PATs further suggesting non-redundant roles in cells.[157,159,167,168] Some have speculated that the size and varied substrate specificities of the DHHC family may explain why unrelated *S*-acylation sequences exist in nature[169]. Certainly DHHC's conserved interaction motifs may obviate the necessity for such a consensus palmitoylation sequence.

Ever since their discovery in humans, DHHC PATs have been implicated in prominent diseases[151] in which they were found to be either silenced, mutated or even highly expressed in some cases. Some of these human illnesses include schizophrenia (DHHC8)[170], learning and cognitive disorders (DHHC5)[126], alopecia and amyloidosis (DHHC13)[171], Huntington's disease (DHHC17)[172], X-linked mental retardation (DHHCs 9,15)[173,174] and cancer (DHHCs 2, 9, 11, 17, 20)[151,175] Accordingly, assigning the functions and identifying the substrates of DHHC proteins is likely to lead to a better understanding of these complex diseases.

With regards to their enzymology, the mechanistic aspects of PAT activity have long been tackled from a qualitative angle given the physical nature of their acyl substrates and the current challenges in isolating and assaying DHHCs[93,176,177]. However, well-planned fluorescent and radiolabeling experiments have now been successful at addressing the transient kinetic behavior of DHHC-mediated thioacylation[41,113,132,156,178]. To this end, many DHHC PATs have been reported to autoacylate when reacted with acylCoAs. However, it was unclear whether this represented a transitory acyl-enzyme intermediate or reflected a stably acylated site on the enzyme. Thus, active site residues had to be determined to properly address this question. To this end, the high sequence conservation of the DHHC-CRD and its predicted cytoplasmic orientation (Figure 1-7) suggested this domain to be responsible for PAT activity[160]. Further support to this hypothesis was provided by a number of mutagenesis studies in which substitutions within the DHHC motif abolished the enzyme's auto- and trans-catalytic activities. Notably, these studies proposed the Asp-

His-Cys residues that were within the conserved motif to be potentially catalytic as each of these point mutants produced a catalytically-incompetent enzyme[179]. Based on these results, some suggested these D-H-C residues to form a catalytic triad by which Asp and His facilitate the formation of a Cys nucleophile that later becomes the thioacyl-enzyme intermediate (Figure 1-8, bottom). However, it was still unclear whether these residues were truly catalytic as the exact site of autoacylation could never be observed.

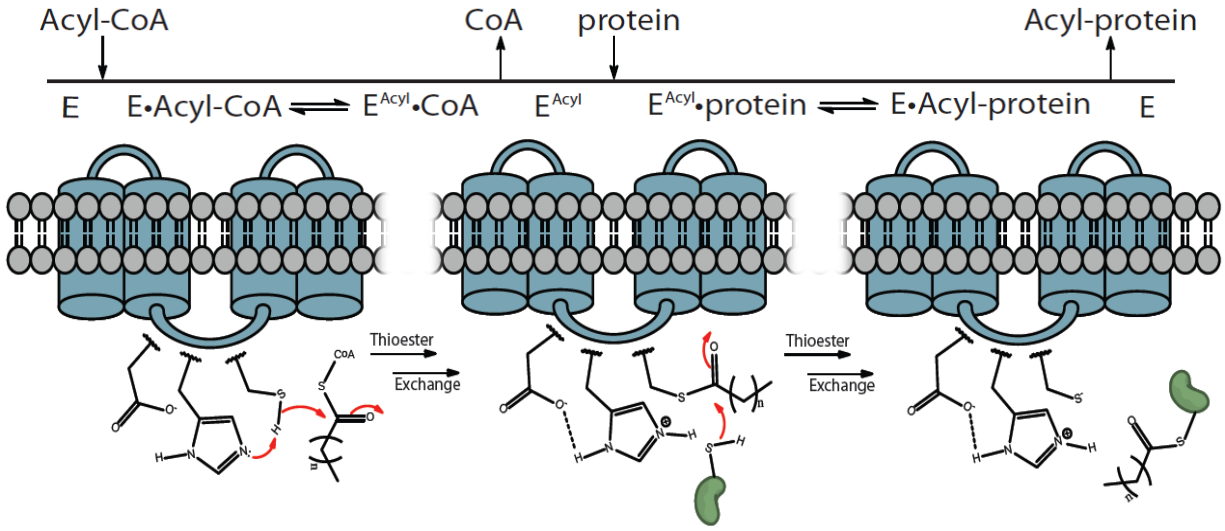

Figure 1-8 The currently accepted kinetic and chemical mechanisms of PAT-catalyzed protein *S*-palmitoylation. Radiolabeling experiments with palmitoyl-CoA have demonstrated that DHHC PAT catalysis follows a bi-bi ping pong kinetic mechanism. The PAT is first esterified by the incoming acyl-CoA substrate and then transfers the acyl group onto the cysteine of an appropriate protein substrate. Many questions still remain regarding how PATs achieve substrate specificity and the molecular basis for this ping pong mechanism.

Further studies have addressed the significance of PAT autoacylation in the context of the overall catalytic reaction. Instead of locating the exact site of the putative intermediate, experiments were designed to test whether such an intermediate existed at all[41,156]; namely, the transient enzyme intermediate would conceivably transfer its acyl chain onto an incoming substrate when presented with one. Investigations from two different DHHC studies confirmed that the PATs indeed transferred their acyl groups via a two step process kinetically referred to as a bi-bi-ping-pong mechanism (Figure 1-8, top). In summary, all of these studies contented that the Cys of the DHHC motif was the site of autoacylation which performed the subsequent thioacyl transfer onto protein substrates. Unfortunately, there still remains a large gap in our understanding of the exact nature of the catalytic residues, substrate specificity and regulation of PATs.

1.5 Pharmacological Agents for the Study of PATs

Considering that both PATs and their palmitoylated proteins are involved in surprisingly diverse cellular activities, it is absolutely imperative to have appropriate means for assessing the functional significance of the thioacyl modification. Unfortunately, a limited number of poorly-defined, protein S-acylation inhibitors exist, many of which have shown to exert pleiotropic cellular effects[117,180–183] (Figure 1-9). These compounds include the lipid-based inhibitors cerulenin, tunicamycin, and 2-bromopalmitate, as well as the high-throughput screen lead compound 2-(2-hydroxy-5-nitro-benzylidene)-benzo[b]thiophen-3-one which is commonly referred to as compound V. It is worth noting that not all palmitoylation inhibitors have been shown to be pharmacologically active towards DHHC PATs with some inhibiting protein palmitoylation events in an unknown fashion. Thus, DHHC-targeting inhibitors have been experimented as mechanistic tools to gain further insight into the enzymology of protein *S*-acyl transfer.[181,184,185] In this section, the details regarding palmitoylation inhibitors that have shown to possess PAT inhibitory activities are described. Thus, the unconfirmed PAT inhibitor, tunicamycin will not be discussed further and the reader is referred elsewhere for more details on this topic[117,180,186,187].

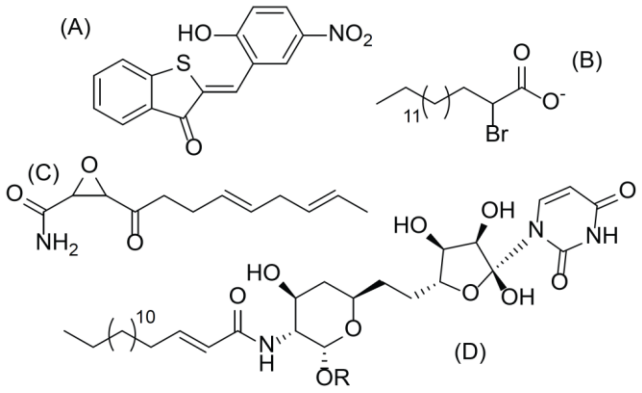

Figure 1-9 The chemical structures of current palmitoylation inhibitors. (A) depicts CV, (B) depicts 2BP, (C) depicts cerulenin and (D) tunicamycin.

2-Bromopalmitate. Among all available *S*-acylation inhibitors, 2-bromopalmitate (2BP) remains the most routinely used agent for the study of *S*-acylation in cells[75,184,188–193]. This brominated palmitate analog has shown to inhibit the catalytic activities of several DHHC enzymes in a time dependent irreversible fashion[185], although, at the time, it was unclear whether it specifically targeted the enzyme's catalytic residues. Akin to other α-halo carbonyl compounds, 2BP is predicted to possess electrophilic reactivity at the α-carbon of the fatty acid; specifically, 2BP is expected to undergo nucleophilic displacement reactions with a variety of physiological nucleophiles including histidine's

imidazole side chain, lysine's ε-amino group and cysteine's thiol functionality (Figure 1-10).

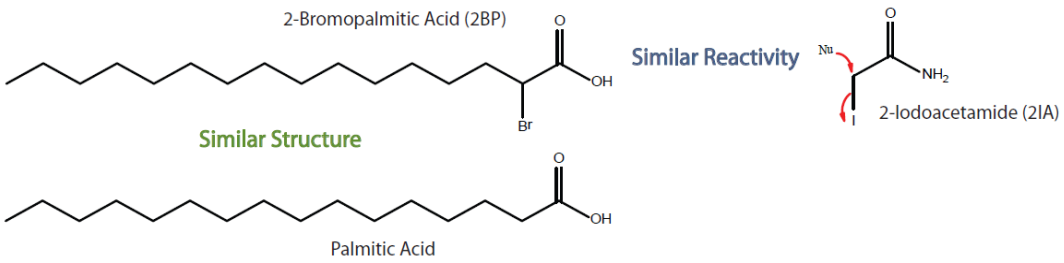

Figure 1-10 2BP structure and reactivity. The alpha-brominated fatty acid retains the activity of common alkylating agents, such as iodoacetamide, but gains access to membrane associated targets due largely to its lipophilic character and similarity to endogenous fatty acids. Thus, under physiological conditions, 2BP possibly partitions into cell membranes where it engages membrane bound enzymes and alkylates their active-sites.

This is quite reasonable since 2BP reactivity should parallel that of iodoacetamide, which is well known for alkylating cysteine residues[110,194–196] but can cross reacting with aforementioned residues[197–199]. Considering its chemical resemblance to ordinary fatty acids, 2BP has been notorious for inhibiting diverse integral and some peripheral membrane proteins[183,200–204]; some of these targets include fat metabolism enzymes such as fatty acid CoA ligase, carnitine palmitoyl transferase-1 and glycerol-3-phosphate acyltransferase as well as other cellular enzymes unrelated to fatty acid processing pathways which include NADPH cytochrome *c* reductase and glucose-6-phosphatase. Despite the reported non-specific effects, 2BP remained and still is the best known, most utilized inhibitor in a large number of studies probing the roles of both DHHC PATs and palmitoylated proteins in general[117]. For this reason, there are obvious uncertainties when interpreting palmitoylation data based on 2BP studies alone. Therefore, revealing the scope of 2BP targets and understanding the mechanism(s) by which it exerts its inhibitory palmitoylation effects will prove useful and impact all current investigations utilizing this inhibitor in probing the physiological role of acylation.

The diverse lipophilic targets of 2BP suggest two main attributes to its mode of inhibition: (1) 2BP primarily targets intrinsic membrane proteins that are intimately associated with hydrophobic components of the lipid bilayer or soluble proteins that bind tightly to fatty acids and molecules alike, and (2) it may react with either functionally conserved, mechanistic or reactive residues of proteins and enzymes (Figure 1-11).

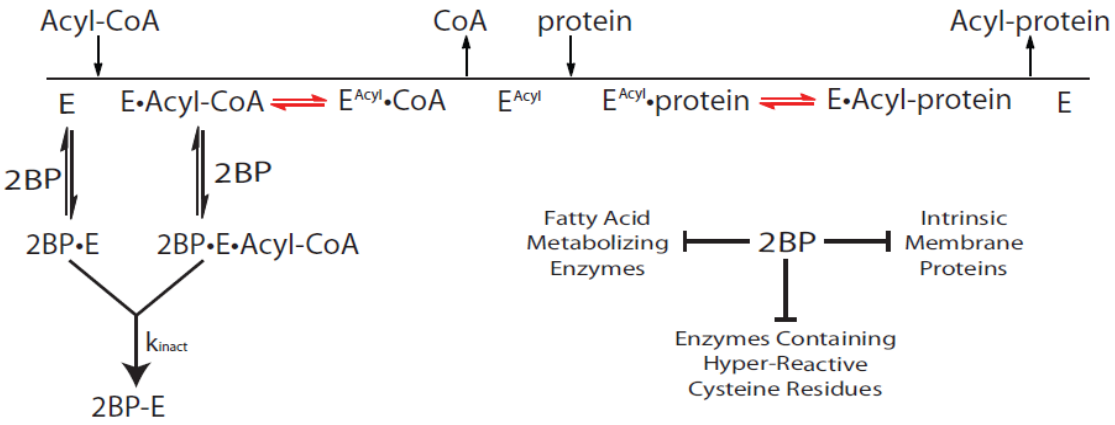

Figure 1-11 2BP inhibits PAT activity and other unrelated cellular enzymes with nucleophilic active-site residues. 2PB has been shown to block protein palmitoylation by inhibiting autoacylation of PATs which strongly suggest that it alkylates catalytic residues necessary for acylation activity. However, given that 2BP reacts with numerous, unrelated biomolecules, there is a possibility that it may inhibit palmitoylation by directly alkylating the incoming cysteines of PAT substrates as well. Catalytic steps colored in red have been shown to be sensitive to 2BP treatment.

With regards to PATs, 2BP has been suggested to covalently modify the catalytic cysteine thiolate of DHHC motif.[188] Although the exact chemical mechanism by which this occurs is incompletely understood, it is evident for a number of DHHCs, that 2BP inhibits PAT-mediated palmitoylation of their protein substrates *in vitro*.[185] These later kinetic studies showed that 2BP inhibits PAT autoacylation reaction, or specifically, the process in which the transient enzyme-acyl intermediate forms. This finding suggested that 2BP may target functional active site residues which normally perform the acyl transfer reaction onto the incoming protein substrate. These studies did not establish however, which of the presumed catalytic side chains were in fact modified by 2BP, although its α-carbonyl electrophilic reactivity suggest it could directly alkylate either the cysteine and or histidine side chains present in the DHHC-CRD. Clearly, there is a need to uncover the molecular basis for 2BP-mediated DHHC inactivation as it may prove useful in the development of PAT-specific, mechanism-based inhibitors, given its broad reactivity towards a number of DHHC members.[188] Altogether, the numerous studies in which 2BP has been employed as a protein acylation inhibitor suggest that the long chain α-halofatty acid may serve as a suitable reactive group in the design of an active site-directed probe for studying both the DHHC family of protein acyltransferases and their palmitoylated protein substrates (Figure 1-12).

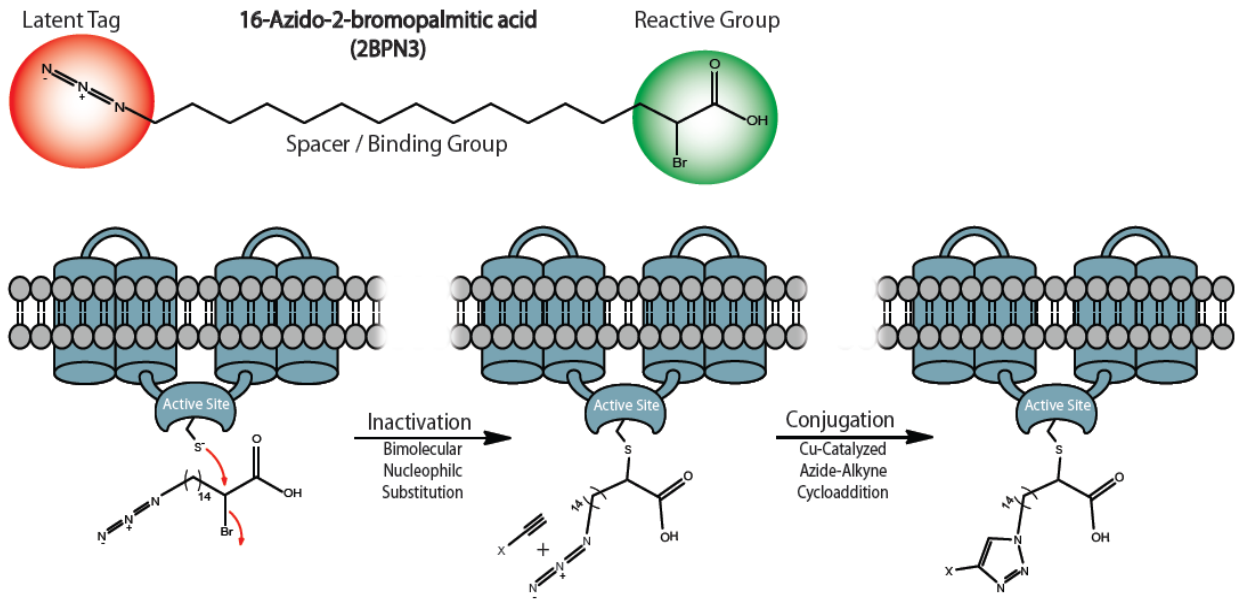

Figure 1-12 A strategy of using 2BP reactivity to enrich membrane associated enzymes such as DHHC PATs. By using a derivative functionalized with a latent affinity tag, such as an azide, 2BP could be used as an enrichment platform for membrane bound enzymes given its broad target specificity.

Cerulenin. Cerulenin, chemically known as [*2R,3S*]-2,3-epoxy-4-oxo-7,10-*trans,trans*-dodecadienoylamide, is a lipid-based natural product derived from the fungus *C. caerulens*[205]. This compound was first described as an antibiotic agent that potently inhibited virtually all known types of biosynthetic fatty acid synthase (FAS) complexes[206], and therefore was expected to impact the levels of fatty acids and metabolically related compounds[207]. Detailed studies of these biosynthetic systems revealed that cerulenin inhibited FAS by modifying the condensing enzyme subunit ß-ketoacyl ACP synthase. Later on, cerulenin was found to inhibit the palmitoylation of various proteins such lipophilin, CD36 and p21Ras[117,180]. In an attempt to improve its selectivity towards inhibiting protein palmitoylation, a series of cerulenin derivatives were synthesized and their effects on protein palmitoylation and FAS activity were examined[208,209]. Interestingly, analogs substituted with longer aliphatic acyl chains demonstrated increased potency with regards to inhibiting Ras isoform palmitoylation and abolished its activity towards FAS.

While this structure-activity relationship (SAR) study was promising to offer a more-targeted palmitoylation inhibitor, the mechanism by which cerulenin blocked palmitoylation remained elusive. The natural cerulenin molecule is composed of a core epoxy-carboxamide group which is α-substituted with an octadienoyl side chain (Figure

1-9). It was noted, that in aqueous solutions, the molecule exists in an equilibrium between two forms, one being the open chain epoxy-carboxamide and the other being the fused bicyclic hydroxylactam. Importantly, the SAR studies and the well-established reactivity of thiols towards activated epoxides suggested the electrophilic epoxy-carboxamide moiety enabled cerulenin to alkylate active site cysteine residues of both FAS and presumably DHHC PATs[208]. Recent studies with clickable cerulenin analogues has demonstrated that similar to 2BP, this inhibitor formed a hydroxylamine-resistant adduct with PATs, but was more potent towards DHHCs than 2BP.[182] This boost in activity was attributed to the nucleophilic preference of thiols for the electrophilic epoxide when compared to the a structurally analogous α-halo carbonyl. Interestingly, mutagenesis studies showed that although cerulenin alkylated PATs it did not modify the putative catalytic cysteine of the enzyme.[182] This result was puzzling as cerulenin has been shown to compete with 2BP alkylation which was confirmed to be dependent on the active state of the enzyme.[188] Thus, the investigators proposed that given its resemblance to coA, cerulenin covalently attached to active site-proximal cysteines which blocked the entry or docking of 2BP and resembling acylCoA substrates. Despite not being a true mechanism-based inhibitor of PATs, the clickable cerulenin reporter was demonstrated to label all human DHHC members whereas 2BP, as will be shown in chapter two, could only label a fraction of tested PATs.

It is worth noting that like 2BP, cerulenin likely exerts pleiotropic effects on cellular fatty acid metabolism as it was shown to inhibit HMG-CoA synthetase activity and result in reduced biosynthesis of cholesterol and related molecules[180]. In addition, cells treated with cerulenin typically demonstrate reduced palmitate incorporation into certain phospholipids.[117] Most importantly, proteomic studies have identified greater than 200 membrane associated cellular targets of cerulenin which include diverse lipid processing enzymes such as LPC acyltransferase and MBOAT7.[182] Lastly, it remains a mystery as to why the combined hydrophobicity and enhanced electrophilicity of cerulenin does not permit its engagement to the catalytic thiol of DHHC active sites.

Compound V. Compound V (CV) is a non-lipid compound that was among five candidate PAT inhibitors discovered via a high-throughput screen of nearly 17,000 small molecules.[210] Lead compounds were selected based on their ability to block

palmitoylation of model substrates in a cell-based assay[180]. Later studies with purified DHHC enzymes revealed that from all the lead inhibitors, only CV had significant pharmacological activity towards PATs though it was shown to be less potent than 2BP (IC_{50} > 10 μM).[185] CV exerted inhibitory effects on both PAT autoacylation and enzyme-mediated protein acylation activities. Initial cell-based screening efforts suggested CV had selective pharmacological action towards *N*-myristoylated but not prenylated palmitoylated proteins, suggesting that this compound may inhibit a subset of DHHCs that exhibit the corresponding substrate specificity. However, this hypothesis was not corroborated in purified PAT studies revealing that CV equally inhibited two DHHC enzymes with apparent differential specificities towards peptides mimicking the aforementioned palmitoylation sites.

As opposed to all other validated PAT drugs, CV is the only compound that does not resemble fatty acids or related biomolecules (Figure 1-9), and appears to exhibit reversible inhibition behavior with PATs given that enzyme activity could be recovered by diluting out the inhibitor. This reversible property was perplexing seeing that CV features an α,ß-unsaturated ketone moiety (i.e. Michael acceptor) which are known to be exceptionally reactive towards and form stable bonds to thiols[211–216] such as those contained in the active sites of DHHCs. It is possible that CV could form a covalent thioether adduct with PATs and that inhibitor reversibility could be conferred through a retro-Michael addition reaction which have been shown to take place in a number of glutathione *S*-transferase-inhibitor Michael-adducts[217,218]. However, this mode of novel PAT inhibition remains to be investigated.

Taken together, the current suit of PAT drugs highlights the need for high affinity, relatively selective PAT inhibitors that could be used to accurately assign the biological roles of enzyme and substrates of this widespread modification. Ideal pharmacological agents would be expected to target DHHC members in a mechanistically related fashion, such as competing with DHHC's specific acylCoA-dependent autoacylation and react at or around the catalytic center of the enzyme. Indeed, efforts towards PAT inhibitor developments have been impeded by the lack of efficient, *in vitro*, high throughput assays which can directly probe acyltransferase activity or active site occupancy. In addition to providing invaluable pharmacological tools, the search for

compounds that exhibit tuned DHHC specificity may yield potential therapeutic agents as the importance of palmitoylation in pathophysiology suggest PAT-specific inhibitors could benefit the treatment of various human diseases.

1.6 Functions of *S*-Acyl-Protein Thioesterases

Due to the unstable thioester linkage, protein palmitoylation undergoes steady hydrolysis in cells, generally with a half-life of less than a few hours. As discussed earlier, this hydrophobic modification is critical for the function, trafficking, and localization of diverse proteins with central roles in adhesion, signaling, and organelle structure. Recent proteomics studies have annotated hundreds of palmitoylated proteins[86,91,124,126,150,219,220], uncovering a widespread role for such a hydrophobic modification. Unlike static modifications like protein prenylation or myristoylation, protein palmitoylation provides a unique mechanism to reversibly regulate the membrane association of modified proteins. Indeed, dynamic palmitoylation of oncogenic HRas is required to mediate cell transformation.[221] Furthermore, activation of Ras or the G-protein $G\alpha_s$ stimulates palmitoylation turnover,[222,223] suggesting palmitoylation dynamics may be an essential trigger in the activation or deactivation of distinct signaling pathways. In this model, protein palmitoyl thioesterases catalyze the de-palmitoylation and release of certain proteins from the plasma membrane, potentially attenuating membrane-coupled signaling pathways (Figure 1-13). The released proteins can then undergo re-palmitoylation by endomembrane-bound DHHC palmitoyl-transferases, restoring palmitoylation and resetting the cycle.

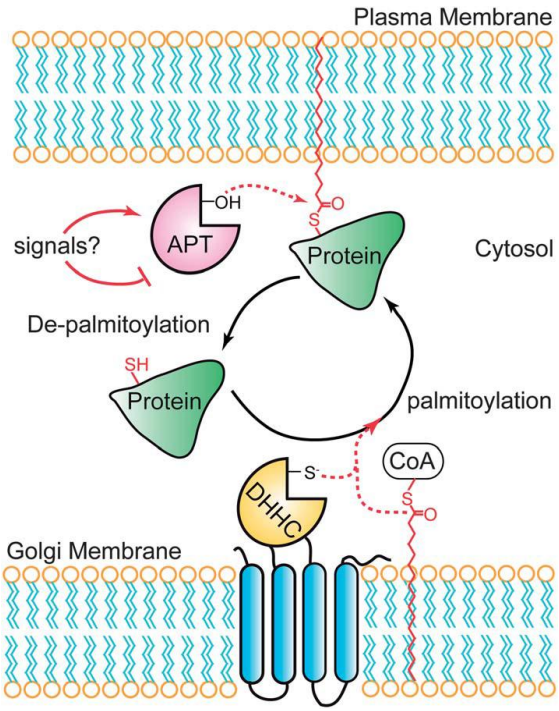

Figure 1-13 A dynamic S-palmitoylation cycle regulates the membrane association and activity of certain palmitoylated proteins. Specific stimuli cause an acyl protein thioesterase to catalyze thioester hydrolysis of palmitoylated cysteine residues. De-palmitoylation liberates the protein from the plasma membrane, allowing it to segregate to the cytosol disrupting interactions with membrane-associated signaling complexes. The protein can then undergo re-palmitoylation by Golgi resident DHHC palmitoyl transferases, transport back to the plasma membrane, and re-associate with signaling partners.

Given the evidence that HRas participates in an acylation/deacylation cycle,[12] a putative HRas thioesterase termed acyl protein thioesterase (APT1) was identified from soluble rat liver fractions.[224] This enzyme was previously characterized as lysophospholipase I (LYPLA1),[225] but has several hundred-fold higher activity as a protein thioesterase. [224] APT1 removes palmitate from diverse palmitoyl protein substrates in vitro.[224,226] Genetic deletion of the yeast homologue of APT1 shows a minor decrease in the turnover of palmitate on $G\alpha_s$, yet has no defects in growth, mating, or deacylation of other palmitoylated proteins.[227] Despite these results, lysates from APT1-knockout yeast lack in vitro $G\alpha_s$ palmitoyl thioesterase activity. [227] Importantly, deletion of APT1 has no effect on lysophosphatidylcholine (LPC) hydrolysis activity, suggesting it is not a functional lysophospholipase. [227]

A second lysophospholipase II (APT2), is 68% homologous toAPT1,[228] but surprisingly is slightly more efficient than APT1 at depalmitoylating semi-synthetic NRas.[229] The axonal protein GAP-43 or HRas are more rapidly de-palmitoylated after APT2 overexpression.[230] Phylogenic analysis shows that invertebrates evolved only one APT enzyme, while vertebrates evolved two (APT1 and APT2) (Figure 1-14).

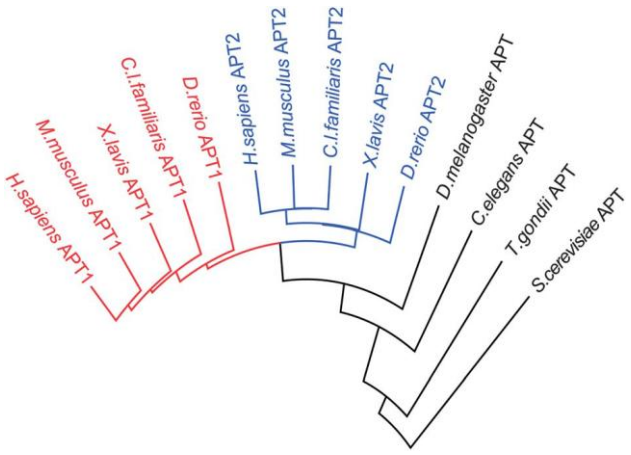

Figure 1-14 Shared homology between vertebrate and invertebrate acyl protein thioesterases. Vertebrates evolved two distinct APT enzymes, whereas invertebrates evolved a single APT enzyme. Phylogeny alignments were generated using DIALIGN, anchored at the catalytic serine residue.

Both APT1 and APT2 have themselves been identified as palmitoylated proteins,[89,219] although the predicted palmitoylation site is not conserved in canine APT1 or in vertebrate APTs. In mammalian neurons, APT1–mRNA is translationally repressed by a synaptic microRNA complex.[231,232] Upon glutamate stimulation, the repressive complex is degraded to allow local translation of APT1 in synaptic spines.[232] APT1expression induces a reduction in spine volume potentially by depalmitoylating $G\alpha_{13}$ and reducing synaptic RhoA activation.[231] In addition, a recent in vivo RNAi screen identified APT2 as a candidate regulator of oncogenic HRas-dependent malignancy.[233] A third more distant

homologue lysophospholipase-like 1(LYPLAL1) contains a narrow substrate-binding pocket unable to accommodate long-chain fatty acids,[234] and genetic studies support a role in obesity.[235] Overall, APT enzymes represent candidate protein palmitoyl thioesterases, but little is known about their substrates or dependence on upstream signals.

To address the proteome-wide dynamics and the contribution of enzymatic de-palmitoylation, we recently applied non-radioactive bioorthogonal labeling approaches to selectively enrich palmitoylated proteins with enhanced turnover dynamics. This approach uses the commercially available fatty acid analogue 17-octadecynoic acid, which upon exogenous addition, is efficiently incorporated into endogenous sites of protein palmitoylation.[124,236] After sufficient labeling, harvested cell lysates are conjugated to biotin–azide by copper-catalyzed click chemistry for subsequent streptavidin enrichment and mass spectrometry annotation. Using “pulse-chase” labeling methods, we profiled de-palmitoylation dynamics in mouse T-cells. Cells were first labeled with 17-ODYA, then after some time “chased” with excess palmitic acid with or without the non-selective lipid-like serine hydrolase inhibitor hexadecylfluorophosphonate (HDFP).[86] This hydrophobic mechanism-based covalent inhibitor targets approximately 20 serine hydrolases characterized by their common preference for lipid-like substrates, including APT1 and APT2, but not LYPLAL1. We hypothesized that any candidate thioesterase is likely a serine hydrolase inhibited by HDFP. Quantitative proteomic analysis identified a subpopulation (<10%) of palmitoylated proteins that undergo rapid cycling mediated by one or more serine hydrolases targeted by HDFP.[86] This subset includes Ras family GTPases, G-proteins, and scaffolding proteins implicated in malignancy. This data confirms that enzymes functionally contribute to palmitoylation hydrolysis in cells, and HDFP inhibition is sufficient to block any enzyme mediated palmitoylation turnover. Furthermore, given the relatively small subset of oncogenic signaling and scaffolding proteins, inhibiting de-palmitoylation may perturb key signaling pathways involved in malignancy.

1.7 Pharmacological Agents for the Study of APTs

As discussed in the previous subchapter, APT enzymes are members of the α/ß-hydrolase family of serine hydrolases.[237] The catalytic serine nucleophile forms a covalent acyl-intermediate with substrates, enabling the development of covalent mechanism-based inhibitors. Over the last decade several small molecule inhibitors of APTs have been described.[92] These include both reversible and irreversible inhibitors, which have been useful tools in several studies supporting a functional role for APTs in enzymatic depalmitoylation. APT inhibition is reported to suppress MAPK signaling and attenuate growth of certain Ras-transduced hematopoietic cells,[238,239] as well as modulating the membrane association of the estrogen receptor in hippocampal slices.[240] APT inhibition also enhances invasion of the parasitic protozoan *T. gondii* into human cells,[241,242] suggesting unique regulation across evolution. In the following paragraphs, each reported APT inhibitor to date is described with regards to its chemotype, details regarding potency, selectivity, and biological evaluation. This includes a discussion on the application of competitive activity-based protein profiling (ABPP) methods to profile inhibitor selectivity and target occupancy in biological systems.[243]

Benzodiazepinediones. Early efforts towards the development of APT1 inhibitors were rationally designed based on substrate mimicry of a dually palmitoylated and farnesylated peptide (Figure 1-15). A peptide-imitating benzodiazepinedione core was fused to S-farnesyl cysteine methyl ester and an acyl-sulfonamide to mimic the serine hydrolase tetrahedral intermediate,[244] yielding a low-nanomolar APT1 inhibitor (compound 10, IC50 = 27 nM). Intermediates lacking the farnesyl moiety were 5-times less potent (compound 6, IC50 = 148 nM), but presumably more soluble, and were tested in cells. Cells microinjected with the inhibitor showed complete mis-localization of NRas away from the plasma membrane, disrupting NRas-dependent PC12 cell neuronal differentiation. Adding 30 µM inhibitor to the cell growth media caused a similar block of neurite outgrowth, suggesting efficient cellular uptake. These impressive initial compounds confirmed the importance of APT enzymes in modulating Ras dynamics in cells, and inspired further efforts to develop more drug-like APT inhibitors.

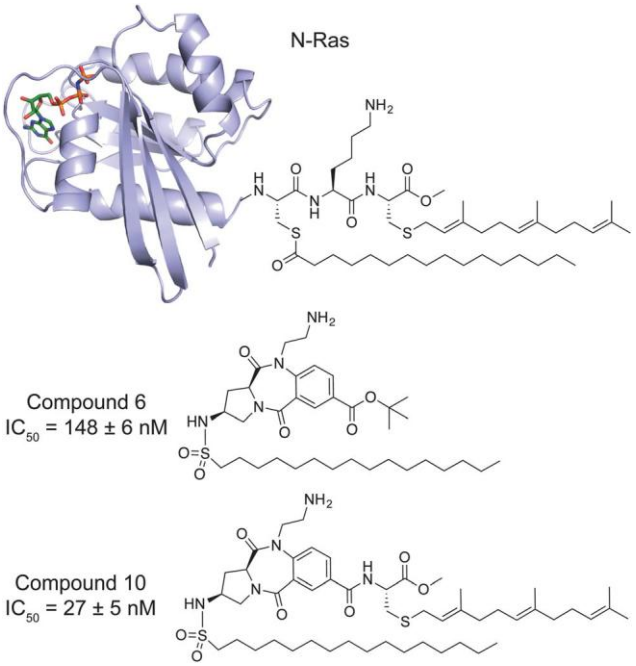

Figure 1-15 Lipidated N-Ras and peptido-mimetic benzodiazepinediones. Lipopeptide mimics for targeting APT1 are based on the C-terminal portion of lipidated N-Ras (Top, PDB 5P21). A peptide-resembling benzodiazepinedione core serves as a central scaffold equipped with both a primary amine to mirror the lysine side-chain and an essential hydrolysis-resistant hexadecylsulfonamide moiety imitating a palmitoyl thioester tetrahedral intermediate. (Middle, 6) was further functionalized with a farnesylated cysteine methyl ester to yield a mimic of the C terminus of a fully processed N-Ras (bottom, 10) which exhibited potent inhibitory activity.

ß-Lactones. ß-Lactone serine hydrolase inhibitors are best characterized by the over-the-counter weight loss drug tetrahydrolipstatin (THL or Orlistat).[245] Originally identified as a natural product from *Streptomyces toxytricini*,[246] THL is representative of diverse bacterial ß -lactones with functional roles as bacterial effectors. Upon oral delivery, THL is a mechanism-based inhibitor of several digestive lipases that acts by preventing fatty acid intestinal absorption. After nucleophilic attack of the lactone ester and ring opening, the subsequent acyl-enzyme hydrolysis is slow, rendering the enzyme predominantly in an inactive state[247] (Figure 1-16A).

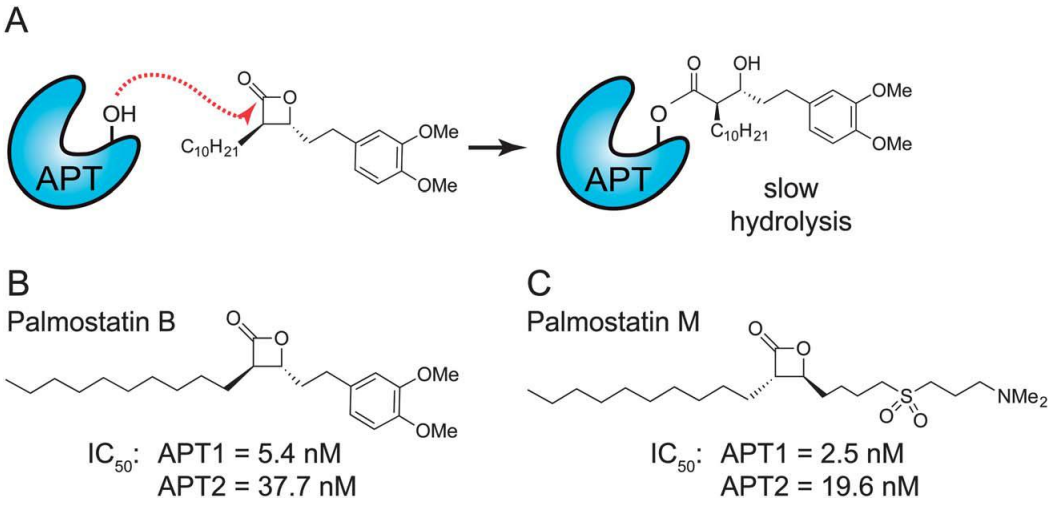

Figure 1-16 Mechanism-based ß-lactones inhibit APT enzymes. (A) APT enzyme inhibition by Palmostatin B. Attack on the electrophilic lactone by the catalytic serine hydroxyl leads to a transient acyl-enzyme adduct, which slowly hydrolyzes to regenerate the active enzyme. (B) Structure of Palmostatin B. This inhibitor was discovered through the synthesis and screening of a small library of compounds on the basis of active-site similarity between APT1 and gastric lipase, and the fact that b-lactones are known

lipase acylating reagents. (C) Structure of Palmostatin M. This inhibitor was developed based on the structural similarity of lysophosphatidylcholine. A common recognition motif was identified, consisting of an electropositive dimethylamino tail imitating choline, an electronegative sulfoxide to mirror the phosphate, a central electrophilic trans-ß-lactone and a lipophilic tail resembling the palmitate moiety to increase affinity to the lipid-binding pocket of the enzyme.

In order to discover novel APT1 inhibitors, a series of ß -lactone derivatives were synthesized and profiled against APT1, leading to the discovery of the chiral *n*-decane substituted ß-lactone Palmostatin B (IC_{50} = 5.4 nM)[248,249] (Figure 1-16B). Palmostatin B is readily membrane-permeable, and directly reacts with APT1 and APT2 as both a substrate and an inhibitor in live cells.[248]

To study the effects of APT inhibition, Palmostatin B treated cells were imaged after microinjection of fluorescently labeled NRas, or following transfection of YFP-NRas in MDCK cells.[248] Palmostatin B addition led to YFP-NRas mis-localization and decreased compartmentalized NRas activation. These experiments likely required high nanomolar concentrations of labeled NRas for fluorescence imaging, which may have encroached on the K_m of APT1 towards palmitoylated NRas (~1 µM)[229] and potentially enhance any observed phenotypes. Further experiments showed that Palmostatin B (50 µM) altered the morphology of oncogenic HRas transformed cells, restoring them to a less spindly appearance with increased E-Cadherin membrane localization. Palmostatin B displays poor stability in cell culture, and was added to cells at effectively 10^4 times the IC50, which may diminish selectivity. Interestingly, siRNA knockdown of APT1 did not statistically alter the ratio of golgi to plasma membrane NRas. This suggests either insufficient APT1 knockdown, or that Palmostatin B inhibits other protein thioesterases, such asAPT2 (Ki = 34 nM)[229] that may contribute to NRas processing. Further experiments showed that addition of 30–100 µM of Palmostatin B dose-dependently impedes the growth of HRas or NRas transduced hematopoietic cells, but does not affect cells transduced with a non-palmitoylated isoform of KRas.[239] Such high inhibitor concentrations may inhibit other intracellular hydrolases, but clearly define a role for de-palmitoylation in Ras regulation. Overall, Palmostatin B has provided important pharmacological evidence of protein palmitoylation dynamics in live cells.

In efforts to selectively target APT isoforms, a polar sulfone moiety was added to the ß-lactone scaffold to mimic the polarity of lysophosphatidylcholine (Figure 1-16C), yielding the improved analogue Palmostatin M (APT1 IC50 = 2.5 nM).[249] Despite

synthesis of a diverse library of greater than 50 compounds, no APT1 or APT2 isoform selective inhibitors were identified, which may signal a structural limitation of the ß-lactone scaffold. Palmostatin M similarly induces NRas mis-localization from the plasma membrane and partially restores E-Cadherin localization at cell–cell junctions in HRas-transformed MDCK cells.[249] Because ß-lactones form a semi-stable covalent complex with their targets, an alkynyl Palmostatin M analogue was synthesized to annotate potential cellular targets.[229] Lysates were labeled with the alkynyl probes, conjugated to a tri-functional rhodamine/biotin–azide by copper-catalyzed click chemistry, enriched with streptavidin, and analyzed by in-gel fluorescence or mass spectrometry to identify candidate target proteins. These experiments confirmed APT1 and APT2 as major Palmostatin M targets, but also identified other serine hydrolases including the lysosomal thioesterase PPT1 and retinoid- inducible serine carboxypeptidase (RISC). While these compounds are exceptionally potent, non-specific inhibition and poor drug-like properties limit the application of these probes for in vivo studies.

Boronic acids. In order to discover new chemotypes that inhibit APT enzymes, an immobilized library of <15 000 natural products and inhibitors was assayed for APT binding.[250] In this approach, inhibitors were covalently attached to glass using a tri-fluoromethylaryldiazirine photo-crosslinking system, and then incubated with recombinant GST-fusions of APT1 or APT2. Binding was detected after incubation with anti-GST antibodies and visualization with fluorescent secondary antibodies. Four similar bis-borinic acid and bisborinate ester structures were identified (Figure 1-17), which were further validated by surface plasmon resonance. Boron-based inhibitors of serine hydrolases act by boronate coordination of the side chain hydroxyl nucleophile of the catalytic serine residue, mimicking the tetrahedral intermediate.[251]

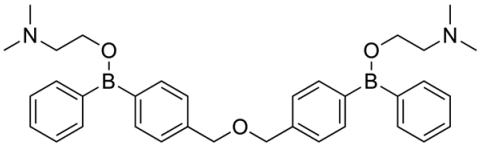

APT1: K_i = 0.99 ± 0.13 μM
APT2: K_i = 0.73 ± 0.20 μM

Figure 1-17 Bis-boronic acid inhibitor of APT enzymes. Representative bisboronic acid-based inhibitor (compound 4) and reported inhibitory values for both APT1 and APT2.

Several boron-containing drugs are in clinical use, including the proteasome inhibitor Bortezomib (Velcade), the DPP4 inhibitor Januvia, ß-lactamase inhibitors, and many

more under development.[251] Kinetic analysis of the diphenylboronic acids showed potent inhibition of APT1 (Ki = 0.99 ± 0.13 μM) and APT2 (Ki = 0.73 ± 0.20 μM).[250] Other analogues were slightly less potent, but showed a slight preference towards APT2. Similar to Palmostatin B, the diphenylboronate ester inhibitors demonstrated a dose-dependent inhibition of Erk1/2 phosphorylation and induced a less spindly phenotype in HRas transduced MDCK cells. While this study does not provide any data on the selectivity of these analogues, it does validate boron-containing inhibitors as a new APT inhibitor chemotype, and provides further phenotypic support that APT enzymes functionally regulate Ras-dependent signaling pathways.

Triazole ureas. Significant progress has been made in the development of selective serine hydrolase inhibitors through optimization of carbamates, leading to analogues with exquisite selectivity and potency as covalent probes.[252] Despite considerable effort, carbamates fail to reach a broad subset of serine hydrolases, including APT enzymes.[253] During efforts to explore novel covalent inhibitor scaffold of serine hydrolases, N-heterocyclic ureas were identified as a new chemotype for serine hydrolase inhibitor development.[254] Both carbamates and N-heterocyclic ureas undergo nucleophilic attack by the active-site nucleophilic serine, leading to formation of a non-hydrolysable carbamylated acyl-intermediate (Figure 1-18A). These inhibitors are bioavailable, selective within the serine hydrolase enzyme family, and maintain activity both in vitro and in vivo.[254,255] Furthermore, a facile, convergent synthesis of triazole ureas accelerated the development of selective sub-nanomolar, in vivo active, selective inhibitors for acyl peptide hydrolase (APEH), as well as low nanomolar inhibitors of PAFAH2 and ABHD11[254] with limited medicinal chemistry efforts.

The development of triazole urea inhibitors was reinforced by guided medicinal chemistry using competitive fluorophosphonate (FP) ABPP probes.[243,256] In this assay, a complex proteome is mixed with a triazole urea analogue to achieve enzyme inhibition. Next, a reporter-tagged FP-probe is added that irreversibly reacts with all active serine hydrolases. Accordingly, any reduction in probe labeling corresponds to inhibition. Typically, the FP-tetramethylrhodamine (FP-TAMRA) is used for rapid gel-based analysis of both the potency and selectivity of a candidate inhibitor across all active serine hydrolases in a specific cell line or tissue isolate. For less abundant enzymes,

quantitative analysis is performed using FP-biotin, followed by streptavidin enrichment and mass spectrometry annotation.[254] This approach guides medicinal chemistry efforts primarily based on both selectivity and potency towards a specific target.

Triazole urea libraries were synthesized by click chemistry of alkynyl variants with azide, followed by conjugation to diverse carbamoyl chlorides.[254] This two-step approach leads to regioisomers at the N_2 (major) and N_1 (minor) positions, which may potentially have differential inhibitory properties.[255] After identification of a candidate triazole urea lead for APT1, 19 additional analogs were synthesized with variable substitutions at the three positions: the substituent at 4-position of the triazole (R_1), the substituent of the piperidine ring (R_2), and the identity of the atom at the 4-position of the piperidine ring (X)[257](Figure 1-18A).

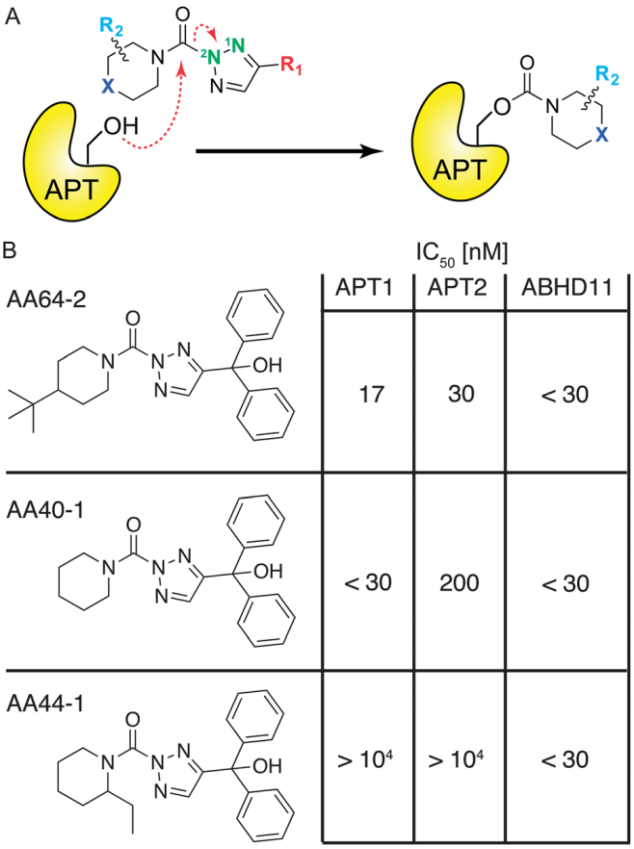

Figure 1-18 Triazole urea covalent APT inhibitors. (A) Mechanism of triazole urea inactivation of APT enzymes. The APT nucleophilic serine hydroxyl attacks the urea, releasing the triazole and leaving a stable carbamate adduct, inactivating the enzyme. (B) Selectivity and potency of optimized triazole urea inhibitors determined by gel-based competitive ABPP. AA64-2 is highly potent and selective for APT enzymes, with the exception of the uncharacterized hydrolase ABHD11. AA44-1 is highly selective for ABHD11, and can be used as a control probe.

Each round of medicinal chemistry was guided by gel-based competitive ABPP profiling. Optimization led to the identification of a highly potent tertbutylpiperidine (R_2, X), and improved selectivity by addition of a bulky diphenyl methanol (R_1).[257] These inhibitors retain potency and selectivity in live cells with no observed toxicity. Despite significant effort, little selectivity was achieved against the unannotated hydrolase ABHD11. This is less of a concern, since highly selective analogues targeting ABHD11 could be used as control probes.[254]

The parasitic protozoan *T. gondii* is a close relative to the malaria parasite *P. falciparum*, which expresses hundreds of palmitoylated proteins, many which are required for infectivity. In order to explore the potential of APT inhibition in the parasitic life cycle, Palmostatin M was compared side by side with a piperidine (X), diphenyl methanol (R_1), triazole urea (AA401).[241] This analogue inhibits human APT1 (IC50 < 30 nM) and APT2 (IC50 = 200 nM), as well as ABHD11, Esterase D, and APEH (Figure Figure 1-18B).[257] These compounds were assayed for inhibition of *T. gondii* invasion, egress, and intracellular growth. By competitive ABPP methods, the *T. gondii* APT homologue TgASH1 was completely inhibited by 10 µM Palmostatin M or as little as 100 nM of AA401. The parasite's lytic cycle is severely inhibited by incubation with 10 µM of either Palmostatin M or AA401, but this result is eliminated when the inhibitor concentration is lowered to 1 µM. Additional analysis showed neither of the compounds had any effect on parasitic egress. Interestingly, Palmostatin M reduces parasitic invasion, while AA401 inhibition may slightly enhance invasion. Furthermore, deletion of TgASH1 had no quantifiable effect on the membrane localization of known *T. gondii* palmitoylated proteins by immunofluorescence and no effect on the growth or life cycle. Since *P. falciparum* does not encode a TgASH1 homologue, it is unclear if TgASH1 accounts for all protein thioesterase activity in apicomplexans.[241] Overall, the potent triazole urea inhibitor AA401 appears to have increased selectivity and less off-target effects, providing a promising alterative to Palmostatin B for *in vivo* studies.

Chloroisocoumarins. In a parallel T. gondii study, a forward chemical genetic screen was assayed to discover modulators of parasitic invasion. This study led to the discovery of compounds that attenuate invasion, including compounds targeting the redox chaperoneTgDJ-1.[258] In addition, the chloroisocoumarin JCP174 and similar derivatives were identified as enhancers of parasitic invasion,[242] and removing the aromatic amine substituent in the position-7 abolished activity, providing an inactive analogue (Figure 1-19B). Enhanced invasion was dose-dependent, and correlated with improved gliding motility, an established indicator of enhanced invasion. Invasion was enhanced within 5 minutes of inhibitor treatment with no observable effects on viability or intracellular replication.

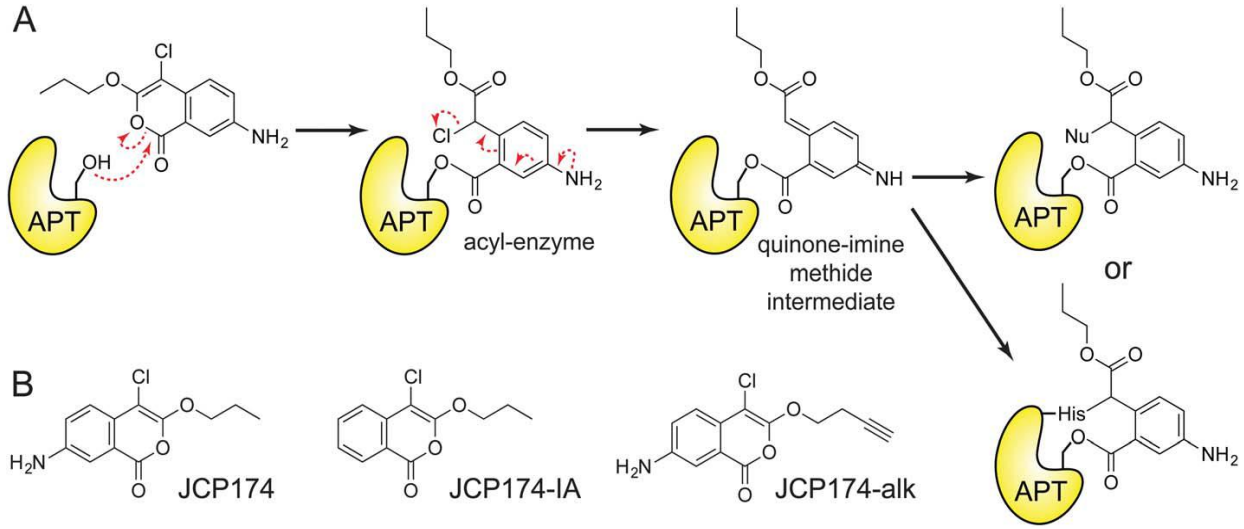

Figure 1-19 Mechanism-based chloroisocoumarin JCP174 inhibits T. gondii APT. (A) Putative mechanism of APT irreversible enzyme inactivation by JCP174. Attack on the electrophilic carbonyl by the catalytic serine hydroxyl leads to the formation of an acyl-enzyme derivative, unmasking a reactive α-chloro carbonyl group. Elimination of chlorine yields a quinone-imine-methide intermediate that is susceptible to nucleophilic attack by either the solvent or the enzyme's catalytic histidine side-chain producing a labile acyl-enzyme derivative or a stable alkylated acyl-enzyme adduct, respectively. (B) Structures of the active chloroisocoumarin inhibitor JCP174 (left), the inactive control lacking 7-amino substitution JCP174-IA (middle) and the click-compatible analog derivatized with an alkyne functional group JCP174-alk (right).

Chloroisocoumarins were first identified as mechanism-based covalent inhibitors of serine proteases.[259] Chloroisocoumarins have limited stability and are susceptible to both serine and cysteine nucleophiles, leading to enhanced reactivity and significant potential off-targets. Indeed, JCP174 originated as a human elastase inhibitor (k_{obs}/[I] = 54,000 M^{-1} s^{-1}),[260] but may also be reactive towards other proteases and hydrolases. This class of double-hit irreversible inhibitors first reacts with the enzyme's serine nucleophile to generate an acyl-enzyme intermediate. Elimination of the α-chloro group produces a highly electrophilic quinone-imine methide, which is susceptible to attack by accessible nucleophiles including the activated histidine of the catalytic triad (Figure 1-19A). While this mechanism was not explicitly demonstrated for TgASH1, the analogous chlorine elimination is predicted to produce a reactive electrophile.

In order to determine the functional target(s) of JCP174, parasite proteomes were treated with FP activity-based probes to profile potential serine hydrolase targets.[242] In-gel competitive ABPP analysis reported a single serine hydrolase target of JCP174. Additionally, an alkynyl analogue, JCP174-alk, was used to directly enrich

targets after copper-catalyzed click chemistry to a biotin–azide and streptavidin enrichment. Mass spectrometry proteomics identified several proteins where JCP174-alk enrichment was reduced by competition with JCP174, including the APT homologue TgASH1 (IC_{50} = 1.32 μM). This finding corroborates the enhanced invasion trend reported after treatment with AA401,[241] although JCP174 induces a stronger and more significant enhancer phenotype. Furthermore, incomplete conditional knockdown of TgASH1 enhanced invasion, while a genetic knockout showed no effect and was unresponsive to JCP174 treatment. Recombinant TgASH1 was able to catalyze the *in vitro* depalmitoylation of established palmitoylated proteins with roles in invasion, and JCP174 treatment similarly enhanced their co-fractionation with membranes, suggestive of altered palmitoylation dynamics. In summary, chloroisocoumarins represent an additional chemotype targeting APT enzymes, and highlight how forward chemoproteomic screens can identify new regulatory pathways in parasitic invasion.

Piperazine amides. While several covalent chemotypes have emerged for APT enzymes, none are selective for either isoform. In the absence of an APT2 crystal structure, rational design of isoform selective inhibitors has been challenging. In collaboration with the NIH Molecular Libraries Production Center Network (MLPCN), both human APT1 and APT2 were assayed against a library of 315 004 compounds[261] to identify new inhibitor chemotypes and explore the potential to identify isoform-selective leads. This high-throughput screening (HTS) effort used a fluorescence polarization-based competitive ABPP assay, termed FluoPol-ABPP[262] (Figure 1-20). In this approach, recombinant APT enzyme is incubated with fixed amount of a candidate inhibitor (10 μM), followed by a short, time-dependent addition of fluorophosphonate–rhodamine (FP-TAMRA). Upon covalent alkylation of the nucleophilic serine, the fluorescence polarization increases relative to enhanced anisotropy of the enzyme–fluorophore complex. Based on these parameters, any loss of polarization identifies potent inhibitors able to effectively compete with the irreversible covalent reaction. This assay routinely yields Z-factors >0.8, providing a robust approach to identify novel isoform selective APT inhibitors. Importantly, the FluoPol-ABPP assay is performed under time-dependent non-equilibrium conditions, providing a primary selection for

inhibitors with potent k_{off} constants, which correlate with enhanced residency time and improved *in vivo* pharmacokinetics.[263]

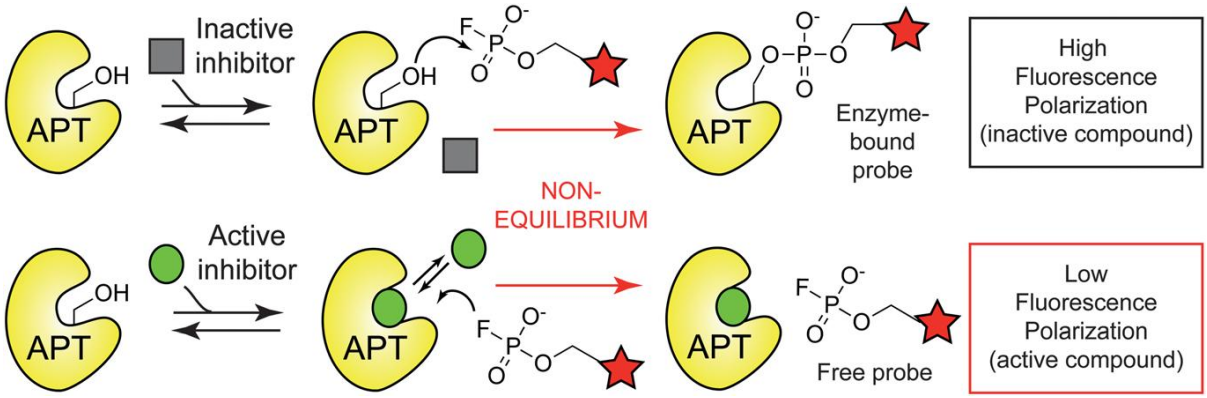

Figure 1-20 FluoPol-ABPP high-throughput competitive assay to discover new APT inhibitor chemotypes. Inhibitor discovery by active site occupancy profiling with the activity-based probe FP-TAMRA. APT enzyme is pre-incubated with inhibitor, and then under non-equilibrium conditions, treated with FP-TAMRA, which irreversibly competes with candidate inhibitors. Activity is reported by a change in fluorescence polarization induced by the increased anisotropy of the enzyme–probe complex.

Separate HTS screens were performed for APT1 and APT2, yielding hit rates of 0.156% and 0.380%, respectively.[257,261] Each hit compound was re-tested in a confirmatory screen, which validated 69% APT1 inhibitors, and 66% APT2 inhibitors. This list was then manually filtered to exclude non-selective compounds identified in similar HTS assays for the serine hydrolases RBBP9 and PME1, and the cysteine-dependent enzyme GSTO.[264] In total, 91 APT1, 61 APT2, and 95 dual APT1/APT2 inhibitors were selected for in-gel ABPP confirmatory analysis. This filtered group of inhibitors included one triazole urea, but largely converged to a common (>1/3) piperazine amide chemotype. This motif bears striking similarity to triazole ureas, since each contain a five-membered ring (furan,thiophene, or triazole) linked across an amide/urea with a *N*-heterocycle. Furthermore, due to the large diversity of the library, a structure–activity relationship emerged, identifying APT1 inhibitors with extensions from the piperazine arm, and APT2 inhibitors with hydrophobic extensions off the thiophene arm. Surprisingly, many of the inhibitors were selective for a specific APT isoform, an elusive property not found with other chemotypes. Overall, the most potent inhibitors were characterized in a fluorogenic substrate assay, providing K_i values in the 200–300 nM range, a surprising success for leads taken directly from the screening library (Figure 1-21). Interestingly, gel-based competitive ABPP shows stark differences in

potency between the APT1 and APT2 compounds, yet steady-state kinetic analyses yielded effectively similar K_i values. These findings suggest the APT inhibitor's potency is derived primarily from its small k_{off} value, and highlight how such non-equilibrium assays can improve selection for compounds with improved residency times.

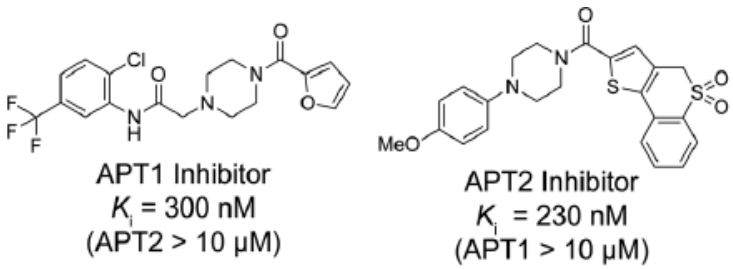

Figure 1-21 Lead isoform-selective inhibitors for APT1 and APT2 identified by FluoPol-ABPP.

Competitive assays with aliphatic FP-TAMRA proceeded to completion quickly under standard conditions, making it difficult to capture the optimal kinetic window in competitive experiments involving reversible inhibitors.[261] To circumvent this problem, competitive ABPP assays were performed using a less reactive hydrophilic probe, FP-PEG-TAMRA. This probe is a poor substrate for APT enzymes, slowing the reaction kinetics enough to assay active site competition. Such findings have significant implications for competitive ABPP selectivity assays with reversible inhibitors, since different enzymes may react with ABPP probe variants with distinct kinetic windows.

For both APT1 and APT2, a small library of <10 analogues were assayed to establish a preliminary structure–activity relationship.[261] For the APT2 lead inhibitor, the (*p*-methoxyphenyl)-piperazine arm was intolerant to substitutions in the ortho and meta positions. Further modifications on the thiophene arm were more tolerant, suggesting opportunities for further optimization. Importantly, the (*o*-methoxyphenyl)-piperazine analogue completely lost activity, providing a non-reactive control analogue. For the APT1 inhibitor, a similar negative control compound was identified with an α-methyl group substituted at the amide linkage. Inhibitor selectivity was confirmed by gel-based competitive ABPP, but also by SILAC-ABPP, a quantitative mass spectrometry method to quantify inhibitor occupancy with increased sensitivity.[254] This approach confirmed isoform selective inhibition across the serine hydrolase enzyme family for each lead inhibitor. These experiments demonstrate how competitive ABPP methods can be used to profile reversible inhibitors in complex proteomes, although the relative reactivity of

each enzyme towards the probe may vary. Therefore, when using competitive ABPP methods to assay reversible inhibitors, it is important to recognize that variable ABPP probe reaction rates can skew observed selectively profiles.

In order to validate target occupancy in vivo, each lead inhibitor was injected into mice.[261] After some time, an alkynyl triazole-urea probe was injected to profile residual active enzymes. This probe is poorly reactive with APT enzymes, providing an appropriate kinetic window to profile target occupancy in vivo. Since the rate of the triazole urea probe reaction with APT enzymes is slow, it was then possible to harvest tissues and analyze the results from the *in vivo* competition. The alkynyl triazole urea probe demonstrated isoform selective APT inhibition in the brain, kidney, lung, and heart. No inhibition was observed in the liver, which accumulates the triazole urea probe and likely distorts the reaction stoichiometry to out-compete the reversible inhibitors. Reduced inhibition was observed in the brain, suggesting these compounds are less efficient at crossing the blood–brain barrier. Overall, piperazine amide APT inhibitors are isoform selective, potent, and *in vivo* active inhibitors of APT1 and APT2 with no identified off-targets, making them the most promising, drug-like inhibitors to date.

In conclusion, the recent development of APT inhibitors has accelerated our understanding of the cellular regulation of palmitoylation, but has also provided a platform to advance new methodologies in inhibitor identification, selectivity profiling, and cellular validation. APT enzymes are conserved in eukaryotic organisms, suggesting a common biological function, which in mammals includes protein de-palmitoylation of certain target proteins. Surprisingly, there are no reported phenotypes for APTs in standard invertebrate model organism, including yeast, drosophila, and *C. elegans*. This raises the possibility that for these invertebrates (1) enzymatic depalmitoylation may not be essential, (2) functionally redundant hydrolases compensate for APT deficiency, or (3) APT enzymes are not primarily de-palmitoylases. Future studies demand the generation of vertebrate knockout systems to profile APT mutant phenotypes in higher organisms. Current data suggest APT enzymes are responsible for regulating dynamic palmitoylation, but many of the reported experiments rely on over-expression studies and report subtle changes, leaving room for additional interpretations. With the development of new potent and selective inhibitors and bio-

orthogonal labeling methods, it is now possible to directly answer these questions on endogenous palmitoylated proteins. Ongoing efforts to optimize APT1 and APT2 inhibitors will require a structural understanding of inhibitor binding, which promises to add structure-guided design principles to focus new medicinal chemistry. Improved competitive inhibitors are the next logical path towards developing selective pharmacological tools for in vivo functional analysis of protein de-palmitoylation.

1.8 Signaling Functions of Dynamic Palmitoylation

Unlike any other lipid-based PTM, *S*-palmitoylation can be subjected to a variety of regulatory mechanisms. This happens because both enzymes that attach and remove this modification are frequently co-employed to tightly control the palmitoylation state and hence activity of a given protein[32,89,103,148,174,265]. This unique mode of protein lipidation, which is now described for numerous palmitoylated proteins, has been suggested to modulate a protein's activity in much of the same way as the highly exploitable protein phosphorylation events.[31,36,63] Signaling proteins in particular, have shown to possess switch-like palmitoylation behaviors that could only be possible if specific palmitoylation and depalmitoylation catalysts were intimately involved in their transduction.[98,178,266,267] Certainly, it is logical for palmitoylation to play such a central role in protein signaling seeing that all extracellular-induced signaling cascades must begin at the plasma membrane and propagate into the aqueous environments of the cell[3]. Thus, it is common for highly dynamic palmitoylated proteins to serve the role of the so-called second messenger as they possess transitory membrane association which allows for shuttling between membrane and cytosolic compartments to transmit the necessary transduction signal[36,268–271] (Figure 1-22).

The number of reports featuring signaling proteins that undergo dynamic palmitoylation cycles has increased dramatically.[89,90,272–275] Throughout these studies, dynamic palmitoylation was shown to be indispensible for transient membrane association, trafficking, and segregation of signaling proteins into lipid microdomains. For example, lipid anchoring of the small GTPase HRas has been shown to be essential for its ability to transduce cellular growth and proliferation.[26,64,276] The palmitoylation behaviors of Ras family members have been well documented since they are all frequently mutated in cancers and potentiate oncogenic growth pathways.[50,277–282] Interestingly, the palmitate turnover of inactive, GDP-bound ,HRas was found to be accelerated by 15-fold upon growth factor stimulation, going from a turnover half-life of almost three hours to just fifteen minutes.[223] Growth factors, which presumably stimulate candidate protein thioesterases, leads rapid de-palmitoylation of HRas, forcing a redistribute from the plasma membrane to the Golgi apparatus, where it is gradually re-palmitoylated and trafficked back to the plasma membrane where the cycle is

restarted[283–285]. Similarly, G-protein alpha subunits are also rapidly de-palmitoylated after activation, as well as multi-domain scaffolding proteins such as the neuronal membrane associated guanylate kinase (MAGUK) PSD-95[286,287]. Despite the growing popularity of dynamic palmitoylation, the exact pairs of opposing enzymes responsible for these events are often unaddressed. A deeper understanding of both the static and dynamic roles of protein palmitoylation is critical for defining the spatial and temporal regulation of cellular growth pathways.

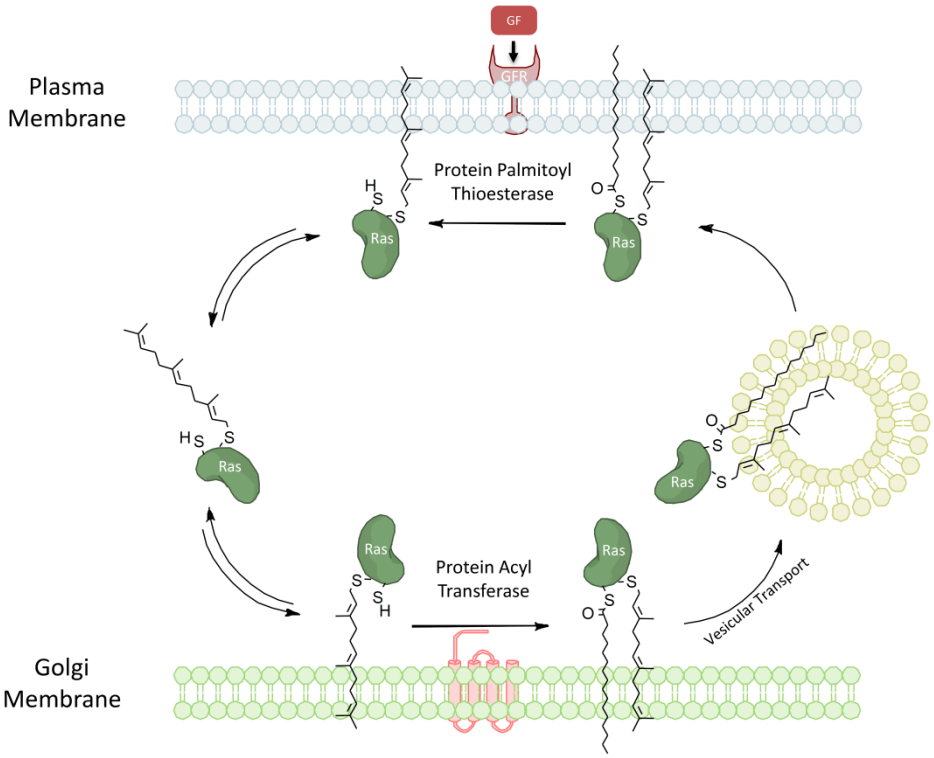

Figure 1-22 The palmitoylation of many, but not all, proteins is dynamic and can be modulated in response to cell stimulation. A specific example is the palmitoylation turnover cycle of NRas, an important growth signaling protein that is mutated in a large number of human cancers. Farnesylated NRas exhibits a weak membrane affinity that mediates its interaction with Golgi membranes. Palmitoylation at this compartment promotes a stable membrane association. The dual-lipid modified Ras can then be trafficked to the plasma membrane by the vesicular transport system to meet up with its signaling partners. In response to a stimulus, such as growth factor binding at its receptor, a putative protein palmitoyl thioesterase hydrolyzes the acyl group, thus decreasing Ras's membrane affinity resulting in membrane release and cytosolic diffusion before re-palmitoylation at the Golgi. Thus, dynamic palmitoylation plays an important role in regulating membrane association, cellular trafficking and activity of many proteins. Other examples of dynamically palmitoylated proteins include GNAS, PSD95 and eNOS, all of which are signal transducers. Please note the neither proteins or lipids depicted are drawn to their relative sizes.

Until recently, direct *in vivo* evidence for a depalmitoylating enzyme has been lacking, although APT proteins have been attributed with multiple in vitro

depalmitoylating activities.[224,227,288] Several exciting findings have emerged from pulse-chase proteomic studies of 17ODYA-enriched proteins. First, palmitoylation sites on most proteins were found to be relatively static.[86] These stable modifications could represent sites from various transmembrane proteins, many of which are known to retain their acyl groups throughout the protein's lifetime[63,88,289]. Therefore, only a small subset of palmitoylated proteins demonstrated accelerated turnover. This dynamically palmitoylated group of proteins comprise of scaffolds, Ras-family GTPases, G-protein alpha subunits, and PDZ-domain containing polarity proteins – all of which are signaling components critical for cellular transformation and tumor initiation[290,291]. Second, the broad-acting serine lipase inhibitor hexadecylfluorophosphonate (Figure 1-5) demonstrated that de-palmitoylation of this subset of signaling/scaffolding proteins was enzymatically-controlled and was likely mediated by member(s) of the serine hydrolase family, specifically those 20 hydrolases inhibited by HDFP. This is the first evidence in over three decades to show that palmitoylation is indeed dynamically regulated by protein thioesterases in mammalian cells. Additionally, based on the unique subset of cancer-related thioesterase substrates, these results motivate the development of thioesterase inhibitors to evaluate their potential as anti-cancer agents.

The proteomic experiments described above identified the tumor suppressor and cell polarity regulator Scribble (Scrib) as the most enzymatically regulated, most rapidly cycling palmitoylated protein (Figure 1-23).

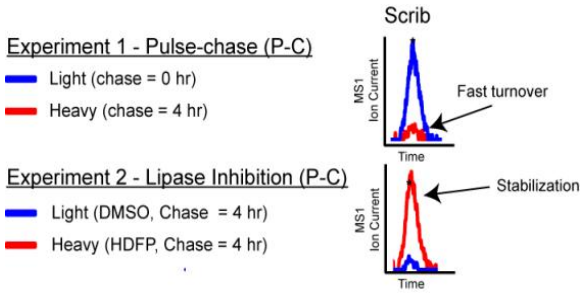

Figure 1-23 Quantitative SILAC palmitoylation proteomics of Scrib demonstrates rapid enzymatic turnover by 17-ODYA pulse-chase analysis. Peptide data has been adapted from Martin et. al.[86]

Scrib is a tumor-suppressor, which unlike Ras proteins, is frequently 'turned off' in cancer, leading to hyperproliferation and thus cooperating with oncogenic Ras signaling.[292,293] Scrib is normally localized to the basolateral cortex membrane of epithelial cells where it controls polarity, junctional integrity, proliferation, and metastasis.[294–296] Interestingly, Scrib and Ras superfamily proteins frequently 'cross

roads' when it comes to cell fate decisions such as migration, cell division, cancer transformation, apoptosis and proliferation (**Error! Reference source not found.**).[297–301].

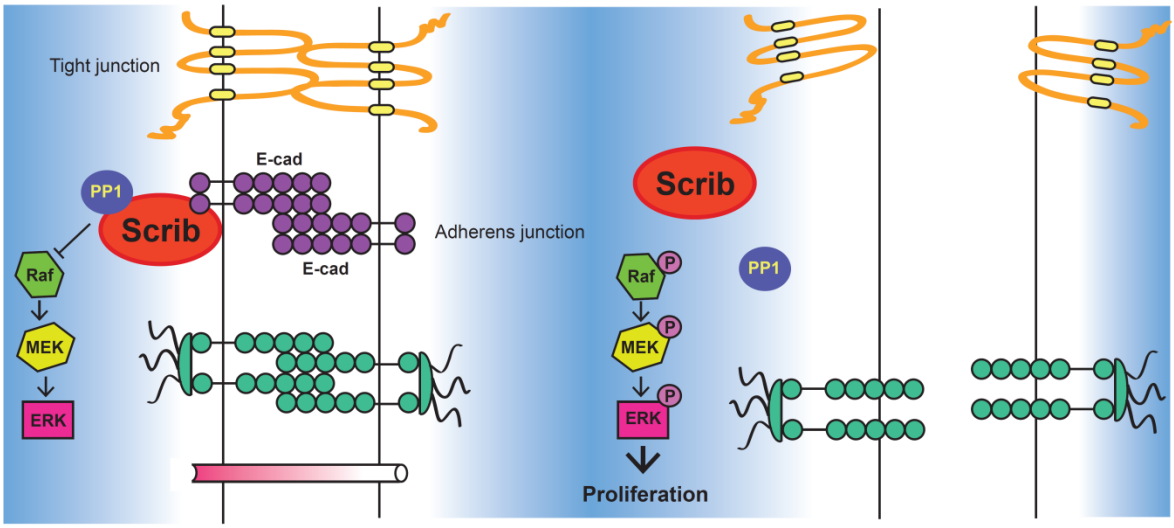

Figure 1-24 The loss of Scrib's membrane anchoring and tumor-suppressor ability correlate with hyperactivated proliferation cascades potentiated by Ras effectors. Scrib normally localizes to adherens junctions at the basolateral cortex where it regulates epithelial polarity, junctional integrity and cell proliferation (left). As cells undergo fibroblastic transformation, dysfunctional, cytosolic Scrib appears to potentiate Ras effectors in an elusive mechanism allowing cells to form hyperplasia (right). It has been suggested that Scrib suppresses the well-known mitogen activated growth cascade through interactions with Raf kinases downstream of Ras GTPases[302], however the spatiotemporal coordination between Scrib and Ras is unknown.

Thus, cells must develop strategies to tightly coordinate the localization of these two, seemingly opposing proteins so that productive signaling of the aforementioned pathways is guaranteed. In human epithelial cells, Scrib mislocalization appears to induce metastatic transformation through a disruption of cell polarity and adhesion junctions, while also enhancing Ras growth signaling to promote cell survival and proliferation (Figure 1-24).[301,303] Furthermore, since malignant cells appear to accelerate the turnover of Scrib palmitoylation[86], Scrib localization, spatial interactions, and tumor suppression may in fact be under this post-translational control (Figure 1-25).

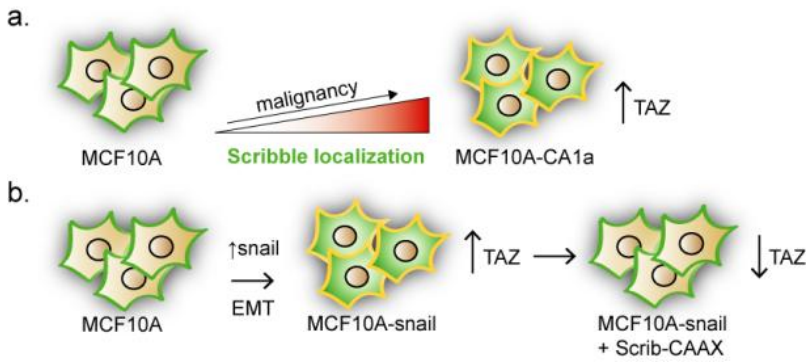

Figure 1-25 Scrib mis-localization and TAZ elevation in increasingly malignant cells. (a) Depicts cell-based models of breast cancer, in which Scrib localization becomes increasingly cytosolic as cells undergo an oncogenic transformation termed epithelial-mesenchymal-transition (EMT) and acquire aggressive fibroblastic traits. (b) Depicts the same benign cells engineered to over-express the EMT-promoting transcription factor Snail, which significantly elevates the protein levels of the anti-apoptotic factor TAZ and redistributes Scrib from the membrane to the cytosol.[304] Interestingly, when Scrib was constitutively anchored to the plasma membrane by over-expression of Scrib containing the prenylation CAAX motif, TAZ accumulation was abolished which abrogates a number of metastatic phenotypes.

In conclusion, dynamic palmitoylation proteomic studies place opposing signaling proteins, e.g. Scrib and Ras, among most dynamically palmitoylated proteins in cells. Not surprising, proteins such as Scrib and Ras share many signaling effectors in common which raises questions like which signaling protein exerts more control over the other and under what cellular circumstances? It appears that within the context of cancer, as shall be discussed later in chapter four, the oncogenic potential of Ras proteins is strengthen all while the tumor-suppressor capacity of Scrib is diminished. In this dissertation work, we suggest that dynamic palmitoylation enzymes may contribute to this and other imbalances seeing that a number of these enzyme have been reported to exhibit expression changes in cancer.[233,305] In this regard, different fractions of palmitoylation and depalmitoylation enzymes may exist in particular cancer cells, and perhaps the concerted action by these enzymes could specifically promote dynamics for Ras but suppress those of Scrib. To complicate the matter, the acylation enzymes themselves ought to be spatially and temporally coordinated to promote effective intracellular trafficking and localization of their substrate proteins[283]. Clearly, the need for better tools to characterize the extent of dynamic palmitoylation regulation and understand how it functions in the context of other regulatory mechanisms cannot be over emphasized enough. This thesis addresses this gap by providing pharmacological agents and characterizing the roles of palmitoylation enzymes in cancer.

1.9 Bibliography

1. Teruel, M. N. & Meyer, T. Translocation and reversible localization of signaling proteins: a dynamic future for signal transduction. *Cell* **103,** 181–184 (2000).

2. Cho, W. & Stahelin, R. V. Membrane-protein interactions in cell signaling and membrane trafficking. *Annu. Rev. Biophys. Biomol. Struct.* **34,** 119–151 (2005).

3. Kholodenko, B. N., Hoek, J. B. & Westerhoff, H. V. Why cytoplasmic signalling proteins should be recruited to cell membranes. *Trends Cell Biol.* **10,** 173–178 (2000).

4. Fishburn, C. S., Pollitt, S. K. & Bourne, H. R. Localization of a peripheral membrane protein: Gβγ targets GαZ. *Proc. Natl. Acad. Sci. U. S. A.* **97,** 1085–1090 (2000).

5. Li, L., Shi, X., Guo, X., Li, H. & Xu, C. Ionic protein-lipid interaction at the plasma membrane: What can the charge do? *Trends Biochem. Sci.* **39,** 130–140 (2014).

6. Mulgrew-Nesbitt, A. *et al.* The role of electrostatics in protein-membrane interactions. *Biochim. Biophys. Acta - Mol. Cell Biol. Lipids* **1761,** 812–826 (2006).

7. Moravcevic, K., Oxley, C. L. & Lemmon, M. a. Conditional peripheral membrane proteins: Facing up to limited specificity. *Structure* **20,** 15–27 (2012).

8. Hurley, J. H. Membrane binding domains. *Biochim. Biophys. Acta* **1761,** 805–811 (2006).

9. Nadolski, M. J. & Linder, M. E. Protein lipidation. *FEBS J.* **274,** 5202–5210 (2007).

10. Hang, H. C. & Linder, M. E. Exploring protein lipidation with chemical biology. *Chem. Rev.* **111,** 6341–6358 (2011).

11. Towler, D. a, Gordon, J. I., Adams, S. P. & Glaser, L. The biology and enzymology of eukaryotic protein acylation. *Annu. Rev. Biochem.* **57,** 69–99 (1988).

12. Olson, E. N. & Spizz, G. Fatty acylation of cellular proteins. Temporal and subcellular differences between palmitate and myristate acylation. *J. Biol. Chem.* **261,** 2458–2466 (1986).

13. Martin, D. D. O., Beauchamp, E. & Berthiaume, L. G. Post-translational myristoylation: Fat matters in cellular life and death. *Biochimie* **93,** 18–31 (2011).

14. Berthiaume, L. G. Wnt acylation: Seeing is believing. *Nat. Chem. Biol.* **10,** 5–7 (2013).

15. Miura, G. I. & Treisman, J. E. Lipid modification of secreted signaling proteins. *Cell Cycle* **5,** 1184–1188 (2006).

16. Nusse, R. Wnts and Hedgehogs: lipid-modified proteins and similarities in signaling mechanisms at the cell surface. *Development* **130,** 5297–5305 (2003).

17. Chang, S.-C. & Magee, A. I. Acyltransferases for secreted signalling proteins (Review). *Mol. Membr. Biol.* **26,** 104–113 (2009).

18. Tate, E. W., Kalesh, K. a, Lanyon-hogg, T., Storck, E. M. & Thinon, E. Global profiling of protein lipidation using chemical proteomic technologies. *Curr. Opin. Chem. Biol.* **24,** 48–57 (2015).

19. Resh, M. D. Covalent lipid modifications of proteins. *Curr. Biol.* **23,** R431–R435 (2013).

20. Triola, G. The Protein Lipidation and Its Analysis. *J. Glycomics Lipidomics* **01,** 1–14 (2012).

21. Mayor, S. & Riezman, H. Sorting GPI-anchored proteins. *Nat. Rev. Mol. Cell Biol.* **5,** 110–120 (2004).

22. Orlean, P. & Menon, A. K. Thematic review series: lipid posttranslational modifications. GPI anchoring of protein in yeast and mammalian cells, or: how we learned to stop worrying and love glycophospholipids. *J. Lipid Res.* **48,** 993–1011 (2007).

23. Menon, A. K. Lipid modifications of proteins. *Biochem. Lipids, Lipoproteins Membr.* 39–58 (2008). doi:10.1016/B978-044453219-0.50004-0

24. Buglino, J. a. & Resh, M. D. *Palmitoylation of Hedgehog Proteins*. *Vitamins and Hormones* **88,** (Elsevier Inc., 2012).

25. Satou, M. & Sugimoto, H. *The study of ghrelin deacylation enzymes. Methods in enzymology* **514,** (Elsevier Inc., 2012).

26. Eisenberg, S. *et al.* The role of palmitoylation in regulating Ras localization and function. *Biochem. Soc. Trans.* **41,** 79–83 (2013).

27. Magee, T. & Seabra, M. C. Fatty acylation and prenylation of proteins: What's hot in fat. *Curr. Opin. Cell Biol.* **17,** 190–196 (2005).

28. Resh, M. D. Trafficking and signaling by fatty-acylated and prenylated proteins. *Nat. Chem. Biol.* **2,** 584–590 (2006).

29. Resh, M. D. & Resh, M. D. Fatty acylation of proteins: new insights into membrane targeting of myristylated and palmitoylated proteins. **1451,** 1–16 (1999).

30. Resh, M. D. Regulation of cellular signalling by fatty acid acylation and prenylation of signal transduction proteins. *Cell. Signal.* **8,** 403–412 (1996).

31. Salaun, C., Greaves, J. & Chamberlain, L. H. The intracellular dynamic of protein palmitoylation. *J. Cell Biol.* **191,** 1229–1238 (2010).

32. Baekkeskov, S. & Kanaani, J. Palmitoylation cycles and regulation of protein function (Review). *Mol. Membr. Biol.* **26,** 42–54 (2009).

33. Sorek, N., Bloch, D. & Yalovsky, S. Protein lipid modifications in signaling and subcellular targeting. *Curr. Opin. Plant Biol.* **12,** 714–720 (2009).

34. Yalovsky, S., Rodríguez-Concepción, M. & Gruissem, W. Lipid modifications of proteins - Slipping in and out of membranes. *Trends Plant Sci.* **4,** 439–445 (1999).

35. Hu, L. Le *et al.* Prediction and analysis of protein palmitoylation sites. *Biochimie* **93,** 489–496 (2011).

36. Smotrys, J. E. & Linder, M. E. Palmitoylation of intracellular signaling proteins: regulation and function. *Annu. Rev. Biochem.* **73,** 559–587 (2004).

37. Linder, M. E. & Deschenes, R. J. Palmitoylation: policing protein stability and traffic. *Nat. Rev. Mol. Cell Biol.* **8,** 74–84 (2007).

38. Linder, M. & Deschenes, R. Protein palmitoylation. *Methods* **40,** 125–126 (2006).

39. Bijlmakers, M. J. & Marsh, M. The on-off story of protein palmitoylation. *Trends Cell Biol.* **13,** 32–42 (2003).

40. Liang, X. *et al.* Heterogeneous Fatty Acylation of Src Family Kinases with Polyunsaturated Fatty Acids Regulates Raft Localization and Signal Transduction. *J. Biol. Chem.* **276,** 30987–30994 (2001).

41. Jennings, B. C. & Linder, M. E. DHHC protein S-acyltransferases use similar ping-pong kinetic mechanisms but display different Acyl-CoA specificities. *J. Biol. Chem.* **287,** 7236–7245 (2012).

42. Hallak, H. *et al.* Covalent binding of arachidonate to G protein alpha subunits of human platelets. *J. Biol. Chem.* **269,** 4713–4716 (1994).

43. Veit, M., Reverey, H. & Schmidt, M. F. Cytoplasmic tail length influences fatty acid selection for acylation of viral glycoproteins. *Biochem. J.* **318 (Pt 1,** 163–172 (1996).

44. Barretina, J. *et al.* The Cancer Cell Line Encyclopedia enables predictive modelling of anticancer drug sensitivity. *Nature* **483,** 603–307 (2012).

45. Wilson, J. P., Raghavan, A. S., Yang, Y.-Y., Charron, G. & Hang, H. C. Proteomic analysis of fatty-acylated proteins in mammalian cells with chemical reporters reveals S-acylation of histone H3 variants. *Mol. Cell. Proteomics* **10,** M110.001198 (2011).

46. Grammel, M. & Hang, H. C. Chemical reporters for biological discovery. *Nat. Chem. Biol.* **9,** 475–84 (2013).

47. Jiang, H. *et al.* SIRT6 regulates TNF-α secretion through hydrolysis of long-chain fatty acyl lysine. *Nature* **496,** 110–3 (2013).

48. Schafer, R. & Rine, J. PROTEIN PRENYLATION : GENES , ENZYMES , TARGETS ,. (1992).

49. Wright, L. P. & Philips, M. R. Thematic review series: lipid posttranslational modifications. CAAX modification and membrane targeting of Ras. *J. Lipid Res.* **47,** 883–891 (2006).

50. Resh, M. D. Targeting protein lipidation in disease. *Trends Mol. Med.* **18,** 206–214 (2012).

51. Gutierrez, J. a *et al.* Ghrelin octanoylation mediated by an orphan lipid transferase. *Proc. Natl. Acad. Sci. U. S. A.* **105,** 6320–6325 (2008).

52. Hofmann, K. A superfamily of membrane-bound O-acyltransferases with implications for Wnt signaling. *Trends Biochem. Sci.* **25,** 111–112 (2000).

53. Gräslund, S. *et al.* Protein production and purification. *Nat. Methods* **5,** 135–146 (2008).

54. Kleuss, C. & Krause, E. Gαs is palmitoylated at the N-terminal glycine. *EMBO J.* **22,** 826–832 (2003).

55. Yu, S., Guo, Z., Johnson, C., Gu, G. & Wu, Q. Recent progress in synthetic and biological studies of GPI anchors and GPI-anchored proteins. *Curr. Opin. Chem. Biol.* **17,** 1006–1013 (2013).

56. Tsai, Y. H., Liu, X. & Seeberger, P. H. Chemical biology of glycosylphosphatidylinositol anchors. *Angew. Chemie - Int. Ed.* **51,** 11438–11456 (2012).

57. Liang, X., Lu, Y., Neubert, T. a. & Resh, M. D. Mass spectrometric analysis of GAP-43/neuromodulin reveals the presence of a variety of fatty acylated species. *J. Biol. Chem.* **277,** 33032–33040 (2002).

58. Liang, X., Lu, Y., Wilkes, M., Neubert, T. a. & Resh, M. D. The N-terminal SH4 region of the Src family kinase Fyn is modified by methylation and heterogeneous fatty acylation: Role in membrane targeting, cell adhesion, and spreading. *J. Biol. Chem.* **279,** 8133–8139 (2004).

59. O'Brien, P. J., St Jules, R. S., Reddy, T. S., Bazan, N. G. & Zatz, M. Acylation of disc membrane rhodopsin may be nonenzymatic. *J. Biol. Chem.* **262,** 5210–5215 (1987).

60. Towler, D. & Glaser, L. Acylation of cellular proteins with endogenously synthesized fatty acids. *Biochemistry* **25,** 878–884 (1986).

61. Olson, E. N., Towler, D. a. & Glaser, L. Specificity of fatty acid acylation of cellular proteins. *J. Biol. Chem.* **260,** 3784–3790 (1985).

62. Dietrich, L. E. P. & Ungermann, C. On the mechanism of protein palmitoylation. *EMBO Rep.* **5,** 1053–1057 (2004).

63. Chamberlain, L. H. & Shipston, M. J. The Physiology of Protein S-acylation. *Physiol. Rev.* **95,** 341–376 (2015).

64. Prior, I. a. & Hancock, J. F. Ras trafficking, localization and compartmentalized signalling. *Semin. Cell Dev. Biol.* **23,** 145–153 (2012).

65. Shahinian, S. & Silvius, J. R. Doubly-lipid-modified protein sequence motifs exhibit long-lived anchorage to lipid bilayer membranes. *Biochemistry* **34,** 3813–3822 (1995).

66. Silvius, J. R. *et al.* Partitioning of lipidated peptides into liquid-ordered lipid ('raft') domains in artificial and biological membranes. *Mol. Biol. Cell* **12,** 0 (2001).

67. Wirth, A. *et al.* Dual lipidation of the brain-specific Cdc42 isoform regulates its functional properties. *Biochem. J.* **456,** 311–22 (2013).

68. El-Husseini, A. E. *et al.* Dual palmitoylation of PSD-95 mediates its vesiculotubular sorting, postsynaptic targeting, and ion channel clustering. *J. Cell Biol.* **148,** 159–171 (2000).

69. Lee, H. *et al.* Palmitoylation of Caveolin-1 at a Single Site (Cys-156) Controls its Coupling to the c-Src Tyrosine Kinase: Targeting of dually acylated molecules (Gpi-linked, transmembrane, or cytoplasmic) to caveolae effectively uncouples c-Src and caveolin-1 (Tyr-14). *J. Biol. Chem.* **276,** 35150–35158 (2001).

70. Fukata, Y. & Fukata, M. Protein palmitoylation in neuronal development and synaptic plasticity. *Nat. Rev. Neurosci.* **11,** 161–175 (2010).

71. Fröhlich, M., Dejanovic, B., Kashkar, H., Schwarz, G. & Nussberger, S. S-palmitoylation represents a novel mechanism regulating the mitochondrial targeting of BAX and initiation of apoptosis. *Cell Death Dis.* **5,** e1057 (2014).

72. Ward, C. W., Lawrence, M. C., Streltsov, V. a., Adams, T. E. & McKern, N. M. The insulin and EGF receptor structures: new insights into ligand-induced receptor activation. *Trends Biochem. Sci.* **32,** 129–137 (2007).

73. Hurley, J. H. & Meyer, T. Subcellular targeting by membrane lipids. *Curr. Opin. Cell Biol.* **13,** 146–152 (2001).

74. Draper, J. M., Xia, Z. & Smith, C. D. Cellular palmitoylation and trafficking of lipidated peptides. *J. Lipid Res.* **48,** 1873–1884 (2007).

75. Adams, M. N., Christensen, M. E., He, Y., Waterhouse, N. J. & Hooper, J. D. The role of palmitoylation in signalling, cellular trafficking and plasma membrane localization of protease-activated receptor-2. *PLoS One* **6,** (2011).

76. Parton, R. G. & Hancock, J. F. Lipid rafts and plasma membrane microorganization: Insights from Ras. *Trends Cell Biol.* **14,** 141–147 (2004).

77. Melkonian, K. a *et al.* Role of lipid modification in targeting proteins to detergent-rsistant membrane rafts. **274,** 3910–3917 (1999).

78. Ernst, A. M., Contreras, F. X., Brügger, B. & Wieland, F. Determinants of specificity at the protein-lipid interface in membranes. *FEBS Lett.* **584,** 1713–1720 (2010).

79. Linder, M. E. & Deschenes, R. J. New insights into the mechanisms of protein palmitoylation. *Biochemistry* **42,** 4311–4320 (2003).

80. Bracher, P. J., Snyder, P. W., Bohall, B. R. & Whitesides, G. M. The Relative Rates of Thiol-Thioester Exchange and Hydrolysis for Alkyl and Aryl Thioalkanoates in Water. *Orig. Life Evol. Biosph.* **41,** 399–412 (2011).

81. Bond, E., General, I. V, Catalyzed, B., Fedor, L. R. & Bruicea, T. C. Nucleophilic Displacement Reactions at the Thiol Ester Bond. IV. General Base Catalyzed Hydrolysis. **5986,** (1965).

82. Haapalainen, A. M., Meriläinen, G. & Wierenga, R. K. The thiolase superfamily: Condensing enzymes with diverse reaction specificities. *Trends Biochem. Sci.* **31,** 64–71 (2006).

83. Hunt, M. C., Siponen, M. I. & Alexson, S. E. H. The emerging role of acyl-CoA thioesterases and acyltransferases in regulating peroxisomal lipid metabolism. *Biochim. Biophys. Acta - Mol. Basis Dis.* **1822,** 1397–1410 (2012).

84. Ellis, J. M., Frahm, J. L., Li, L. O. & Coleman, R. a. Acyl-coenzyme A synthetases in metabolic control. *Curr. Opin. Lipidol.* **21,** 212–217 (2010).

85. Yang, W. & Drueckhammer, D. G. Understanding the relative acyl-transfer reactivity of oxoesters and thioesters: Computational analysis of transition state delocalization effects. *J. Am. Chem. Soc.* **123,** 11004–11009 (2001).

86. Martin, B. R., Wang, C., Adibekian, A., Tully, S. E. & Cravatt, B. F. Global profiling of dynamic protein palmitoylation. *Nat. Methods* **9,** 84–89 (2011).

87. Stahelin, R. V & Cho, W. Differential roles of ionic, aliphatic, and aromatic residues in membrane-protein interactions: a surface plasmon resonance study on phospholipases A2. *Biochemistry* **40,** 4672–4678 (2001).

88. Blaskovic, S., Blanc, M. & Van Der Goot, F. G. What does S-palmitoylation do to membrane proteins? *FEBS J.* **280,** 2766–2774 (2013).

89. Kong, E. *et al.* Dynamic palmitoylation links cytosol-membrane shuttling of acyl-protein thioesterase-1 and acyl-protein thioesterase-2 with that of proto-oncogene H-Ras product and growth-associated protein-43. *J. Biol. Chem.* **288,** 9112–9125 (2013).

90. Wedegaertner, P. B. *Reversible palmitoylation in g protein signaling*. *Handbook of Cell Signaling, 2/e* **2,** (Elsevier Inc., 2010).

91. Kang, R. *et al.* Neural palmitoyl-proteomics reveals dynamic synaptic palmitoylation. *Nature* **456,** 904–909 (2008).

92. Tom, C. T. M. B. & Martin, B. R. Fat chance! Getting a grip on a slippery modification. *ACS Chem. Biol.* **8,** 46–57 (2013).

93. Planey, S. L. & Zacharias, D. a. Palmitoyl acyltransferases, their substrates, and novel assays to connect them (Review). *Mol. Membr. Biol.* **26,** 14–31 (2009).

94. Aicart-Ramos, C., Valero, R. A. & Rodriguez-Crespo, I. Protein palmitoylation and subcellular trafficking. *Biochim. Biophys. Acta - Biomembr.* **1808,** 2981–2994 (2011).

95. Blanc, M., Blaskovic, S. & van der Goot, F. G. Palmitoylation, pathogens and their host. *Biochem. Soc. Trans.* **41,** 84–8 (2013).

96. Veit, M. Palmitoylation of virus proteins. *Biol. Cell* **104,** 493–515 (2012).

97. Schmidt, M. F. G. & Lambrecht, B. On the structure of the acyl linkage and the function of fatty acyl chains in the influenza virus haemagglutinin and the glycoproteins of Semliki Forest virus. *J. Gen. Virol.* **66,** 2635–2647 (1985).

98. Yount, J. S., Zhang, M. M. & Hang, H. C. Emerging roles for protein S-palmitoylation in immunity from chemical proteomics. *Curr. Opin. Chem. Biol.* **17,** 27–33 (2013).

99. Washbourne, P. Greasing Transmission: Palmitoylation at the synapse. *Neuron* **44,** 901–902 (2004).

100. Howie, J., Tulloch, L. B., Shattock, M. J. & Fuller, W. Regulation of the cardiac Na(+) pump by palmitoylation of its catalytic and regulatory subunits. *Biochem. Soc. Trans.* **41,** 95–100 (2013).

101. He, M., Jenkins, P. & Bennett, V. Cysteine 70 of ankyrin-G is S-palmitoylated and is required for function of ankyrin-G in membrane domain assembly. *J. Biol. Chem.* **287,** 43995–44005 (2012).

102. el-Husseini, A. el-D. & Bredt, D. S. Protein palmitoylation: a regulator of neuronal development and function. *Nat. Rev. Neurosci.* **3,** 791–802 (2002).

103. Shipston, M. J. Ion channel regulation by protein palmitoylation. *J. Biol. Chem.* **286,** 8709–8716 (2011).

104. Frénal, K., Kemp, L. E. & Soldati-Favre, D. Emerging roles for protein S-palmitoylation in Toxoplasma biology. *Int. J. Parasitol.* **44,** 121–131 (2014).

105. Zhou, F., Xue, Y., Yao, X. & Xu, Y. CSS-Palm: Palmitoylation site prediction with a clustering and scoring strategy (CSS). *Bioinformatics* **22,** 894–896 (2006).

106. Bharadwaj, M. & Bizzozero, O. a. Myelin P0 glycoprotein and a synthetic peptide containing the palmitoylation site are both autoacylated. *J. Neurochem.* **65,** 1805–1815 (1995).

107. Bizzozero, O. a., McGarry, J. F. & Lees, M. B. Autoacylation of myelin proteolipid protein with acyl coenzyme A. *J. Biol. Chem.* **262,** 13550–13557 (1987).

108. Quesnel, S. & Silvius, J. R. Cysteine-containing peptide sequences exhibit facile uncatalyzed transacylation and acyl-CoA-dependent acylation at the lipid bilayer interface. *Biochemistry* **33,** 13340–13348 (1994).

109. Constantinides, P. P. & Steim, J. M. Physical properties of fatty acyl-CoA. Critical micelle concentrations and micellar size and shape. *J. Biol. Chem.* **260,** 7573–7580 (1985).

110. Hill, B. G., Reily, C., Oh, J. Y., Johnson, M. S. & Landar, A. Methods for the determination and quantification of the reactive thiol proteome. *Free Radic. Biol. Med.* **47,** 675–683 (2009).

111. Bulaj, G., Kortemme, T. & Goldenberg, D. P. Ionization-reactivity relationships for cysteine thiols in polypeptides. *Biochemistry* **37,** 8965–8972 (1998).

112. Duncan, J. a & Gilman, a G. Autoacylation of G protein alpha subunits. *J. Biol. Chem.* **271,** 23594–23600 (1996).

113. Dunphy, J. T. *et al.* Differential effects of acyl-CoA binding protein on enzymatic and non-enzymatic thioacylation of protein and peptide substrates. **1485,** 185–198 (2000).

114. Schroeder, H. *et al.* S-acylation and plasma membrane targeting of the farnesylated carboxyl- terminal peptide of N-ras in mammalian fibroblasts. *Biochemistry* **36,** 13102–13109 (1997).

115. Conibear, E. & Davis, N. G. Palmitoylation and depalmitoylation dynamics at a glance. *J. Cell Sci.* **123,** 4007–4010 (2010).

116. Veit, M., Ponimaskin, E. & Schmidt, M. F. G. Analysis of s-acylation of proteins. *Methods Mol. Biol.* **446,** 163–182 (2008).

117. Resh, M. D. Use of analogs and inhibitors to study the functional significance of protein palmitoylation. *Methods* **40,** 191–197 (2006).

118. Used, C. & In, T. COMMONLY USED TECHNIQUES IN BIOCHEMISTRY AND MOLECULAR Detection and Quantitation of Radiolabeled Proteins and DNA in Gels and Blots. *Mol. Biol.* 1–10 (1999).

119. Glatz, J. a N. F. C., Luiken, J. J. F. P. & Bonen, A. Membrane Fatty Acid Transporters as Regulators of Lipid Metabolism : Implications for Metabolic Disease. *Physiol. Rev.* **90,** 367–417 (2010).

120. Knudsen, J. Acyl-CoA-binding protein (ACBP) and its relation to fatty acid-binding protein (FABP): an overview. *Mol. Cell. Biochem.* **98,** 217–223 (1990).

121. Su, X. & Abumrad, N. a. Cellular fatty acid uptake: a pathway under construction. *Trends Endocrinol. Metab.* **20,** 72–77 (2009).

122. Li, L. O., Klett, E. L. & Coleman, R. a. Acyl-CoA synthesis, lipid metabolism and lipotoxicity. *Biochim. Biophys. Acta - Mol. Cell Biol. Lipids* **1801,** 246–251 (2010).

123. Peseckis, S. M., Deichaite, I. & Resh, M. D. Iodinated fatty acids as probes for myristate processing and function: Incorporation into pp60v-src. *J. Biol. Chem.* **268,** 5107–5114 (1993).

124. Martin, B. R. & Cravatt, B. F. Large-scale profiling of protein palmitoylation in mammalian cells. *Nat. Methods* **6,** 135–138 (2009).

125. Hannoush, R. N. & Sun, J. The chemical toolbox for monitoring protein fatty acylation and prenylation. *Nat. Chem. Biol.* **6,** 498–506 (2010).

126. Li, Y., Martin, B. R., Cravatt, B. F. & Hofmann, S. L. DHHC5 protein palmitoylates flotillin-2 and is rapidly degraded on induction of neuronal differentiation in cultured cells. *J. Biol. Chem.* **287,** 523–530 (2012).

127. Wan, J., Roth, A. F., Bailey, A. O. & Davis, N. G. Palmitoylated proteins: purification and identification. *Nat. Protoc.* **2,** 1573–1584 (2007).

128. Roth, A. F., Wan, J., Green, W. N., Yates, J. R. & Davis, N. G. Proteomic identification of palmitoylated proteins. *Methods* **40,** 135–142 (2006).

129. Brewer, C. F. & Riehm, J. P. Evidence for possible nonspecific reactions between N-ethylmaleimide and proteins. *Anal. Biochem.* **18,** 248–255 (1967).

130. Rexach, J. E. *et al.* Quantification of O-glycosylation stoichiometry and dynamics using resolvable mass tags. *Nat. Chem. Biol.* **6,** 645–651 (2010).

131. Ishikawa-Ankerhold, H. C., Ankerhold, R. & Drummen, G. P. C. Advanced fluorescence microscopy techniques-FRAP, FLIP, FLAP, FRET and FLIM. *Molecules* **17,** 4047–4132 (2012).

132. Hamel, L. D., Deschenes, R. J. & Mitchell, D. a. A fluorescence-based assay to monitor autopalmitoylation of zDHHC proteins applicable to high-throughput screening. *Anal. Biochem.* **460,** 1–8 (2014).

133. Kenworthy, A. K. Fluorescence-based methods to image palmitoylated proteins. *Methods* **40,** 198–205 (2006).

134. Aoki, K. & Matsuda, M. Visualization of small GTPase activity with fluorescence resonance energy transfer-based biosensors. *Nat. Protoc.* **4,** 1623–1631 (2009).

135. Odell, I. D. & Cook, D. Immunofluorescence Techniques. *J. Invest. Dermatol.* **133,** e4 (2013).

136. Gao, X. & Hannoush, R. N. Single-cell in situ imaging of palmitoylation in fatty-acylated proteins. *Nat. Protoc.* **9,** 2607–2623 (2014).

137. Patterson, G. H., Knobel, S. M., Sharif, W. D., Kain, S. R. & Piston, D. W. Use of the green fluorescent protein and its mutants in quantitative fluorescence microscopy. *Biophys. J.* **73,** 2782–2790 (1997).

138. De Angelis, D. a, Miesenböck, G., Zemelman, B. V & Rothman, J. E. PRIM: proximity imaging of green fluorescent protein-tagged polypeptides. *Proc. Natl. Acad. Sci. U. S. A.* **95,** 12312–12316 (1998).

139. Navarro-Lérida, I., Alvarez-Barrientos, A., Gavilanes, F. & Rodriguez-Crespo, I. Distance-dependent cellular palmitoylation of de-novo-designed sequences and their translocation to plasma membrane subdomains. *J. Cell Sci.* **115,** 3119–3130 (2002).

140. Hughes, T. E., Zhang, H., Logothetis, D. E. & Berlot, C. H. Visualization of a Functional G??q-Green Fluorescent Protein Fusion in Living Cells. Association with the plasma membrane is disrupted by mutational activation and by elimination of palmitoylation sites, but not by activation mediated by receptors or AlF4. *J. Biol. Chem.* **276,** 4227–4235 (2001).

141. Grabowska, D. *et al.* Postnatal induction and localization of R7BP, a membrane-anchoring protein for regulator of G protein signaling 7 family-G??5 complexes in brain. *Neuroscience* **151,** 969–982 (2008).

142. Dietzen, D. J., Hastings, W. R. & Lublin, D. M. Caveolin is palmitoylated on multiple cysteine residues. Palmitoylation is not necessary for localization of caveolin to caveolae. *Journal of Biological Chemistry* **270,** 6838–6842 (1995).

143. Izawa, I., Nishizawa, M., Hayashi, Y. & Inagaki, M. Palmitoylation of ERBIN is required for its plasma membrane localization. *Genes to Cells* **13,** 691–701 (2008).

144. Carrero, G., McDonald, D., Crawford, E., De Vries, G. & Hendzel, M. J. Using FRAP and mathematical modeling to determine the in vivo kinetics of nuclear proteins. *Methods* **29,** 14–28 (2003).

145. Trembecka, D. O., Kuzak, M. & Dobrucki, J. W. Conditions for using FRAP as a quantitative technique-influence of the bleaching protocol. *Cytom. Part A* **77,** 366–370 (2010).

146. Lele, T. P. & Ingber, D. E. A mathematical model to determine molecular kinetic rate constants under non-steady state conditions using fluorescence recovery after photobleaching (FRAP). *Biophys. Chem.* **120,** 32–35 (2006).

147. Henis, Y. I., Rotblat, B. & Kloog, Y. FRAP beam-size analysis to measure palmitoylation-dependent membrane association dynamics and microdomain partitioning of Ras proteins. *Methods* **40,** 183–190 (2006).

148. Milde, S. & Coleman, M. P. Identification of Palmitoyltransferase and Thioesterase Enzymes That Control the Subcellular Localization of Axon Survival Factor Nicotinamide Mononucleotide Adenylyltransferase 2 (NMNAT2). *J. Biol. Chem.* **289,** 32858–32870 (2014).

149. Young, F. B., Butland, S. L., Sanders, S. S., Sutton, L. M. & Hayden, M. R. Putting proteins in their place: Palmitoylation in Huntington disease and other neuropsychiatric diseases. *Prog. Neurobiol.* **97,** 220–238 (2012).

150. Ivaldi, C. *et al.* Proteomic analysis of S-Acylated proteins in human B cells reveals palmitoylation of the immune regulators CD20 and CD23. *PLoS One* **7,** 1–9 (2012).

151. Greaves, J. & Chamberlain, L. H. New links between S-acylation and cancer. *J. Pathol.* **233,** 4–6 (2014).

152. Linder, M. E. & Deschenes, R. J. Model organisms lead the way to protein palmitoyltransferases. *J. Cell Sci.* **117,** 521–526 (2004).

153. Mitchell, D. a., Farh, L., Marshall, T. K. & Deschenes, R. J. A polybasic domain allows nonprenylated Ras proteins to function in Saccharomyces cerevisiae. *J. Biol. Chem.* **269,** 21540–21546 (1994).

154. Bartels, D. J., Mitchell, D. a, Dong, X. & Deschenes, R. J. Erf2, a novel gene product that affects the localization and palmitoylation of Ras2 in Saccharomyces cerevisiae. *Mol. Cell. Biol.* **19,** 6775–6787 (1999).

155. Greaves, J. & Chamberlain, L. H. S-acylation by the DHHC protein family. *Biochem. Soc. Trans.* **38,** 522–524 (2010).

156. Mitchell, D. a., Mitchell, G., Ling, Y., Budde, C. & Deschenes, R. J. Mutational analysis of Saccharomyces cerevisiae Erf2 reveals a two-step reaction mechanism for protein palmitoylation by DHHC enzymes. *J. Biol. Chem.* **285,** 38104–38114 (2010).

157. Ohno, Y., Kashio, A., Ogata, R., Ishitomi, A. & Yamazaki, Y. Analysis of substrate specificity of human DHHC protein acyltransferases. 1–23

158. Linder, M. E. & Jennings, B. C. Mechanism and function of DHHC S-acyltransferases. *Biochem. Soc. Trans.* **41,** 29–34 (2013).

159. Greaves, J. & Chamberlain, L. H. DHHC palmitoyl transferases: Substrate interactions and (patho)physiology. *Trends Biochem. Sci.* **36,** 245–253 (2011).

160. Putilina, T., Wong, P. & Gentleman, S. The DHHC domain: A new highly conserved cysteine-rich motif. *Mol. Cell. Biochem.* **195,** 219–226 (1999).

161. Ohno, Y., Kihara, A., Sano, T. & Igarashi, Y. Intracellular localization and tissue-specific distribution of human and yeast DHHC cysteine-rich domain-containing proteins. *Biochim. Biophys. Acta - Mol. Cell Biol. Lipids* **1761,** 474–483 (2006).

162. Thomas, G., Hayashi, T., Chiu, S. L., Chen, C. M. & Huganir, R. Palmitoylation by DHHC5/8 Targets GRIP1 to Dendritic Endosomes to Regulate AMPA-R Trafficking. *Neuron* **73,** 482–496 (2012).

163. Li, Y. *et al.* DHHC5 interacts with PDZ domain 3 of post-synaptic density-95 (PSD-95) protein and plays a role in learning and memory. *J. Biol. Chem.* **285,** 13022–13031 (2010).

164. Fukata, Y., Iwanaga, T. & Fukata, M. Systematic screening for palmitoyl transferase activity of the DHHC protein family in mammalian cells. *Methods* **40,** 177–182 (2006).

165. Brigidi, G. S. *et al.* Palmitoylation of δ-catenin by DHHC5 mediates activity-induced synapse plasticity. *Nat. Neurosci.* **17,** 522–32 (2014).

166. Mitchell, D. a. *et al.* The Erf4 subunit of the yeast Ras palmitoyl acyltransferase is required for stability of the Acyl-Erf2 intermediate and palmitoyl transfer to a Ras2 substrate. *J. Biol. Chem.* **287,** 34337–34348 (2012).

167. Huang, K. *et al.* Neuronal palmitoyl acyl transferases exhibit distinct substrate specificity. *FASEB J.* **23,** 2605–2615 (2009).

168. Korycka, J. *et al.* Human DHHC proteins: A spotlight on the hidden player of palmitoylation. *Eur. J. Cell Biol.* **91,** 107–117 (2012).

169. Iwanaga, T., Tsutsumi, R., Noritake, J., Fukata, Y. & Fukata, M. Dynamic protein palmitoylation in cellular signaling. *Prog. Lipid Res.* **48,** 117–127 (2009).

170. Mukai, J. *et al.* Evidence that the gene encoding ZDHHC8 contributes to the risk of schizophrenia. *Nat. Genet.* **36,** 725–731 (2004).

171. Saleem, A. N. *et al.* Mice with alopecia, osteoporosis, and systemic amyloidosis due to mutation in Zdhhc13, a gene coding for palmitoyl acyltransferase. *PLoS Genet.* **6,** 1–15 (2010).

172. Singaraja, R. R. *et al.* Altered palmitoylation and neuropathological deficits in mice lacking HIP14. *Hum. Mol. Genet.* **20,** 3899–3909 (2011).

173. Mitchell, D. a. *et al.* Mutations in the X-linked intellectual disability gene, zDHHC9, alter autopalmitoylation activity by distinct mechanisms. *J. Biol. Chem.* **289,** 18582–18592 (2014).

174. Greaves, J., Carmichael, J. a & Chamberlain, L. H. The palmitoyl transferase DHHC2 targets a dynamic membrane cycling pathway: regulation by a C-terminal domain. *Mol. Biol. Cell* **22,** 1887–1895 (2011).

175. Yeste-Velasco, M., Linder, M. E. & Lu, Y.-J. Protein S-palmitoylation and cancer. *Biochim. Biophys. Acta - Rev. Cancer* **1856,** 107–120 (2015).

176. Hiol, A., Caron, J. M., Smith, C. D. & Jones, T. L. . Characterization and partial purification of protein fatty acyltransferase activity from rat liver. *Biochim. Biophys. Acta - Mol. Cell Biol. Lipids* **1635,** 10–19 (2003).

177. Budde, C., Schoenfish, M. J., Linder, M. E. & Deschenes, R. J. Purification and characterization of recombinant protein acyltransferases. *Methods* **40,** 143–150 (2006).

178. Wang, J., Xie, Y., Wolff, D. W., Abel, P. W. & Tu, Y. DHHC protein-dependent palmitoylation protects regulator of G-protein signaling 4 from proteasome degradation. *FEBS Lett.* **584,** 4570–4574 (2010).

179. Guan, X. & Fierke, C. a. Understanding protein palmitoylation: Biological significance and enzymology. *Sci. China Chem.* **54,** 1888–1897 (2011).

180. Draper, J. M. & Smith, C. D. Palmitoyl acyltransferase assays and inhibitors (Review). *Mol. Membr. Biol.* **26,** 5–13 (2009).

181. Davda, D. *et al.* Profiling targets of the irreversible palmitoylation inhibitor 2-bromopalmitate. *ACS Chem. Biol.* **8,** 1912–1917 (2013).

182. Zheng, B., Zhu, S. & Wu, X. Clickable Analogue of Cerulenin as Chemical Probe to Explore Protein Palmitoylation. *ACS Chem. Biol.* **10,** 115–121 (2015).

183. Hagve, T. a & Christophersen, B. O. In vitro effects of alpha-bromopalmitate on metabolism of essential fatty acids studied in isolated rat hepatocytes: sex differences. *Biochim. Biophys. Acta* **917,** 333–336 (1987).

184. Pedro, M. P. *et al.* 2-Bromopalmitate Reduces Protein Deacylation by Inhibition of Acyl-Protein Thioesterase Enzymatic Activities. *PLoS One* **8,** (2013).

185. Jennings, B. C. *et al.* 2-Bromopalmitate and 2-(2-hydroxy-5-nitro-benzylidene)-benzo[b]thiophen-3-one inhibit DHHC-mediated palmitoylation in vitro. *J. Lipid Res.* **50,** 233–242 (2009).

186. DeJesus, G. & Bizzozero, O. a. Effect of 2-fluoropalmitate, cerulenin and tunicamycin on the palmitoylation and intracellular translocation of myelin proteolipid protein. *Neurochem. Res.* **27,** 1669–1675 (2002).

187. Patterson, S. I. & Skene, J. H. P. Novel inhibitory action of tunicamycin homologues suggests a role for dynamic protein fatty acylation in growth cone-mediated neurite extension. *J. Cell Biol.* **124,** 521–536 (1994).

188. Zheng, B. *et al.* 2-Bromopalmitate analogues as activity-based probes to explore palmitoyl acyltransferases. *J. Am. Chem. Soc.* **135,** 7082–7085 (2013).

189. Chen, X. *et al.* 2-Bromopalmitate modulates neuronal differentiation through the regulation of histone acetylation. *Stem Cell Res.* **12,** 481–491 (2014).

190. Webb, Y., Hermida-matsumoto, L. & Resh, M. D. Inhibition of Protein Palmitoylation , Raft Localization , and T Cell Signaling by 2-Bromopalmitate and Polyunsaturated Fatty Acids Inhibition of Protein Palmitoylation , Raft Localization , and T Cell Signaling by 2-Bromopal. **275,** 261–270 (2000).

191. Mikic, I. *et al.* A Live Cell, Image-Based Approach to Understanding the Enzymology and Pharmacology of 2-Bromopalmitate and Palmitoylation. *Methods Enzymol.* **414,** 150–187 (2006).

192. Varner, A. S. *et al.* Characterization of human palmitoyl-acyl transferase activity using peptides that mimic distinct palmitoylation motifs. *Biochem. J.* **373,** 91–99 (2003).

193. Krishnamurthy, K. *et al.* Depalmitoylation preferentially downregulates AMPA induced Ca2+ signaling and neurotoxicity in motor neurons. *Brain Res.* **1529,** 143–153 (2013).

194. Smythe, C. V. The reaction of iodoacetate and of iodoacetamide with various sulfhydryl groups, with urease, and with yeast preparations. *J. Biol. Chem.* **114,** 601–612 (1936).

195. Takahashi, N. & Hirose, M. Determination of sulfhydryl groups and disulfide bonds in a protein by polyacrylamide gel electrophoresis. *Anal. Biochem.* **188,** 359–365 (1990).

196. Van Geel, R., Pruijn, G. J. M., Van Delft, F. L. & Boelens, W. C. Preventing thiol-yne addition improves the specificity of strain-promoted azide-alkyne cycloaddition. *Bioconjug. Chem.* **23,** 392–398 (2012).

197. Weerapana, E., Simon, G. M. & Cravatt, B. F. Disparate proteome reactivity profiles of carbon electrophiles. *Nat. Chem. Biol.* **4,** 405–407 (2008).

198. Boja, E. S. & Fales, H. M. Overalkylation of a protein digest with iodoacetamide. *Anal. Chem.* **73,** 3576–3582 (2001).

199. Ohgi, K., Watanabe, H., Emman, K., Yoshida, N. & Irie, M. Alkylation of a ribonuclease from Streptomyces erythreus with iodoacetate and iodoacetamide. *J. Biochem.* **90,** 113–123 (1981).

200. Oakes, N. D. *et al.* Development and initial evaluation of a novel method for assessing tissue-specific plasma free fatty acid utilization in vivo using (R)-2-bromopalmitate tracer. *J. Lipid Res.* **40,** 1155–1169 (1999).

201. Oku, H., Tokuda, M. & Umino, T. The effects of 2-bromopalmitate on the fatty acid composition in differentiating adipocytes of red sea bream (Pagrus major). *Comp. Biochem. Physiol. Part B Biochem. Mol. Biol.* **152,** 370–375 (2009).

202. Chase, J. F. & Tubbs, P. K. Specific inhibition of mitochondrial fatty acid oxidation by 2-bromopalmitate and its coenzyme A and carnitine esters. *Biochem. J.* **129,** 55–65 (1972).

203. Coleman, R. a, Rao, P., Fogelsong, R. J. & Bardes, E. S. 2-Bromopalmitoyl-CoA and 2-bromopalmitate: promiscuous inhibitors of membrane-bound enzymes. *Biochim. Biophys. Acta* **1125,** 203–209 (1992).

204. Chu, C., Mao, L. F. & Schulz, H. Estimation of peroxisomal beta-oxidation in rat heart by a direct assay of acyl-CoA oxidase. *Biochem. J.* **302 (Pt 1,** 23–29 (1994).

205. Omura, S. The antibiotic cerulenin, a novel tool for biochemistry as an inhibitor of fatty acid synthesis. *Bacteriol. Rev.* **40,** 681–697 (1976).

206. Kawaguchi, a, Tomoda, H., Nozoe, S., Omura, S. & Okuda, S. Mechanism of action of cerulenin on fatty acid synthetase. Effect of cerulenin on iodoacetamide-induced malonyl-CoA decarboxylase activity. *J. Biochem.* **92,** 7–12 (1982).

207. Okuda, S. & Awaya, J. Cerulenin Resistance in a Cerulenin-Producing Fungus Isolation of Cerulenin Insensitive Fatty Acid Synthetase Cerulenin is an antifungal antibiotic isolated from a culture filtrate of the fungus Cephalosporium caerulens (1) and has the potent and noncom. **197,** 30–35 (1979).

208. Lawrence, D. S., Zilfou, J. T. & Smith, C. D. Structure-activity studies of cerulenin analogues as protein palmitoylation inhibitors. *J. Med. Chem.* **42,** 4932–4941 (1999).

209. De Vos, M. L., Lawrence, D. S. & Smith, C. D. Cellular pharmacology of cerulenin analogs that inhibit protein palmitoylation. *Biochem. Pharmacol.* **62,** 985–995 (2001).

210. Ducker, C. E. *et al.* Discovery and characterization of inhibitors of human palmitoyl acyltransferases. *Mol. Cancer Ther.* **5,** 1647–1659 (2006).

211. Schilling, B., Yoo, C. B., Collins, C. J. & Gibson, B. W. Determining cysteine oxidation status using differential alkylation. *Int. J. Mass Spectrom.* **236,** 117–127 (2004).

212. Sippel, T. O. New fluorochromes for thiols: maleimide and iodoacetamide derivatives of a 3-phenylcoumarin fluorophore. *J. Histochem. Cytochem.* **29,** 314–316 (1981).

213. Dardennes, E., Labano, S., Simpkins, N. S. & Wilson, C. Michael addition-electrophilic quenching chemistry of maleimides using dialkylzinc reagents. *Tetrahedron Lett.* **48,** 6380–6383 (2007).

214. Kim, Y. *et al.* Efficient site-specific labeling of proteins via cysteines. *Bioconjug. Chem.* **19,** 786–791 (2008).

215. Tyagarajan, K., Pretzer, E. & Wiktorowicz, J. E. Thiol-reactive dyes for fluorescence labeling of proteomic samples. *Electrophoresis* **24,** 2348–2358 (2003).

216. Mattson, G. *et al.* A practical approach to crosslinking. *Mol. Biol. Rep.* **17,** 167–183 (1993).

217. Chen, J. & Armstrong, R. N. Stereoselective catalysis of a retro-Michael reaction by class mu glutathione transferases. Consequences for the internal distribution of products in the active site. *Chem. Res. Toxicol.* **8,** 580–585 (1995).

218. Dietze, E. C. *et al.* Thiol ester hydrolysis catalyzed by glutathione S-transferase A1-1. *Biochemistry* **37,** 14948–14957 (1998).

219. Yang, W., Di Vizio, D., Kirchner, M., Steen, H. & Freeman, M. R. Proteome scale characterization of human S-acylated proteins in lipid raft-enriched and non-raft membranes. *Mol. Cell. Proteomics* **9,** 54–70 (2010).

220. Jones, M. L., Collins, M. O., Goulding, D., Choudhary, J. S. & Rayner, J. C. Analysis of protein palmitoylation reveals a pervasive role in Plasmodium development and pathogenesis. *Cell Host Microbe* **12,** 246–258 (2012).

221. Willumsen, B. M., Cox, A. D., Solski, P. A., Der, C. J. & Buss, J. E. Novel determinants of H-Ras plasma membrane localization and transformation. *Oncogene* **13,** 1901–1909 (1996).

222. Wedegaertner, P. B. & Bourne, H. R. Activation and depalmitoylation of Gs alpha. *Cell* **77,** 1063–1070 (1994).

223. Baker, T. L., Zheng, H., Walker, J., Coloff, J. L. & Buss, J. E. Distinct rates of palmitate turnover on membrane-bound cellular and oncogenic H-Ras. *J. Biol. Chem.* **278,** 19292–19300 (2003).

224. Duncan, J. A. & Gilman, A. G. A cytoplasmic acyl-protein thioesterase that removes palmitate from G protein α subunits and p21(RAS). *J. Biol. Chem.* **273,** 15830–15837 (1998).

225. Sugimoto, H., Hayashi, H. & Yamashita, S. Purification, cDNA cloning, and regulation of lysophospholipase from rat liver. *J. Biol. Chem.* **271,** 7705–7711 (1996).

226. Hirano, T. *et al.* Thioesterase activity and subcellular localization of acylprotein thioesterase 1/lysophospholipase 1. *Biochim. Biophys. Acta - Mol. Cell Biol. Lipids* **1791,** 797–805 (2009).

227. Duncan, J. a. & Gilman, A. G. Characterization of Saccharomyces cerevisiae acyl-protein thioesterase 1, the enzyme responsible for G protein α subunit deacylation in vivo. *J. Biol. Chem.* **277,** 31740–31752 (2002).

228. Toyoda, T., Sugimoto, H. & Yamashita, S. Sequence, expression in Escherichia coli, and characterization of lysophospholipase II. *Biochim. Biophys. Acta - Mol. Cell Biol. Lipids* **1437,** 182–193 (1999).

229. Rusch, M. *et al.* Identification of acyl protein thioesterases 1 and 2 as the cellular targets of the ras-signaling modulators palmostatin B and M. *Angew. Chemie - Int. Ed.* **50,** 9838–9842 (2011).

230. Tomatis, V. M., Trenchi, A., Gomez, G. a. & Daniotti, J. L. Acyl-protein thioesterase 2 catalizes the deacylation of peripheral membrane-associated GAP-43. *PLoS One* **5,** (2010).

231. Siegel, G. *et al.* A functional screen implicates microRNA-138-dependent regulation of the depalmitoylation enzyme APT1 in dendritic spine morphogenesis. *Nat. Cell Biol.* **11,** 705–716 (2009).

232. Banerjee, S., Neveu, P. & Kosik, K. S. A Coordinated Local Translational Control Point at the Synapse Involving Relief from Silencing and MOV10 Degradation. *Neuron* **64,** 871–884 (2009).

233. Beronja, S. *et al.* RNAi screens in mice identify physiological regulators of oncogenic growth. *Nature* **501,** 185–190 (2013).

234. Burger, M. *et al.* Crystal structure of the predicted phospholipase LYPLAL1 reveals unexpected functional plasticity despite close relationship to acyl protein thioesterases. *J. Lipid Res.* **53,** 43–50 (2012).

235. Fox, C. S. *et al.* Genome-wide association for abdominal subcutaneous and visceral adipose reveals a novel locus for visceral fat in women. *PLoS Genet.* **8,** (2012).

236. Hernandez, J. L., Majmudar, J. D. & Martin, B. R. Profiling and inhibiting reversible palmitoylation. *Curr. Opin. Chem. Biol.* **17,** 20–26 (2013).

237. Long, J. Z. & Cravatt, B. F. The metabolic serine hydrolases and their functions in mammalian physiology and disease. *Chem. Rev.* **111,** 6022–6063 (2011).

238. Dekker, F. J. & Hedberg, C. Small molecule inhibition of protein depalmitoylation as a new approach towards downregulation of oncogenic Ras signalling. *Bioorganic Med. Chem.* **19,** 1376–1380 (2011).

239. Xu, J. *et al.* Inhibiting the palmitoylation/depalmitoylation cycle selectively reduces the growth of hematopoietic cells expressing oncogenic Nras. *Blood* **119,** 1032–1035 (2012).

240. Tabatadze, N., Smejkalova, T. & Woolley, C. S. Distribution and posttranslational modification of synaptic ERα in the adult female rat hippocampus. *Endocrinology* **154,** 819–830 (2013).

241. Kemp, L. E. *et al.* Characterization of a serine hydrolase targeted by acyl-protein thioesterase inhibitors in Toxoplasma gondii. *J. Biol. Chem.* **288,** 27002–27018 (2013).

242. Child, M. a *et al.* Small-molecule inhibition of a depalmitoylase enhances Toxoplasma host-cell invasion. *Nat. Chem. Biol.* **9,** 651–6 (2013).

243. Cravatt, B. F., Wright, A. T. & Kozarich, J. W. Activity-based protein profiling: from enzyme chemistry to proteomic chemistry. *Annu. Rev. Biochem.* **77,** 383–414 (2008).

244. Deck, P. *et al.* Development and biological evaluation of acyl protein thioesterase 1 (APT1) inhibitors. *Angew. Chemie - Int. Ed.* **44,** 4975–4980 (2005).

245. Shi, Y. & Burn, P. Lipid metabolic enzymes: emerging drug targets for the treatment of obesity. *Nat. Rev. Drug Discov.* **3,** 695–710 (2004).

246. Weibel, E. K., Hadvary, P., Hochuli, E., Kupfer, E. & Lengsfeld, H. Lipstatin, an inhibitor of pancreatic lipase, produced by Streptomyces toxytricini. I. Producing organism, fermentation, isolation and biological activity. *J. Antibiot. (Tokyo).* **40,** 1081–1085 (1987).

247. Hadváry, P., Sidler, W., Meister, W., Vetter, W. & Wolfer, H. The lipase inhibitor tetrahydrolipstatin binds covalently to the putative active site serine of pancreatic lipase. *J. Biol. Chem.* **266,** 2021–2027 (1991).

248. Dekker, F. J. *et al.* Small-molecule inhibition of APT1 affects Ras localization and signaling. *Nat. Chem. Biol.* **6,** 449–456 (2010).

249. Hedberg, C. *et al.* Development of highly potent inhibitors of the ras-targeting human acyl protein thioesterases based on substrate similarity design. *Angew. Chemie - Int. Ed.* **50,** 9832–9837 (2011).

250. Zimmermann, T. J. *et al.* Boron-Based Inhibitors of Acyl Protein Thioesterases 1 and 2. *ChemBioChem* **14,** 115–122 (2013).

251. Smoum, R., Rubinstein, A., Dembitsky, V. M. & Srebnik, M. Boron containing compounds as protease inhibitors. *Chemical Reviews* **112,** 4156–4220 (2012).

252. Bachovchin, D. a. & Cravatt, B. F. The pharmacological landscape and therapeutic potential of serine hydrolases. *Nat. Rev. Drug Discov.* **11,** 52–68 (2012).

253. Bachovchin, D. a *et al.* Superfamily-wide portrait of serine hydrolase inhibition achieved by library-versus-library screening. *Proc. Natl. Acad. Sci. U. S. A.* **107,** 20941–20946 (2010).

254. Adibekian, A. *et al.* Click-generated triazole ureas as ultrapotent in vivo-active serine hydrolase inhibitors. *Nat. Chem. Biol.* **7,** 469–478 (2011).

255. Hsu, K.-L. *et al.* DAGLβ inhibition perturbs a lipid network involved in macrophage inflammatory responses. *Nature Chemical Biology* (2012). doi:10.1038/nchembio.1105

256. Liu, Y., Patricelli, M. P. & Cravatt, B. F. Activity-based protein profiling: the serine hydrolases. *Proc. Natl. Acad. Sci. U. S. A.* **96,** 14694–14699 (1999).

257. Adibekian, A. *et al.* Optimization and characterization of a triazole urea inhibitor for alpha/beta hydrolase domain-containing protein 11 (ABHD11): anti-probe for LYPLA1/LYPLA2 dual inhibitor ML211. **11,** 1–35

258. Hall, C. I. *et al.* Chemical genetic screen identifies Toxoplasma DJ-1 as a regulator of parasite secretion, attachment, and invasion. *Proc. Natl. Acad. Sci. U. S. A.* **108,** 10568–10573 (2011).

259. Powers, J. C., Asgian, J. L., Ekici, Ö. D. & James, K. E. Irreversible inhibitors of serine, cysteine, and threonine proteases. *Chem. Rev.* **102,** 4639–4750 (2002).

260. Kerrigan, J. E., Oleksyszyn, J., Kam, C. M., Selzler, J. & Powers, J. C. Mechanism-based isocoumarin inhibitors for human leukocyte elastase. Effect of the 7-amino substituent and 3-alkoxy group in 3-alkoxy-7-amino-4-chloroisocoumarins on inhibitory potency. *J. Med. Chem.* **38,** 544–552 (1995).

261. Adibekian, A. *et al.* Confirming target engagement for reversible inhibitors in vivo by kinetically tuned activity-based probes. *J. Am. Chem. Soc.* **134,** 10345–10348 (2012).

262. Bachovchin, D. a, Brown, S. J., Rosen, H. & Cravatt, B. F. Identification of selective inhibitors of uncharacterized enzymes by high-throughput screening with fluorescent activity-based probes. *Nat. Biotechnol.* **27,** 387–394 (2009).

263. Lu, H. & Tonge, P. J. Drug-target residence time: Critical information for lead optimization. *Curr. Opin. Chem. Biol.* **14,** 467–474 (2010).

264. Tsuboi, K. *et al.* Potent and selective inhibitors of glutathione S-transferase omega 1 that impair cancer drug resistance. *J. Am. Chem. Soc.* **133,** 16605–16616 (2011).

265. Davda, D. & Martin, B. R. Acyl protein thioesterase inhibitors as probes of dynamic S-palmitoylation. *Medchemcomm* **5,** 268 (2014).

266. Wang, W., Runkle, K. B., Terkowski, S. M., Ekaireb, R. I. & Witze, E. S. Protein Depalmitoylation Is Induced by Wnt5a and Promotes Polarized Cell Behavior. *J. Biol. Chem.* **290,** 15707–15716 (2015).

267. Mumby, S. M. Reversible palmitoylation of signaling proteins. *Current Opinion in Cell Biology* **9,** 148–154 (1997).

268. James, G. & Olson, E. N. Fatty acylated proteins as components of intracellular signaling pathways. *Biochemistry* **29,** 2623–2634 (1990).

269. Resh, M. D. Palmitoylation of ligands, receptors, and intracellular signaling molecules. *Sci. STKE* **2006,** re14 (2006).

270. Casey, P. J. Protein lipidation in cell signaling. *Science* **268,** 221–225 (1995).

271. Dunphy, J. T. & Linder, M. E. Signalling functions of protein palmitoylation. *Biochim. Biophys. Acta - Lipids Lipid Metab.* **1436,** 245–261 (1998).

272. Drenan, R. M. *et al.* Palmitoylation regulates plasma membrane-nuclear shuttling of R7BP, a novel membrane anchor for the RGS7 family. *J. Cell Biol.* **169,** 623–633 (2005).

273. Jia, L., Linder, M. E. & Blumer, K. J. G i/o signaling and the palmitoyltransferase DHHC2 regulate palmitate cycling and shuttling of RGS7 family-binding protein. *J. Biol. Chem.* **286,** 13695–13703 (2011).

274. Noritake, J. *et al.* Mobile DHHC palmitoylating enzyme mediates activity-sensitive synaptic targeting of PSD-95. *J. Cell Biol.* **186,** 147–160 (2009).

275. Neve, K. a., Qanbar, R. & Bouvier, M. Role of palmitoylation/depalmitoylation reactions in G-protein-coupled receptor function. *Pharmacol. Ther.* **97,** 1–33 (2003).

276. Schmick, M. & Bastiaens, P. I. H. The interdependence of membrane shape and cellular signal processing. *Cell* **156,** 1132–1138 (2014).

277. Hofmann, I. *et al.* K-RAS Mutant Pancreatic Tumors Show Higher Sensitivity to MEK than to PI3K Inhibition In Vivo. *PLoS One* **7,** (2012).

278. Stephen, A. G., Esposito, D., Bagni, R. G. & McCormick, F. Dragging ras back in the ring. *Cancer Cell* **25,** 272–281 (2014).

279. Vigil, D., Cherfils, J., Rossman, K. L. & Der, C. J. Ras superfamily GEFs and GAPs: validated and tractable targets for cancer therapy? *Nat. Rev. Cancer* **10,** 842–857 (2010).

280. Martínez-Lacaci, I. *et al.* RAS transformation causes sustained activation of epidermal growth factor receptor and elevation of mitogen-activated protein kinase in human mammary epithelial cells. *Int. J. Cancer* **88,** 44–52 (2000).

281. Hernández-Martín, a & Torrelo, a. Rasopathies: developmental disorders that predispose to cancer and skin manifestations. *Actas Dermosifiliogr.* **102,** 402–416 (2011).

282. Horiguchi, K. *et al.* Role of Ras signaling in the induction of snail by transforming growth factor-?? *J. Biol. Chem.* **284,** 245–253 (2009).

283. Rocks, O. *et al.* The palmitoylation machinery is a spatially organizing system for peripheral membrane proteins. *Cell* **141,** 458–471 (2010).

284. Rocks, O. *et al.* An acylation cycle regulates localization and activity of palmitoylated Ras isoforms. *Science* **307,** 1746–1752 (2005).

285. Hancock, J. F., Magee, a I., Childs, J. E. & Marshall, C. J. All ras proteins are polyisoprenylated but only some are palmitoylated. *Cell* **57,** 1167–1177 (1989).

286. Fukata, M., Fukata, Y., Adesnik, H., Nicoll, R. A. & Bredt, D. S. Identification of PSD-95 palmitoylating enzymes. *Neuron* **44,** 987–996 (2004).

287. Tsutsumi, R. *et al.* Identification of G protein alpha subunit-palmitoylating enzyme. *Mol. Cell. Biol.* **29,** 435–447 (2009).

288. Duncan, J. a & Gilman, A. G. CELL BIOLOGY AND METABOLISM : A Cytoplasmic Acyl-Protein Thioesterase A Cytoplasmic Acyl-Protein Thioesterase That Removes Palmitate from G Protein ␣Subunits and p21 RAS *. **273,** 15830–15837 (1998).

289. Charollais, J. & Van Der Goot, F. G. Palmitoylation of membrane proteins (Review). *Mol. Membr. Biol.* **26,** 55–66 (2009).

290. Subbaiah, V. K., Kranjec, C., Thomas, M. & Banks, L. PDZ domains: the building blocks regulating tumorigenesis. *Biochemical Journal* **439,** 195–205 (2011).

291. Radhika, V. & Dhanasekaran, N. Transforming G proteins. *Oncogene* **20,** 1607–1614 (2001).

292. Pagliarini, R. A. & Xu, T. A genetic screen in Drosophila for metastatic behavior. *Science* **302,** 1227–1231 (2003).

293. Brumby, A. M. & Richardson, H. E. scribble mutants cooperate with oncogenic Ras or Notch to cause neoplastic overgrowth in Drosophila. *EMBO J.* **22,** 5769–5779 (2003).

294. Bilder, D. & Perrimon, N. Localization of apical epithelial determinants by the basolateral PDZ protein Scribble. *Nature* **403,** 676–680 (2000).

295. Gateff, E. Malignant neoplasms of genetic origin in Drosophila melanogaster. *Science* **200,** 1448–1459 (1978).

296. Dow, L. E. *et al.* hScrib is a functional homologue of the Drosophila tumour suppressor Scribble. *Oncogene* **22,** 9225–9230 (2003).

297. Audebert, S. *et al.* Mammalian scribble forms a tight complex with the βPIX exchange factor. *Curr. Biol.* **14,** 987–995 (2004).

298. Dow, L. E. *et al.* The tumour-suppressor Scribble dictates cell polarity during directed epithelial migration: regulation of Rho GTPase recruitment to the leading edge. *Oncogene* **26,** 2272–2282 (2007).

299. Zeng, X., Singh, S. R., Hou, D. & Hou, S. X. Tumor suppressors Sav/Scrib and oncogene ras regulate stem-cell transformation in adult Drosophila malpighian tubules. *J. Cell. Physiol.* **224,** 766–774 (2010).

300. Wu, M., Pastor-Pareja, J. C. & Xu, T. Interaction between Ras(V12) and scribbled clones induces tumour growth and invasion. *Nature* **463,** 545–548 (2010).

301. Doggett, K., Grusche, F. a, Richardson, H. E. & Brumby, A. M. Loss of the Drosophila cell polarity regulator Scribbled promotes epithelial tissue overgrowth and cooperation with oncogenic Ras-Raf through impaired Hippo pathway signaling. *BMC Dev. Biol.* **11,** 57 (2011).

302. Young, L. *et al.* An MRAS, SHOC2, and SCRIB complex coordinates erk pathway activation with polarity and tumorigenic growth. *Mol. Cell* **52,** 679–692 (2013).

303. Yamanaka, T. & Ohno, S. Role of Lgl/Dlg/Scribble in the regulation of epithelial junction, polarity and growth. *Front. Biosci.* **13,** 6693–6707 (2008).

304. Cordenonsi, M. *et al.* The hippo transducer TAZ confers cancer stem cell-related traits on breast cancer cells. *Cell* **147,** 759–772 (2011).

305. Tian, H. *et al.* Systematic siRNA Screen Unmasks NSCLC Growth Dependence by Palmitoyltransferase DHHC5. *Mol. Cancer Res.* **13,** 784–794 (2015).

Chapter 2:
Analysis of 2-Bromopalmitate Proteome Reactivity and Utility as a Probe for Protein S-Acyltransferases

2.1 Abstract

2-Bromohexadecanoic acid, or 2-bromopalmitate,was introduced nearly 50 years ago as a nonselective inhibitor of lipid metabolism. More recently, 2-bromopalmitate re-emerged as a general inhibitor of protein *S*-palmitoylation. Here, we investigate the cellular targets of 2-bromopalmitate through the synthesis and application of click-enabled analogues. In cells, 2-bromopalmitate is converted to 2-bromopalmitoyl-CoA, although less efficiently than free palmitate. Once conjugated to CoA, probe reactivity is dramatically enhanced. Importantly, both 2-bromopalmitate and 2-bromopalmitoyl-CoA label DHHC palmitoyl acyltransferases (PATs), the enzymes that catalyze protein *S*-palmitoylation. Mass spectrometry analysis of enriched 2-bromopalmitate targets identified PAT enzymes, transporters, and many palmitoylated proteins, with no observed preference for CoA-dependent enzymes. These data question whether 2-bromopalmitate (or 2-bromopalmitoyl-CoA) blocks *S*-palmitoylation by inhibiting protein acyl transferases, or by blocking palmitate incorporation by direct covalent competition. Overall, these findings highlight the promiscuous reactivity of 2BP and validate clickable 2BP analogues as activity-based probes of diverse membrane associated enzymes.

Individual contributions. Most of the work in this chapter was produced by me with the following exceptions. As for principle investigators, Dr. Brent R. Martin provided the major funding, conceived the project and directed all experimental designs. Dr. Robert T. Kennedy provided funding for and directed the metabolomic experiments. As for postdoctoral fellows, Dr. Mahmoud A. El Azzouny performed the metabolomic experiments with 2BP. Dr. Jeannie L. Hernandez generated DHHC2 active site point-

mutants and assayed the activities of DHHC members towards 2BP. Dr. Jaimeen Majmudar helped with the proteomic analysis of 2BP targets and Cristopher T. M. B. Tom synthesized the 2BP-CoA derivative.

2.2 Introduction

2-bromopalmitate (2BP) is an irreversible inhibitor of many membrane-associated enzymes.[1] It was initially reported as an inhibitor of β-oxidation[2,3] but later shown to inhibit mono-, di-,and triacylglycerol transferases, fatty acyl CoA ligase, glycerol-3-phosphate acyltransferase, as well as nonlipid processing enzymes such as NADPH cytochrome-C reductase and glucose-6-phosphatase at submillimolar concentrations.[1] Importantly, each of these enzymes has cysteine residues in or near the enzyme active site, suggesting α-halo-carbonyl electrophilic alkylation mediates the observed irreversible inhibition. This reactivity was later confirmed by labeling rat liver fractions with millimolar concentrations of 1-[^{14}C],2-bromopalmitate.[1] After separation by SDS-PAGE and autoradiography, radioactivity was detected across many unique proteins, highlighting the promiscuous reactivity and potential issues associated with this nonspecific covalent inhibitor.

Despite these issues, 2BP was later shown to block the *S*-palmitoylation and microdomain recruitment of the Src-family kinases Lck and Fyn.[4] Inhibition with 100 μM 2BP attenuated Jurkat T-cell calcium activation and blocked tyrosine phosphorylation of LAT, PLC-γ, ZAP-70, and Vav.[4] This finding established 2BP as the only pharmacological tool to block protein S-palmitoylation. Over the past decade, 2BP has become deeply rooted in the palmitoylation field, often referenced as a selective inhibitor of protein S-palmitoylation. Indeed, many studies have used 2BP-induced phenotypes as evidence of the importance of palmitoylation in parasitic infection,[5] differentiation,[6] and various other cellular phenotypes.[7]

2BP inhibition is thought to block protein palmitoylation by inhibiting a family of conserved protein acyl transferases (PATs).[8] Mammals express 23 distinct PAT enzymes that are presumed to regulate the profile of palmitoylated proteins, either by PAT localization, protein interactions, or active site selectivity.[7,8] Knockdown of specific PAT enzymes reduces palmitoylation of select substrates. For example, a hypomorphic gene-trap mouse model of DHHC5 demonstrates reduced flotilliin-2 palmitoylation, disrupted stem cell differentiation, and defective hippocampal-dependent learning.9 Other genetic models of PAT enzymes reveal a wide array of phenotypes in cancer, neurodegeneration, hair loss, and amyloidosis.[7] Similarly, overexpression of certain

PATs are implicated in cancer progression, malignancy, and metastasis.[7] Given the array of novel biology regulated by PAT enzymes, selective pharmacological reagents are critical for advancing our basic understanding of protein palmitoylation in disease.

Each PAT enzyme contains a highly conserved cysteine-rich domain anchored by the four amino acid Asp-His-His-Cys (DHHC) motif. Mutation of the DHHC-cysteine residue to serine abolishes enzyme activity, suggesting this cysteine is the catalytic nucleophile and site of acyl-transfer.[10,11] Addition of palmitoyl-CoA to purified, detergent solubilized PAT enzymes induces autopalmitoylation and formation of the enzyme-acyl intermediate,[12] which then transfers the palmitoyl group to a cysteine residue on the substrate. *In vitro*, 2BP covalently blocks the formation of the PAT acyl-intermediate (IC50 of 10μM).12 Similarly, GAP43-YFP plasma membrane localization is inhibited in live cells by 2BP at nearly the same potency (IC50 =14.9 μM).[13] These experiments strongly suggest DHHC proteins are unlikely to require a CoA conjugate for inhibition.

Bioorthogonal alkyne and azide palmitate analogues have been introduced for metabolic labeling and detection of native sites of protein palmitoylation.[14,15] This approach uses the endogenous palmitoylation machinery to covalently tag palmitoylated proteins, which are then labeled using Cu(I) catalyzed click chemistry to azide or alkyne-linked reporters. The successful metabolic incorporation of these analogues demonstrates the broad tolerance of minor terminal acyl modifications in palmitoylation, and suggests α-brominated analogues may be useful mechanistic probes to profile the cellular targets of 2BP alkylation.

Historically, 2BP was recognized as a nonselective inhibitor of lipid metabolism.1 Over the past decade, the promiscuity of 2BP has been overshadowed by significant need for pharmacological tools to study protein palmitoylation. Here, we present the synthesis and evaluation of a click-enabled 2BPanalogue and the corresponding CoA conjugate to explore the targets and mechanism of 2BP inhibition in cells, and annotate the consequences of promiscuous 2BP inhibition in palmitoylation analysis.

2.3 Materials and Methods

General synthetic methods. All reagents were used as received unless otherwise noted. All reactions were conducted in flame-dried glassware under nitrogen atmosphere. Flash column chromatography was performed with silica gel (Grade 923, 100–200 mesh). Thin-layer chromatography (TLC) was performed on silica gel GHLF plates (250 microns) purchased from Analtech. Developed TLC plates were visualized with a UV lamp at 254 nm or by an appropriate chemical stain. Extraction solutions were dried over $MgSO_4$ prior to concentration. ^{1}H and ^{13}C spectra were obtained in $CDCl_3$ at RT (25 ^{o}C), unless otherwise noted, on a Varian Mercury 400 or Varian Unity 500 MHz instrument. Chemical shifts of ^{1}H NMR spectra were recorded in parts per million (ppm) on the δ scale from an internal standard of residual chloroform (7.27 ppm). Chemical shifts of ^{13}C NMR spectra were recorded in ppm from the central peak of CDCl3 (77.0 ppm) on the δ scale. Low resolution electrospray mass spectra were obtained on a Micromass LCT spectrometer, and high resolution electrospray mass spectra were obtained on a Micromass AutoSpec Ultima spectrometer at the University of Michigan Mass Spectrometry Laboratory.

*Synthesis of 16-azidohexadecanoic acid (**1**).* To a solution of 16-bromohexadecanoic acid (250 mg, 0.75 mmol) in DMF (2 mL) was added sodium azide (100 mg, 1.5 mmol) and the reaction was heated to 85 °C and stirred for 12 h. It was then cooled to room temperature, diluted with CH2Cl2 and quenched with 0.1 *N* HCl. The organic layer was dried over MgSO4, filtered and concentrated to afford **1** as a white solid (183 mg, 82%) and was used without further purification. Rf 0.51 (30% EtOAc : hexanes). IR (thin film on NaCl): cm-1 = 2098 (-N3). 1H NMR (400 MHz, CDCl3): δ (ppm) = 3.18 (t, *J* = 7.0 Hz, 2H), 2.27 (t, *J* = 7.5 Hz, 2H), 1.58 – 1.49 (m, 4H), 1.30 – 1.19 (m, 22H). HRMS: *m/z* calculated for C16H30N3O2: 296.2338, found 296.2340 $[M - H]^{-}$.

*Synthesis of 16-azido-2-bromohexadecanoic acid, 2BPN3 (**2**).* **1** (2.0 g, 6.7 mmol) was dissolved in thionyl chloride (40 mL) and stirred at reflux for 1 h. Then, bromine (450 FL, 8.7 mmol) was added dropwise over 3 h and the reaction was further refluxed for 3 h. The mixture was then cooled to room temperature, concentrated, dissolved in H2O and stirred at room temperature for 12 h. The aqueous solution was

extracted with diethyl ether (3x), and the organic layers were combined, washed with 0.1 *N* HCl, dried over MgSO4, filtered and concentrated to afford an orange solid. Purification of this solid by flash chromatography (30% EtOAc : hexanes) yielded **2** (1.0 g, 40%) as a white solid. Rf 0.13 (30% EtOAc : hexanes). 1H NMR (400 MHz, CDCl3): δ (ppm) = 4.20 (t, *J* = 7.4 Hz, 1H), 3.21 (t, *J* = 7.0 Hz, 2H), 2.05 – 1.92 (m, 2H), 1.59 – 1.52 (m, 2H), 1.47 – 1.17 (m, 22H). HRMS: *m/z* calculated for C16H29BrN3O2: 374.1443, found 374.1439 [*M* - H]$^-$.

*Synthesis of N-(2-bromohexadecanoyl)succinimide (**3**).* The succinimidyl ester was prepared as previously described[25]. 2-bromopalmitic acid (500 mg, 1.49 mmol, Sigma) was added to a solution of *N*-hydroxysuccinimide (172 mg, 1.49 mol) in dry ethyl acetate (5 mL). *N,N'*-diisopropylcarbodiimide (257 µL, 1.64 mol) was added at room temperature, and the mixture was allowed to react overnight. Precipitated diisopropylurea was removed by filtration through a glass wool plug. The solvent was evaporated yielding a white powder, which was then recrystallized from absolute ethanol, to afford **3** (457 mg, 70.8%) as white crystals. ^{1}H NMR (400 MHz, CDCl3): δ (ppm) = 4.43 (dd, *J* = 7.8, 6.9 Hz, 1H), 2.84 (s, 4H), 2.22 – 2.05 (m, 2H), 1.58 - 1.38 (m, 2H) 1.39 – 1.14 (m, 22H), 0.86 (t, *J* = 7 Hz, 3H). ^{13}C NMR (100 MHz, CDCl3): δ (ppm) = 168.44, 165.64, 40.90, 34.79, 31.90, 29.66, 29.65, 29.63, 29.61, 29.54, 29.42, 29.34, 29.21, 28.70, 26.93, 25.58, 22.67, 14.11.

*Synthesis of 2-bromohexadecanoyl coenzyme A, 2BP-CoA (**4**).* The acyl CoA was synthesized using a modified literature procedure[26]. **3** (26 mg, 61 µmol) was dissolved in freshly distilled THF (0.6 mL) and mixed with a solution of coenzyme A trilithiate dihydrate (5 mg, 6.1 µmol, Fisher) dissolved in deionized water (0.3 mL). Triethylamine (8.5 uL, 61 µmol) was added to the reaction and the homogeneous mixture was stirred on a rotisserie rotator for 3 hours at room temperature. The crude product was precipitated by adding 5% perchloric acid (1.2 mL) and excess THF was removed by rotary evaporation. The precipitate was collected by centrifugation (5 min, 3220x g, 4 ˚C) and the supernatant was discarded. The precipitate was washed, sonicated and centrifuged sequentially with 0.8% perchloric acid (2.5 mL), acetone (4 X 1.5 mL) and diethyl ether (3 X 1 mL) to remove excess starting materials. The white residue was extracted with 2-(*N*-morpholino)ethanesulfonic acid buffer (0.4 mL, 50 mM,

pH 5) and insoluble side-products were removed by centrifuging the mixture. The product was precipitated again with 5% perchloric acid (0.6 mL). The precipitate was washed, sonicated and centrifuged sequentially with 0.8% perchloric acid (1 mL), acetone (3 x 0.5 mL), and dried under vacuum to afford **4** (1.3 mg, 19%) as a white powder. HRMS: *m/z* calculated for $C_{37}H_{63}BrN_7O_{17}P_3S_2^-$: 540.6204, found 540.6194 [*M* - 2H]$^-$.

*Synthesis of N-(16-azido-2-bromohexadecanoyl)succinimide (**5**).* Following the procedure used to prepare *N*-(2-bromohexadecanoyl)succinimide, **2** (23 mg, 0.061 mmol), *N*-hydroxysuccinimide (7 mg, 0.061 mol), *N,N'*-diisopropylcarbodiimide (11 µL, 0.067 mol) in ethyl acetate (1 mL) were used to yield **5** (7.2 mg, 25%) as white crystals.

*Synthesis of 16-azido-2-bromohexadecanoyl coenzyme A, 2BPN$_3$-CoA (**6**).* Following the procedure used to synthesize 2-bromohexadecanoyl coenzyme A, **5** (7.2 mg, 15.7µmol), coenzyme A trilithiate dihydrate (1.3 mg, 1.57 µmol), and triethylamine (2.2uL, 15.7 µmol) in THF (200 µL) and deionized water (100 µL) were employed to afford **6** (1.6 mg, 24%) as a white powder HRMS: *m/z* calculated for $C_{37}H_{62}BrN_{10}O_{17}P_3S^{2-}$: 561.1211 [M – 2H]-, found 561.1240 [M - 2H]-.

Qualitative characterization of acyl-CoA conjugates. The purity of 2BP-CoA and 2BPN3-CoA were assessed by TLC*3* and the thioester content of the preparations were determined spectroscopically[27,28]. The products were eluted on C18-bonded silica reverse phase TLC plates using *n*-butanol/water/acetic acid (5:3:2) as the solvent system. 2BP-CoA and 2BPN3-CoA were visualized under UV light, each revealing a single spot with R_f-value of 0.55 and 0.57 respectively (palmitoyl-CoA authentic standard R_f = 0.53). In addition, these spots gave a positive nitroprusside test for free thiol groups only after treatment with methanolic NaOH. 2BPCoA and 2BPN3-CoA were dissolved in 75% isopropanol, 1 mM acetic acid to make 1 g / L stocks for spectroscopic analyses. The UV spectrum of each product was measured against an authentic palmitoyl-CoA (Sigma), with each acyl-CoA featuring a peak at 232 and at 260 nm. Furthermore, the 232 nm absorbance disappeared after methanolic NaOH treatment, indicating hydrolysis of the thioester bond. The relative concentrations of thioester to adenine in each acyl-CoA preparation was determined by measuring the ratio of the 232

nm over 260 nm absorptions and using experimentally calculated extinction coefficients at 232 and 260 nm for the authentic palmitoyl-CoA standard.

Cell culture. HEK293T cells were grown in Dulbecco's Modified Eagle Medium (DMEM, Invitrogen) supplemented with 10% (vol/vol) fetal bovine serum (FBS, JR Scientific) and 1% (vol/vol) 10,000 units penicillin, 10,000 µg streptomycin, 29.2 mg L-glutamate solution (PSQ, Invitrogen). Cells grown to ~60% confluency were transfected with pcDNA3 vectors expressing FLAG-epitope tagged proteins using Fugene HD transfection reagent (Promega). Cells were cultured for 48 hours to allow for sufficient protein expression.

Mass spectrometry-based metabolomic analysis of CoA conjugates. 2-bromopalmitate and palmitate were both dissolved in BSA free fatty acid (0.05%) to achieve 1:6 molar ratio of BSA : fatty acid. INS-1(832/3) cells were incubated with 50 µM 2BP or 50 µM palmitic acid for 30 minutes in Kreb's Ringer Buffer with 0 mM glucose at 37°C. Cells were quenched and extracted as previously described[5], and normalized to protein concentrations using the BCA protein assay kit (Pierce). Detection was performed on an Agilent Technologies LC/MSD TOF using a dual electrospray ionization (ESI) source in negative-ion mode and analyzed as previously described[29]. The concentration of 2BP was determined by standard addition method, where a known concentration of standard was added to the unknown sample (pooled extract of 2BP treated cell, n = 4). Data was acquired from 2 biological replicates of 4 technical replicates processed on separate days. INS-1(832/3) cells were kindly provided by Dr. Christopher Newgard (Sarah W. Stedman Nutrition and Metabolism Center, Duke University, Durham, NC).

Metabolic labeling. Labeling media was prepared with DMEM, 10% dialyzed FBS (Gemini Bio-Products), and 1% PSQ. 16-Azido-2-bromopalmitic acid (2BPN3) or 2 bromopalmitic acid (2BP, Sigma) was dissolved in DMSO to make a 50 mM (1000X) stock, then diluted in labeling media and briefly sonicated, and then added to cells at ~100% confluency. Cells were labeled with 2BP or 2BPN3 at the concentrations described for the indicated time period. Cells were collected by centrifugation at 800x g, washed twice with PBS, and then stored at -80ºC as cell pellets.

Lysate preparation. Pellets were re-suspended in phosphate buffered saline (without magnesium and calcium, PBS, Invitrogen), and sonicated briefly at 4oC. Cell debris was removed by low-speed centrifugation at 800x g for 2 minutes, and supernatant was placed into a new conical tube. Lysates were separated into soluble and membrane particulate fractions by ultracentrifugation at 100,000x g for 45 minutes. The insoluble pellet was sonicated in PBS to homogenize the lysate. The protein concentration was determined using the BCA assay (Biorad) using a Tecan F500 plate reader. Membrane particulate fractions were diluted in PBS to 1 mg / mL of proteome, then reacted with the indicated probe at the concentrations described for one hour at room temperature.

Copper-catalyzed azide-alkyne cycloaddition. 1 mg / mL of proteome was combined with 20 µM Carboxytetramethylrhodamine-alkyne (TAMRA-Alkyne, Click Chemistry Tools), 1 mM Tris(2-carboxyethyl)phosphine (TCEP, Sigma-Aldrich), 100 µM Tris((1-benzyl-1H-1,2,3-triazol-4-yl)methyl)amine (TBTA, Sigma-Aldrich), and 1 mM CuSO4 in PBS (25 µl) at room temperature (~22°C). After 1 hour, samples were mixed with SDS loading buffer and denatured at 90°C for 10 minutes. 8 µg of protein was loaded into each lane of a 10% SDS-PAGE, separated over 180 V-hours and fluorescence scanned on an Amersham Bioscience Typhoon scanner.

Mass spectrometry-based proteomic analysis. Samples were prepared as previously described*6*, but biotin alkyne (Click Chemistry Tools) was substituted at 20 µM. Furthermore, samples were chloroform/methanol precipitated following the click reaction to remove unreacted biotin-alkyne. Higher concentrations of biotin-alkyne led to increased non-specific background. Mass spectrometry analysis was performed as previously described[30], using an Agilent 1100 HPLC coupled to a Thermo LTQ mass spectrometer using a 5-step MuDPIT protocol. Data analysis was performed using previously reported algorithms.

Immunoblotting. Proteins were transferred to 0.45 um polyvinylidine difluoride membrane (Immobilon-P, Millipore) and blocked with 5% bovine serum albumin (BSA, Fisher) in Tris buffered saline-Tween 20 buffer (TBS-T, pH 7.4) for 1 hour at room temperature. After washing, the membrane was incubated with a primary mouse-anti-FLAG antibody (M2 monoclonal, Sigma, 1 µg / mL antibody, 5% BSA, 0.02% NaN3,

TBS-T) for 1 hour at room temperature, washed, and probed with a secondary Alexa Fluor 647 nm donkey-anti-mouse antibody conjugate (IgG H +L, Invitrogen, 2 µg / mL antibody, 0.06% w/v NaN_3, TBS-T) for 1 hour at room temperature. For streptavidin-based detection, the membrane was probed with a Cy5-streptavidin conjugate (50 ng / mL conjugate, 2.5% BSA, 0.06% NaN3, TBS-T) for 1 hour at room temperature, and the washed as before. Blots were fluorescence scanned on an Amersham bioscience typhoon scanner.

2.4 Results

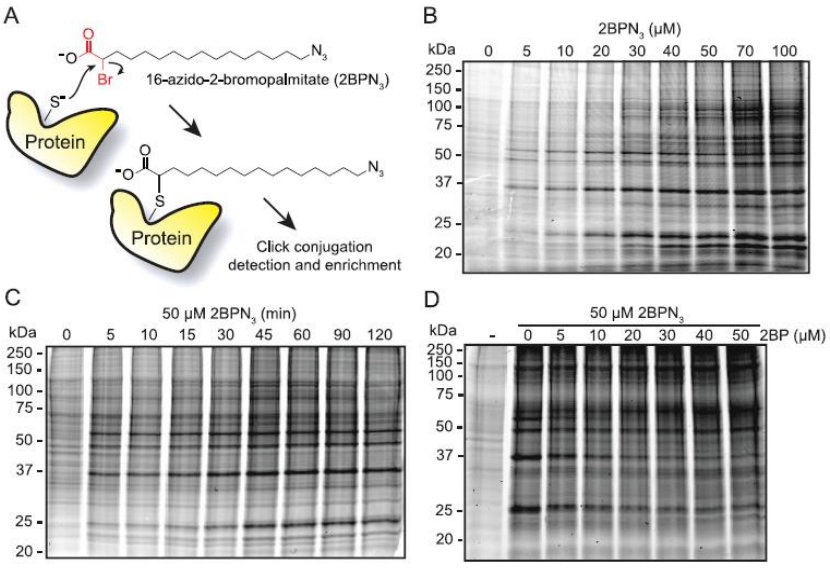

Figure 2-1 Metabolic labeling with 2BPN3 allows click-enabled detection of cellular targets. (A) Schematic of 2BPN3 alkylation of cysteine thiolates on proteins by attack of the α-halo-carbonyl group, followed by click chemistry detection of labeled proteins. (B) Concentration-dependent metabolic labeling with 2BPN3 in 293T cells. (C) Time-dependent metabolic labeling with 2BPN3 in 293T cells. (D) Preincubation with 2BP attenuated 2BPN3 labeling at higher concentrations. Each inhibitor was added for 1 h at the described concentrations. For each gel, lysates were reacted with rhodamine-alkyne and separated by SDS-PAGE gel followed by fluorescence analysis.

Given the broad use of 2BP as a palmitoylation inhibitor, we sought to test the utility of this scaffold as an activity-based probe for DHHC PAT enzymes. Such probes would covalently label endogenous targets for click chemistry conjugation to alkyne-linked reporters, including fluorescent dyes for gel-based detection, or biotin for mass spectrometry annotation (Figure 2-1A).

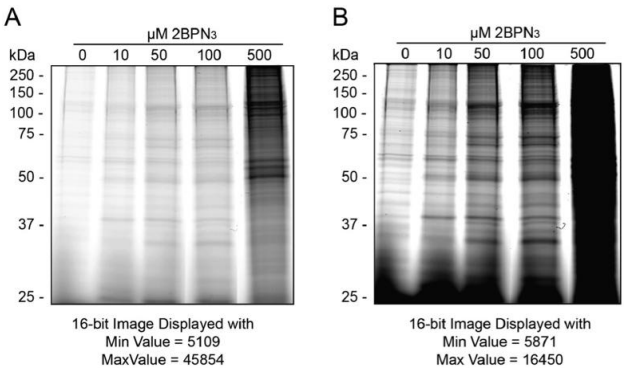

Figure 2-2 2BPN3 labeling is significantly increased at higher concentrations in 293T cells. Cells were labeled for 1 hour. (A) 2BPN3 labeling adjusted to maximize contrast at 10-fold higher than the standard labeling concentration. (B) 2BPN3 labeling adjusted to maximize contrast at 50 μM.

Because of the generic scaffold and electrophilic reactive group, we anticipated this approach would likely label a profile of proteins involved in lipid metabolism. The ω-azido analogue of 2BP (2BPN3) was synthesized and added directly to the growth media of human 293T cells at varying concentrations. After 1 h, the cells were harvested and lysed for copper catalyzed azide−alkyne cycloaddition to rhodamine-alkyne for gel-based detection. Membrane

fractions demonstrated significant contrast and dose-dependent labeling of 2BPN3 (Figure 2-1B).

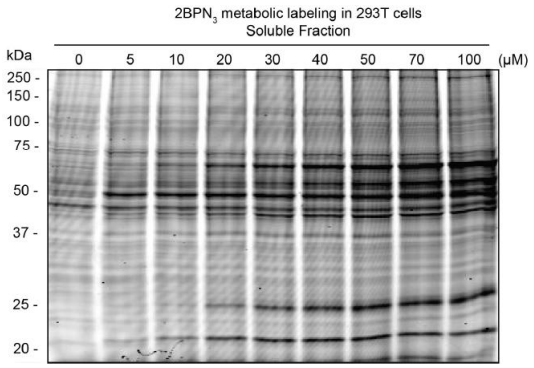

Figure 2-3 Soluble cell fractions show significant labeling with rhodamine alkyne in the absence of 2BPN3. 293T cells were labeled with 2BPN3 for 1 hour, then lysed by sonication and centrifuged at 100,000x g for 45 minutes. The soluble fraction was quantified using the BCA assay and mixed with 20 μM rhodamine-alkyne and remaining click chemistry reagents for 1 hour. Samples were separated using a 4-20% gradient SDS-PAGE gel.

Higher concentrations led to enhanced labeling (Figure 2-2) but also pronounced cytotoxicity. In contrast, analysis of soluble fractions was complicated by nonspecific, alkyne-dependent background (Figure 2-3). Copper-free strain promoted cycloaddition with rhodamine-linked aza-dibenzocyclooctyne (DIBAC)[16] showed dramatically enhanced labeling but did little to improve the overall contrast (Figure 2-4). These findings corroborate recent reports quantifying thiol cross-reactivity of strain-promoted cycloadditions.[1]

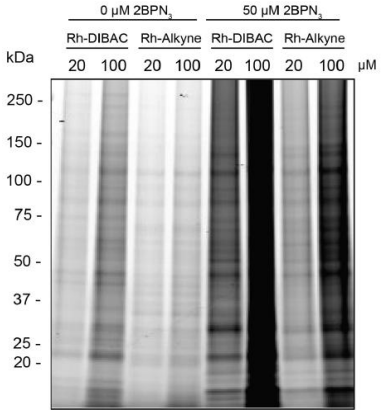

Figure 2-4 Comparison of copper and copper-free click chemistry labeling of 2BPN3. Cells were labeled for 1 hour with 2BPN3, followed by incubation with either rhodamine-alkyne or rhodamine-aza-dibenzocyclooctyne (DIBAC). Samples were separated using a 4-20% gradient gel. DIBAC labeling is significantly more efficient, but has no clear increase in contrast over no-probe controls.

Surprisingly, 2BPN3 labeling occurs within 5 min and gradually increases until ~60 min (Figure 2-1C). This rapid labeling suggests direct action of the native probe but also may involve metabolic activation to the CoA conjugate. Based on these results, we selected 50 μM 2BPN3 for 1 h as an effective protocol for labeling live cells. These conditions are consistent with cell-based experiments of palmitoylation inhibition and the reported IC50 for PAT inhibition of 10−15 μM.[13] In cells, preincubation with 50 μM 2BP reduced but did not eliminate 2BPN3 metabolic labeling (Figure 2-1D). *In vitro*, higher 2BP concentrations could effectively compete with 2BPN3 (Figure 2-5), suggesting poor cellular uptake and distribution in live cells. Moreover, 2BPN3 addition reduced but did not eliminate

metabolic incorporation of 17-octadecynoic acid (17-ODYA), suggesting a significant fraction of protein palmitoylation is highly stable or nonenzymatic (Figure 2-6).

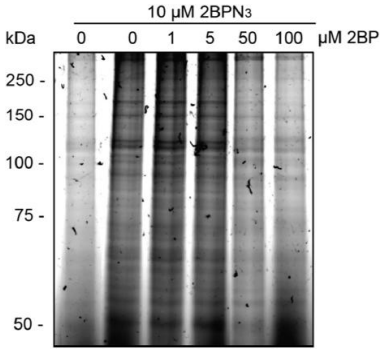

Figure 2-5 Efficient in vitro competition of 2BPN3 labeling with 2BP. 293T cell lysates were labeled with increasing concentrations of 2BP for 1 hour, followed by labeling with 2BPN3 for 1 hour. Competition in vitro is by far more effective than live cell competition, as shown in Error! Reference source not found.D.

2BP is believed to undergo activation to the CoA intermediate in live cells, which then directs reactivity toward CoA-dependent enzymes. Metabolic labeling with 2BPN3 is ~10-fold less efficient than *in vitro* labeling (Figure 2-7A), but the profile of labeled proteins appears largely similar. This discrepancy may be due to insufficient probe solubility and uptake in culture. In order to establish metabolic activation of 2BP to the CoA conjugate, cells were incubated with 2BP or palmitic acid for 30 min, followed by extraction, chromatographic separation, and high-resolution mass spectrometry analysis (Figure 2-7B).

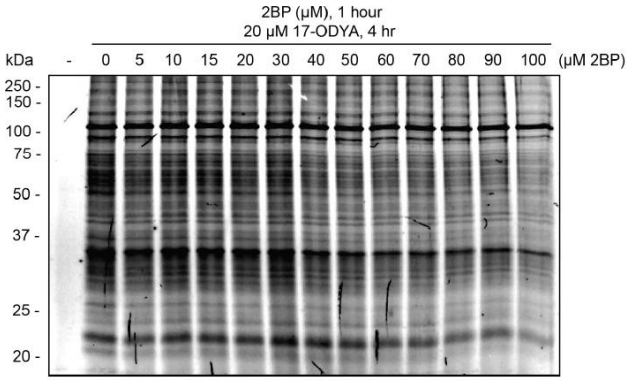

Figure 2-6 2BP reduces metabolic incorporation of the palmitate analogue 17-octadecynoic acid (17-ODYA) in cells. 293T cells were labeled for 1 hour with varying concentrations of 2BP, followed by addition of 17-ODYA for 4 additional hours. Palmitoylation levels are reduced most effectively at the highest concentrations of 2BP. Samples were separated using a 4-20% gradient SDS-PAGE gel.

Synthetic 2BP-CoA was shown to ionize similarly (99.8 ± 0.3%, standard error) to palmitoyl-CoA across a series of dilutions (Figure 2-8). Basal palmitoyl-CoA levels were measured as 250 ± 31 pmol/mg of protein, yet were elevated 3.2-fold (805 ± 101 pmol/mg) after a 30 min incubation with 50 μM palmitic acid. Addition of 50 μM 2BP led to the formation of 36 ± 4 pmol/mg of 2BPCoA but had no major effect on palmitoyl-CoA levels (205 ± 17pmol/mg). 2BP-CoA was nearly 6-fold lower than endogenous levels of palmitoyl-CoA, which likely competes with 2BP-CoA for access to CoA processing

enzymes. These data confirm 2BP metabolic conversion in live cells to the CoA conjugate within 30 min, although at reduced efficiency as compared to palmitoyl-CoA.

Next, a 2BPN3−CoA conjugate was synthesized for analysis in cell lysates. 2BPN3−CoA (cLogP = 4.4) is predicted to be much more water-soluble than 2BPN3 (cLogP = 7.7). Furthermore, 2BP is negatively charged at physiological pH, which increases the electron density and delocalization at the carboxylate and reduces the electrophilic character of the α-carbon. Thioesterification is predicted to reduce the delocalization and enhance the carbonyl dipole to promote α-substitution, resulting in improved probe reactivity. Experimentally, the CoA conjugate achieved equivalent labeling with10-fold less probe (Figure 2-7C), and unexpectedly labeled a similar profile of targets as the free acid. Furthermore, 2BPN3 and 2BPN3−CoA react with different targets than 2-iodacetamide-rhodamine (Figure 2-7D). Whether the enhanced reactivity of 2BPN3−CoA is a function of the CoA motif, or a manifestation of the thioester linkage remains to be investigated. Overall, we observe that 2BP is coupled to CoA in cells at a reduced efficiency, yet the conjugate is exceptionally reactive.

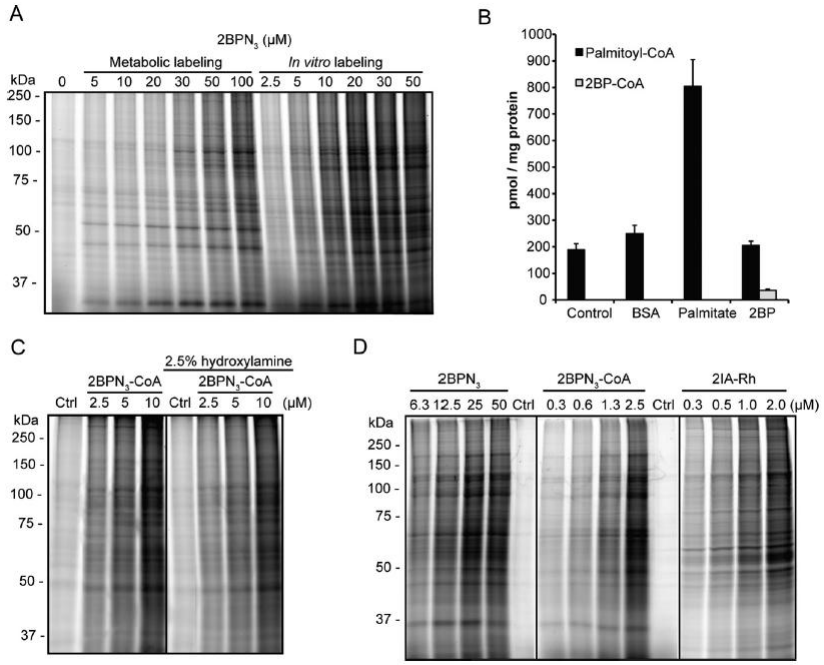

Figure 2-7 2BPN3 is conjugated to CoA in cells, resulting in an increase in probe reactivity. (A) Comparison of 2BPN3 metabolic labeling and in vitro labeling. Cells or lysates were labeled for 1 h with 2BPN3. Lower probe concentrations were required for equivalent labeling in vitro compared to metabolic labeling. (B) 2BP is marginally converted to 2BP-CoA in cells. Control samples were collected immediately after transfer from RPMI to ringer's solution. The remaining cells were left for 30 min in the presence of fatty acid free BSA, BSA bound to 50 μM palmitic acid, or BSA bound to 50 μM 2BP. Cells were quenched and metabolites were extracted and analyzed in quadruplicate by high-resolution LC-MS.

Samples were run as biological quadruplicates and standard errors are shown. Synthetic palmitoyl-CoA and 2BP-CoA were used to generate a standard curve to calculate endogenous metabolite concentrations. (C) Labeling of cell lysates with increasing concentrations of 2BPN3−CoA in vitro. The control lane is lysate incubated with 50 μM 2BP-CoA, which did not show significant labeling following the click chemistry reaction. (D) Comparison of 2BPN3, 2BPN3−CoA, and 2-iodoacetamide-rhodamine (2IA-Rh) shows probe-specific labeling in vitro. The control lanes are lysates incubated with either 50 μM 2BP (left) or 2.5 μM 2BPCoA (center). 2BPN3−CoA labeling is more reactive but labels a similar pattern of proteins. 2IA-Rh labels a distinct pattern of proteins.

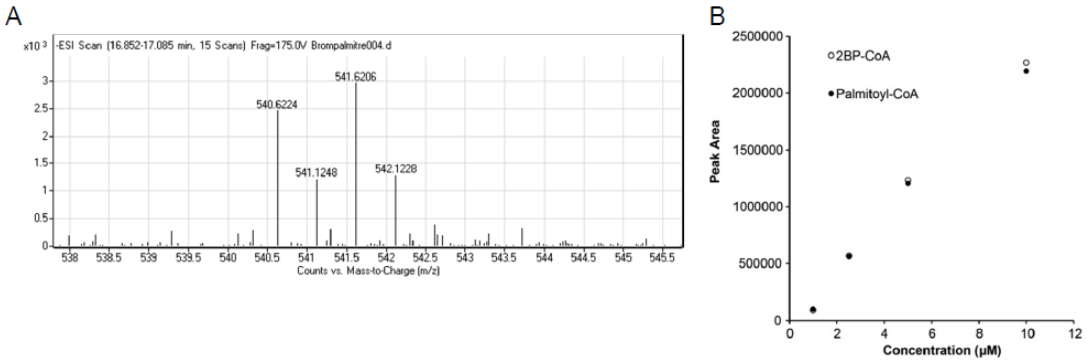

Figure 2-8 Equal ionization efficiency of palmitoyl-CoA and 2BP-CoA in negative mode electrospray ionization mass spectrometry. (A) Synthetic standards of palmitoyl-CoA and 2BP-CoA ([M - 2H] shown) were doped into cell extracts and analyzed by LC-MS. The observed isotopic distribution correlates with the bromine adduct. (B) Equivalent intensities were measured across a 4-point dilution series. This data demonstrates equivalent ionization efficiency and allows direct comparison of ion intensities in profiling experiments.

The DHHC PAT family contains a cysteine-rich domain with seven highly conserved cysteines, including the cysteine present in the Asp-His-His-Cys (DHHC) catalytic motif.[8] Mutation of the conserved DHHC cysteine to serine (DHHS) abolishes acyl-transferase activity, and prevents palmitoyl-CoA dependent formation of the enzyme-acyl intermediate.[10,11] Other residues may also be involved in catalysis, potentially by acyl-transfer between other active site catalytic cysteines. To explore the mechanism of DHHC catalysis, 2BPN3 was added to cells overexpressing epitope-tagged DHHC2 or DHHS2(C157S), and conjugated to rhodamine-alkyne for gel-based analysis. DHHC2 was efficiently labeled in transfected cells (Figure 2-9A), but labeling of the catalytic dead DHHS2 mutant was nearly abolished.

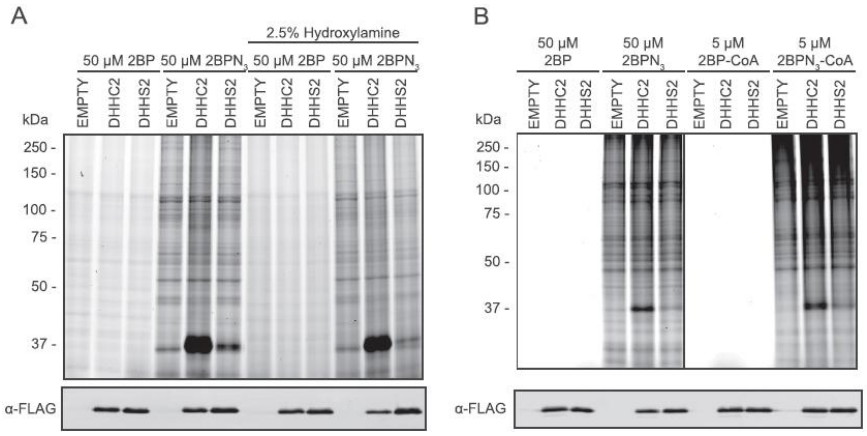

Figure 2-9 2BPN3 and 2BPN3-CoA are activity-based probes for DHHC2. (A) 2BPN3 labels FLAG epitope-tagged DHHC2 but not DHHS2 (C157S) by metabolic labeling in live cells. Labeling is resistant to hydroxylamine, demonstrating the absence of a stable acyl-intermediate. (B) 2BPN3 and 2BPN3−CoA both label DHHC2, but not DHHS2 (C157S) in vitro. Anti-FLAG Western blots show recombinant protein expression levels.

DHHC2 labeling was not affected by hydroxylamine addition, demonstrating the absence of the acyl intermediate and formation of the covalent alkylation product. Further detailed analysis of selected proximal cysteines (C146S,C149S, and C163S) showed reduced 2BPN3 labeling (Figure 2-10).

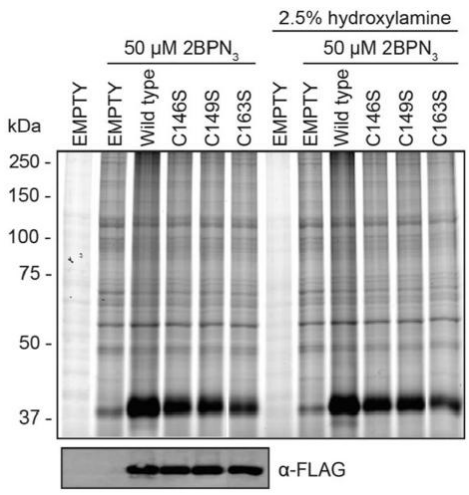

Figure 2-10 Mutational analysis of select cysteines in the DHHC2 active site. 293T cells were transfected with FLAG epitope-tagged DHHC2 mutants and labeled with 50 μM 2BPN3 for 1 hour. Control lanes were labeled with 50 μM 2BP. Mutants showed reduced labeling, especially C163S. Labeling was not sensitive to hydroxylamine treatment, demonstrating stable alkylation of the enzyme.

These results confirm that other cysteine residues are functionally important in the maturation and/or mechanism of DHHC PAT-catalyzed protein palmitoylation.[18] Importantly, these results reinforce existing evidence for more complex catalysis in the DHHC PAT active site,[18] potentially through multiple reactive thiolates. Finally, these experiments validate 2BPN3 as an activity-based probe for select DHHC PAT enzymes, which may be useful for competitive assays to profile active site occupancy. Indeed, transfection studies show robust 2BPN3 alkylation of six of nine tested epitope-tagged DHHC PATs (Figure 2-11).

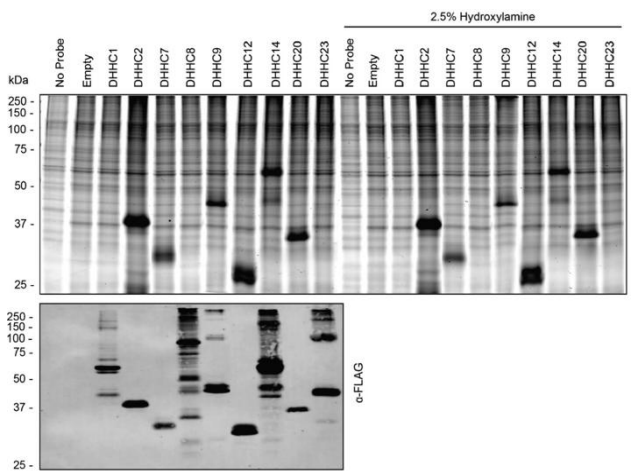

Figure 2-11 Over-expressed DHHC PAT enzymes metabolically labeled with 2BPN3. Nine epitope-tagged DHHC PAT cDNAs were transfected into 293T cells for 48 hours, and labeled with 2BPN3 for 1 hour. Over-expressed DHHC PAT enzymes are clearly visible in transfected lysates as dominant bands, and confirmed by anti-FLAG western blotting.

Metabolic conversion of 2BP to 2BP-CoA is thought to guide inhibition to CoA-dependent enzymes. To examine the role of CoA in DHHC PAT inhibition, membrane lysates were prepared from cells overexpressing DHHC2 and DHHS2 and labeled in vitro with 2BPN3 or 2BPN3−CoA (Figure 2-9B). Similar to metabolic labeling, in vitro labeling showed DHHC2 reactivity but not DHHS2. Importantly, both $2BPN_3$ and 2BPN3−CoA demonstrate activity-dependent labeling of DHHC2, although at different optimal probe concentrations. These results corroborate previous reports that DHHC2 is directly inhibited by 2BP,[12,19] and suggest CoA conjugation accelerates inhibition without altering the profile of labeled targets. Furthermore, these findings confirm the predominant reactivity of the catalytic DHHC cysteine over other proximal cysteine residues.

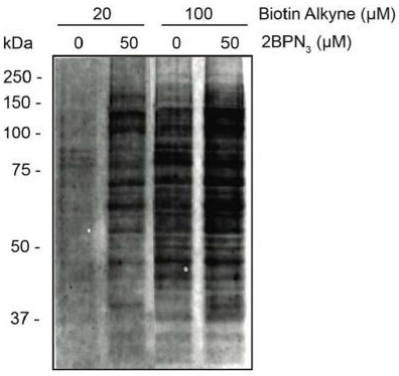

Figure 2-12 Enhanced background at higher concentrations of biotin-alkyne in 2BPN3-labeled lysates. Biotin-alkyne click chemistry was more selective at 20 μM than at 100 μM concentrations. 20 μM Biotin-alkyne was selected for further enrichment for mass spectrometry.

In order to annotate the targets of 2BPN3, cells were metabolically labeled with 2BP or 2BPN3 for 1 h. After lysis, membrane proteomes were conjugated to biotin-alkyne for streptavidin enrichment, trypsin digestion, and mass spectrometry analysis. Biotin−alkyne conjugation required careful optimization of labeling concentrations to reduce alkyne-dependent nonspecific reactions (Figure 2-12). Mass spectrometry results were filtered to include proteins with ≥2 average spectral counts, identified in 2 of 3 replicates, and ≥5-fold enrichment as compared to the 2BPcontrols. Approximately 450 protein targets of $2BPN_3$ were annotated (Appendix A),

including carriers, transporters, and channels. The most frequently identified targets in 293T cells of 2BPN3 were the voltage-dependent anion channel, SERCA Ca2+ ATPase, heme oxygenase 2, and CKAP4; all validated palmitoylated proteins (Table 2).[20] Importantly, five palmitoyl transferases were annotated, including DHHC5, DHHC6, DHHC7, DHHC17, and DHHC20. In addition, another nine PAT enzymes were identified that failed to pass the stringent thresholds, likely due to their low abundance (Table 3). This list does not include DHHC1, DHHC8, and DHHC23, which similarly failed to label with 2BPN3 when overexpressed in 293T cells (Figure 2-11). While this enzyme family is broadly inhibited by 2BP, it is by no means privileged or selective. Early reports demonstrated that 2BP inhibition of carnitine palmitoyl transferase activity blocked mitochondrial long-chain fatty acid oxidation in cells.[3,21] Our results confirm that CPT1 is indeed labeled with 2BPN3 in cells, suggesting broad disruption of cellular lipid metabolism. Other identified targets include lipid-modifying enzymes, detoxifying enzymes, regulators of redox stress. The surprising breadth of targets demonstrates the broad reactivity of this promiscuous inhibitor in cells.

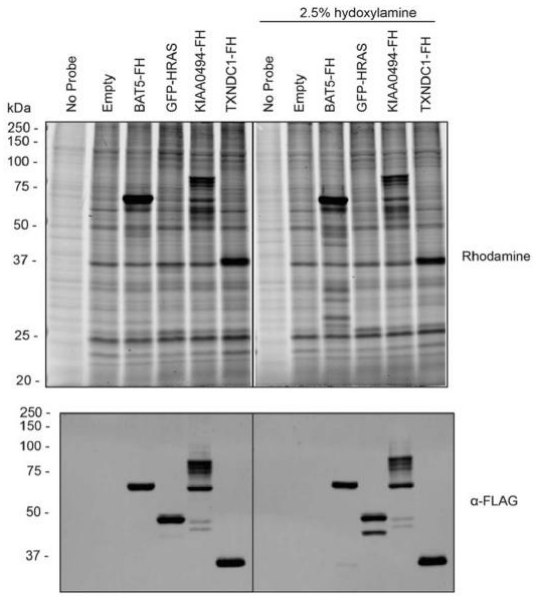

Figure 2-13 Select palmitoylated proteins are metabolically labeled with 2BPN3. Cells were transfected for 48 hours with epitope-tagged cDNAs for annotated palmitoylated proteins, and labeled for 1 hour with 2BPN3. Labeling was resistant to hydroxylamine treatment, showing it is not due to a thioester linkage.

Importantly, a significant fraction of the metabolically labeled targets are themselves palmitoylated proteins, such as MTDH,HRAS, GNAI2, and FAM108B.[15] Further investigation of validated palmitoylated proteins showed robust 2BPN3 labeling of the unannotated serine hydrolase ABHD16A (ABHGA), EF-hand calcium-binding domain-containing protein 14 (EFCAB14), FAM108A, KIAA0152, and thioredoxin-related transmembrane protein 1 (TXNDC1) (Figures 2-13 and 2-14).

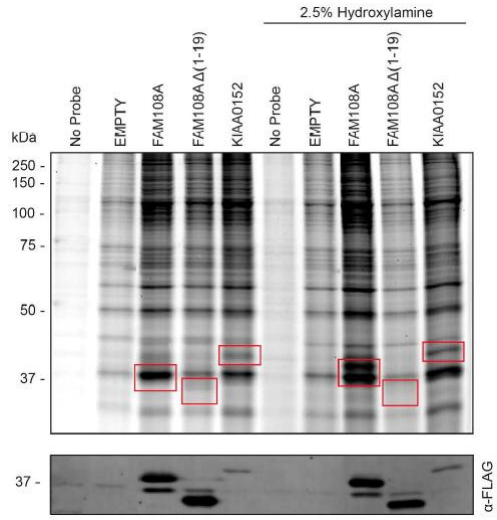

Figure 2-14 2BP competes with palmitoylation sites on FAM108A. FAM108A and FAM108(Δ1-19) were C-terminally tagged with the FLAG epitope and transfected in 293T cells. The palmitoylated protein KIAA0152 was also included. After 48 hours, cells were labeled with 50 μM 2BPN3 for 1 hour, conjugated to rhodamine-alkyne, and detected after separation by SDS-PAGE with or without incubation with 2.5% hydroxylamine. Red boxes denote recombinant protein bands.

FAM108A is palmitoylated at 5 N-terminal cysteines and is readily labeled by 2BPN3 in cells. Deletion of the N-terminal 19 residues blocked 2BPN3 labeling, despite the presence of seven additional cysteines present in the remaining 291 amino acids (Figure 2-14). In addition, 2BP labeling of ABHD16A did not reduce fluorophosphonate reactivity (Figure 2-15), suggesting 2BP alkylation occurs outside of the conserved *α/β*-hydrolase active site. Even though they label with 17-ODYA,[22] neither H-Ras nor H-Ras-(G12 V) labeled effectively with 2BPN3 when overexpressed (Figure 2-16). Based on these findings, we propose that 2BPN3 labeling of annotated palmitoylated proteins may instead highlight sites of nonenzymatic palmitoylation, such as activated thiol residues that preferentially react with palmitoyl-CoA by thioester exchange. Thus, these labeled proteins may represent a pool of DHHC-independent palmitoylated proteins. Indeed, Gα_{i1} is reported to undergo autoacylation at sites of palmitoylation by direct, nonenzymatic, thioester exchange with palmitoyl-CoA.[23] It is therefore not surprising to find the homologues GNAI2 and GNAI3 as targets of 2BP in cells.

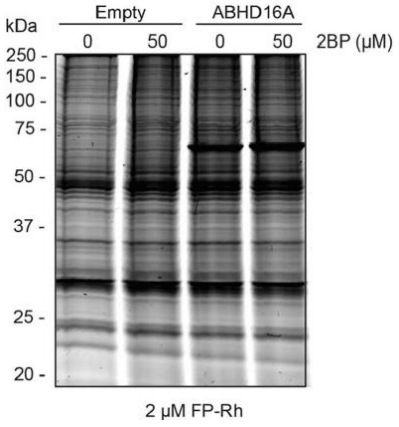

Figure 2-15 ABHD16A activity is unaffected by 2BP labeling. ABHD16A transfected 293T cells were labeled with 50 FM 2BP for 1 hour, and then lysates were labeled with the serine hydrolase activity-based probe fluorophosphonate-rhodamine for 1 hour. There is no observed inhibition of ABHD16A by 2BP, suggesting non-catalytic residues, such as sites of palmitoylation, are labeled by 2BP in cells.

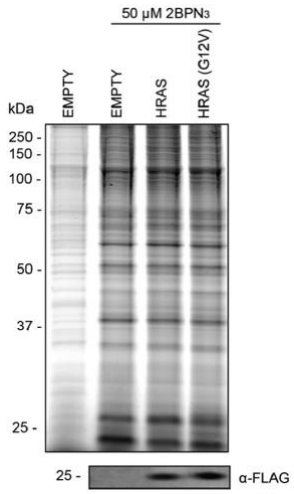

Figure 2-16 H-Ras is not effectively labeled with 2BPN3. 293T cells were transfected with FLAG-H-Ras, FLAG-H-Ras (G12V), or empty vector and labeled with 2BPN3 for 1 hour. Labeling is equivalent across all experiments. Longer incubation times do lead to enhanced H-Ras labeling (not shown).

Farnesylated Ras-family GTPases are carboxymethylated at their C-termini, which acts to reduce charge repulsion[24] and enhance membrane anchoring. 2BP alkylation products yield a negatively charged free carboxylate, which may itself attenuate membrane association. Accordingly, our data supports at least two modes of palmitoylation inhibition by 2BP: either by covalent inactivation of DHHC PATs, or by directly competing for palmitoylation at select cysteine residues. The functional consequences of each mechanism are presumably very different, since some proteins are left unpalmitoylated, while others are irreversibly alkylated. Importantly, 2BP may block incorporation of [^{3}H]- palmitate onto palmitoylated proteins, which superficially suggests a reduction in palmitoylation, but in reality may

protein	description	$2BPN_3$	2BP
VDAC2	voltage-dependent anion channel 2	255 ± 51	11 ± 3
ATP2A2	SERCA Ca(2+)-ATPase	167 ± 14	3 ± 2
HMOX2	heme oxygenase 2	134 ± 29	0 ± 0
CKAP4	cytoskeleton-associated protein 4	128 ± 32	2 ± 0
SLC25A5	ADP/ATP translocase 2	89 ± 6	17 ± 5
MGST3	microsomal glutathione S-transferase 3	77 ± 10	2 ± 0
COMT	catechol O-methyltransferase	69 ± 27	1 ± 1
VDAC3	voltage-dependent anion-selective channel protein 3	69 ± 9	6 ± 0
CYB5B	cytochrome b5	63 ± 25	1 ± 1
RPL38	60S ribosomal protein L38	56 ± 11	2 ± 0
MTCH2	mitochondrial carrier homologue 2	54 ± 17	1 ± 1
ACAA1	3-ketoacyl-CoA thiolase	46 ± 13	3 ± 1
SLC25A5	adenine nucleotide translocator 2	45 ± 10	0 ± 0
AGPAT6	1-acyl-sn-glycerol-3-phosphate acyltransferase ζ	42 ± 10	0 ± 0
RTN4	reticulon-4	42 ± 9	3 ± 2
HSDL1	hydroxysteroid dehydrogenase-like protein 1	40 ± 6	1 ± 1
FAM62B	FAM62B	37 ± 4	1 ± 1
RTN3	reticulon-3	37 ± 10	1 ± 1
AYTL2	1-acylglycerophosphocholine O-acyltransferase 1	35 ± 10	1 ± 0
SCP2	sterol carrier protein 2	35 ± 9	1 ± 0
TOMM40	mitochondrial import receptor subunit TOM40	34 ± 2	2 ± 1
REEP5	receptor expression-enhancing protein 5	31 ± 2	0 ± 0
A8K3B9	uncharacterized reticulon-like protein	29 ± 16	1 ± 1
GNPAT	dihydroxyacetone phosphate acyltransferase	29 ± 10	1 ± 1
SLC25A4	ADP/ATP translocase 1	29 ± 3	0 ± 0
PRAF2	PRA1 family protein 2	28 ± 9	0 ± 0
MTDH	protein LYRIC	27 ± 9	2 ± 0
PTPLAD1	protein-tyrosine phosphatase-like A domain-containing protein 1	26 ± 5	1 ± 1
SCAMP3	SCAMP3	25 ± 7	1 ± 1
TFRC	transferrin receptor protein 1	25 ± 7	1 ± 0

Table 2 Most abundant 2BPN3-labeled proteins identified by mass spectrometry. 293T cells were labeled with 2BPN3 and reacted with biotin-alkyne for enrichment, trypsin digestion, and mass spectrometry analysis. Proteins analyzed by spectral counting, a label-free quantification method for measuring relative abundance based on the number of fragmentation scans assigned to peptides from a specific protein. Standard errors are shown.

report 2BP-alkylation at the site of palmitoylation. Future experiments will examine the competition between 2BP and palmitoylation to shed light on the predicted role of nonenzymatic palmitoylation.

Protein	$2BPN_3$-1	$2BPN_3$-2	$2BPN_3$-3	2BP-1	2BP-2
ZDHHC3	0	4	1	0	0
ZDHHC4	0	2	0	0	0
ZDHHC5	7	9	6	1	0
ZDHHC6	3	13	10	0	0
ZDHHC7	6	3	2	0	0
ZDHHC9	1	1	2	0	0
ZDHHC12	1	2	0	0	0
ZDHHC13	0	3	0	0	0
ZDHHC14	0	1	0	0	0
ZDHHC17	0	6	1	0	0
ZDHHC18	1	2	2	0	0
ZDHHC20	7	5	5	0	0
ZDHHC21	1	0	0	0	0
ZDHHC24	1	3	0	0	0

Table 3 DHHC PAT enzymes identified by mass spectrometry profiling. Only DHHC5, 6, 7, 17 and 20 passed the filter thresholds, as described in the main text.

2.5 Discussion

In this study, the mechanism and targets of the popular palmitoylation inhibitor, 2-bromopalmitate (2BP), were characterized utilizing an analogue functionalized with a latent fluorescent reporter or an affinity handle. With this probe we profiled active PAT enzymes by mass spectrometry and analyzed the activities of wild type, mutant enzymes and palmitoylated proteins with 2BP. A major goal of this chapter was to employ 2BP as a mechanistic probe to provide insight into how PAT enzymes may catalyze acyl transfer between Coenzyme A and protein substrates. Given that other DHHC2 active-site cysteines contributed to $2BPN_3$ Labeling (i.e. C163), it is likely that catalytic transfer is mediated by more than one cysteine. In connection to this point, a recent study demonstrated that the yeast PAT Erf2 employs its cofactor Erf4 in maintaining the stability of its catalytic acyl-enzyme intermediate. Interestingly, in the absence of Erf4, the PAT could still autoacylate, however, its *trans*acylation activity was abrogated and instead it exhibited acylCoA thioesterase (ACOT) behavior.[31] These results confirm that PATs use other residues besides the cysteine of the DHHC motif to maintain proper catalytic acyl transfer.

Although it was not directly addressed, we could have demonstrated 2-BP's broad amino acid reactivity by showing that in addition to cysteines, it was likely to react with lysine and histidine side-chains under the favorable circumstances. In principle, to demonstrate 2BP's chemical selectivity towards cysteine-thiols, one would need to prove that prior treatment of a lysate with a thiol-directed alkylating agent such as *N*-ethylmaleimide (NEM) or 2-Iodoacetamide (2IA), would abolish 2BPN3 labeling in a dose-dependent manner. However, we did not observe this type of competition in our studies (data not shown), suggesting that 2BP chemical reactivity parallels that of other α-halo carbonyls, and is expected to target other functional protein residues beyond reactive cysteines. Additionally, the lipophilic character of 2BP may direct its reactivity towards even smaller subsets of nucleophile-containing proteins while preventing its access to others. This is certainly true in the case of intrinsic membrane proteins in which the brominated acyl chains may partition into the lipid bilayer, thereby increasing their local effective concentrations and therefore reactivity with membrane-resident enzymes.

Overall, we present click-enabled activity-based probes for profiling the targets of 2BP inhibition. The probes preferentially label the active site of DHHC PATs, but similarly label hundreds of other proteins, including transporters, channels, enzymes, and chaperones. Nonetheless, 2BPN3 labeling reports the active state of DHHC PATs, and thus may be useful in inhibitor discovery or selectivity profiling in DHHC overexpressing cells. Importantly, 2BP has been used in nearly every paper in the last 15 years studying protein palmitoylation. In light of this study, and a recent report describing ω-alkynyl 2BP analogues,[19] 2BP is clearly a nonselective probe with many targets beyond palmitoyl transferases. This finding has broad implications in the palmitoylation field, given the widespread use of 2BP in hundreds of published reports. Clearly, greater caution should be used when interpreting the phenotypic consequences of 2BP-inhibition in cell-based experiments.

2.6 Bibliography

1. Coleman, R. A., Rao, P., Fogelsong, R. J., and Bardes, E. S. G. (**1992**) 2-Bromopalmitoyl-CoA and 2-bromopalmitate: Promiscuous inhibitors of membrane-bound enzymes *Biochim. Biophys. Acta* 1125, 203– 209

2. Burges, R. A., Butt, W. D., and Baggaley, A. (**1968**) Some effects of α-bromopalmitate, an inhibitor of fatty acid oxidation, on carbohydrate metabolism in the rat *Biochem. J.* 109,38P– 39P

3. Chase, J. F. and Tubbs, P. K. (**1972**) Specific inhibition of mitochondrial fatty acid oxidation by 2-bromopalmitate and its coenzyme A and carnitine esters *Biochem. J.* 129,55– 65

4. Webb, Y., Hermida-Matsumoto, L., and Resh, M. D. (**2000**) Inhibition of protein palmitoylation, raft localization, and T cell signaling by 2-bromopalmitate and polyunsaturated fatty acids *J. Biol. Chem.* 275, 261– 270

5. Jones, Matthew L., Collins, Mark O., Goulding, D., Choudhary, Jyoti S., and Rayner, Julian C. (**2012**) Analysis of protein palmitoylation reveals a pervasive role in plasmodium development and pathogenesis *Cell Host Microbe* 12, 246– 258

6. Leong, W. F., Zhou, T., Lim, G. L., and Li, B. (**2009**) Protein palmitoylation regulates osteoblast differentiation through BMP-induced osterix expression *PLoS One* 4,e4135

7. Tom, C. T. and Martin, B. R. (**2013**) Fat chance! Getting a grip on a slippery modification *ACS Chem. Biol.* 8, 46– 57

8. Fukata, M., Fukata, Y., Adesnik, H., Nicoll, R. A., and Bredt, D. S. (**2004**) Identification of PSD-95 palmitoylating enzymes *Neuron* 44, 987– 996

9. Li, Y., Martin, B. R., Cravatt, B. F., and Hofmann, S. L. (**2012**) DHHC5 protein palmitoylates flotillin-2 and is rapidly degraded on induction of neuronal differentiation in cultured cells *J. Biol. Chem.* 287, 523– 530

10. Roth, A. F., Feng, Y., Chen, L., and Davis, N. G. (**2002**) The yeast DHHC cysteine-rich domain protein Akr1p is a palmitoyl transferase *J. Cell Biol.* 159, 23– 28

11. Lobo, S., Greentree, W. K., Linder, M. E., and Deschenes, R. J. (**2002**) Identification of a Ras palmitoyltransferase in Saccharomyces cerevisiae *J. Biol. Chem.* 277, 41268–41273

12. Jennings, B. C., Nadolski, M. J., Ling, Y., Baker, M. B., Harrison, M. L., Deschenes, R. J., and Linder, M. E. (**2009**) 2-Bromopalmitate and 2-(2-hydroxy-5-nitro-benzylidene)-benzo[b]thiophen-3-one inhibit DHHC-mediated palmitoylation in vitro *J. Lipid Res.* 50,233– 242

13. Mikic, I., Planey, S., Zhang, J., Ceballos, C., Seron, T., von Massenbach, B., Watson, R.,Callaway, S., McDonough, P. M., Price, J. H., Hunter, E., and Zacharias, D. (**2006**) A live cell, image-based approach to understanding the enzymology and pharmacology of 2-bromopalmitate and palmitoylation. In *Methods in Enzymology* (James, I., Ed.), pp 150–187, Academic Press, Waltham, MA.

14. Hang, H. C., Geutjes, E. J., Grotenbreg, G., Pollington, A. M., Bijlmakers, M. J., and Ploegh, H. L. (**2007**) Chemical probes for the rapid detection of fatty-acylated proteins in mammalian cells *J. Am. Chem. Soc.* 129, 2744– 2745

15. Martin, B. R. and Cravatt, B. F. (**2009**) Large-scale profiling of protein palmitoylation in mammalian cells *Nat Methods* 6, 135– 138

16. Debets, M. F., van Berkel, S. S., Schoffelen, S., Rutjes, F. P., van Hest, J. C., and van Delft, F. L. (**2010**) Aza-dibenzocyclooctynes for fast and efficient enzyme PEGylation via copper-free (3 + 2) cycloaddition *Chem. Commun. (Camb.)* 46, 97– 99

17. van der Linden, W. A., Li, N., Hoogendoorn, S., Ruben, M., Verdoes, M., Guo, J., Boons,G. J., van der Marel, G. A., Florea, B. I., and Overkleeft, H. S. (**2012**) Two-step bioorthogonal activity-based proteasome profiling using copper-free click reagents: A comparative study *Bioorg. Med. Chem.* 20, 662– 666

18. Mitchell, D. A., Hamel, L. D., Ishizuka, K., Mitchell, G., Schaefer, L. M., and Deschenes, R. J. (**2012**) The Erf4 subunit of the yeast Ras palmitoyl acyltransferase is required for stability of the Acyl-Erf2 intermediate and palmitoyl transfer to a Ras2 substrate *J. Biol. Chem.* 287, 34337– 34348

19. Zheng, B., DeRan, M., Li, X., Liao, X., Fukata, M., and Wu, X. (**2013**) 2-Bromopalmitate analogues as activity-based probes to explore palmitoyl acyltransferases *J. Am. Chem. Soc.* 135, 7082– 7085

20. Kang, R., Wan, J., Arstikaitis, P., Takahashi, H., Huang, K., Bailey, A. O., Thompson, J. X., Roth, A. F., Drisdel, R. C., Mastro, R., Green, W. N., Yates Iii, J. R., Davis, N. G., and El-Husseini, A. (**2008**) Neural palmitoyl-proteomics reveals dynamic synaptic palmitoylation *Nature* 456, 904– 909

21. Buechler, K. F. and Lowenstein, J. M. (**1990**) The involvement of carnitine intermediates in peroxisomal fatty acid oxidation: A study with 2-bromofatty acids *Arch. Biochem. Biophys.*281, 233– 238

22. Martin, B. R., Wang, C., Adibekian, A., Tully, S. E., and Cravatt, B. F. (**2012**) Global profiling of dynamic protein palmitoylation *Nat Methods* 9, 84– 89

23. Duncan, J. A. and Gilman, A. G. (**1996**) Autoacylation of G protein α-subunits *J. Biol. Chem.* 271, 23594– 23600

24. Philips, M. R., Pillinger, M. H., Staud, R., Volker, C., Rosenfeld, M. G., Weissmann, G., and Stock, J. B. (**1993**) Carboxyl methylation of Ras-related proteins during signal transduction in neutrophils *Science* 259, 977– 980

25. Lapidot, Y., Rappoport, S., and Wolman, Y. (1967) Use of esters of N-hydroxysuccinimide in the synthesis of N-acylamino acids, *J Lipid Res 8*, 142-145.

26. Al-Arif, A., and Blecher, M. (1969) Synthesis of fatty acyl CoA and other thiol esters using N-hydroxysuccinimide esters of fatty acids, *J Lipid Res 10*, 344-345.

27. Pullman, M. E. (1973) A convenient and versatile method for the purification of CoA thiol esters, *Anal Biochem 54*, 188-198.

28. Seubert, W. (1960) S-Palmitoyl CoA, *Biochem Prep 7*, 80-83.

29. Lorenz, M. A., El Azzouny, M. A., Kennedy, R. T., and Burant, C. F. (2013) Metabolome Response to Glucose in the beta-Cell Line INS-1 832/13, *J Biol Chem 288*, 10923-10935.

30. Martin, B. R., and Cravatt, B. F. (2009) Large-scale profiling of protein palmitoylation in mammalian cells, *Nat Methods 6*, 135-138.

31. Mitchell, D., Hamel, L., Ishizuka, K. et. al. (2012) The Erf4 subunit of the yeast Ras palmitoyl acyltransferase is required for stability of the acyl-Erf2 intermediate and palmitoyl transfer to a Ras2 substrate, *J Biol Chem 287*, 34337-34248.

Chapter 3:
Structural and Biochemical Studies of LYPLA1/2 Active Site Selectivity toward Small Molecule Inhibitors ML348 and ML349

3.1 Abstract

Human LYPLA1 and 2, more commonly referred to as APT1 and 2, are poorly defined members of the *α/β* family of metabolic serine hydrolases. Although LYPLAs have shown to process multiple substrates across unrelated classes of biomolecules, these enzymes are thought to function primarily as *S*-acyl-protein thioesterases in the context of regulating the palmitoylation and membrane association of key signaling and scaffolding proteins implicated in cancer and neurological disorders. Recently, a competitive ABPP screen identified two potent, *in vivo* active piperazinyl amide compounds, named ML348 and ML349, that selectively and reversibly inhibit LYPLA1 and 2 hydrolase activity, respectively. Since direct structural information was unavailable, it was unclear how the inhibitors achieve target selectivity given the enzymes' high level of sequence homology. Here, we solve the co-crystal structures of human LYPLA1 and 2 bound to their selective inhibitors and use this information to define structural determinants that give rise to the observed selectivity. To confirm the significance of key residues, enzyme kinetic analyses were performed on point mutants in which the considered residue was exchanged for the analogous residue present in the homolog. Orthogonal inhibition measurements confirmed the requirement of I75 in LYPLA1 and Q83 and H152 in LYPLA2 for binding and discriminating the two ligands. We propose that these residues may contribute to active site conformational dynamics which could confer substrate specificity by gating access to physiological substrates. Taken together, these findings offer molecular insights into LYPLA divergent ligand recognition and suggest that it may have evolved from differences in their active-site loop dynamics.

Individual contributions. Although I invested a large portion of my time in the this chapter's project, a number of individuals from the Martin lab have contributed significantly to the work and conclusions presented herein. Namely, Dr. Kristin J. Labby is credited with initiating this study by performing crystallization trials, characterizing the activities of a number of ML349 derivatives and helping to generate both diffractable crystals and LYPLA site-directed mutants. Dr. Jeannie L. Hernandez was instrumental in interpreting the crystal structures and highlighting their structural disparities. Dr. Jaimeen Majmudar synthesized and oversaw the synthesis of ML348, ML349 and its derivatives, most of which were generated by Andrea Chong. Sin Ye Hwang carried out K_i value measurements for all compounds and enzymes studied. Michael Sang Jun Won was involved in measuring k_{off} values and in key discussions leading to a number of hypotheses. Christina and Laura Rodriguez helped to purify all the enzymes that were assayed. Rachel Pricer and I made all the PyMol structures of the cocrystal structures. Kira Armacost performed theoretical studies and simulations of compounds binding to LYPLAs. My principle investigator Dr. Brent R. Martin, conceived the project, provided funding for all the efforts described in this chapter, and oversaw the experimental design. My own part in this work was to develop and direct the kinetic measurements, help to design all experiments, offer insight into the binding modes of the inhibitors, provide a hypothesis-driven strategy for the project and write this chapter. The crystal structures were solved in collaboration with Dr. Jeanne Stuckey from University of Michigan's Center for Structural Biology. The use of the Advanced Photon Source was supported by the U. S. Department of Energy, Office of Science, Office of Basic Energy Sciences, under Contract No. DE-AC02-06CH11357. Use of the LS-CAT Sector 21 was supported by the Michigan Economic Development Corporation and the Michigan Technology Tri-Corridor for the support of this research program (Grant 085P1000817). Lastly, Dr. David Smith of LS-CAT helped with remote data collection. Coordinates for the APT1-CP83 and APT2-CP115 structures have not been deposited in the PDB yet.

3.2 Introduction

The human serine hydrolases (SHs) form one of the largest enzyme families consisting of more than 240 members and therefore constitute ~1% of the proteome.[1] SHs include both serine proteases as well as metabolic hydrolases, the latter of which act primarily on metabolites and short peptides.[2] The majority of metabolic SHs adopt an *α/ß* hydrolase (abhydrolase) fold[3] featuring the classic Ser-His-Asp catalytic triad and are further organized into subfamilies comprised of esterases, lipases, peptidases and amidases[2]. Many metabolic hydrolases have been thoroughly studied over the years and details regarding their *in vivo* substrates and biochemical functions are well defined (e.g. FAAH[4] and acetylcholinesterase[5]). However, nearly half of the members, especially hydrolases that act on larger classes of macromolecules, are still completely uncharacterized.[6]

Lysophospholipases 1 and 2, here throughout referred to as LYPLA1 and 2, are ~25 kDa proteins that are paralogs belonging to a subclass of serine esterases within the abhydrolase superfamily.[7] LYPLA proteins are conserved across eukaryotic species, with orthologues present from humans to unicellular microorganisms such as *S. cerevisiae*, although only vertebrates possess two distinct isoforms.[8] In spite of the high sequence homolgy observed between LYPLA isoforms (~68% similarity in humans, Figure 3-1), it is probable that LYPLA1 and 2 have diverged sufficiently in higher organisms to perform non-redundant roles.

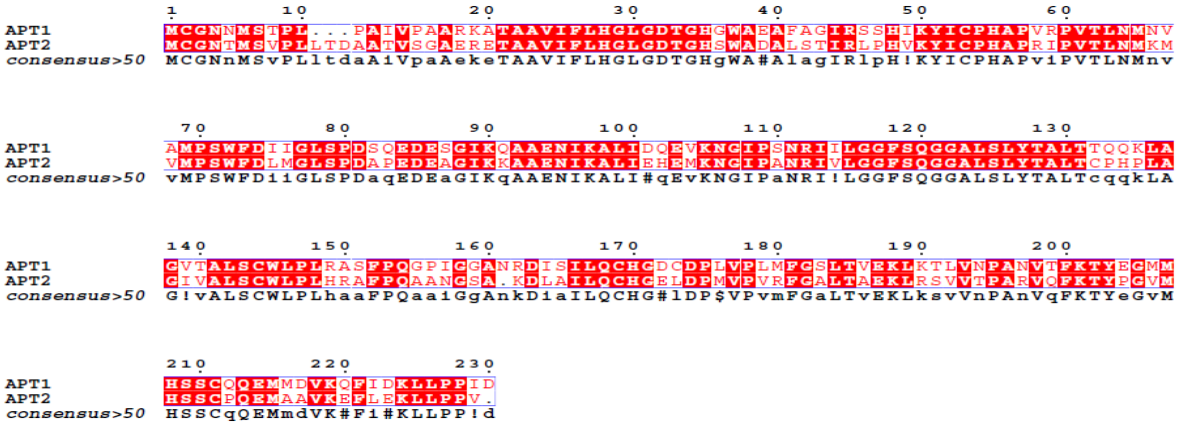

Figure 3-1 Multiple sequence alignment highlights divergent residues between LYPLA1 and 2.

Regardless, the conserved orthology of LYPLAs implies these enzymes perform biological duties that are indispensible for the proper functioning of eukaryotic

organisms[6], even though yeast knockout studies have not demonstrated an obvious physiological impairment[9]. Interestingly, phylogenetic analysis shows that LYPLAs are somewhat related to a clan of nonspecific carboxylesterases[7] and a group of lysophospholipase-like proteins, which have preferred hydrolytic activities towards short-chain acyl-linked substrates[10], contrasting with the reported biochemical activities of LYPLAs.

From a historical standpoint , it has been difficult to confidently assign LYPLA1 and 2 specific cellular roles due partly to the diverse range and nature of their substrate biomolecules (Figure 3-2). These enzymes were initially described as lysophospholipid esterases, hence their name, capable of hydrolyzing a variety of lysophosphatidyl choline, ethanolamine, serine and inositol molecules (LPC, LPE, LPS and LPI respectively) with moderate specificity constants (k_{cat}/K_m ~ 2.5 x 10^3 M^{-1} s^{-1} calculated from[11–13]). In addition, LYPLAs were also shown to cleave acetyl esters from platelet activating factor (PAF) like molecules but did not accept traditional diacylglycerophospholipids as substrates.[12–14] Given these amphiphilic substrates are likely to partition into nonpolar phases such as micelles[15,16], it was surprising to discover that LYPLAs lack the characteristic 'interfacial activation' kinetics observed for most lipases[17–19], though a few other lipase members (e.g. cutinases) lack this activity as well[20,21]. Nevertheless, LYPLA1 and 2 activities shows dependence on the micellar surface density of their substrates[13,14] which is consistent with all lipases that act on poorly soluble, aggregated hydrophobic substrates.

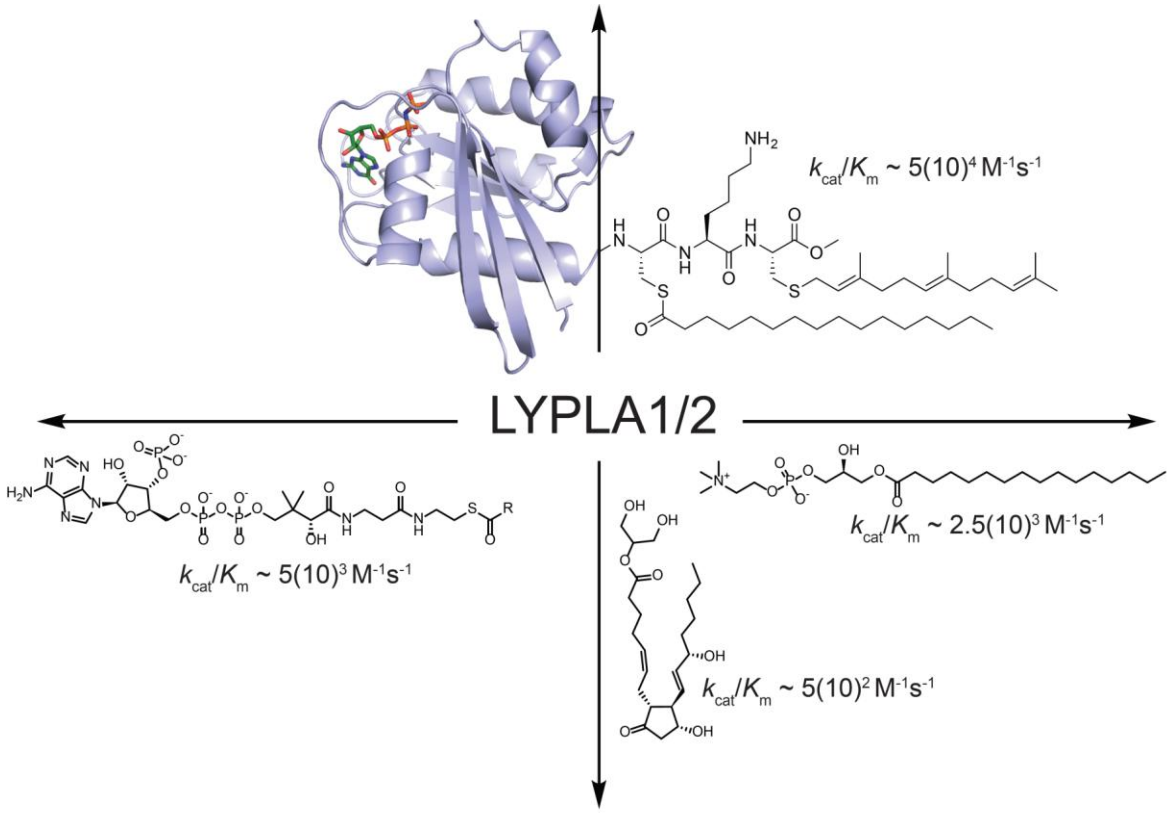

Figure 3-2 LYPLA1 and LYPLA2 breadth of physiological substrates embodies their widespread tolerance for hydrophobic acyl substrate. Initially described as lysophospholipid-specific esterases, LYPLAs exclude diacylglycerophospholipids as substrates. Later these enzymes were identified as protein and metabolic acyl thioesterases catalyzing acyl chain removal from both acyl CoAs, Ras and G*α* subunits. More recently, they have been reported to hydrolyze inflammatory prostaglandin esters with similar K_m values to S-acylated protein substrates. All specificity constants were calculated based on published average published k_{cat} and K_m values that are referenced in the main text.

Later on, LYPLAs were rediscovered as principle *S*-acyl-protein thioesterases (APTs) that cleave thioester linked fatty acids from a variety of signaling proteins, including G*α* subunits[22], Ras family members[23] and eNOS.[24] At that point, it was recognized that LYPLAs demonstrated higher kinetic efficiencies with palmitoylated proteins (k_{cat}/K_m ~ 5 x 10^4 M^{-1} s^{-1} for N-Ras[23]), and hence, LYPLA1 and 2 were given the names APT1 and 2, respectively, to reflect their dominant role as protein thioesterases in cells. Still, in the general sense, thioester hydrolysis is considered to be intrinsically more efficient but less specific than oxo-ester hydrolysis due to the labile nature of the scissile bond, and this may explain why greater k_{cat} values are observed with thioester substrates.[25] Affirming this point, LYPLA1 and 2 have since re-emerged as enzymes that process biomolecules unrelated to *S*-acylated proteins; LYPLA1 was reported to hydrolyze ester-linked octanoyl chains from both the short peptide hormone

ghrelin[11,26] and neuraminidase prodrug laninamivir octanoate[27], whereas LYPLA2 was shown to posses monoacylglycerol (MAG) esterase activity toward a variety of prostaglandin glycerol (PGE) and acylglycerol (AG) substrates in a regio- and stereospecific manner[28]. Overall, LYPLA1 and 2 catalyze a plethora of physiologically distinct reactions, however, their substrates share a common motif: possessing a hydrophobic acyl handle that is thought to aid in active site recognition (Figure 3-2). Indeed, knowledge of the three-dimensional architecture of these enzymes complexed to physiological substrates or analogs may inform on the scope of suitable substrates and, in turn, provide insight into their true functional roles.

While a few abhydrolase structures related to LYPLAs are known, to date, only human LYPLA1 crystal structure has been solved[29]. LYPLA1 exhibits a near-canonical abhydrolase fold closely resembling that of its distant homolog lysophospholipase-like 1(LYPLAL1)[7] and the poorly characterized carboxylesterase from *P. fluorescence.* (CPf)[30]. Together with LYPLA1, these are the only members of the lysophospholipase/related-carboxylesterase subfamily (here collectively referred to as the LC family) for which three-dimensional structures are available. These particular proteins feature the core unit of the abhydrolase fold, namely the ß-pleated sheet structure flanked by α-helices and variable loops (Figure 3-3).[12]

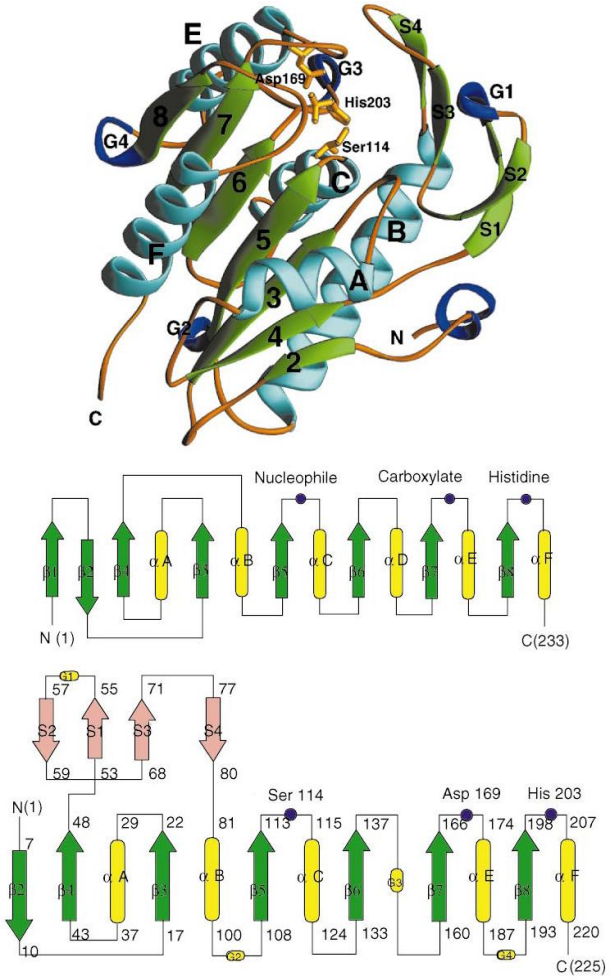

Figure 3-3 Previously solved human LYPLA1 secondary and tertiary structures show significant deviation from classic abhydrolase fold. (a) Ribbon diagram highlighting the geometry of secondary structural element which are designated according to the structure of the canonical abhydrolase. Seven ß-strands are numbered sequentially from 2 to 8. Four short ß irregular strands are denoted S1–S4. Five α helices are labeled from A to. Four short helical

segments are labeled from G1 to G4. The displayed numbering of the shown catalytic S114, D169, and H210 are actually 5 units less than that of the full-length sequence of LYPLA1. (b) Topology diagram of a canonical abhydrolase. (c) Topology of human LYPLA1. See text for further details. This Figure has been taken directly from the original publication of LYPLA1's crystal structure[29] solely for illustrative purposes.

Unlike typical abhydrolases however, these enzymes are considerably smaller, lack the first beta strand of the core sheet and exhibit non-traditional insertions composed of long winding loops and irregular ß-sheets[7,29,30]. Interestingly, in spite of LYPLA1's documented lipolytic activity, it lacks the structural topology of common lipases, most notably, the well defined lid-structure that is triggered to open and mobilize active site residues when docking to the lipid-water interface[31,32]. Instead, LYPLA1, along with other LC family members, are thought to use their atypical loops and sheets as a 'flexible' hydrophobic channel for the purpose of substrate acquisition, thereby conferring the enzyme substrate specificity. This proposition is substantiated by the fact that among structurally-characterized LC family members, the length of the channel's cavity correlates with the observed substrate specificities of the enzyme; for instance, LYPLAL1 features an obstructed hydrophobic channel and demonstrates a strong preference towards short acyl chain substrates[7], whereas LYPLA1 favors longer acyl lengths[29] correlating with its more accommodating hydrophobic tunnel.

The quaternary structure of LC family members may represent another point of departure from prototypical abhydrolases, which are almost always monomeric in nature. While CPf has been shown biochemically and structurally to exist as a strict homodimer in solution[10,33], crystal packing analysis suggests that LYPLAL1 is likely monomeric[7]. LYPLA1 is anticipated to form weak dimers which may hinder active site entry, and therefore, has been suggested to further augment and restrict the enzyme's substrate scope.[29] However, this mode of dimerization has not been fully characterized in solution and is unclear whether it is also featured in the homologous LYPLA2 enzyme. Indeed, a molecular structure for LYPLA2 is needed for a complete description of differences between LYPLAs, which may answer the question of why a pair of isoforms have evolved in higher eukaryotic species?

A recent study applied an activity-based probe strategy to screen for specific inhibitors of LYPLA1 and 2 in hopes of discovering isoform selective molecules that could be used to assay the exact cellular contributions of each LYPLA.[34] In this

approach, the broadly-reactive SH suicide inhibitor, diethyl fluorophosphonate, was conjugated to a rhodamine fluorophore and used in a competition experiment to assay active site occupancy of small molecules[35], yielding hit compounds that displayed either covalent or competitive inhibition behavior. Indeed, this methodology is geared towards discovery of compounds with prolonged drug-target residency times, an important facet that has shown to confer enhanced efficacy and selectivity *in vivo.*[36–38] The high throughput screen of the NIH molecular libraries yielded a number of compounds that exhibited modest to strong active site occupancy (Figure 3-4A). Noteworthy among these hits were two potent reversible inhibitors, termed ML348 and ML349, that selectively inhibited either LYPLA1 or 2, respectively (Figure 3-4B)[14]. An orthogonal enzyme activity assay confirmed that each of the leads exhibited modest K_i values between 200-300nM, and had approximately 50 to 200-fold selectivity towards their corresponding target(Figure 3-4D and E). Above all, these reversible compounds are the first inhibitors to display isoform specificity between LYPLAs, making it possible to assay their biological contributions in a physiologically relevant manner.

Molecular structures of these lead inhibitors are noticeably different though both inhibitors incorporate an unsaturated 5-membered heterocycle (furan in ML348 and thiophene in ML349) substituted at carbon 2 by an amide-linked piperazine ring (Figure 3-4B). This unexpected finding proved that in spite of the sequence and probable structural similarities of human LYPLAs, their active sites have diverged enough to give rise to the observed ligand selectivity. To better understand the structure activity relationship (SAR) of the molecules, the authors compiled a small library of derivatives, and described some of the pharmacophoric moieties present within each lead.[39] It was found that for ML348, altering either the substitution or regiochemistry about the 2,5-disubstituted anilide (Cl-CF_3Anil) functionality diminished both its potency towards LYPLA1 and its target selectivity against LYPLA2.

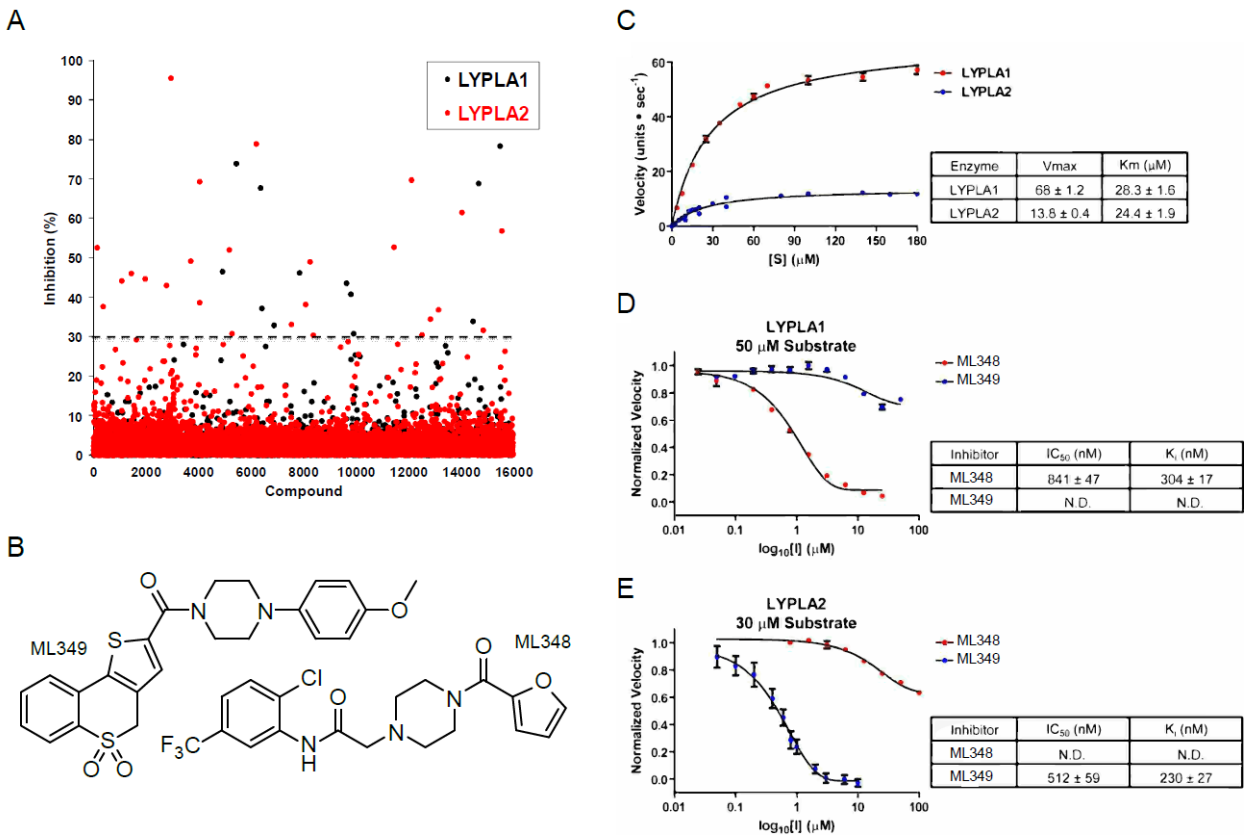

Figure 3-4 Active site residency-time screen yields paralog selective, reversible LYPLA1/2 inhibitors. (A) Fluopol-ABPP screening results for representative 16,000 compounds of the NIH small-molecule library B. Chemical structures of top hits from the ABPP screen that selectively inhibit LYPLA1 and 2 with negligible cross-reactivity. ML348 and ML349 inhibitory activities were examined further by employing a fluorogenic resorufin acetate substrate hydrolysis assay (as discussed in the main text) with 10 nM purified human LYPLA1 and 2. C. Micaelis-Menten kinetic analysis of LYPLA1 and 2 with reported K_m and V_{max} values. D and E show ML348 and ML349 dose-dependent inhibition of hydrolase activities of LYPLA1 (D) and LYPLA2 (E). K_i values for ML348 and ML349 were calculated using the Cheng-Prusoff relation for competitive inhibitors. All values represent means ± SEM for four independent experiments. These images have been borrowed from the original publication of the HTS screen that found ML348 and ML349 (ref). Again, this figure is for illustrative purposes only.

As for ML349, the relative *para*-configuration about the methoxyphenyl (*p*MeOPh) group was shown to be absolutely critical for inhibitory activity. Interestingly, substituting the sulfone of the thiochromene dioxide portion of the molecule for a bulky hydrophobic moiety yielded inhibitors with activities that mirrored the parent ML349 compound. Overall, the SAR study addressed some of the structural requirements that were necessary for inhibitor potency, however, knowledge of the exact ligand-specificity determinants in LYPLAs were still lacking.

Here we crystallized LYPLA1 and 2 in the presence of their selective compounds and provide a structural basis for inhibitor selection between LYPLA1 and 2. Employing

both steady-state and transient kinetic experiments we show that Ile75 residue in LYPLA1 and Pro86 and His152 residues in LYPLA2 are part of an essential gate-keeping mechanism which selects for appropriate inhibitor scaffolds and may have implications for enzymatic specificities towards physiological substrates. Furthermore, we use the activities from a series of ML349 derivatives towards LYPLA1 and 2 to inform on the specific location of groups that may give rise to potency and selectivity of the ML349 molecule. Taken together, we propose that differences in the hydrophobic character and conformational dynamics about LYPLA active sites are primarily responsible for this ligand specificity.

3.3 Materials and Methods

Chemical and biological reagents. HindIII and BamHI restriction enzymes, T4 DNA ligase, Superscript III reverse transcriptase, TRIzol reagent, pTrcHis2A vector, *E. coli.* BL21(DE3)pLysS and Top10 cells, dehydrated LB-Miller broth were all purchased from Thermo Fisher. *Pfu Turbo* polymerase was purchased from Stratagene. The sequencing, amplification and mutagenic primers were purchased from Eurofins Genomics. The immobilized cobalt affinity resin was purchased from Clontech. Dimethyl sulfoxide (DMSO), Resorufin *O*-acetate, Pluronic F-127, sodium acetate were purchased from Sigma. Phosphate-buffered saline (PBS) was purchased from Gibco.

Molecular cloning and site-directed mutagenesis. Jurkat cell RNA was extracted with TRIzol and corresponding cDNA was generated by RT-PCR. Custom-made PCR primers were then used to amplify human LYPLA1 and LYPLA2 genes from Jurkat cell cDNA. PCR products were inserted into a pTrcHis2A bacterial expression vector via ligation-dependent cloning techniques in which BamHI and EcoRI restriction sites were used for an in-frame fusion to a C-terminal hexahistidine (His_6) affinity tag. During the cloning process, each gene was deliberately truncated to eliminate the first 5 residues to initiate translation at the second methionine residue. The genes were then sub-cloned into a pMCSG7 bacterial expression vector[40] (generously gifted by Dr. Jeanne Stuckey) via ligation-independent cloning techniques in which custom-made PCR primers were used for an in-frame fusion to an N-terminal His_6 tag followed by a tabbaco etch virus (TEV) cleavage site. Site-directed mutagenesis was carried out on pMCSG7 vectors encoding the LYPLAs 1 and 2 following the Quik-Change PCR strategy (Stratagene) by using custom-made mutagenic primers and *Pfu Turbo* as the DNA polymerase. The sequence of the mutated genes were confirmed by an automated chain termination-based DNA sequencer (ABI Model 3730XL) at our institution's DNA sequencing core facility (University of Michigan). The recombinant wild type and mutant containing plasmids were transformed into chemically competent *E. coli.* cells for either plasmid amplification (Top10) or protein purification (BL21(DE3)pLysS).

Protein expression and purification. All recombinant protein were purified as follows. After reaching an optical density of 0.5 at 600 nm, 1 L Lysogeny broth[41] cultures of transformed BL21(DE3)pLysS cells were induced for 4 h with 1 mM IPTG

and shaken in a bacterial incubator at 250 RPM at 37 ^{o}C. The following steps were carried out at 4 ^{o}C unless otherwise noted. Cells were sedimented by centrifugation at 5,000 x g for 5 min and pellets were stored at -80C^{o} until further processing. Frozen cell pellets were resuspended in 40 mL of lysis buffer (50 mM Tris pH 8.0, 150 mM NaCl) supplemented with 10 % v/v glycerol and lysed to homogeneity using a an ultrasonic probe. Cell debris was pelleted by centrifugation at 12,000 x g for 30 min. Recombinant His_6-tagged proteins were then purified using Talon immobilized cobalt affinity resin according to the manufacturer's protocol. Briefly, the supernatant was incubated with the cobalt resin, washed with 5 column volumes of lysis buffer supplemented with 1mM imidazole, and eluted over 4 steps with lysis buffer supplemented with 5, 10, 25 and 50 mM imidazole. Fractions containing recombinant protein were identified by Coomassie stained SDS-PAGE gels, pooled and transferred to a dialysis tubing (10,000 MWCO). For kinetic experiments, recombinant proteins were dialyzed sequentially against 3 L of lysis buffer and their protein concentration was measured using the DC protein assay (Bio-Rad). Proteins were then diluted to 10 mg/mL in lysis buffer supplemented with 50 % v/v glycerol, divided into 20 µL aliquots, flash-frozen in an ethanol-dry ice bath and stored at -80 ^{o}C until further processing. For crystallographic experiments, recombinant proteins were dialyzed sequentially against 2 L of 20 mM Tris pH 8.0 with 30 mM NaCl. The His_6 tag was cleaved off by the addition of TEV protease during the first round of dialysis. The proteolyzed solution was incubated with the cobalt resin for 1 hr, collected and concentrated using an Amicon ultracentrifugal filter unit (Millipore) operated according to manufacturer's protocol. All recombinant proteins were purified to >90% purity as determined by SDS-PAGE analysis in typical yields of ~10-20mg protein / g of wet cell paste.

Protein Crystallization. Prior to crystallization, purified proteins were concentrated to 8 mg/mL and dithiothreitol (DTT) was added to a final concentration of 5 mM. LYPLA1 was incubated with 0.5 - 5 mM of ML348 and LYPLA2 was incubated with 0.5 - 3 mM of ML349 for at least one hour at 4 °C before setting crystal trays. Trays were set at room temperature and incubated at 20 °C Crystals were produced by sitting drop vapor diffusion with drops containing 2 µL of protein-inhibitor solution and 2 µL of reservoir solution. For LYPLA1 with ML348, the best-diffracting crystals were formed

from reservoir solution containing 0.1 M sodium citrate, 22-24% PEG 3350, and 200 mM $MgCl_2$. For LYPLA2 with ML349, the best-diffracting crystals were formed from reservoir solution containing 0.1 mM sodium citrate pH 5.5, 20-24% PEG 3350. To obtain large diffractable crystals, drops were microseeded 24 hours after setup. After 1-2 weeks, thin plate crystals formed. Cryopreservation solutions used to harvest each crystal contained reservoir solution reagents at the concentrations listed above with the addition of 25% ethylene glycol.

Data Collection and Structure Determination. Diffraction data for LYPLA1-ML348 and LYPLA2-ML349 were collected on the Advanced Photon Source LS-CAT beamlines 21-ID-D and 21-ID-G, respectively. The data were processed with MOSFLM[42] and scaled with SCALA[43]. LYPLA1-ML348 was solved to 1.55 Å resolution by molecular replacement using MOLREP[44] with the A chain of apo LYPLA1 (PDB ID 1FJ2) as the search model. The structure of LYPLA2-ML349 was solved to 1.64 Å resolution by molecular replacement via Balbes[45], which also used the apo LYPLA1 structure as the search model. Both structures went through iterative rounds of electron density fitting and structural refinement in Coot[46]and Buster[47]. Difference electron density maps contoured at 3σ showed the presence of an inhibitor associated with each protein chain (Figure 3-5).

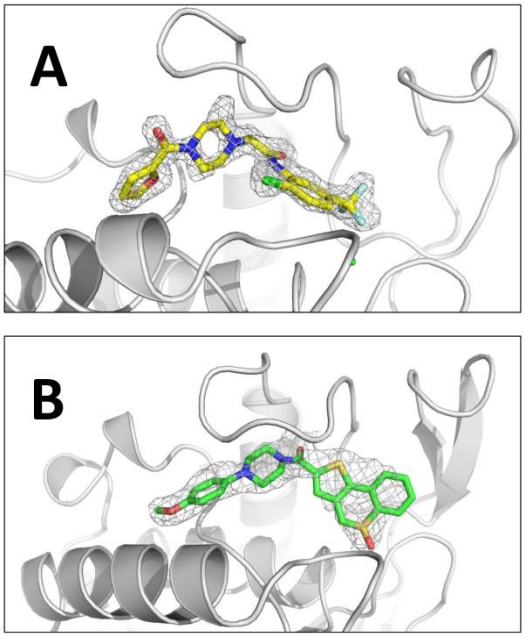

Figure 3-5 Omit electron density maps for ML348 (A) and ML349 (B). The A chain of LYPLA1 and LYPLA2 are displayed as grey cartoons with their respective ligands in sticks. ML348 is shown with carbon atoms in yellow, nitrogens in blue and oxygens in red. ML349 has its carbons colored green. The Fo-Fc omit electron density maps are shown as black grids contoured at the 3α level.

Coordinates and restraint files for each ligand were created by Grade[47] with the mogul+qm option. Two molecules of LYPLA1 were refined per asymmetric unit. Residues 8 – 230 for both chains were visible in the electron density 2Fo-Fc maps. Four molecules of LYPLA2 were present in the asymmetric unit.

Residues 9 – 231 were visible in the electron density maps for chains A and B and residues 10 - 231 were present in chains C and D with the exception of residue 160 missing from chain C. Data collection and refinement statistics for each structure are listed in Table 4.

Steady-state resorufin acetate hydrolytic assays. Resorufin acetate, ML348, ML349, and ML349 derivatives were all dissolved to 10 mM in anhydrous DMSO and stored as aliquots at -80^{o}C. Assay buffer was prepared by adjusting PBS to pH 6.5 with sodium acetate (ca. 10mM) and supplementing it with 0.5 g/L Pluronic F-127. For steady-state substrate-dependence experiments, 5 µL of varying substrate concentration was dispensed into wells of a black-bottom, half-area, 96-well plate (Corning). Purified recombinant enzyme was diluted into assay buffer and allowed to equilibrate to room temperature for 20 minutes. The assay was initiated with 95 µL of 50 nM enzyme using a multi-channel pipette, and then quickly mixed with the pipette several times. The absorbance from the wells were then measured at room temperature every 35 seconds for 20 minutes on a Tecan F500 plate reader using a 525/35 nm excitation filter, a 600/10 nm emission filter, and a 560 LP dichroic filter. Each enzyme was assayed in two separate runs, each consisting of 4 replicates per substrate concentration and performed simultaneously with another 4 replicates using the appropriate catalytic-dead enzymes S119A.LYPLA1 and S122A.LYPLA2. Initial reaction velocities were calculated by measuring the slope about the absorbance time course within the first 6-7 minutes. For each enzyme, the velocities from the two separate runs were combined and background hydrolytic rates were subtracted using the averaged rate from the appropriate catalytic-dead reactions. The baseline-subtracted data consisting of 8-replicates were imported into the Graphpad Prism 6 software and nonlinear regression analysis was used to measure the steady-state parameters V_{max} and K_m by fitting the curve to the standard Michaelis-Menten kinetic equation:

$$\boldsymbol{V_i(S) = \frac{V_{max}[E]_t \times [S]}{K_m + [S]}} \qquad \textit{Equation 1}$$

Where V_i is the initial reaction velocity measured at a given substrate concentration, V_{max} is the maximum rate achieved under saturating substrate concentration, K_m is the

substrate concentration at which the reaction rate is half of V_{max}, $[E]_t$ is the total enzyme concentration used and [s] represents the initial substrate concentration at time zero.

A similar experimental scheme was followed for the inhibitor-dose response measurements except for the initial setup used in preparing the 96-well plate. Namely, 50 nM enzyme was pre-incubated in assay buffer containing varying inhibitor concentrations and a fixed 2 % v/v DMSO concentration for 30 minutes at room temperature. 95µL of solution were then dispensed into wells containing 5uL of a fixed resorufin acetate concentration to give 50µM substrate and 7 % v/v DMSO final reaction concentrations. Absorbance rate measurements were acquired as before and after subtraction of the catalytic dead activities, the initial velocities were divided by the velocities measured in the vehicle control treatments (denoted V_0). The normalized data, consisting of 8 replicates per inhibitor concentration, was then imported into GraphPad Prism 6, transformed into Log_{10} units and nonlinear regression analysis was used to calculate a steady-state IC_{50} value by fitting the curves to a four parameter logistic equation of the form:

$$\boldsymbol{V_i^{res}(I) = \lim_{[I]\to\infty} V_i^{res} + \frac{Span}{1+10^{(LogIC_{50}-[I])\times Hill}}} \qquad \textit{Equation 2}$$

Where [I] is the total inhibitor concentration used, V_i^{res} is the residual velocity measured at a given [I], $lim_{[I]\to\infty}V_i^{res}$ is the limit of residual velocity as [I] approaches infinity, Span is the range observed in the dose-response curve, Hill is the slope associated with the curve and IC_{50} is the inhibitor concentration at which residual velocity is half of the maximal velocity V_0. The equilibrium inhibitory K_i constants for each compound towards either wild type or mutant enzyme were then derived using the Cheng-Prusoff equation[48]:

$$\boldsymbol{K_i = \frac{IC_{50}}{1+\frac{[s]}{K_m}}} \qquad \textit{Equation 3}$$

***Transient fluorophosphonate rhodamine binding assays*.** Assay buffer was prepared by combining final concentrations of 50 mM Tris pH 8, 150mM NaCl and 0.5 g/L Pluronic F-127. 125 nM of purified recombinant enzyme was pre-incubated in assay buffer containing either 12.5 µM of the indicated inhibitor or 2.5 % v/v DMSO for 30 minutes at room temperature. 1µM of FP-PEG-TAMRA was then added to the mixture

to initiate the reaction. At the indicated time points, 20 µL of reaction mixture was removed, combined with 4 µL of 5 x Laemmli sample buffer and heat-inactivated at 85^{o}C, for 5 minutes. Mixtures were separated by SDS-PAGE using a 4% - 20% polyacrylamide precast Tris-Glycine gels (Invitrogen) and imaged using a Typhoon 9200 fluorescence scanner. The fluorescence intensity of each band was integrated and quantified on the ImageJ software. For each run, the band intensity at every time point was divided by the band intensity of the final time point, thereby transforming the raw fluorescence intensities into fraction bound values. The normalized data were imported into the GraphPad Prism 6 software and nonlinear regression analysis was used to calculate the observed rate constant k_{obs} by fitting the curve to a single-phase exponential association equation of the form:

$$\boldsymbol{F_{bound}(t) = 1 - e^{-k_{obs} \times t}} \qquad \textbf{\textit{Equation 4}}$$

Where t is time, F_{bound} is the fraction of enzymes that are bound to the fluorophore at a given time and k_{obs} is observed pseudo-first-order rate constant associated with the binding reaction in the presence of an inhibitor. Thus, the off rate constant (k_{off}) for the decomposition of the competitive enzyme-inhibitor complex can be equated to k_{obs} when it is the rate-limiting step in a two-step 'release-then-pull' kinetic experiment described in the results section.

3.4 Results

Protein crystallization. In light of the recent discovery of isoform-selective reversible inhibitors for LYPLA1 and 2, we wanted to understand how these highly homologous enzymes achieve exquisite specificity towards their corresponding inhibitors ML348 and ML349. For this purpose, we sought to obtain crystal structures for both uninhibited and inhibitor-bound LYPLA1 and 2 so that structural determinants and possible ligand-induced conformational changes may be examined on a molecular level. To this end, crystal trays of human recombinant proteins were prepared in which wild type LYPLAs were precipitated in their unliganded (apo) form or in the presence of saturating concentrations (>5 times the reported K_i values[34]) of their corresponding inhibitors. LYPLA1 yielded diffraction-quality crystals for both the ML348-complexed and apo forms (data not shown), the latter of which a crystal structure has been previously solved by employing anomalous scattering from bromide ions introduced into the cryoprotectant solution[29]. Despite our efforts at screening numerous crystallization conditions, we were unable to grow well-ordered crystals for apo LYPLA2. It is possible that LYPLA2 contains intrinsically disordered regions imparting greater flexibility to its secondary structural elements and this can result in lattice irregularities during the crystallization process.[49] We therefore conjectured that LYPLA2 will benefit from crystallization in the presence of its inhibitor ML349, as competitive inhibitors have shown to act as stabilizing ligands[50] and may 'rigidify' the protein structure generating higher-quality crystals[51]. Indeed, adding the compound to the protein solution during the crystallization trials improved crystallogenensis and yielded cocrystals with good diffraction properties.

Quality of the models. The proteins studied in this work contain an N-terminal, 5-residue deletion, resulting in amino acid sequences that begin at the sixth methionine. Nevertheless, the amino acid numbering reported herein refers to the original sequences of the human enzymes acquired from the Consensus Coding DNA Sequence Database (ID numbers CCDS6157.1 and CCDS241.1). The molecular models for both protein-inhibitor complexes were refined to high resolution, yielding atomic structures of 1.55Å for LYPLA1 and 1.64Å for LYPLA2. Table 4 summarizes the

acquisition parameters, refinement statistics and model quality associated with the solved structures.

Table 4 Crystallography Data Collection and Refinement Statistics.

Data Collection	APT1-CP83	APT2-CP115
PDB Code	N/A	N/A
SpaceGroup	P2 21 21	C2
Unit Cell a, b, c (Å)	71.67, 73.69, 81.82	78.21, 79.79, 138.61 β=93.3°
Wavelength (Å)	0.9792	0.9786
Resolution (Å)[1]	1.55 (1.57-1.55)	1.64 (1.67-1.64)
Rmerge	0.057 (0.42)	0.095 (0.488)
<I/σ□>[2]	18.5 (4.2)	7.1 (2.0)
Completeness (%)[3]	100 (100)	93.2 (84.5)
Redundancy	8.1 (7.8)	3.7(2.9)
Refinement		
Resolution (Å)	1.55	1.64
Rwork [4]	0.1784	0.2210
Rfree[5]	0.1972	0.2523
Monomers/ASU	2	4
Protein atoms	6909	6615
Heterogen atoms	470	546
Water molecules	362	310
Unique Reflections	63533	97049
R.m.s.d.[6]	See main text	See main text
Bonds	0.01	0.01
Angles	1.10	1.06
MolProbity Score[7]	1.12	1.08
Clash Score[7]	2.85	1.79
Z-Score[8] (A,B,C,D) chain	0.09, 0.29	0.01, 0.07, 0.89, 0.53
RSR[8] (A,B,C,D) chain	0.128, 0.161	0.091, 0.088, 0.080, 0.103
RSCC[8] (A,B,C,D) chain	0.819, 0.848	0.960, 0.959, 0.962, 0.954

[1]Statistics for highest resolution bin of reflections in parentheses.
[2]Intensity signal-to-noise ratio.
[3]Completeness of the unique diffraction data.
[4]Rwork = Σ_h I $IF_oI - IF_cI$ I / $\Sigma_h IF_oI$, where F_o and F_c are the observed and calculated structure factor amplitudes for reflection h.
[5]R_{free} is calculated against a 5% random sampling of the reflections that were removed before structural refinement.
[6]Root mean square deviation of bond lengths and bond angles.
[7] REF MOLPROBITY
[8]REF EDS

The stereochemical quality of the molecules modeled in the ML348•LYPLA complexes is quite high as assessed by MolProbity[52], which showed that across backbone atoms, ~100% of the residues had dihedral angles of the most favored φ/ψ conformations with no outliers. On the other hand, not all bond geometries present in the atomic model of ML349•LYPLA2 complexes were of the most favored Ramachandran angles, although all were of allowed dihedral angles. Indeed, particular regions of low electron density prevented the refinement algorithms from fitting the corresponding structure with totally accurate dihedral angles. The weak X-ray scattering observed only in certain high-mobility regions of LYPLA2, but not in the corresponding region of LYPLA1, further supports the existence of intrinsically flexible domains within its polypeptide chain which may contribute to its unique affinity to ML349. Regardless, the electron density surrounding at least one of the LYPLA2 chains was well-defined throughout the structure and the relative conformation and location of the associated ligand atoms were well-resolved due to their inherent planar arrangement (Figure 3-5).

To facilitate comparisons with related abhydrolase structures, the subsequent description of secondary structural elements follows the nomenclature of the canonical abhydrolase fold developed by Ollis *et al.*[3] For consistency, deviations from the prototypical fold and unique structural insertions are named in the same fashion as reported in the previous LYPLA1 crystal structure paper.[29] Unless otherwise noted, discussions concerning either LYPLA complex refer to analyses exclusively performed on the A chains and their associated ligands as these had the highest overall quality statistics for both ligand and macromolecule. (Table 4).

Overall structures of LYPLA1 and LYPLA2 reveal highly similar abhydrolase folds. To begin to explore the elements that confer ligand selectivity to these enzyme, we chose to consider the structural commonalities and disparities present in these homologues. We envisioned that structurally-divergent components might help to locate ligand-specific residues. Broadly speaking, the cocrystal structure of LYPLA2 was found to be highly analogous to that of LYPLA1 (PDB ID: 1FJ2), as it adopts the same atypical *α*/*ß* hydrolase fold (Figure 3-6A and B). LYPLAs feature the same central, six-stranded, mostly parallel *ß*-sheet, corresponding to strands *ß*2-*ß*8, which are joined by variable lengths of loops, helices and strands.

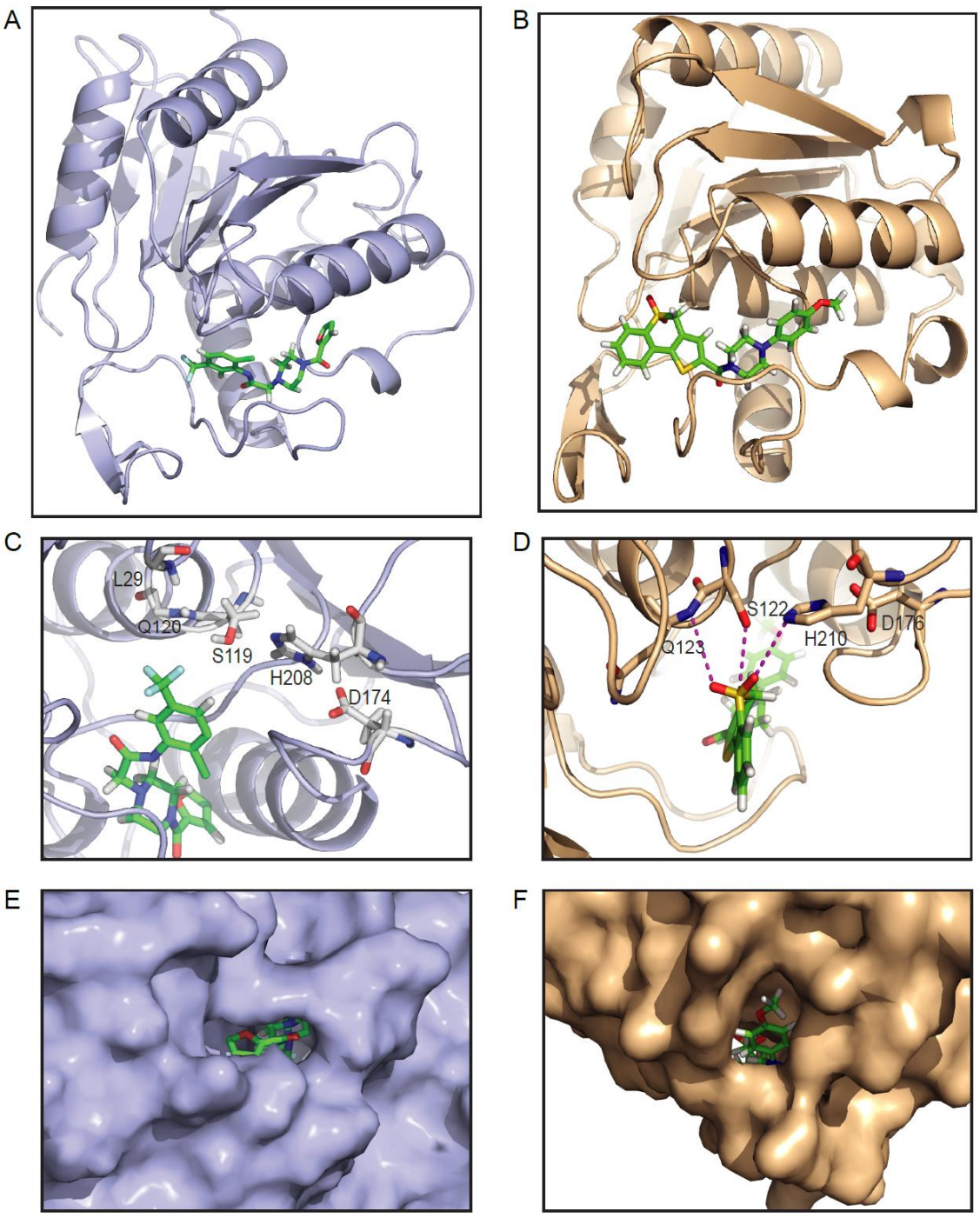

Figure 3-6 Crystal structures of LYPLA1 and 2 bound to their corresponding inhibitors reveal distinc inhibitor binding modes. (A) and (B) are ribbon representations of LYPLA1 (A) and LYPLA2 (B) tertiary structure and relative positions of their respective inhibitors. (C) and (D) are close-ups of the active-site conformations in which proximity contacts between LYPLA catalytic side-chain and ML348 (C) and ML349 (D) are highlighted. (E) and (F) are surface representations of solvent exposure and accessibility of the bound ligands in APT1 (E) and APT2(F) complexes. The ligands are shown in sticks with green carbon atoms, red oxygen atoms, blue nitrogen atoms, orange phosphorus atoms, and a yellow sulfur atom.

As in all abhydrolyases, the core sheet structure is surrounded by a network of helices, five of which appear in all LC family members; *α*A and *α*F positioned on one side of the *ß*-sheet while *α*B, *α*C and *α*E located on its opposite face (refer to Figure 3-3 for a detailed topological map). It is worth noting that all structurally-documented LC members have replaced the forth α-helix of the classic fold (i.e. *α*D) with a short helical segment named *G*3. Akin to LYPLA1, LYPLA2 contains the same short, irregular 4-stranded anti-parallel *ß*-sheet insertion, referred to as *sß*1-*sß*4, which is spliced between the *ß*4 strand and the *α*A helix. Together with the unique short helical segments *G*1 and *G*3, we refer to this portion of the protein as the short *ß-G-ß-G* motif. The exclusive occurrence of this structural motif among LC family members reinforces the notion that these enzymes belong to a structurally conserved, and perhaps functionally distinct subfamily of abhydrolases.

LYPLAs exhibit near-identical active site architecture. In addition to sharing the LC-family fold, LYPLAs incorporate the same trypsin-like catalytic triad, and in LYPLA2 it is composed of Ser122, His210 and Asp176 housed within the short loops of its central *ß*-sheet structure (Figure 3-6C and D). The nucleophilic serine assumes a typical strained conformation located at the apex of the enzyme's 'catalytic elbow', and the catalytic histidine and aspartate side chains form the classic charge relay system. In addition, the location and orientation of the oxyanion hole with respect to the triad is identical in both LYPLAs, with backbone amides composed of the same Leu and Glu residues, which in LYPLA2 are located at positions 29 and 120, respectively. In essence, LYPLAs share comparable 'neighborhoods' (~90% amino acid conservation) within a 4A radius of their catalytic triads suggesting that ligand specificity arising from this region may require more than just unique inhibitor contacts, and may involve different conformational dynamics[53].

LYPLAs feature putative substrate channels of differing plasticity. The other most likely region of LYPLAs to yield specificity would be the putative acyl binding channel defined primarily by the short *ß-G-ß-G* motif. Seeing that it encapsulates the majority of both ligands (Figure 3-6A, B, and surface representations in E and F) we surmised that this tunnel may harbor discriminatory residues to which critical interaction are made. We

propose that the majority of this channel is actually formed by the *sß*3 and *sß*4 anti-parallel strands basing this claim on the shared space that is populated by the different ligands. The entrance proximal to the active site is formed by the *G*1 helical segment and the *ß*3-*α*A loop whereas the helical *G*3 segment exclusively makes up the distal end of the cavity (Figure 3-3). Oddly enough, LYPLA2's *G*3 segment, which in LYPLAL1 has been shown to determine acyl length specificity, is connected to a flexible loop structure that is predicted to be highly mobile as evaluated from crystallographic temperature factors (data not shown). It is therefore very plausible that this high-mobility loop affects the dynamics about the *G*1 'cap', giving this hydrophobic channel plastic properties that are unique to LYPLA2. Overall, residues that map to this cavity are highly conserved between the enzymes although LYPLA point differences may still be sufficient to give rise to selectivity.

Considering only their backbone conformations, LYPLA1 and 2 appear to be virtually superimposable as shown by least-squares alignments of their main chain structures (Figure 3-7A); the exact C_α root mean squared differences (RMSD) reveal that LYPLAs share near-identical backbone conformations with the only key exception being that of the *G*3-proximal high-mobility loop.

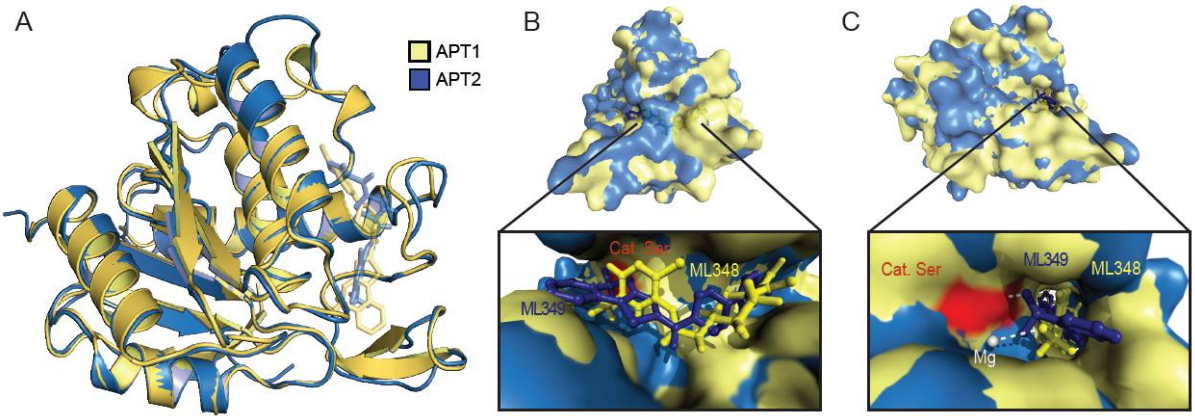

Figure 3-7 Least-squares structure overlay of LYPLA1/2 shows Low Cα-RMSD between cocrystal structures. A structural overlay of the multiple sequence alignment shows nearly identical tertiary folds with low (>2Å) RMSD over all backbone C_α atoms. Front (B) and side (C) projections show the compounds threading through structurally homologous hydrophobic tunnels in both enzymes. Both inhibitors seem to occupy the same topological surface resembling a shallow valley.

In fact, the disordered region algorithm DisEMBL[54] predicts this loop to exist in multiple conformations in LYPLA2 but not LYPLA1 amino acid sequence. With this description of their tertiary structures in mind, we decided to address comprehensive protein features

before we systematically look at differences between the enzymes' specific contacts with their inhibitors.

Global structural differences may contribute to active site ligand specificity: Since LYPLAs share much of the same architecture about their active sites and putative substrate channels, it is possible that all-encompassing factors may account for the observed ligand specificities. For example, the electrostatic potential distribution about an enzyme's molecular surface has been shown to contribute to the distinct substrate activities of esterases and lipases.[31,55] To this regard, LYPLAs show true disparities in their surface charge characters, with LYPLA1 having an unexpectedly more polar character with scattered hydrophobic patches. Conversely, LYPLA2 shows a contiguous set of hydrophobic surfaces which may be useful for engaging the lipid phase where its endogenous substrate is likely to be found (Figure 3-8).

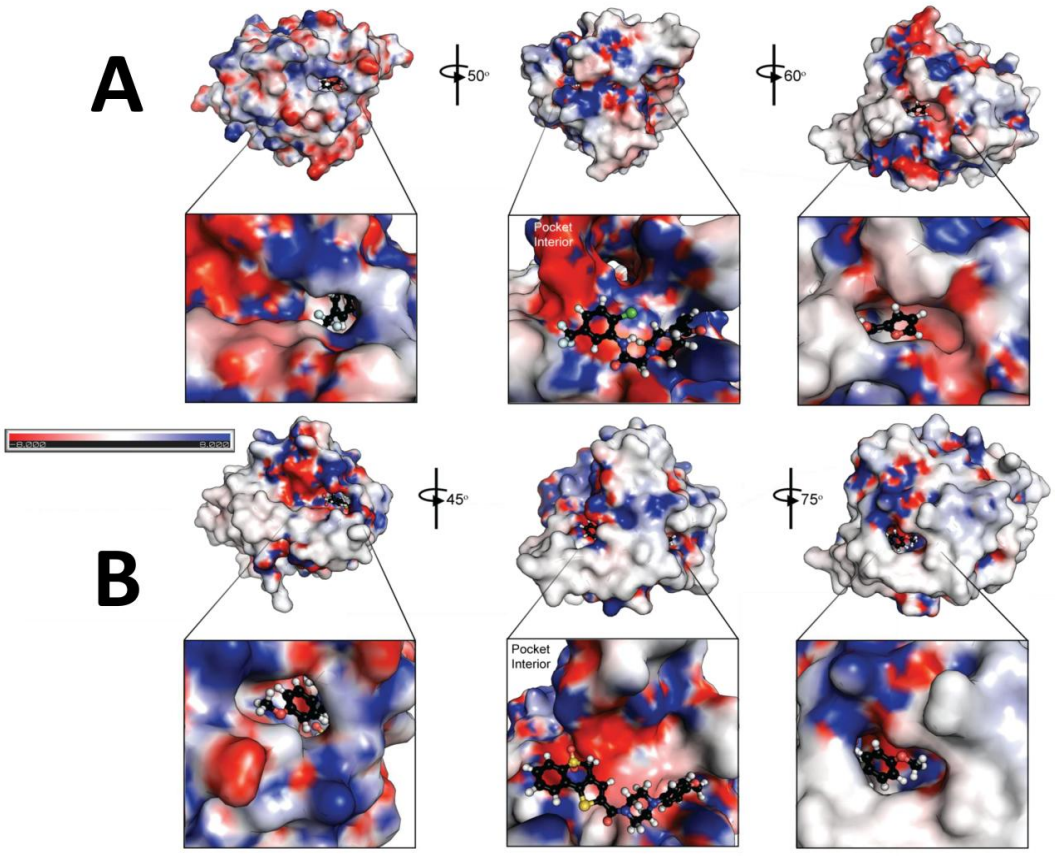

Figure 3-8 Surface electrostatic comparison between LYPLA1 and 2 shows LYPLA2 has more contiguous hydrophobic interface suitable for lipolytic activity. The adaptive Poisson-Bolzmann solver (APBS) was used to compute the effective surface electrostatics for both LYPLA1 (A) and LYPLA (2) which clearly demonstrate that LYPLA2 has more hydrophobic character surrounding its active site.

Indeed, surface electrostatics alone suggest that LYPLA2 is a more suitable lipophilic attractant and may better lure hydrophobic compounds like ML348 and ML349 into its active site. These inhibitors are expected to have comparable hydrophobicities (2.92 and 2.63 cLogP values for ML348 and ML349, respectively) and are therefore predicted to be highly attracted to LYPLA2. However, the slightly more lipophilic ML348 shows only faint activity towards LYPLA2 signifying that other electronic and steric elements must shield the active site from this inhibitor. Nevertheless, LYPLA1 and 2 surface characters are vastly more hydrophobic than LYPLAL1[7], which exhibits pronounced surface charge which is reasonable given its preferential short chain hydrolytic activity.

It is also plausible that the unique surface polarity of each LYPLA may contribute to totally different oligomerization states[56,57]. Indeed, the crystal asymmetric units of the two LYPLA complexes are strikingly different in spite of being grown in virtually identical crystallization conditions; this implies that observed crystal packing is a consequence of either the presence of different ligands and or the protein's particular amino acid sequence. LYPLA1 contains two chains in its asymmetric unit, each, with its associated ML348 ligand, forms a dimer interface that is dissimilar to that observed in the previously reported unliganded structure (Figure 3-9). The apo LYPLA1 dimer interface is composed of cognate *sß*2-strand and *ß*8-loop interactions as well as a *ß*7-loop to an *α*A-helix inter-subunit interaction, whereas the non-covalent ML348•LYPLA1 complex displays a totally different dimeric interface forming novel inter-subunit interactions between all *sß*-strands and *ß*3, *ß*7 and *ß*8 loops (see Figure 3-3 for reference). Without additional in-solution characterization, it is challenging to conclude whether this alternative subunit arrangement results from trivial cocrystal packing or may actually reflect an ML348-induced dimerization of LYPLA1 in solution. On the other hand, the asymmetric unit of the ML349•LYPLA2 cocrystal contains four chains, each of which is complexed to an ML349 ligand. The four macromolecules appear to form two distinct crystallographic dimers which are further stacked in an extended tetrameric conformation. Each dimeric interface is unlike any of those described in other LC family structures, solely consisting of symmetric interactions between the termini of each subunit: an anti-parallel sheet composed of inter-subunit *ß*2-strands and an anti-parallel

helical bundle composed of inter-subunit F*α* helices. Although it is tempting to suggest that LYPLA ligand specificity could arise from exclusive subunit interactions, it is unknown how closely do the quaternary structures present in these crystals represent the oligomeric states in solution. Thus, to better understand the specificities of the ligands, we examined their contacts carefully as the following details.

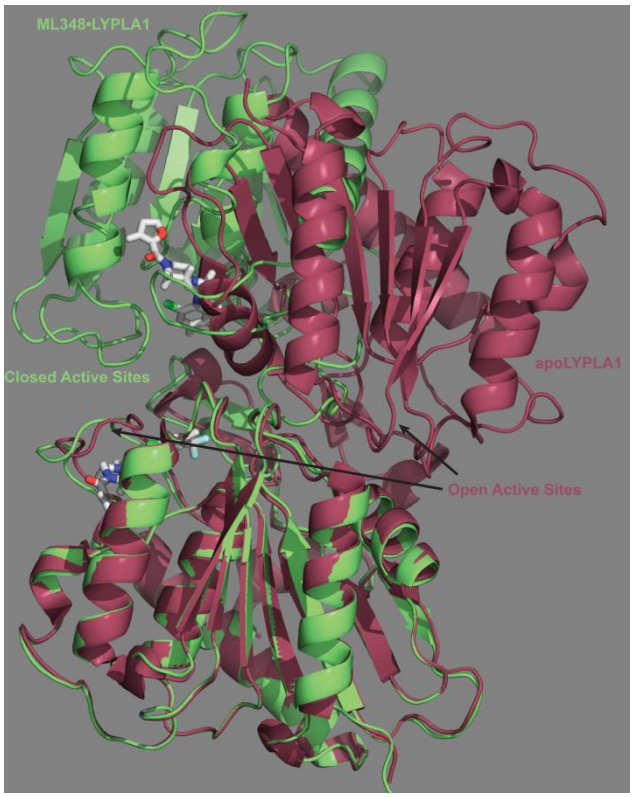

Figure 3-9 Comparison between apoLYPLA1 asymmetric unit to that of LYPLA1•ML348 complex shows significantly different mutual dispositions between their respective dimer interfaces.

Apo LYPLA1 conformational resemblance to ML348•LYPLA complex suggest a lock-and-key binding mechanism. Although both inhibitors are said to be specific for their targets, ML348 and ML349 do not exhibit the same degree of specificity; the former displays less than 35-fold selectivity towards LYPLA1 and the latter displays greater than 200-fold selectivity towards LYPLA2 as judged by the ratio of their inhibitory equilibrium constants (K_i). Thus, whereas ML349 is virtually an exclusive LYPLA2 ligand, ML348 is active towards both enzymes with LYPLA1 being the high affinity target. The promiscuous behavior of ML348 can be rationalized by the molecule's predicted degrees of freedom allowing it to better compensate for the differential electronic and steric requirements of LYPLAs. To this point, it can be seen

from the cocrystal structure that this complex features ML348 in an unexpected conformation; there appears to be an intramolecular hydrogen bond that forces the molecule into a bent shape (Figure 3-7B). This configuration is made possible due to the presence of two sp^2 hybridized atoms: the exocyclic methylene group and the tertiary amine of the piperazine ring (Figure 3-4B). These particular atoms enable the molecule to form a very stable hydrogen bond between the amide hydrogen and the lone pair of the tertiary amine of the piperazine ring, however it is unclear whether this configuration can be favored outside the active site.

To address this question, we superimposed the apo and the liganded LYPLA1 structures and inspected for obvious changes that could explain the unpredictable conformation of ML348. Overall, there were no pronounced backbone conformational differences between the crystal structures as can be seen from the asymmetric unit alignments. This suggested that ML348 binds in a complementary fashion to the ground-state conformation of the enzyme. Remarkably, most amino acid side chains within 4Å radius of ML348 did not show much conformational changes between the structures with the exception of the active site proximal residues R149 and I75 and L78 (Figure 3-10).

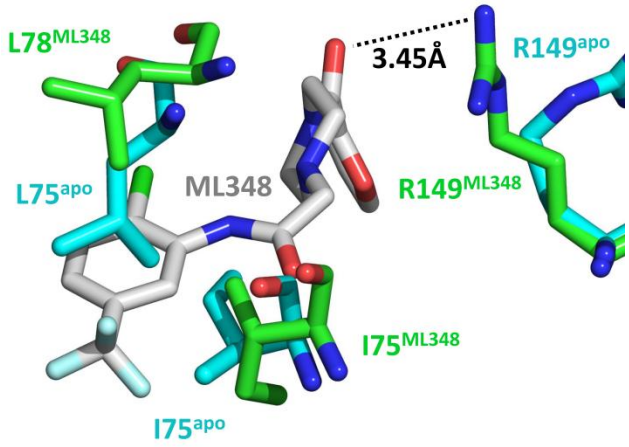

Figure 3-10 Superposition of apo and ML348-occupied LYPLA1 reveal inhibitor engaging and disengaging proximal active site residues.

Whereas both I75 and L78 side chains had shifted back to accommodate the anilide and piperazine respectively, R149 guanidino group seems engage the carbonyl of the 2-furoyl amide. Certainly, R149 could be interacting with the carbonyl via hypothetical hydrogen bonds but this does not explain the kink observed in the inhibitor. Intriguingly,

3 highly stationary, active site-resident waters (as judged by their crystallographic placement factors) were found to coordinate the amide carbonyl of the disubstituted anilide through a network of hydrogen bonds (Figure 3-11).

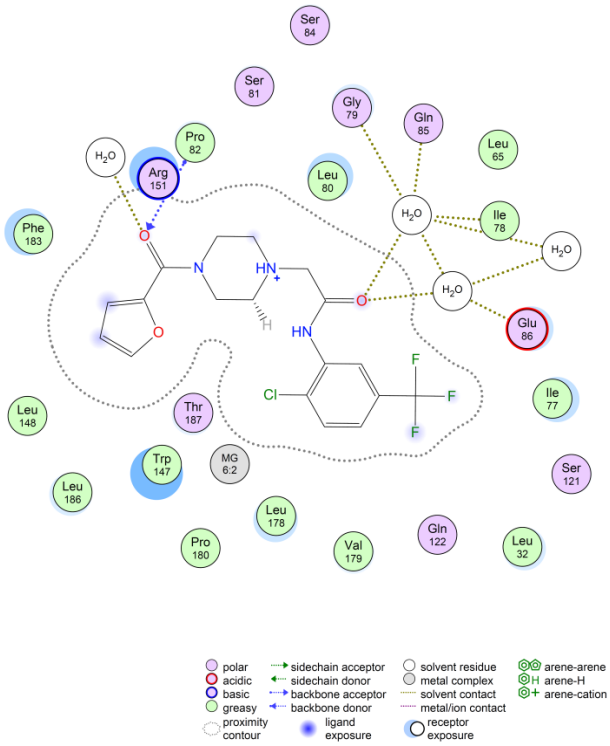

Figure 3-11 Two-dimensional representation of relevant LYPLA1-ML348 contacts observed in the cocrystal. The Molecular Operating Environment (MOE) protein ligand analysis software was used to automatically generate this ligand interaction diagram.[58]

These active site waters, which are present in both LYPLAs, may be contributing to the observed intramolecular hydrogen bonding of ML348 as they can draw electron density away from the amide's hydrogen making it partially positive and highly attracted to the piperazine's lone pair. Thus, LYPLA1 appears to stabilize the contortion about its ligand by employing conserved water molecules to donate hydrogen bonds to the carbonyl amides of the molecule.

Both LYPLAs exhibit a so-called 'open' active site with the catalytic triad and oxyanion hole exposed to the bulk solvent (Figure 3-6A and B). Therefore, a competitive inhibitor directed towards this class of active sites would be expected to prevent substrate binding by limiting its access to the conspicuous catalytic triad. Indeed, the sterically-demanding disubstituted analide group of ML348 appears to occlude both the catalytic triad and the entrance to the substrate channel (Figure 3-6A, Figure 3-7B and Figure 3-11). The hydrophobic CF_3 group seems to contribute most to this effect seeing that it makes close contacts to a number of hydrophobic side chains including those of active site proximal L30 and L176 and of the hydrophobic channel entry residue I75. Aside from the two hydrogen bonds mentioned earlier, the majority of the ML348 molecule appears to be held in the substrate channel (Figure 3-7B and C) via hydrophobic interactions with Trp, Phe and Leu residues which are conserved between

LYPLA homologues and therefore not likely to confer ligand specificity. Altogether, ML348 seems to bind LYPLA1 through a combination of hydrophobic attractions and specific hydrogen bonds through its carbonyls. ML348 in turn, binds LYPLA1 in a 'lock-and-key' fashion as the ligand bends around the active site of the enzyme without inducing noticeable conformational changes about its secondary elements.

Distinct ligand interactions mediate LYPLA2-ML349 interactions. Seeing that many, but not all of ML348 contacts to LYPLA1 were to residues that were also present in LYPLA2, it was still plausible that key substitutions in proximity to the compounds were important for ligand specificity. To explore this hypothesis, we turned our attention to the ML349•LYPLA2 complex for clues to finding unshared residues that conferred specific ligand associations (Figure 3-12).

Figure 3-12 Two-dimensional representation of relevant LYPLA2-ML349 contacts observed in the cocrystal. Again, The Molecular Operating Environment (MOE) protein ligand analysis software[58] was used to automatically generate this ligand interaction diagram.

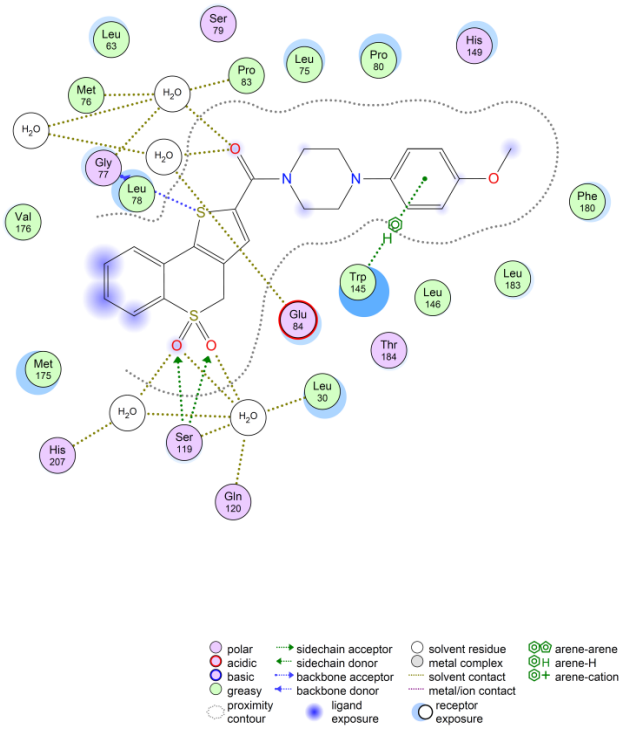

To this end, we noticed that ML349 occluded active site entry like ML348, although it did so in a very different fashion; namely, the fused benzene of the thiochromene dioxide ring was engaging, via a sulfur-π interaction, the thioether of M178 while the sulfone of ML349 was within hydrogen bonding distances to the catalytic S122 hydroxyl and H210 imidazole, and oxyanion residues Q123 and L33 (Figure 3-6B and Figure 3-12). This is in sharp contrast to the mode by which ML348 blocks active site entry which appeared to be dependent on its CF_3 group interacting with aliphatic side chains. ML349, however, uses its sulfone moiety to mimic the tetrahedral intermediate and or transition-state that is featured in ester hydrolysis, and this depiction is consistent with the fact that ML349 exhibits tighter binding to its target

compared to ML348 (Figure 3-6D). Although it may contribute to the potency of the compound, the tetrahedral analog feature of ML349 does not explain its exquisite selectivity for LYPLA2. Perhaps other portions distal from the catalytic residues of LYPLA2 may extend unique contact to ML349 to poise it in the optimal geometry for hydrogen bonding.

The hydrophobic channel was examined next to ascertain the existence of discriminatory residues which prefer the docking of ML349 but not of ML348. It is clear that for both compounds, more than half of the ligand is lodged into the putative acyl tunnel (Figure 3-6E and F, and Figure 3-7B and C). Therefore, we anticipated that at least one residue from this cavity could directly contribute to the formation of a selective complex. Remarkably, LYPLAs exhibit a high degree of conservation about the exterior of the channel defined by the *sß*3-*sß*4 sheet, but contain two different amino acids that flank the ends of this sheet, $I75^{LYPLA1}/L78^{LYPLA2}$ which is proximal to the active site and $P86^{LYPLA1}/Q83^{LYPLA2}$ which is distal (Figure 3-17). In addition, $R149^{LYPLA1}$ which was coordinating the amide of ML348 is substituted for a $H152^{LYPLA2}$ which together with the conserved Trp and Phe residues clamp down on the phenylmethoxy group of ML349. Thus, it appeared that 3-4 differential residues between LYPLAs were potential candidates that could give rise to the observed inhibitor selectivities of ML348 and ML349. These amino acids are:
$I75^{LYPLA1}/L78^{LYPLA2}$, $P86^{LYPLA1}/Q83^{LYPLA2}$, $R149^{LYPLA1}/ H152^{LYPLA2}$ and $L176^{LYPLA1}/M178^{LYPLA2}$ which are all evident by inspection and comparison of LYPLAs ligand interaction maps (Figure 3-11and Figure 3-12).

Steady-state and transient inhibition measurements of ML348 and ML349 with LYPLA mutants confirm residues that confer inhibitor selectivity. We sought to test our predictions by assaying the activities of the compounds toward point mutants wherein the candidate residue was swapped with the corresponding residue present in the homologous enzyme. We term this special type of substitution, a homologous inversion mutation, or inversion for short. In this manner, we generated 3 point inversion mutants for LYPLA1 and 4 for LYPLA2. We first measured both the mutant and wild type activities with the previously employed[34] substrate analog resorufin *O*-acetate (Res-*O*-Ac) to ensure they all had comparable activities (Figure 3-13A).

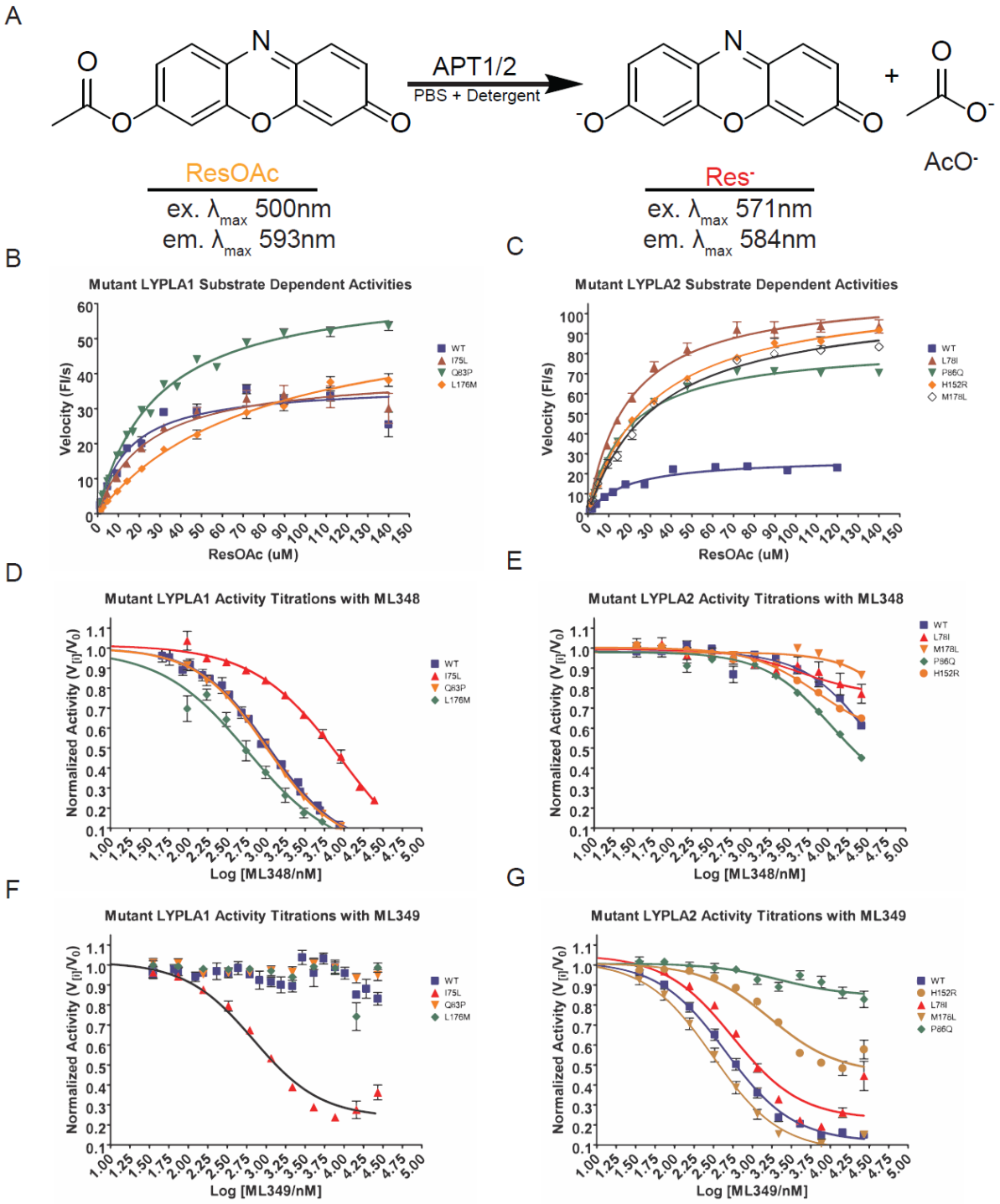

Figure 3-13 Steady-state kinetic analysis of APT1/2 with resorufin acetate. (A) The fluorogenic acetoxy derivative of the phenoxazinone resorufin was employed as a substrate analog for assaying the steady-state hydrolytic activities of wild type and mutant LYPLA1 and 2 variants. (B) and (C) depict the substrate dependent velocities of LYPLA1 and 2 variants, respectively. (D) and (E) depict the dose-dependent inhibition curves for ML348 towards LYPLA1 and 2 variants, respectively. (F) and (G) depict the dose-dependent inhibition curves for ML349 towards LYPLA1 and 2 variants, respectively.

Importantly, all mutants exhibited negligible differences in their K_m towards Res-*O*-Ac (Figure 3-13B and C). This was critical because the K_m value is directly used in the calculations of inhibitor affinities[48] and we wanted to be sure that any changes observed in the mutants' drug sensitivities were largely due to altered enzyme-drug interactions and due to altered enzyme-substrate interactions. No changes in V_{max}, and hence k_{cat}, were observed for LYPLA1, but interestingly, all LYPLA2 mutants exhibited improved k_{cat} values (~10-fold) compared to wild type. This could indicate that LYPLA2 mutants were more efficient at either turning over Res-*O*-Ac or at clearing their active site by hydrolyzing the remaining acetyl adduct. Regardless, neither k_{cat} or V_{max} constants are used for calculating a drug's equilibrium inhibitor constant K_i and therefore this variation was unlikely to interfere with our measurements. These steady-state activities demonstrated that ML348 and ML349 drug binding to all enzyme variants could be carried out to determine which residues were are in fact discriminating between these compounds (Table 5).

Table 5 Summary of steady-state kinetic parameters measured for LYPLA mutants. All enzymes were assayed at 50 nM for both substrate dependence experiments and inhibitor dose-dependence measurements. The values reflect a mean of 8 independent replicate measurements with the error value represented by standard deviations. The estimated Ki measurementes are reported.

Enzyme	ResOAc Km (μM)	ResOAc Vmax (Fi/s)	ML348 Ki (μM)	ML349 Ki (μM)
LYPLA1	14.99 ± 2.075	37.01 ± 1.399	0.300	> 30
I75L.LYPLA1	23.33 ± 3.676	40.41 ± 2.022	3.147	0.218
Q83P.LYPLA1	27.81 ± 1.274	65.93 ± 1.016	0.361	> 30
L176M.LYPLA1	76.94 ± 8.408	60.09 ± 3.245	0.354	> 30
LYPLA2	17.91 ± 2.562	27.9 ± 1.220	> 30	0.230
L78I.LYPLA2	19.35 ± 1.392	111.9 ± 2.396	> 30	0.156
P86Q.LYPLA2	18.71 ± 0.6510	84.72 ± 0.8729	3.09	> 30
M178L.LYPLA2	32.35 ± 1.739	106.6 ± 2.046	> 30	0.122
H152R.LYPLA2	30.48 ± 1.211	111.6 ± 1.550	2.93	5.35

Dose-dependent inhibition experiments were performed in which both inhibitors were assayed against all enzyme variants (Figure 3-13D-G). A few clear trends were already apparent from the steady-state IC_{50} measurements. First, among LYPLA1 point mutation, only the I75L substitution showed a true inversion of inhibitor selectivity as it lost considerable potency towards M348 (~10-fold) and gain exceptional binding properties to ML349 (K_i ~ 220 nM) (Figure 3-13D and F, respectively). This suggested that Ile75, which resides at the entrance to the acyl cavity, discriminates between ligands in LYPLA1 presumably based on bulk hydrophobic radius which was not clearly evident in the cocrystal structure. As per LYPLA2 variants, none of the inversion mutants were able gain LYPLA1-like sensitivity towards ML348 with P86Q having the closest K_i value which was still 10-fold higher than wild type LYPLA1 (Figure

3-13E). However, P86Q and H152R were the only LYPLA2 mutants to lose virtually all binding to ML349 with the P86Q substitution demonstrating a complete loss of ML349 sensitivity (Figure 3-13G). These experimental outcomes (Table 5) were very surprising because the apparent specificity-conferring residue of LYPLA1(Ile75) had no inverting-effect when substituted into LYPLA2. This implied that other differential residues must be in place to ensure ligand specificity for LYPLA2.

We then sought to use an orthogonal means to measure the sensitivities of the inhibitors towards all inversion mutants as we wished to validate these unforeseen findings. Drug target residency time measurements were thus performed to complement the thermodynamic data obtained for binding of the compounds to the mutants. To accomplish this goal, the active site-directed, covalent serine hydrolase probe fluorophosphonate rhodamine (FPRh)[59,60] was employed in a classic, two-step kinetic experiment known as the 'release, then pull' reaction (Figure 3-14A).

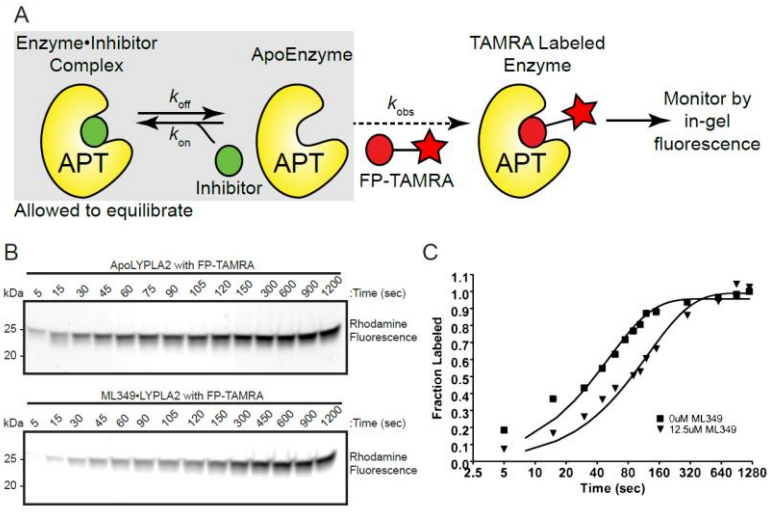

Figure 3-14 Residency time measurements with pre-formed inhibitor-enzyme complex can be used to corroborate steady-state inhibition studies. (A) shows the order in which the reactions are performed. (B) Is a representative gel in which the time-course of FPRh labeling was followed and (C) is the densitometric analysis of the gel band fluorescence intensities. Residency time measurement of LYPLA2 with ML349 yields a ~5 minute half-life ($t_{1/2}$) complex decomposition.

In this rendition of the residency time experiment[37,61,62], the enzyme is pre-incubated with a saturating concentration (>5 times K_i) of inhibitor to form the predominant inhibitor•enzyme complex species. The reaction with excess amount of FPRh is then initiated wherein the inhibitor•enzyme complex must fall apart before FPRh can engage the active site. That being said, the speed at which this probe labels the active site is rate limited by the speed in which the inhibitor dissociates from the enzyme, and hence the dissociation rate constant (k_{off}) of the inhibitor can be measured directly (Figure 3-14B and C) from the observed rate constant of this reaction (k_{obs}).

Using this method, we showed that indeed, the I75L.LYPLA1 mutant exhibits true inversion of selectivity displaying a smaller off rate with ML349 ($t_{1/2}$ ~ 4 min), which is on par with that of the wild type LYPLA2 ($t_{1/2}$ ~ 5 min), and a modestly larger k_{off} constant compared to wild type LYPLA1 (Figure 3-15A). As with P86Q.LYPLA1 off rate kinetics, it exhibited a similar trend to that observed in steady-state experiments, showing rapid reactivity with FPRh when pre-incubated with either inhibitor (Figure 3-15B). Two possible scenarios may give rise to this result, one being complete loss of initial inhibitor binding characterize by infinitely slow on-rates, and the other being exceptionally fast off-rates which preclude the detection of an inhibitor•enzyme complex. Either way, we were able to confirm via two unrelated kinetic measurements that I75^{LYPLA1} and Q86^{LYPLA2} were in fact responsible for the selectivity and potency of the drugs, respectively.

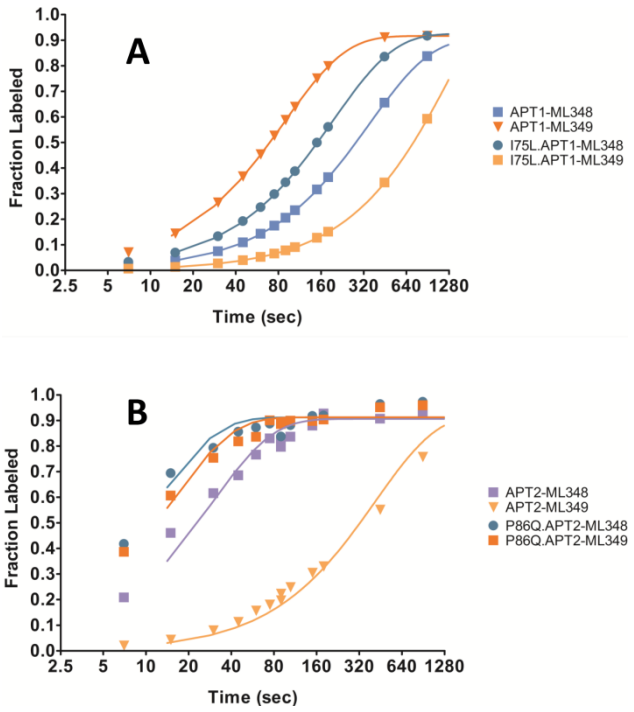

Figure 3-15 k_{off} measurements of ML348 and ML349 towards LYPLA inversion point mutants corroborate IC_{50} measurements further implicating L75 in LYPLA1 and P86Q in LYPLA2 in discriminating active site ligands.

Binding of ML349 derivatives define additional steric and electronic requirements for differential ligand specificity between LYPLA1 and 2. Seeing that a number of structural observations from the ML349-APT2 complex were not addressed by our current inversion mutant studies, we were interested in testing our structure-based hypotheses using a series of ML349 derivatives. The LYPLA2 cocrystal structure suggested that ML349 activity was partly due its sulfone functionality which appeared to serve as transition-state analog for the nucleophilic serine hydroxyl. To confirm this speculation, we synthesized two derivatives with varying degrees of oxidation about the sulfone moiety, termed ML349-sulfoxide and ML349-thioether. We theorized that if the oxygen atoms of the sulfone were indeed engaged in hydrogen bonding then their removal

would be detrimental to the activity of ML349 towards LYPLA2. Indeed, this sulfur series displayed the expected order of potency with the sulfone being having the highest affinity (0.15 µM) and the thioether having the weakest (>20 µM) (right panel of Figure 3-16). These substitutions suggested that the sulfone was likely mimicking a tetrahedral intermediate in LYPLA2.

We also synthesized a series of molecules to investigate the SAR about the opposite end of the ML349 molecule, here referred to as the phenylmethoxy series. Our structural studies of LYPLA2 highlighted that the predominantly hydrophobic channel may be involved in both acquisition and specificity of acyl substrates. Since ML349 appeared in an extended, linear-like disposition whereas ML348 was heavily contorted, we surmised that maybe these conformations reflect the different steric and geometric requirements of each hydrophobic channel. To explore this idea, we synthesized the phenylmethoxy series which contained four derivatives, two of which have a longer *O*-alkyl or *O*-alkynyl substitution stemming from ring and the other two exhibit truncations in which either a methyl or a hydroxyl group is substituted for the methoxy substituent (Left panel of Figure 3-16).

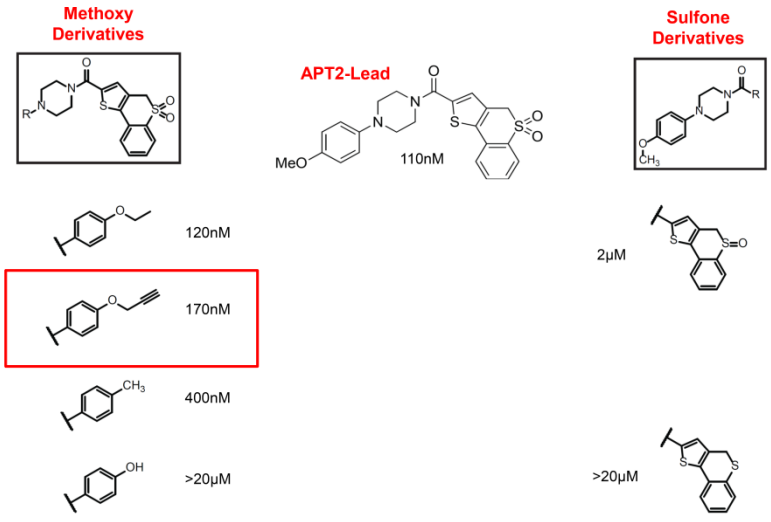

Figure 3-16 Summary of ML349 derivative structures and their estimated Ki values. Invariant scaffolds for each set of derivatives are placed at the top of their column and are boxed in black. Values listed correspond to the estimated K_i of the compounds towards LYPLA2. The propargyl substituted ML349 (left column, 2nd from top) exhibited 3-fold larger K_i value towards LYPLA1.

Interestingly, increasing chain length about the phenyl ring correlated with increased potency, suggesting that maybe aliphatic chains were protruding out of the channel and or favorably interacting with LYPLA2's hydrophobic surfaces. Importantly, the hydroxy-substituted ML349 was the least potent of all phenylmethoxy derivatives signifying that a strong polar character was unfavorable in the putative acyl binding channel. Lastly, an ML349 derivative, the alkynyl compound,

was successfully synthesized which lost LYPLA selectivity at the expense of slightly reduced potency towards LYPLA2 (~1.5-fold). It could be that LYPLA1 is more restrictive about the geometry of the aliphatic chain to be inserted into its channel, however the electronics from the alkyne functionality might contribute to the observed binding of this derivative.

Phylogenetics-based structural analysis suggest a functional conservation for LYPLA2 but evolutionary adaptability for LYPLA1. Our structural studies suggest that these reversible inhibitors may share a number of commonalities with endogenous substrates such as occupying the same hydrophobic channel and interacting with key active site residues. Seeing that ligand specificity was conferred by select residues in each homolog, we wanted to determine whether the human discriminatory residues were conserved across LYPLA orthologues. Conservation of these residues would suggest two things, (1) that the active sites of the corresponding orthologues may be selectively targeted by these compounds, and (2) that these residues may represent conserved features between the active sites of LYPLAs and hence may shape the scope of acceptable substrates for each enzyme.

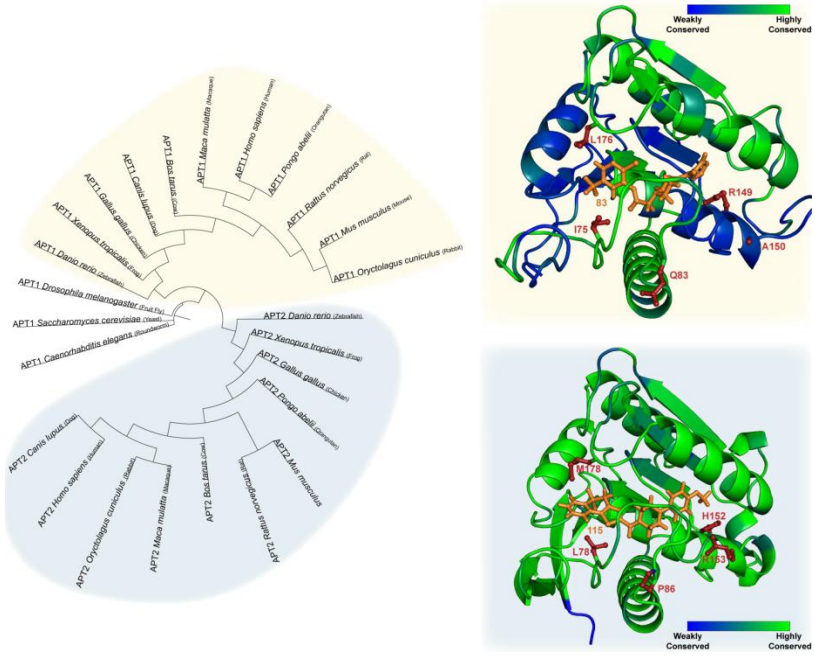

Figure 3-17 Enzyme conservation corroborates active site discriminatory residues that confer inhibitor selectivity between LYPLA1 and 2. The degree of evolutionary conservation was used to measure the significance of amino acid differences between the two enzyme isoforms in an effort to highlight residues that dictate inhibitor binding selectivity. Phylogeny alignments were generated using DIALIGN, anchored at the catalytic serine residue. The degree of sequence conservation shown in the scale bar corresponds to the weight scores used by DIALIGN to assess the degree of similarity among the sequences. In the ideal case, the analysis of the two isoforms would yield secondary structural elements that differ in a subset of residues, one or more of which was responsible for dictating ligand specificity. Beyond this notion, these multiple sequence alignments suggest different evolutionary adaptations between the two thioesterases: a divergent LYPLA1 and an evolutionary-conserved LYPLA2. Based on sequence conservation alone, LYPLA2 is predicted to be under higher selective pressures than LYPLY1, implying that the latter has

evolved to process an assortment of substrates across different organisms, whereas the former has a more defined scope of substrates.

Therefore, we performed multiple sequence alignments (MSAs) across 14 vertebrate species for LYPLA1 and 11 species for LYPLA2. LYPLA co-crystal structures were then color-coded according to the degree of amino acid conservation observed in the MSA (Figure 3-17). It can be seen that the most conserved components between all LYPLA1 orthologues and LYPLA2 orthologues are the *sß*3-*sß*4 anti-parallel sheet and the *α*B helix structures. Importantly, the discriminatory residues confirmed in the mutagenesis studies were all conserved within each family of orthologues, although the selectivity residues of LYPLA2 (i.e. P86 and H152) corresponded to residues within the most divergent portion of LYPLA1 orthologs, helix *α*C. This indicated that within each family of orthologs, the specificity conferring residues were functionally significant and may contribute to conserved and likely divergent substrate specificities.

3.5 Discussion

The major goals of this study were to define the critical interactions between the selective reversible inhibitors ML348 and ML349 and their cognate enzyme active sites, and to determine protein structural features giving rise the observed activities. LYPLA1 and 2 share extensive sequence identity and bear seemingly superimposable main chain structures yet have very different competitive inhibitor specificities. Prior to solving these structures one would have surmised that selectivity would be born out of simple steric and electrostatic differences in their putative substrate binding sites. The co-crystal structures of human LYPLAs revealed a very different story. Specifically, similar to LYPLA1, LYPLA2 possesses a canonical *α/ß* serine hydrolase fold featuring the same signature catalytic triad, oxyanion hole and putative substrate channel (Figure 3-6). In spite of being crystallized in the presence of different compounds, LYPLA1•ML348 and LYPLA2•ML349 exhibit pronounced structural similarities with each other and with the previously published apo LYPLA1 structure[29]. In contrast to other members of the LC-family such as the carboxylesterase from *p. fluorescence* and the distant homologue LYPLAL1, the short irregular *ß*-strands that are part of the exterior of the hydrophobic tunnel are even more peculiar in LYPLA1 and 2 in which they form a 'frustrated' *ß*-sheet structure and could indicate localized flexibility of LYPLAs.

These structural studies have also highlighted isoform-specific differences, namely regarding specificity determining regions. The first of these specificity regions is the so-called high-mobility loop structure which as stated previously, is juxtaposed to the *G*1 helical segment that caps the putative acyl docking channel (Figure 3-3). Interestingly, the amino acid sequence in this loop is highly conserved in LYPLA2 but not in LYPLA1, suggesting a significant role in LYPLA2's catalytic activity. Although distant from the hydrophobic channel, this region displays high-temperature factors and would be expected to affect the channel as it directly links to it via helices and flexible loops. This could also explain why LYPLA2 did not form well-ordered crystals in the absence of ML349. Furthermore, this may have physical implication on the mechanism of substrate acquisition and the nature of substrates processed by LYPLA2. One could imagine these loops to be highly mobile enabling their movement during the ejection of lipid substrates from their endogenous hydrophobic phases.

We and others[63] have suggested that LYPLA's *G*1 helical segment could function as clamp situated at the end of the hydrophobic channel. This would endow this region with 'plastic' properties which may be unique to LYPLA2 given its high-mobility loop. Regardless, as was shown for the LYPLAL1, the *G1* segment may aid in determining the size and stereochemistry of physiological acyl substrates (left panel of Figure 3-16). The third potential specificity region would be the exterior portion of the hydrophobic channel defined by the flexible *sß*3-*sß*4 anti-parallel sheet which could theoretically restrict acyl substrates as it define the major, if not only, entry into this site. This proposition is based on the observation that the residues flanking this structure were among the only amino acids that differed within 4A away from the ligands which also corresponded to inversion mutants that displayed the most significant perturbations in ligand specificities.

In terms of ligand specificities, It is hard to believe that a minor Ile to Leu substitution can revert the selectivity of LYPLA1 (i.e. I75L mutation sensitizes LYPLA1 to ML349 and desensitizes it to ML348), but this is indeed the case, and could possibly be rationalized by the ground-state structures of LYPLA1 and 2 (Figure 3-18); the ß-methyl substituent of I75.LYPLA1 could be clashing with both thiophene sulfur and carbonyl oxygen atoms of ML349, whereas the γ-methyl substituent of L78.LYPLA2 appears to come into contact with the aromatic trifluoromethyl group of ML348.

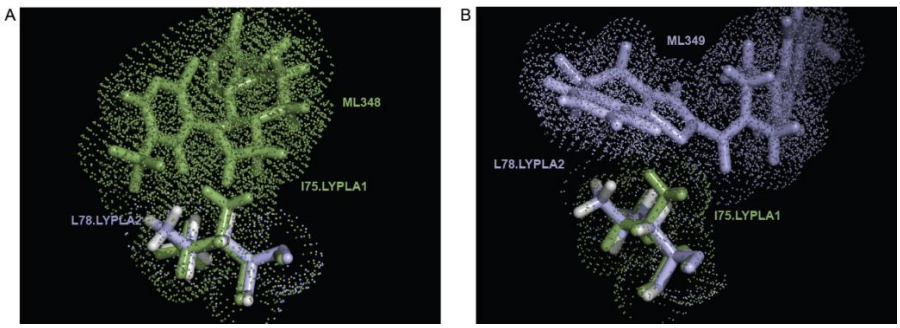

Figure 3-18 Surface-filling representations of possible ground-state interactions between ML348/ML349 and the very similar side chains of $I75^{LYPLA1}$ and $L78^{LYPLA2}$.

However, these static observations should be tested at least on a theoretical level. Defining LYPLA2's selectivity determinant(s) is more of a challenge since a simple Ile-to-Leu substitution is definitely not sole determinant of LYPLA2 inhibitor selectivity given that L78I.LYPLA2 , the corresponding reversed mutant, doesn't exhibit inversion of inhibitor selectivity. On the other hand, P86Q, and to some extent H152R substitution in LYPLA2 certainly abolishes ML349

binding and could be an important prerequisite for ML348 binding as it renders the mutant almost twice as sensitive to ML348 relative to wild type (Table 5). It is possible that multiple amino acid substitutions (e.g. Leu and Pro) are required to establish an energetically-favorable interaction between LYPLA2 and ML348.

As implied earlier, ML348 is predicted to have more rotational degrees of freedom compared to ML349 since it contains a greater number of freely rotating bonds, and thus is expected to interact most favorably with a more rigid, stiff active-site. In LYPLA2, L78 and P86 flank the lower active-site capping loop (these residues correspond to I75 and Q83 in LYPLA1, see Figure 3-17), and could possibly affect the conformational dynamics of this loop and ultimately the accessibility of inhibitors and or substrates into the active-site. Perhaps substituting Pro and Leu together in LYPLA2 produces a more rigid active-site, which effectively "pays" the entropic cost associated with binding and restricting the conformational flexibility of ML348, but again this needs to be tested from a physical standpoint. To summarize, we were able to account for LYPLA1 selectivity for ML348 and against ML349 by a single L75 residue; however, although it was clear that H152 and Q86 are necessary for ML349 binding, it remains ambiguous why LYPLA2 selects for ML349 and not ML348. Maybe future double, triple or even loop-segment inversion[64] mutants may shed more light on this matter.

In conclusion, our data suggest that binding is primarily driven by the hydrophobic interaction, i.e. entropic exclusion of solvent from the lipid docking site. Therefore, we propose that ligand selectivity may be also influenced by intrinsic protein dynamics, such as the flexibility of the aforementioned disordered loops and side chains in vicinity of the active site. Future studies may benefit from probing the dynamics of about the flexible loops of LYPLAs either via NMR- or MS-based methods such hydrogen-deuterium exchange experiments[65] or three-dimensional nuclear relaxation techniques[66], respectively. Thus, the molecular basis for ligand selectivity may arise from differences in both the physical structure and conformational dynamics of LYPLA enzymes.

3.6 Bibliography

1. Otrubova, K., Srinivasan, V. & Boger, D. L. Discovery libraries targeting the major enzyme classes: The serine hydrolases. *Bioorganic Med. Chem. Lett.* **24,** 3807–3813 (2014).

2. Long, J. Z. & Cravatt, B. F. The metabolic serine hydrolases and their functions in mammalian physiology and disease. *Chem. Rev.* **111,** 6022–6063 (2011).

3. Ollis, D. L. *et al.* The α/ß hydrolase fold. **5,** 197–211 (1990).

4. McKinney, M. K. & Cravatt, B. F. Structure and function of fatty acid amide hydrolase. *Annu. Rev. Biochem.* **74,** 411–432 (2005).

5. Quinn, D. M. Acetylcholinesterase: enzyme structure, reaction dynamics, and virtual transition states. *Chem. Rev.* **87,** 955–979 (1987).

6. Simon, G. M. & Cravatt, B. F. Activity-based proteomics of enzyme superfamilies: Serine hydrolases as a case study. *J. Biol. Chem.* **285,** 11051–11055 (2010).

7. Burger, M. *et al.* Crystal structure of the predicted phospholipase LYPLAL1 reveals unexpected functional plasticity despite close relationship to acyl protein thioesterases. *J. Lipid Res.* **53,** 43–50 (2012).

8. Davda, D. & Martin, B. R. Acyl protein thioesterase inhibitors as probes of dynamic S-palmitoylation. *Medchemcomm* **5,** 268 (2014).

9. Duncan, J. a & Gilman, A. G. CELL BIOLOGY AND METABOLISM : A Cytoplasmic Acyl-Protein Thioesterase A Cytoplasmic Acyl-Protein Thioesterase That Removes Palmitate from G Protein ␣Subunits and p21 RAS *. **273,** 15830–15837 (1998).

10. Hong, K. H., Jang, W. H., Choi, K. D. & Yoo, O. J. Characterization of Pseudomonas fluorescens carboxylesterase: cloning and expression of the esterase gene in Escherichia coli. *Agric. Biol. Chem.* **55,** 2839–2845 (1991).

11. Satou, M., Nishi, Y., Yoh, J., Hattori, Y. & Sugimoto, H. Identification and characterization of acyl-protein thioesterase 1/lysophospholipase I as a ghrelin deacylation/lysophospholipid hydrolyzing enzyme in fetal bovine serum and conditioned medium. *Endocrinology* **151,** 4765–4775 (2010).

12. Sugimoto, H., Hayashi, H. & Yamashita, S. Purification, cDNA cloning, and regulation of lysophospholipase from rat liver. *J. Biol. Chem.* **271,** 7705–7711 (1996).

13. Toyoda, T., Sugimoto, H. & Yamashita, S. Sequence, expression in Escherichia coli, and characterization of lysophospholipase II. *Biochim. Biophys. Acta - Mol. Cell Biol. Lipids* **1437,** 182–193 (1999).

14. Wang, a, Yang, H. C., Friedman, P., Johnson, C. a & Dennis, E. a. A specific human lysophospholipase: cDNA cloning, tissue distribution and kinetic characterization. *Biochim. Biophys. Acta* **1437,** 157–169 (1999).

15. D'Arrigo, P. & Servi, S. Synthesis of lysophospholipids. *Molecules* **15,** 1354–1377 (2010).

16. Kessi, J. *et al.* Short-chain phosphatidylcholines as superior detergents in solubilizing membrane proteins and preserving biological activity. *Biochemistry* **33,** 10825–10836 (1994).

17. Jain, M. K. & Berg, O. G. The kinetics of interfacial catalysis by phospholipase A2 and regulation of interfacial activation: hopping versus scooting. *Biochim. Biophys. Acta* **1002,** 127–156 (1989).

18. Gelb, M. H., Jain, M. K., Hanel, a M. & Berg, O. G. Interfacial enzymology of glycerolipid hydrolases: lessons from secreted phospholipases A2. *Annu. Rev. Biochem.* **64,** 653–688 (1995).

19. Carrière, F. *et al.* Pancreatic lipase structure-function relationships by domain exchange. *Biochemistry* **36,** 239–248 (1997).

20. Roussel, A. *et al.* A Cutinase from Trichoderma reesei with a Lid-Covered Active Site and Kinetic Properties of True Lipases. *J. Mol. Biol.* **426,** 3757–3772 (2014).

21. Longhi, S. *et al.* Crystal structure of cutinase covalently inhibited by a triglyceride analogue. *Protein Sci.* **6,** 275–286 (1997).

22. Duncan, J. A. & Gilman, A. G. A cytoplasmic acyl-protein thioesterase that removes palmitate from G protein α subunits and p21(RAS). *J. Biol. Chem.* **273,** 15830–15837 (1998).

23. Rusch, M. *et al.* Identification of acyl protein thioesterases 1 and 2 as the cellular targets of the ras-signaling modulators palmostatin B and M. *Angew. Chemie - Int. Ed.* **50,** 9838–9842 (2011).

24. Hernandez, J. L., Majmudar, J. D. & Martin, B. R. Profiling and inhibiting reversible palmitoylation. *Curr. Opin. Chem. Biol.* **17,** 20–26 (2013).

25. Hedstrom, L., Szilagyi, L. & Rutter, W. J. Converting trypsin to chymotrypsin: the role of surface loops. *Science* **255,** 1249–1253 (1992).

26. Shanado, Y., Kometani, M., Uchiyama, H., Koizumi, S. & Teno, N. Lysophospholipase I identified as a ghrelin deacylation enzyme in rat stomach. *Biochem. Biophys. Res. Commun.* **325,** 1487–1494 (2004).

27. Koyama, K. *et al.* Identification of bioactivating enzymes involved in the hydrolysis of laninamivir octanoate, a long-acting neuraminidase inhibitor, in human pulmonary tissue. *Drug Metab. Dispos.* **42,** 1031–1038 (2014).

28. Manna, J. D. *et al.* Identification of the Major Prostaglandin Glycerol Ester Hydrolase in Human Cancer Cells. *J. Biol. Chem.* **289,** 33741–33753 (2014).

29. Devedjiev, Y., Dauter, Z., Kuznetsov, S. R., Jones, T. L. Z. & Derewenda, Z. S. Crystal structure of the human acyl protein thioesterase I from a single X-ray data set to 1.5 ?? *Structure* **8,** 1137–1146 (2000).

30. Kim, K. K. *et al.* Crystal structure of carboxylesterase from Pseudomonas fluorescens, an alpha/beta hydrolase with broad substrate specificity. *Structure* **5,** 1571–1584 (1997).

31. Fojan, P., Jonson, P. H., Petersen, M. T. N. & Petersen, S. B. What distinguishes an esterase from a lipase: A novel structural approach. *Biochimie* **82,** 1033–1041 (2000).

32. Cambillau, C., Longhi, S., Nicolas, A. & Martinez, C. Acyl glycerol hydrolases: Inhibitors, interface and catalysis. *Curr. Opin. Struct. Biol.* **6,** 449–455 (1996).

33. Fonnum, F., Sterri, S. H., Aas, P. & Johnsen, H. Carboxylesterases, importance for detoxification of organophosphorus anticholinesterases and trichothecenes. *Fundam. Appl. Toxicol.* **5,** S29–S38 (1985).

34. Adibekian, A. *et al.* Confirming target engagement for reversible inhibitors in vivo by kinetically tuned activity-based probes. *J. Am. Chem. Soc.* **134,** 10345–10348 (2012).

35. Lone, A. M. *et al.* A substrate-free activity-based protein profiling screen for the discovery of selective PREPL inhibitors. *J. Am. Chem. Soc.* **133,** 11665–11674 (2011).

36. Lu, H. & Tonge, P. J. Drug-target residence time: Critical information for lead optimization. *Curr. Opin. Chem. Biol.* **14,** 467–474 (2010).

37. Copeland, R. a., Basavapathruni, A., Moyer, M. & Scott, M. P. Impact of enzyme concentration and residence time on apparent activity recovery in jump dilution analysis. *Anal. Biochem.* **416,** 206–210 (2011).

38. Dahl, G. & Akerud, T. Pharmacokinetics and the drug-target residence time concept. *Drug Discov. Today* **18,** 697–707 (2013).

39. Adibekian, A. *et al.* Characterization of a Selective , Reversible Inhibitor of Lysophospholipase 1 (LYPLA1). **1,** 1–14 (2015).

40. Stols, L. *et al.* A new vector for high-throughput, ligation-independent cloning encoding a tobacco etch virus protease cleavage site. *Protein Expr. Purif.* **25,** 8–15 (2002).

41. Bertani, G. Studies on lysogenesis. I. The mode of phage liberation by lysogenic Escherichia coli. *J. Bacteriol.* **62,** 293–300 (1951).

42. The CCP4 suite: Programs for protein crystallography. *Acta Crystallogr. Sect. D Biol. Crystallogr.* **50,** 760–763 (1994).

43. Evans, P. R. An introduction to data reduction: Space-group determination, scaling and intensity statistics. *Acta Crystallogr. Sect. D Biol. Crystallogr.* **67,** 282–292 (2011).

44. Vagin, A. & Teplyakov, A. Molecular replacement with MOLREP. *Acta Crystallogr. Sect. D Biol. Crystallogr.* **66,** 22–25 (2010).

45. Long, F., Vagin, A. a., Young, P. & Murshudov, G. N. BALBES: A molecular-replacement pipeline. *Acta Crystallogr. Sect. D Biol. Crystallogr.* **64,** 125–132 (2007).

46. Emsley, P. & Cowtan, K. Coot: Model-building tools for molecular graphics. *Acta Crystallogr. Sect. D Biol. Crystallogr.* **60,** 2126–2132 (2004).

47. Smart, O. S. *et al.* Exploiting structure similarity in refinement: Automated NCS and target-structure restraints in BUSTER. *Acta Crystallogr. Sect. D Biol. Crystallogr.* **68,** 368–380 (2012).

48. Cheng, Y. & Prusoff, W. H. Relationship between the inhibition constant (K1) and the concentration of inhibitor which causes 50 per cent inhibition (I50) of an enzymatic reaction. *Biochem. Pharmacol.* **22,** 3099–3108 (1973).

49. Dobrianov, I., Caylor, C., Lemay, S. . G., Finkelstein, K. . D. & Thorne, R. . E. X-ray diffraction studies of protein crystal disorder. *J. Cryst. Growth* **196,** 511–523 (1999).

50. Vedadi, M. *et al.* Chemical screening methods to identify ligands that promote protein stability, protein crystallization, and structure determination. *Proc. Natl. Acad. Sci. U. S. A.* **103,** 15835–15840 (2006).

51. Doerr, A. Widening the protein crystallization bottleneck. *Nat. Methods* **3,** 961 (2006).

52. Davis, I. W. *et al.* MolProbity: All-atom contacts and structure validation for proteins and nucleic acids. *Nucleic Acids Res.* **35,** 375–383 (2007).

53. Hedstrom, L., Farr-Jones, S., Kettner, C. & Rutter, W. Converting Trypsin to Chymotrypsin: Groun-State Binding Does Note Determine Substrate Specificity. *Biochemistry* **33,** 8764–8769 (1994).

54. Linding, R. *et al.* Protein disorder prediction: Implications for structural proteomics. *Structure* **11,** 1453–1459 (2003).

55. Neves Petersen, M. T., Fojan, P. & Petersen, S. B. *How do lipases and esterases work: The electrostatic contribution*. *Journal of Biotechnology* **85,** (2001).

56. Young, L., Jernigan, R. L. & Covell, D. G. A role for surface hydrophobicity in protein-protein recognition. *Protein Sci.* **3,** 717–729 (1994).

57. Tsai, C. J., Lin, S. L., Wolfson, H. J. & Nussinov, R. Studies of protein-protein interfaces: a statistical analysis of the hydrophobic effect. *Protein Sci.* **6,** 53–64 (1997).

58. Clark, A. M. & Labute, P. 2D depiction of protein - Ligand complexes. *J. Chem. Inf. Model.* **47,** 1933–1944 (2007).

59. Schopfer, L. M., Voelker, T., Bartels, C. F., Thompson, C. M. & Lockridge, O. Reaction kinetics of biotinylated organophosphorus toxicant, FP-biotin, with human acetylcholinesterase and human butyrylcholinesterase. *Chem. Res. Toxicol.* **18,** 747–754 (2005).

60. Liu, Y., Patricelli, M. P. & Cravatt, B. F. Activity-based protein profiling: the serine hydrolases. *Proc. Natl. Acad. Sci. U. S. A.* **96,** 14694–14699 (1999).

61. Chang, A. *et al.* Rational optimization of drug-target residence time: Insights from inhibitor binding to the staphylococcus aureus FabI enzyme-product complex. *Biochemistry* **52,** 4217–4228 (2013).

62. Copeland, R. A., Pompliano, D. L. & Meek, T. D. Drug–target residence time and its implications for lead optimization.

63. Hs, H. LYPLA1 Antibody Product data sheet Tested Species Reactivity. **3723,**

64. Fold, S. P., Perona, J. J. & Craik, C. S. Minireview Evolutionary Divergence of Substrate Specificity within the Chymotrypsin-like. 29987–29990 doi:10.1074/jbc.272.48.29987

65. Ring, A. Y., Sours, K. M., Lee, T. & Ahn, N. G. Distinct patterns of activation-dependent changes in conformational mobility between ERK1 and ERK2. *Int. J. Mass Spectrom.* **302,** 101–109 (2011).

66. Gray, F. L. V, Murai, M. J., Grembecka, J. & Cierpicki, T. Detection of disordered regions in globular proteins using ^{13}C-detected NMR. *Protein Sci.* **21,** 1954–60 (2012).

Chapter 4:
APT2 Modulates the Activities of Oncogenes and Tumor-Suppressors of the MAPK Pathway During Epithelial-Mesenchymal Transition

4.1 Abstract

Metastatic cancers exploit the MAPK signal transduction cascade to enable invasive outgrowth, making attractive drug targets of the molecular players within this pathway. Numerous scaffolds, including the tumor suppressor and cell polarity protein Scribble, appear to direct MAPK by assembling complexes that either increase or decrease activation of this pathway. Scrib's ability to control MAPK depends on its localization at the plasma membrane, but its localization becomes increasingly cytosolic in aggressive cancers. In the cytosolic milieu, however, Scrib now functions as a tumor-promoting factor that paradoxically includes enhancement of MAPK activity. Here, we define a molecular mechanism responsible for regulating Scrib's cellular localization and tumor-suppressor potential. We demonstrate that Scribble *S*-palmitoylation is essential for membrane engagement in epithelial cells, and that its palmitoylation is disrupted in transformed epithelial cancer cell lines. These malignant lines show skewed activity of the palmitoylation enzymes involved in attaching and detaching palmitate modification in proteins, resulting in a decrease in steady-state palmitoylation and membrane-bound Scrib. Lastly, we show that small molecule inhibition of the depalmitoylating enzyme APT2, but not APT1, restores Scrib membrane localization and suppress MAPK activity in transformed cell lines. Thioesterases may therefore regulate the palmitoylation of cell polarity proteins, including scaffolding proteins like Scrib. This work highlights a new strategy to attenuate MAPK signaling in malignant cells by restoring the activity of an associated scaffold.

Individual contributions. With a few exceptions, the majority of the work presented in this chapter was performed by me and Dr. Jeannie Hernandez. My principle investigator Dr. Brent R. Martin, conceived the project, provided funding for all the efforts described in this study, and oversaw the experimental design. Sirisha Pasupuleti helped to generate Scrib encoding epitope vectors for both transfection and transduction experiments. Margery Gang performed the localization assays of transiently expressed Scrib variants in MCF10a parent and Snail lines. Michael Sang Jun Won helped to perform the DHHC qRT-PCR measurements. Dr. Jaimeen Majmudar analyzed and processed all proteomic samples that I and Dr. Jeannie Hernandez had prepared. Dr. Jeannie Hernandez generated MDCK and MCF10a control and Snail stable cell lines, performed Scrib localization assays for all stably-generated and human-derived cancer cell lines, conducted all acyl-biotin exchange experiments and 17ODYA enrichments, designed and carried out qRT-PCR experiments, and performed, acquired and analyzed the high-content image analysis data. As for my own part in this work, I generated MDCK and MDCK-Snail lines stably expressing GFP-tagged Scrib variants, performed localization assays of stably expressed Scrib variants in MDCK parent and Snail lines, conducted the growth time course experiments, optimized the acyl biotin exchange protocol, performed the FP-biotin enrichments, carried out all EGF stimulation experiments and subsequent probing of MAPK component activities, helped to design all experiments, offered insight into the bioinformatics analysis for all proteomic data, provide a hypothesis-driven strategy for the project and write this chapter.

4.2 Introduction

The Mitogen Activated Protein Kinase (MAPK) pathway is a conserved, three-tiered phosphorylation cascade that leads to the activation of RAF, MEK, and ERK kinases in response to extracellular stimuli, resulting in transcription of genes involved in proliferation, differentiation, and apoptosis (Figure 1-24).[1,2] Enhanced MAPK activity is a signature of many cancers, making valuable drug targets of the key components that make up this pathway.[3,4] Various extracellular cues have been shown to stimulate MAPK, the most well-characterized route being executed through the Ras-coupled receptor tyrosine kinase (RTK), the epidermal growth factor receptor (EGFR).[5–7] Upon receptor activation, the necessary membrane recruitment of core MAPK proteins is promoted by an interaction between inactive cytoplasmic Raf kinases and membrane-anchored active Ras members, and culminates in a cell-wide phosphorylation cascade.[8] Although once considered a linear pipeline, MAPK phosphorylation events are now thought to receive and elicit multiple positive and negative inputs and outputs via signaling channels outside this local network.[9–13] A deeper understanding of MAPK regulation could therefore reveal useful drug targets for cancer - beyond the kinases associated with the core pathway.[14]

Scaffolding proteins like the archetypal Ste5 are well-established modulators of MAPK assembly and activation in yeast.[15] In addition to serving as a tethering platform, Ste5 and its mammalian counterparts facilitate context-specific organization by spatially confining signaling components from extraneous cellular noise.[16,17] MAPK scaffolding proteins can be thought of as signal-specific catalysts which provide additional fine-tuning of signal intensity and duration.[18–21] The leucine rich repeat (LRR) protein SHOC2 is one scaffold in mammalian cells that assembles a MAPK-specific phosphatase holoenzyme complex needed for activating Raf kinases in tumor cells.[22,23] Conversely, the LRR and PDZ (LAP) scaffold protein Scribble (Scrib) complexes to SHOC2 and antagonizes RAF1 activation by sequestering and preventing the catalytic protein phosphatase 1α (PP1α) from dephosphorylating RAF1 serine 259[24]. A molecular understanding of how scaffold complexes are coordinated is an essential component of describing the MAPK pathway in cancer.

Originally described in *D. melanogaster*, Scrib functions as a neoplastic tumor suppressor within the Scribble, Discs Large, Lethal Giant Larvae (Scrib/Dlg/Lgl) basolateral polarity complex.[25] This highly conserved complex plays a determining role in planar cell polarity, suppresses tissue outgrowth, and promotes cell adhesion in epithelial cells.[26] Importantly, Scrib's ability to suppress oncogenic signaling pathways is highly correlated with its localization at the plasma membrane, which is frequently cytosolic in highly metastatic, de-differentiated tumors that have undergone epithelial-mesenchymal transition (EMT).[27,28] EMT is a morphogenic transformation of epithelial cells into mesenchymal-like, migratory cells capable of organogenesis in development.[29,30] The process of EMT continues in adult tissues as a form of wound-healing, but disruption of the pathways that control this process could confer normal cells with developmental-like invasive properties that define metastasis.[31,32] Cytosolic Scrib appears to exchange its membrane-bound, tumor suppressor functions for pro-oncogenic traits in EMT, potentially working in synergy with constitutively active Ras to boost MAPK activity and promote proliferation and metastasis.[33,34] Notably, rescue of membrane-targeted, but not cytosolic, Scrib expression lead to a reversal of malignant EMT features in epithelial cell lines.[28,35,36] Scrib's localization at cell-junctions appears to be critical for its antitumor activities, particularly its ability to regulate MAPK.[37–39]

The precise molecular mechanisms that dictate Scrib's localization are currently unknown. Peripheral membrane proteins are typically targeted to the membrane phase through either protein interactions or post-translational modifications (PTMs) that enable direct interaction with the lipid bilayer.[40–43] The idea of a protein interaction was explored in a recent report that found the cytoskeletal protein Spectrin contributing to Scrib membrane attachment via a conserved interaction motif.[44] The collective absence of genetic mutations in the Scrib gene in malignant cancer biopsies suggests that membrane localization may be influenced by other targeting mechanisms, such as lipid modifications.[45,46] The activities of numerous scaffolding and signaling proteins, such as PSD95 and HRas, are known to be modulated by some form of lipid modification[47,48], most prominently through protein *S*-Palmitoylation. Palmitoylation is an enzymatically-driven process by which specific proteins are reversibly equipped with long-chain fatty acids via a thioester linkage to their cysteine residue(s).[49] This labile acyl moiety

enables signaling components to actively engage the cell membrane in a “switch-like” manner, intrinsically limiting or accelerating their transduction potential.[50,51] Indeed, palmitoylation is known to be a critical PTM that contributes to neurotransmission, immune response, and cell growth.[52,53]

In humans, two distinct enzyme families catalyze the attachment and removal of thioester-linked acyl moieties: the DHHC protein acyl transferase (PAT) family, which consists of 23 members sharing a catalytic Asp-His-His-Cys (DHHC) motif[54–56], and the serine hydrolases acyl protein thioesterases (APTs) 1 and 2, which oppose PATs by catalyzing the cleavage of acyl chains off of proteins.[57–59] Representatives from both enzyme families have been connected to central regulatory functions in neurological disorders and cancer.[60–62] In particular, a recent genome-wide RNAi screen found the thioesterase APT2 among likely candidates that promote oncogenic growth in a mouse model of HRasG12V-driven hyperplasia.[63] Further investigation with epithelial-derived fibroblasts transformed with HRasG12V reported the dual-APT1/2 inhibitor palmostatin B capable of suppressing MAPK signaling, leading to a partial reversion of the mesenchymal phenotype.[64] Downregulation of MAPK was attributed to disruption in the palmitoylation dynamics of Ras proteins; however, the exact APT isoform and its corresponding *in vivo* substrate(s) were not explicitly confirmed. Taken together, APTs are likely involved in MAPK regulation, suggesting that metastasis could be offset by restoring normal palmitoylation dynamics.

Here we demonstrate that Scrib is a palmitoylated protein that requires this PTM to engage the plasma membrane in epithelial cells. Furthermore, we show that APT2 controls the steady-state palmitoylation levels of Scrib but not Ras proteins, and both sets of proteins exhibit altered palmitoylation stoichiometries after EMT. We propose that Scrib’s cytosolic localization in metastatic cancers is partly due to changes in the expression of opposing palmitoylation enzymes, which heavily distorts palmitoylation equilibrium in the direction of thioester hydrolysis. We explore this hypothesis by inhibiting APT2 in induced EMT lines to restore Scrib palmitoylation, and therefore its ability to suppress aberrant MAPK signaling.

4.3 Materials and Methods

Cloning and generation of Scrib Variants. To prevent interference with putative N-terminal palmitoylation sites, we generate a C-terminal FLAG and GFP epitope tagged plasmids. To generate the GFP plasmid (here referred to as pcDNA-GFP), custom-made primers (Eurofins MWG Operon) flanked by 5'-BamHI and 3'-KpnI restriction sites were used in a polymerase chain reaction (PCR) with Phusion DNA polymerase (ThermoFisher) to amplify emerald GFP (emGFP) from a pcDNA6.2 vector (ThermoFisher) according to manufacturer's instructions. PCR products were test-digested with Fast-Digest KpnI and BamHI enzymes (ThermoFisher), and then purified by agarose gel extraction. The mammalian expression plasmid pcDNA3 (ThermoFisher) was then double-digested with BamHI and KpnI, purified by gel extraction, and ligated to emGFP digest product using T4-DNA ligase (ThermoFisher). C-terminal incorporation of GFP was confirmed by automated DNA sequencing.

The cDNA encoding full-length human Scribble gene with a cytosolic mutation in the LRR domain (P305L) was obtained from AddGene (plasmid #24601). The proline was restored by site-directed mutagenesis with custom-made primers (Eurofins) and confirmed by DNA sequencing. PCRs with custom-made 5'-HindIII and either 3'-BamHI or 3'-FLAG-BamHI primers were used to amplify full-length wild-type (WT) Scribble cDNA from the plasmid, as well as several truncated variants. The PCR products were digested with Fast-Digest HindIII and BamHI enzymes (ThermoFisher), and then purified by gel extraction. Amplified cDNAs were cloned as described before into either parent pcDNA3 or our custom-made pcDNA3-GFP vectors to produce both GFP and FLAG C-terminally tagged Scrib constructs.

To generate Scrib viral plasmids, the epitope-tagged Scrib variants were sub-cloned into a modified pCLNCX viral plasmid (Novus Biologicals, here referred to as pCLHCX) in which the neomycin resistance gene was swapped for a hygromycin resistance gene[65], enabling differential selection of mammalian cells for stable expression of two genes under hygromycin B and geneticin selections as described next.

Cell culture, transfection, and development of stable lines. Patient-derived stable cell lines were obtained from ATCC and cultured according to published

recommendations. Madin-Darby Canine Kidney (MDCK) and MCF10a were a generous gift from Dr. Ben Margolis (University of Michigan, Department of Internal Medicine). To generate virus encoding the transcriptional repressor Snail, 293T cells were utilized as a packaging medium and transfected with 2.5 µg total plasmid DNA comprised of equal parts of pVSVG (Clontech) and pGAG/Pol (Cell Biolabs), and pPGS-hSnail-NEO (also gifted by Dr. Ben Margolis), a neomycin-selectable plasmid encoding human FLAG-tagged Snail under the control of a CMV promoter. The medium was changed 24 hours post-transfection, harvested 48h post-transfection and filtered through a 0.45 µm filter unit fitted to a Luer-lock syringe to remove traces of packaging cells and debris. The filtered medium was then supplemented with 8 µg/ml polybrene (Sigma) to increase infection of target lines with the virus. The medium was then added to sub-confluent MDCK and MCF10a. Cells were allowed to grow to confluency and then passaged in medium containing 0.6 mg/ml G418 (Gibco). Following the same protocol described for developing Snail lines, epithelial parental lines and their Snail derivatives were transduced with pCLHCX containing cDNAs encoding WT, P305L and truncated constructs of Scrib. To develop a stable over-expressing line, 48h post-infection, cells were passaged in medium containing 150 µg/ml Hygromycin B (Sigma). For transient expression studies, 293T or MCF10a cells were cultured in 6 cm-diameter dishes to 25% confluence. Cells at ~40% confluency were transfected using FugeneHD (Promega) according to manufacturer's instructions. Briefly, in sterile 1.5mL conical tubes, 2 µg of pcDNA-FLAG and pcDNA-GFP vectors were complexed with 3% v/v FugeneHD transfection reagent in a total of 200 µL of Opti-MEM (Gibco) and solution was incubated for 15 minutes at room temperature. The mixture was then added to Cells which were experimented and harvested 48h post-transfection.

siRNA-mediated knockdowns. MCF10a and MDCK cells were seeded into 6 cm-diameter dishes and grown in their respective complete growth media. Cells at ~50% confluency were transfected with predesigned siRNA pools (Dharmacon, ON-TARGETplus P/N L-010007-00-0005, L-009256-00-0005 and D-001810-10-05) according to manufacturer's recommendations (GE Healthcare). Briefly, in sterile 1.5mL conical tubes,125nM of siRNA pool was complexed with 1.25% v/v transfection reagent (DharmaFECT Dharmacon T-2005) in a total of 800 µL of Opti-MEM (Gibco) and

solution was incubated for 5 minutes at room temperature. The mixture was then further diluted 5-fold into the appropriate complete growth medium to a final volume of 4mL.Cells were washed with 1mL of DPBS (Gibco) and transfected with Dahrmafect-complexed siRNAs (4mL total) and were cultured for 48 before experimentations.

EGF stimulation assays. Cells were seeded at 20-25% confluency into 6 cm-diameter plates and cultured in their respective complete media modified with the corresponding dialyzed sera. After 24 hours, the medium was supplemented with final concentrations of either 5 µM inhibitor or 0.1% v/v vehicle (DMSO), and cells were allowed to grow overnight. The next day, the cells were washed with DPBS (Gibco) and cultured in basal medium lacking all supplements for 1-2 hours. Cells were treated with either vehicle (DPBS) or 20 ng/mL human recombinant EGF (Shenandoah-BT, P/N 100-26-AF) for either 5 minutes or up to a 120 minute stimulation time course. Cells were washed with DPBS, harvested at designated time points, then immediately lysed in 20 g/L SDS and 62.5 mM Tris pH 7.4 lysis buffer to disrupt all enzymatic activity. Sample protein concentrations were quantified using the DC protein assay (Bio-Rad) and then processed for western blot analysis of target proteins.

Immunofluorescence. For live cell imaging, parent and Snail MDCK and MCF10a lines stably expressing Scrib variants were grown to sub-confluency and were imaged on a Nikon Eclipse TE2000-S inverted microscope customized with laser sources and filters appropriate for DAPI, GFP and mCherry fluorescence imaging. For fixed cell imaging, MDCK and MCF10a parent and stably-overexpressed Snail lines were plated onto glass coverslips, placed into 12-well plates and treated overnight with either DMSO vehicle or indicated final concentrations of inhibitors at 0.1% v/v final DMSO concentration. The following day, confluent cells were fixed with ice cold methanol for 10 minutes, followed by a 1 minute wash with ice cold 100% acetone. Coverslips were washed once with PBS, then incubated with gentle agitation in SuperBlock (ThermoScientific, P/N 37515) for 15 minutes. Coverslips were then incubated for at least 24 hours at 4 ^{o}C in primary antibody solutions containing species-controlled combinations of the following antibodies in PBS supplemented with 0.3% v/v Triton X-100 (PBST): goat-anti-Scribble (SCBT, P/N sc1149) diluted 1:200, mouse-anti-N-cadherin (BD Bioscience, P/N 10920) diluted 1:250 and mouse-anti-E-cadherin (BD

Bioscience, P/N 610181) diluted 1:250. After primary antibody incubation, coverslips were washed 3 times for 5 minutes each in PBST. The coverslips were then incubated in species-matched, species-controlled AlexaFluor secondaries diluted in PBST for an additional hour at room temperature, protected from light. The coverslips were then washed, stained with DAPI, and washed an additional two times before mounting onto slides with Fluoromount (Sigma, P/N F4680). Images were obtained using the above Nikon epifluorescent microscope.

High-content fluorescence imaging microscopy. Cells were plated at identical conditions as described above onto either 384-well or 96-well PerkinElmer ViewPlates using sterile cassettes of a Thermo MultiDrop Dispenser. APT1 and APT2 inhibitors were titrated and diluted in complete medium with dialyzed serum before adding to sub-confluent cells using either MultiDrop Dispenser or automated program on a Rainin Multichannel pipettor. Cells were fixed after inhibitor incubation with either cold methanol/acetone as described above, or with 4% PFA supplemented with 1% Triton X-100 in PBS to permeabilize samples for staining. Immunofluorescence was performed as described above, with the exception of the mounting step. In the multi-well plates, PBS was added to half the volume of the well before imaging. Automated imaging was performed on the Molecular Devices ImageXpress Micro XLS High-Content Analysis System. 3-5 pre-defined regions per well were imaged and quantified using a custom MetaXpress analysis module that defined cell boundaries one of two ways: (1) First a cell-scoring watershed algorithm was used to identify cell boundaries by specifying individual cells based on the correspondence of their nuclear DAPI signal with a diffusive positive cell marker. For Snail cells, this diffusive marker was defined as that originating from the cytosolic Scrib signal recorded by the AlexaFluor 488 secondary. The cell boundary thickness was defined by standard graphical grow and shrink logical operations which set this value between 2-5μm to effectively account for Scrib cell perimeter colocalization. All positive Scrib signals were thresholded based on vehicle-treated wells such that any pixel value intensity that fell below the noise and above the saturation level were set to 0 while all remaining pixel values were given a value of 1. Thus, total Scrib signal and fractional cytosolic and membrane quantities were calculated per cell, averaged across cells per condition and errors were computed as

the standard deviations of the mean values. The membrane fraction values calculated for vehicle-treated cells were defined as the basal value for statistical comparisons to compound-treated or knock-down cells. (2) We also quantified Scrib signal at the membrane by measuring co-localization with a membrane-bound protein, although this initially presented some challenges because the expression and localization of so many proteins are heavily altered upon Snail induction. Using un-enriched SILAC proteomics to compare protein abundances between empty vector (EV) and Snail cell lines, we found the membrane-bound Na^{+}/K^{++} ATPase pump α-1 subunit did not change in expression levels after EMT induction (data not shown). The monoclonal mouse antibody directed to this subunit (Millipore, P/N 05-369) was used at 1:500 in PBST for immunofluorescence in combination with goat-anti-Scrib and DAPI. Co-localization of Scrib with ATPase was obtained by measuring the overlap of their corresponding thresholded values which were generated as described earlier. Data obtained from these two separate analytical workflows were pooled and imported into GraphPad Prism 6 for nonlinear regression analysis. Scrib membrane fraction was plotted as a function of Log_{10} drug concentration to generate a dose-response curve which was fit to the following 4-parameter logistic curve:

$$F_{membrane} = min + \frac{max - min}{1 + 10^{(LogEC_{50} - [I]) \times Slope}} \qquad \textit{Equation 5}$$

Where $F_{membrane}$ is defined as the fraction of Scrib's signal at the membrane, *min* is $F_{membrane}$ of MDCK-Snail line without drug treatment, *max* is the limit of $F_{membrane}$ as the drug concentration approaches infinity, Slope is the steepness associated with the dose-response curve and EC_{50} is the concentration of drug that provokes a response halfway between the baseline (*min*) and maximum response (*max*).

Western blot analyses. Frozen cell pellets collected from confluent plates were resuspended in PBS (Gibco), and then lysed by ultrasonic cavitation with a sonicator probe. The protein concentrations were determined by the DC protein assay (Bio-Rad), and for each sample processed, 15-25 µg of protein was separated by SDS-PAGE on home-made[66] 8% or 12% polyacrylamide gels for 1 hour at 180V. The proteins were then transferred to a methanol-activated PVDF membrane (Millipore) for 2 hours at 75V[67]. After complete transfer, the membrane was blocked with 50 g/L of either non-fat

Milk of BSA (Fisher) in Tris-buffered saline supplemented with 0.5% v/v Tween20 (TBST) for 1 hour at room temperature. The membranes were then incubated overnight on a rotisserie at 4 ^{o}C with the following primary antibody solutions prepared in TBST supplemented with 50 g/L of either milk or BSA according to manufacturer's recommendations: Mouse-anti-Scribble (Millipore, P/N MAB1820) diluted 1:500, mouse-anti-E-cadherin (BD Bioscience, P/N 610181) diluted 1:5000, mouse-anti-αTubulin (Sigma, P/N T6074) diluted 1:2000, mouse-anti-FLAG M2 (Sigma, P/N F1804) diluted to 1:5000, rabbit-anti-LYPLA2 (Pierce, P/N PA5-27653) diluted 1:500, rabbit-anti-p259.Raf1 (Cell Signaling Tech., P/N 4694) diluted 1:500, rabbit-anti-p338.Raf1(Cell Signaling Tech., P/N 9427) diluted 1:500, mouse-anti-panRas (Millipore, P/N 50-171-675) diluted 1:1000, mouse-anti-Mek1/2 (Cell Signaling Tech., P/N 4694) diluted 1:500 and rabbit-anti-pMek1/2 (Cell Signaling Tech., P/N 9154) diluted 1:500. Membranes were washed thrice with TBST and blots were incubated with appropriate TBST solutions of goat and donkey AlexaFluor fluorescent secondary antibodies (ThermoFisher) diluted according to manufacturer's recommendations. The blots were washed thrice then scanned on a Typhoon Phosphoimager (GE Healthcare) using 488nm, 532nm, 633nm excitation laser and appropriate emission filters.

Acyl-Biotin Exchange. Overexpressed or compound-treated cells were lysed and quantified at high proteome concentrations, then whole cell proteomes were diluted to 5 mg/mL in 40 g/L final SDS in DPBS with a resulting pH around 6. Proteins were alkylated with 50 mM final N-ethyl maleimide for 2 hours at room temperature with rotation, then excess NEM was methanol-chloroform extracted and thoroughly washed with methanol before proceeding. Samples were re-suspended in DPBS and thioesters were cleaved by boiling samples at 95 ^{o}C for 5 minutes in the presence of either neutralized NH_2OH (+, 500 mM final) or NaCl (-, 500 mM final). Both + and - samples were immediately extracted by methanol-chloroform, thoroughly washed with methanol, then resuspended in 20 g/L SDS in DPBS and reacted with 200 µM final biotin-PEG-maleimide probe (Click Chemistry Tools) to capture newly-liberated thiols. Samples were incubated with the probe for 90 minutes at room temperature with end-over-end rotation before the final methanol-chloroform precipitation to remove excess probe, then resuspended in 10 g/L SDS w/v in DPBS and quantified. 40-60ug of proteome from

each sample was saved for loading onto one or two lanes of denaturing polyacrylamide gels. 0.5-1 mg/mL of proteomes were then combined with 20uL of streptavidin agarose (Millipore) in 200 µL final of 2.5 g/L SDS in DPBS and the suspensions were incubated for 90 minutes at room temperature with end-over-end rotation. The resin was washed with 200 µL of 2 g/L SDS in DPBS 4 times and then with 200 µL of DPBS twice. The resin was resuspended in 2 resin volumes of 1x Laemmli sample buffer and boiled for 10 minutes at 95 ^{o}C to denature and elute proteins off the resin. The samples were spun down at 2000 rcf for 30 seconds, the supernatants were loaded on homemade 8% and 12% denaturing polyacrylamide gels for SDS-PAGE separation and western blot analysis.

qRT-PCR measurements. Total RNA was extracted from parental and Snail MCF10a cell lines using Trizol reagent (Invitrogen) according to manufacturer's recommendations. Equal amounts of only high-quality RNA template were reverse-transcribed using iScriptTM Advanced cDNA Synthesis Kit (Bio-Rad), and equal volumes of cDNAs were loaded onto a customized 96-well qPCR plates containing Prime PCR Assay primers to genes of interest (Bio-Rad). SsoAdvanced Universal SYBR Green Supermix (Bio-Rad) was used for qPCR amplification. All samples were run as three biological replicates, each analyzed in triplicate. qPCR reactions were measured on a StepOne Plus instrument (Applied Biosystems) using SYBR Green detection. Baselines, thresholds, and Ct values were computed according to Applied Biosystems recommendations. All cycle threshold (Ct) values were normalized to that of the ß-actin housekeeping gene expression, which protein levels were found to be identical between parent and Snail lines. The relative expression level for each gene of interest was determined using the $2^{-\Delta\Delta-C}{}_{T}$ method[68], and all transcript fold-changes were calculated relative to the parent line.

17ODYA-enriched proteomic sample preparation. Stable isotopic labeling of amino acids in cell culture (SILAC) proteomics was used to measure palmitoylation changes upon induction of EMT with the oncogene Snail. Briefly, heavy and light isotopically-labeled MCF10a parent and Snail cells were generated by 10 sequential passages in SILAC DMEM-F12 complete growth media prepared from basal DMEM:F12 deficient in both L-lysine and L-arginine (Thermo, P/N 88215) supplemented

with 5% v/v dialyzed horse serum (Valley Biomedical, P/N NC9739549), 20 ng/mL recombinant human EGF (Shenandoah-BT, P/N 100-26AF), 0.5 mg/L cortisol (Sigma, P/N H0888), 0.1 mg/L CTX (Sigma, P/N C8052), 10 mg/L insulin (Gibco, P/N12585) and 1X pen-strep (Gibco, P/N 15140). Isotopic heavy and light lysine and arginine amino acids were then added to a final concentration of 100 mg/mL to generate SILAC-light and SILAC-heavy media, respectively. Sub-confluent 15 cm-diameter plates for each cell line were treated overnight with compounds directed against APT1 and APT2[69]. The following day, near-confluent cells were incubated with 20 µM final of the alkyne fatty acid 17-octadecynoic acid (17-ODYA, Cayman Chemical, N/P 90270) for 6 hours. Cells were then washed in DPBS, harvested and lysed by sonication in DPBS supplemented with 1 µM HDFP. Samples were fractionated by ultracentrifugation at 100,000 x g at 4 ^{0}C, the supernatant was discarded and the insoluble fraction was resolubilized by sonication in DPBS. Protein concentrations were measure using the DC protein assay (Bio-Rad) and isotopic lysates were combined 1:1 molar ratio in both heavy and light directions, i.e. heavy(EV):light(Snail) and heavy(Snail):light(EV). Samples were diluted in PBS and then reacted at 5 mg/mL with the following Click reagents: 1mM final copper sulfate, 1mM tris(2-carboxyethyl)phosphine (TCEP, Sigma, N/P 93284), 17uM final Tris[(1-benzyl-1H-1,2,3-triazol-4-yl)methyl]amine (TBTA, Sigma, N/P 678937) ligand, and 500 µM final biotin-azide[70]. Samples were incubated with agitation for 1 hour at room temperature, then proteins were methanol-chloroform extracted[71] to remove unreacted Click reagents. Proteins were resuspended to 1 mg/mL in 2 g/L SDS in DPBS with 6 M urea (2SB). Disulfides were reduced with 10 mM final neutralized TCEP, then liberated thiols were capped by alkylation with 50 mM N-ethyl-maleimide (NEM). SILAC pairs were then diluted 10-fold in (2SB) and 10% final volume of pre-washed streptavidin resin was added to each tube, followed by 1 hour of end-over-end rotation at room temperature. The resin was then washed twice with 10 resin volumes of 2SB and four additional washes with 10 resin volumes of PBS to eliminate SDS. Cleared resin was resuspended in 2 M urea, 25 mM ammonium bicarbonate, 100mM CaCl2, and 1ug of sequencing-grade Trypsin (Promega) *per* 1mg total proteome starting material. The samples were moved to a shaker at 37C for 4 hours. The resin and two additional resin washes were pelleted and supernatants were lyophilized on a Savant

SpeedVac concentrator before being resuspended in LCMS buffer containing mass spectrometry-grade 5-20 fmol alcohol dehydrogenase (ADH, Waters, P/N 186002328) 20 mM ammonium bicarbonate (Sigma), 3% v/v acetonitrile, 0.1 % v/v formic acid, pH 10.

Serine hydrolase-enriched proteomic sample preparation. The serine hydrolase profiles of MCF10a parent and Snail lines were measured by using FP-PEG-Biotin activity-based probe to enrich enzymes across SILAC-generated cell lines as described previously[70]. SILAC lines were made as described earlier and cells were seeded into 15 cm-diameter plates. Confluent cell dishes were washed with DPBS and harvested into 1.5mL conical tubes. Cell pellets were lysed in DPBS by ultrasonication and protein concentrations were measured by the DC protein assay (Bio-Rad). Isotopic proteome pairs of EV and Snail lines were combined in 1:1 molar ratio to yield 1mL of 1 mg/mL proteome which was reacted with 5µM FP-PEG-biotin for 1 hour at room temperature with agitation. The proteome was then chloroform-methanol extracted thoroughly to remove excess free probe and the precipitate was resolubilized in 1mL 10g/L SDS in DPBS. Proteome was diluted further in DPBS to a final SDS concentration of 1 g/L before mixing with 100uL of streptavidin agarose for biotin enrichment. The subsequent washes, Trypsinization, and clean-up steps were all performed as described above for the 17ODYA-enriched proteomic sample prep.

Mass Spectrometry and Data Analysis. Tryptic digests were separated using a Waters NanoAcquity UPLC system equipped with a 5 µm Symmetry C_{18} (180 µm × 20 mm) trap column and a 1.8 µm high-strength silica (HSS-T3) analytical column (75 µm × 150 mm) heated to 35 °C coupled to a picotip emitter (New Objective). Tryptic peptides were loaded onto the trap column over 3 min, followed by analytical separation over a 90 min gradient (3% ACN to 40% ACN over 90 min). Peptides were analyzed using a Waters Synapt G2S HDMS time-of-flight mass spectrometer with ion mobility separation and data independent fragmentation algorithms. The quadruple mass analyzer was manually set for mass 500, 600, and 700. The sampling cone was adjusted to 32 eV, and the nano flow gas was set to flow at 0.2 bar. The purge gas was set to flow at 50 L/h, and the source temperature was set at 70 °C. For all measurements, the mass spectrometer was operated in V-mode (resolution mode) with a resolving power of at

least 20 000 fwhm (full width at half-maximum) in positive-mode ESI. The time-of-flight analyzer of the mass spectrometer was calibrated with a 100 fmol/μL solution of [Glu1]-fibrinopeptide B from *m*/*z* 50–1250 to within 0.5 ppm. The data were corrected in postacquisition analysis using the doubly charged monoisotopic ion of [Glu1]-fibrinopeptide B (*m*/*z* = 785.8426) collected every 30 s from a separate calibrant fluidics source coupled to a tapertip emitter (New Objective). Accurate mass data were collected in data-independent acquisition (DIA) mode in combination with in-line ion mobility separation (IMS). For IMS, the wave height was set as 40 V and IMS wave velocity as 600 m/s. The spectral acquisition time in each mode was 0.5 s. In low-energy MS mode, data were collected without applying collision energy in the trap or the transfer stage. A collision energy (CE) ramp from 15–45 eV during each 0.5 s integration was used as standard setting for the elevated energy MS scan in the transfer region for HDMS^E mode. LC–MS spectra were collected in continuum mode and searched using the ProteinLynx Global SERVER version 3.0.2 (Waters) against the reviewed human reference proteome (UniProtKB downloaded on 2014–08–01). Precursor- and fragment-ion mass tolerances were automatically determined by PLGS 3.0.2 based on the following search criteria: (i) trypsin as digestion enzyme, (ii) a maximum of one missed cleavage, (iii) lysine (+8) or arginine (+10) defined as fixed modifier reagent group, (iv) carbamidomethyl cysteine as a fixed modification and methionine oxidation as the variable modification, (v) a minimum of two identified fragment ions per peptide and a minimum of five fragments per protein, and (vi) at least two identified peptides/protein. The false discovery rate (FDR) for peptide and protein identification was set at 1% using a reversed database. By using in-house Python scripts, all data from technical and biological replicates were merged by removing any precursors greater than ± 10 ppm in mass difference from the calculated theoretical mass. SILAC ratios were computed based on MS1 intensities of the SILAC precursor pairs. All reported ratios in the manuscript are consolidated ratios from runs in each direction and from merging technical replicates.

4.4 Results

Scrib membrane localization correlates with hyper-activated MAPK pathway in metastatic cancer lines. Scrib's cytoplasmic localization is prevalent in progressive, malignant carcinomas, particularly those already initiating a full-fledged EMT program. As such, we sought to develop and investigate cell lines that model Scrib's cellular localization before and after induction of EMT. We first profiled a number of patient-derived, stable cell lines to assess their level of malignancy and their degree of Scrib mislocalization. We expected an inverse correlation between metastatic potential and the expression of E-cadherin (E-cad), a cell adhesion protein indicative of differentiated epithelia.[72] Aggressive cancers typically show complete loss of E-cad, although its loss is not universally correlated across all cancer EMT lines.[73] The more differentiated, benign cell lines like SW1990 and MCF10a showed strong co-localization of E-cad and Scrib at the plasma membrane. More aggressive lines like MDA-MB-231 and OVCAR3 expressed virtually no E-cad, and Scrib expression appeared predominantly cytosolic. Interestingly, the mutant KRas-driven metastatic Panc1 line[74] is positive for E-cad, but exhibits Scrib localization that is diffuse within the cytosol. Thus, Panc1 line demonstrates that Scrib membrane targeting is independent of E-cad expression (Figure 4-1A) and hence other perturbations during EMT are likely to account for its localization.

Madin-Darby Canine Kidney (MDCK) and MCF10a human breast epithelial cell lines were chosen for further examination of EMT-induced changes due to their defined epithelial morphology and the ability to resolve, by immunofluorescence, whether Scrib is localized at the membrane or cytosol. Corresponding EMT cell models were generated through stable overexpression of the oncogenic transcription factor Snail.[75] Snail expression positively correlates with activation of epigenetic circuits involved in EMT[76], namely the transcriptional repression of E-cad, and causes cells to adopt a mesenchymal-like morphology with signatures of late-stage malignant tumors[77]. After selection in G418, the resulting empty vector (EV) control and Snail lines were analyzed for E-cad and Scrib expression and cellular localization. MDCK and MCF10a EV lines expressed high levels of E-cad, which co-localized with Scrib at the cell peripheries. MDCK-Snail and MCF10a-Snail lines exhibited pronounced spindle-like morphology

and showed a complete loss of E-cad expression, confirming initiation of the EMT program. Importantly, Snail cells displayed a redistribution of Scrib from the membrane to the cytosol, while overall expression levels decreased only slightly (Figure 4-1B and C).

Mislocalization of Scrib in metastatic cancers is frequently accompanied by hyperactivation of growth pathways, namely the MAPK cascade[27]. We therefore aimed to compare specific nodes of activation and de-activation before and after EMT to confirm that these cell models could recapitulate the scenario observed in malignancy. The signal intensity and duration of several MAPK components were assessed in Snail and EV-derived lines by a serum starvation period followed by brief stimulation with EGF to trigger the MAPK cascade. In all EV lines examined, EGF treatment resulted in little to no detectable levels of pMEK1/2 (S217/S221) and pS338-RAF1. In contrast, the Snail lines were much more responsive to EGF, exhibiting about 3- and 5-fold enhancement in active RAF1, and MEK1/2 levels after stimulation (Figure 4-1D). These observations may be attributed to changes in gene expression induced by EMT, leading to upregulation of activators (e.g. SHOC2) or downregulation of repressors of MAPK. Both EMT lines interestingly displayed overall reductions in total Ras expression as detected with pan-Ras antibody, in spite of enhanced EGF-response of its downstream effectors. This result supports the idea of a Snail transcriptional program that silences the expression of MAPK-antagonizers, rendering the cascade increasingly excitable.

Scrib has been shown to suppress MAPK by directly interacting with ERK via two highly conserved kinase interaction motif (KIM) docking sites.[78,79] This association is necessary for ERK-mediated phosphorylation of two distinct serine residues of Scrib, one of which is located within Scrib's second PDZ domain (PDZ-2)[80]. We found a commercial monoclonal antibody raised against Scrib PDZ-2 to be highly sensitive to chemical modifications within this target antigenic epitope, and therefore could serve as a reporter of any dynamic changes specific to this domain, such as its phosphorylation state. To establish whether a link may exist between MAPK hyperactivation and mis-regulation of Scrib in EMT, we use this antibody to monitor EGF-induced posttranslational changes in Scrib's PDZ-2 in the

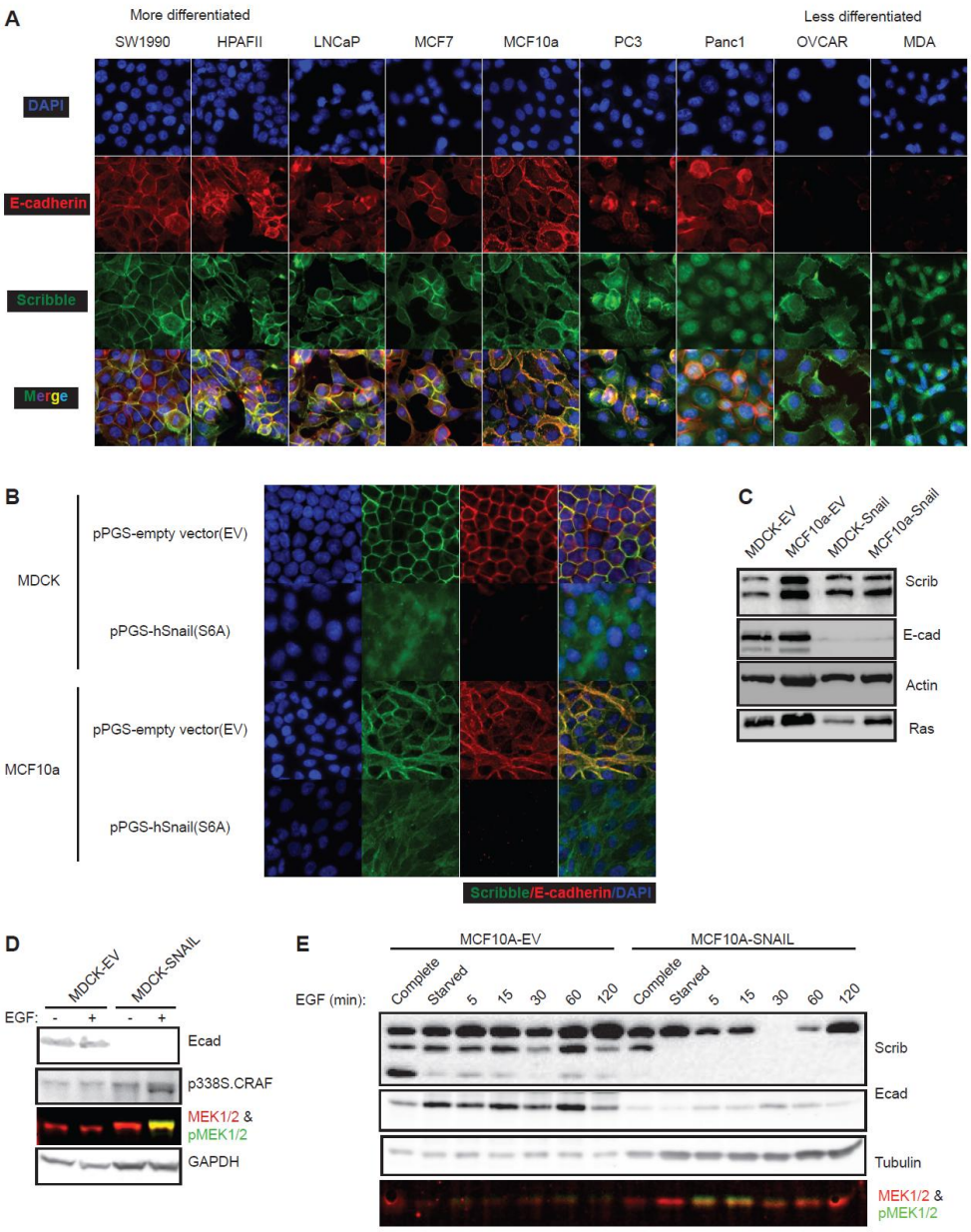

Figure 4-1 Cell models of EMT show a common theme where Scrib cytoplasmic localization coincides with elevated MAPK activation.

a. *Immunofluorescnece analysis of patient-derived stable cell lines show correlation between increasing metastatic markers and Scrib localization.*
b. *Snail-induced EMT program in model epithelial cells results in predominant cytoplasmic relocalization of the polarity tumor suppressor Scrib.*
c. *EMT changes induce a marked decrease in overall Ras isoforms but not Scrib levels. Ras protein expression level was probed by a pan H-, N- and K-Ras4B monoclonal antibody.*
d. *Snail EMT program results in increased MAPK output signified by elevated MEK1/2, CRAF activities in MDCK-pPGS/Snail.*
e. *MCF10a-pPGS/Snail EGF stimulation time course also displays enhanced MAPK signaling accompanied by concomitant post-translational modification of Scrib's second PDZ domain.*

background of a MEK1/2 stimulation time course. As expected, EGF treatment of serum-starved MCF10a-EV cells did not elicit detectable levels of phosphorylated MEK1/2; however, a stable signal was observed for Scrib PDZ-2, indicating that this domain was not modified in response to EGF in these cells. On the other hand, EGF-stimulated MCF10a-Snail cells exhibited MEK1/2 activity throughout the time course, with phosphorylation detectable between 5 to 30 minutes post treatment. Interestingly, the Snail line also demonstrated corresponding time-dependent changes in the Scrib phosphorylation, which disappeared completely at the peak of MEK1/2 activation and returned as MEK1/2 activation plateaued to basal levels (Figure 4-1E). Importantly, the interplay observed between PDZ-2 and MEK1/2 occurs only after Snail-induced malignancy, suggesting that the cellular response to EGF changes significantly upon in EMT, when Scrib is in the cytosol. Mis-localization of Scrib to the cytosol creates a dominant-negative effect, where this protein's ability to repress MAPK is lost in malignant cells. This is reasonable, since the MAPK cascade affects the activation of Snail family transcription factors[81], and EMT is thought to exploit this signaling pathway to abolish growth suppression.

Scrib is palmitoylated and requires this PTM for membrane localization and tumor suppressor function. Scrib is a member of the leucine rich repeat (LRR) and PSD95/DLG1/ZO1 (PDZ) family of proteins, also known as LAP proteins, which includes three additional members, Lano, Densin and Erbin (Figure 4-2A).[82,83] This multi-functional family of scaffolds is characterized by sixteen N-terminal LRRs and four C-terminal PDZ domains, which account for over a dozen combinatorial protein-protein interactions involved in a plethora of physiological activities.[84,85] Multiple sequence alignments of the N-terminal region upstream of the first LRR display significant sequence homology, highlighting conserved residues that may be functionally important for LAP proteins (Figure 4-2A). Erbin and Densin both require palmitoylation of their N-terminal cysteine residues for proper membrane targeting and function.[86,87] N-terminal *S*-palmitoylation of the close relative Scrib, however, has not been biochemically verified, although the Scrib protein has appeared in a number of palmitoylation proteomic data sets.[70,88] To test whether Scrib N-terminus was essential for its membrane association, we generated plasmids encoding wild type Scrib (WT) along

with the known cytosolic LRR point-mutant (P305L)[89], and a truncated variant missing the first 22 residues (Δ22) containing the three N-terminal cysteine residues C4, C10 and C22, the first two of which being the hypothetical palmitoylation sites based on sequence homology with Erbin and Densin (Figure 4-2A). GFP-tagged Scrib variants were transfected into both MDCK and MCF10a EV cells, and *in vivo* localization of variants were assessed by fluorescence microscopy. WT appeared predominantly at cell membranes and faintly within the cytosol, while the P305L and Δ22 mutants were located entirely within the cytosol (Figure 4-2B), suggesting the N-terminus of Scrib is required for membrane-localization.

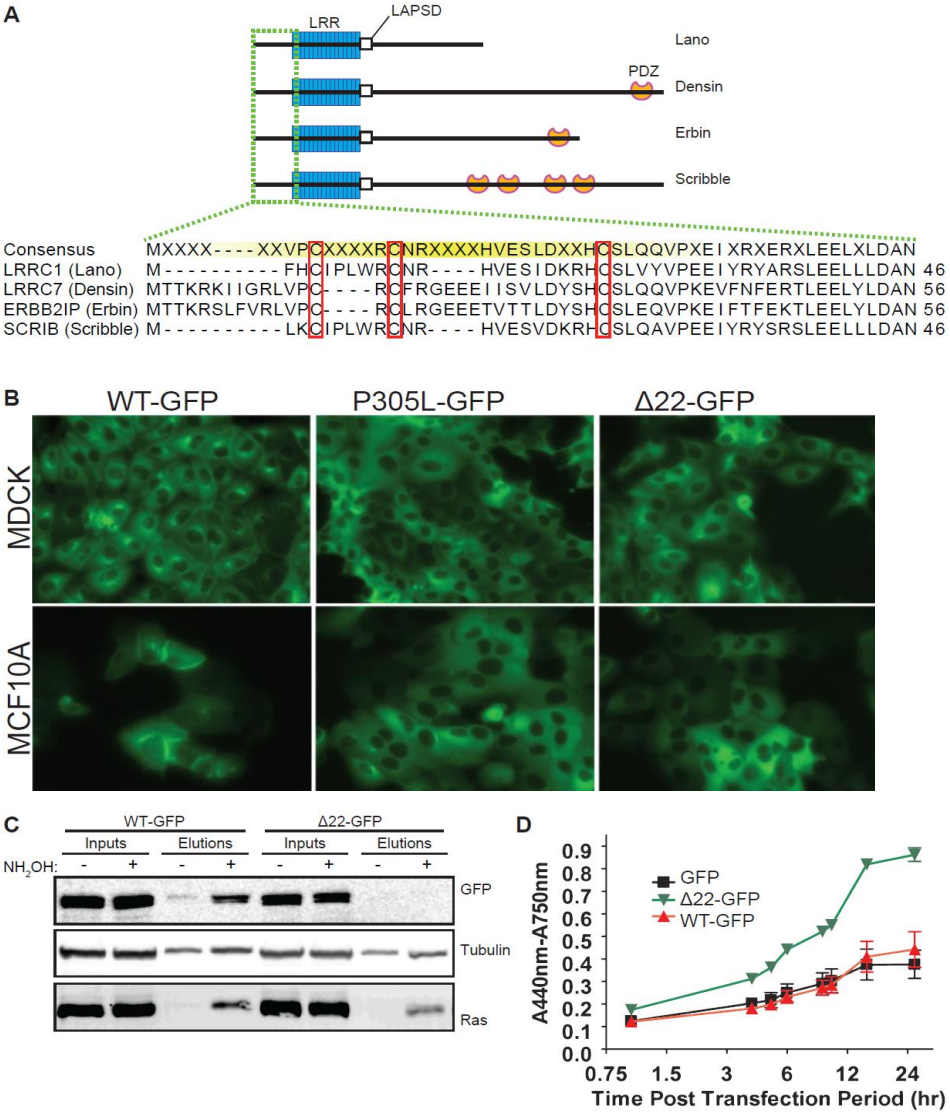

Figure 4-2 Scrib is palmitoylated, which is required for proper membrane localization and tumor suppressor function in epithelial cell models.

a. *Multiple sequence alignment and modular domain organization of LAP family members highlight additional conserve regions upstream of LRR domain suggesting that N-terminal cysteines of Scrib are palmitoylated in vivo.*
b. *GFP-tagged Scrib variants demonstrate that both N-terminus and intact LRR are required for proper membrane localization in MDCK and MCF10a.*
c. *GFP-tagged Scrib variants show that both N-terminus and intact LRR are required for palmitoylation. ABE shows loss of palmitoylation in Δ22.Scrib-GFP compared to wild-type.*
d. *Transiently expressed cytoplasmic Scrib variants lead to increased cell proliferation in MCF10a cells corroborated by various studies of cytosolic Scrib mutants. Cell proliferation was measured via the WST-1 assay (ref) which correlates the light absorbance of the WST1 probe to the approximate density of cells present in the dish, hence the A440nm-A750nm measurement.*

To test whether Scrib was palmitoylated and determine if the first 22 residues contained the sites of this PTM, we transfected WT and Δ22 GFP variants into HEK-293T cells and assessed their palmitoylation levels using a modified acyl-biotin exchange protocol[71]. After cell lysis, free thiols were alkylated with N-ethylmaleimide (NEM), followed by hydrolysis of thioester-linked fatty acids with hydroxylamine (NH_2OH). Newly liberated thiols can then be captured with an NEM-functionalized biotin probe and enriched on streptavidin agarose. In the absence of NH_2OH, the thioesterified proteins are left intact and therefore not enriched in the process. This control condition was used to account for non-specific biotin labeling and streptavidin binding during enrichment. Both (+) and (-) NH_2OH samples were reacted with the maleimide-biotin affinity probe, and all newly-generated free thiols in the NH_2OH treatment were captured by streptavidin agarose. The attached proteins were eluted off in strongly denaturing SDS loading buffer and loaded on SDS-PAGE for analysis by western blot. Only WT and not Δ22 Scrib was seen in the elution with NH_2OH, suggesting the N-terminus of Scrib is required for palmitoylation (Figure 4-2C).

Many reports cite that mislocalized Scrib can enhance tumorigenesis by activating growth signals of the Akt/mTOR/S6K and MAPK pathways.[39,90–92] We assessed whether introduction of our cytosolic Scrib mutants in a benign cell line like MCF10a was sufficient to replicate the growth phenotypes of malignant cancers. MCF10a cells were transiently transfected with GFP constructs expressing WT, P305L, or Δ22 Scrib variants. The cytosolic Scrib variants significantly accelerated MCF10a proliferation as measured by WST1 metabolic assay, while growth of cells expressing

the WT protein did not change compared to empty vector transfection control (Figure 4-2D).

Snail-induced EMT alters palmitoylation machinery in favor of thioester hydrolysis. A large number of signaling proteins undergo post-translational modification by reversible palmitoylation, which fundamentally contributes to their cellular activity.[93–96]

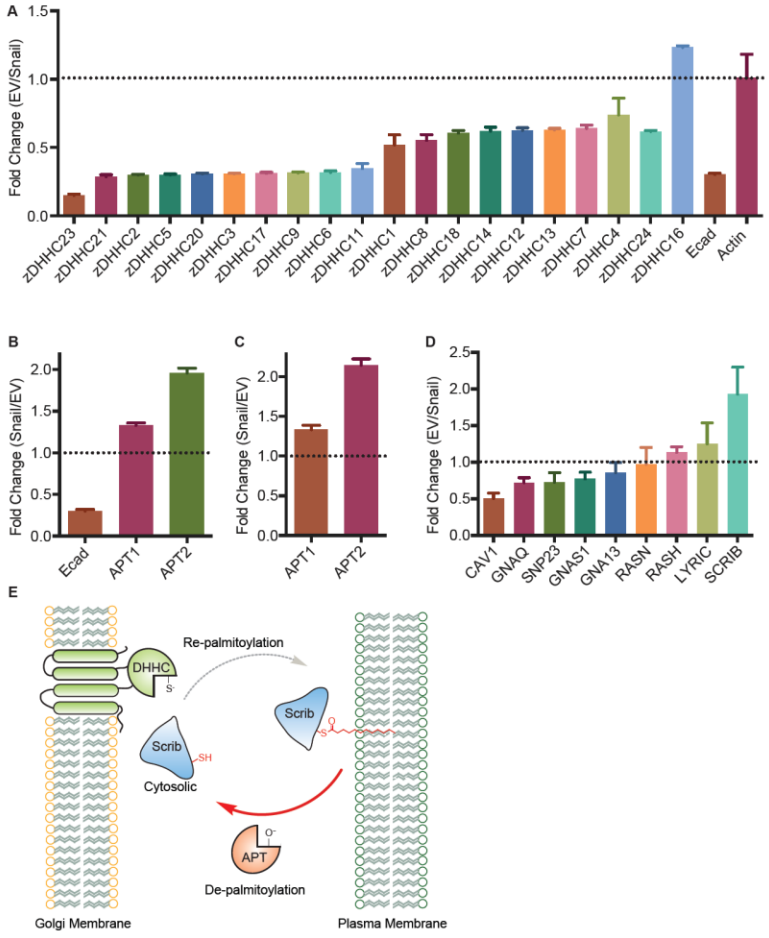

Figure 4-3 Snail-induced EMT causes a transcriptional imbalance in the expression of the palmitoylation machinery.

a. *qPCR demonstrates that DHHC expression decreased across the board in MCF10a*
b. *qPCR suggests that APT1 and 2 transcripts are elevated in MCF10a-Snail*
c. *Potentially elevated serine hydrolases upon Snail induction are confirmed by ABPP SILAC in MCF10a proteomics.*
d. *17ODYA-enriched proteomics reveals a decrease in steady-state palmitoylation of Scrib in MCF10a-Snail.*
e. *Model by which Scrib palmitoylation may have decreased in malignant cancer cells*

These dynamic palmitoylation events demand an exquisitely tuned cycle of de-palmitoylation/re-palmitoylation, allowing the protein to localize appropriately during the course of signal transmission.[59] Indeed, disrupted palmitoylation dynamics in Ras isoforms have been shown to alter MAPK signal transduction.[97,98] We therefore conjectured that EMT programs may distort palmitoylation equilibrium by biasing the expression profile of the palmitoylation machinery and in turn drive Scrib off the membrane. To test this hypothesis in the Snail-induced model, we determined the relative expression levels of enzymes that make up this so-called machinery. We first performed a quantitative real-time PCR measurement of all human PATs (ZDHHC1-9 and 11-24) and APTs 1 and 2 in MCF10a cells before and after induction of EMT. We found that in MCF10a-Snail, nearly all DHHC mRNAs were reduced in expression, most drastically DHHC23, which exhibited a near 8-fold reduction when compared to MCF10a-EV (Figure 4-3A). Conversely, MCF10a-Snail cells showed elevated expression of APT1 (1.2 fold increase) and APT2 (2 fold increase), contrasting with the overall trend observed with DHHC PATs (Figure 4-3B).

To determine whether APTs were also upregulated on the protein (activity) level, we applied an activity-based proteomics approach combined with stable isotopic labeling of amino acids in cells (SILAC)[70,99] to profile and compare the expression levels of serine hydrolases between EV and Snail derived MCF10a lines. Changes in protein levels of APT1 and 2 were in remarkable agreement with corresponding changes mRNA levels, with both measurements showing a 1.2 and 2-fold increase in MCF10a-Snail APT1 and 2 levels, respectively (Figure 4-3C). Our data demonstrate that while PATs may be downregulated in EMT, APTs are certainly upregulated, confirming an oncogenic role for these thioesterases[100] similar to other serine hydrolases from the superfamily to which these enzymes belong[101,102]. These results also suggest that Scrib's cytosolic redistribution and loss of tumor suppressor function in metastatic cancers could be due to changes in the overall protein expression of opposing enzymatic palmitoylation machineries (Figure 4-3E).

Acyl-protein Thioesterase 2 inhibition restores palmitoylation of Scrib and attenuates MAPK in Snail-induced EMT models. Earlier work in malignant T cell hybridomas showed that inhibiting thioesterase activity with the non-selective lipase

inhibitor hexadecylfluorophosphonate (HDFP) caused a marked stabilization in the palmitoylation levels of numerous key signaling proteins including Ras isoforms and Scrib.[70] Since the EMT program likely distorts palmitoylation equilibrium in favor of hydrolysis, we theorized that inhibitors of acyl protein thioesterases may be used to restore the balance by increasing the steady-state fraction of palmitoylated proteins. To test this hypothesis, we chose to use previously reported isoform-selective APT1 and 2 inhibitors[69] which would aid in parsing out the contributions from each enzyme to thioester hydrolysis of particular palmitoylated substrates. EV and Snail-derived MCF10a cultures were treated overnight with either vehicle (DMSO) or the APT2 inhibitor ML349 and the steady-state palmitoylation levels of both Ras isoforms and Scrib were assayed by ABE. The vehicle-treated samples showed that Scrib was indeed less palmitoylated after Snail-induction (Figure 4-4A), corroborating our proteomics findings that were obtained orthogonally by the 17ODYA SILAC proteomics approach (Figure 4-3D). On the other hand, even though Ras isoforms protein levels decreased in the Snail line, the fraction of palmitoylated Ras remained proportional to the levels observed in the EV line (Figure 4-3D and Figure 4-4A). This suggested that a higher steady-state fraction of Ras molecules were more palmitoylated post EMT. Importantly, small molecule inhibition of APT2 in both EV and Snail lines led to a 2- and 4-fold increase in palmitoylated Scrib, whereas Ras palmitoylation levels did not change significantly (Figure 4-4B). Thus, Scrib, and not Ras, steady-state palmitoylation fraction declines in our Snail model, and selective inhibition of APT2 activity can boost palmitoylated Scrib levels even after EMT.

Our ABE data supported the notion that EMT induces a hyper-active MAPK via dysregulated Scrib palmitoylation, therefore, we were eager to perform phenotypic assays to confirm that disrupted palmitoylation was indeed responsible for Scrib's mislocalization and function. EV and Snail induced MDCK lines were treated overnight with either vehicle, the APT1-selective inhibitor ML348 or ML349, fixed onto coverslips and immunostained to ascertain Scrib membrane localization. As demonstrated by the fluorescence microscopy images, small molecule inhibition of APT2, but not APT1, led to a noticeable increase in Scrib membrane signal in MDCK-Snail cells (Figure 4-4C).

Thus, it appears that APT2 is a physiologically-relevant depalmitoylase of Scrib that is transcriptionally upregulated in EMT to force Scrib off the membrane.

The qualitative nature of our microscopy results prompted us to employ a more quantitative approach to accurately confirm that Scrib was in fact membrane targeted in a ML349 dose-dependent manner. To this end, we developed a high-content analysis-based microscopy protocol that combines powerful measurement statistics with a more detailed criterion for measuring membrane-localized Scrib (Figure 4-4D). Namely, cell monolayers fixed onto 384-well plates are first immunostained with Scrib, a stable plasma membrane marker (Na^+/K^+ ATPase) and the nuclear dye DAPI. Unbiased high resolution, near-confocal images are then captured by an automated microscope. Our custom-designed analytical modules then process these fluorescent images, by counting the cells and defining their boundaries using the appropriate fluorescent signals. The Scrib fraction at the membrane is then defined as the membrane marker-

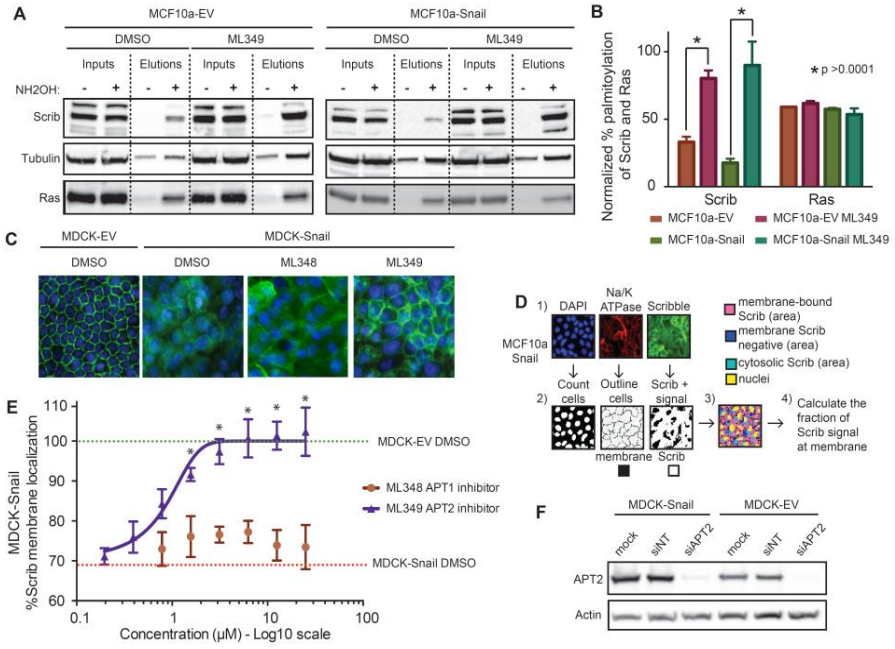

Figure 4-4 Small molecule targeting of APT2 enhances Scrib but not Ras palmitoylation leading to MAPK attenuation in snail-induced EMT models.

a. *APT2 inhibitor enhances Scrib palmitoylation as assayed by ABE in MCF10a EV and Snail lines.*
b. *Densitometric quantitation of ABE results demonstrate APT2-inhibitor rescue of Scrib but not Ras palmitoylation in MCF10a-Snail.*
c. *APT2 inhibitor treatment enhances Scrib membrane-localization as judged by pronounced immunofluorescence signals at the cell peripheries compared to vehicle treatment.*
d. *High-content screen-based membrane localization workflow in MDCK cells.*

e. *EC_{50} quantitation of ML349 dose-dependent induction of Scrib membrane re-localization. Error bars represent standard deviations across all cell measurements. Asterisks indicate statistically significant ($p<0.05$) membrane relocalization responses between the two compound treatment groups as revealed by the analysis of variance statistical test.*

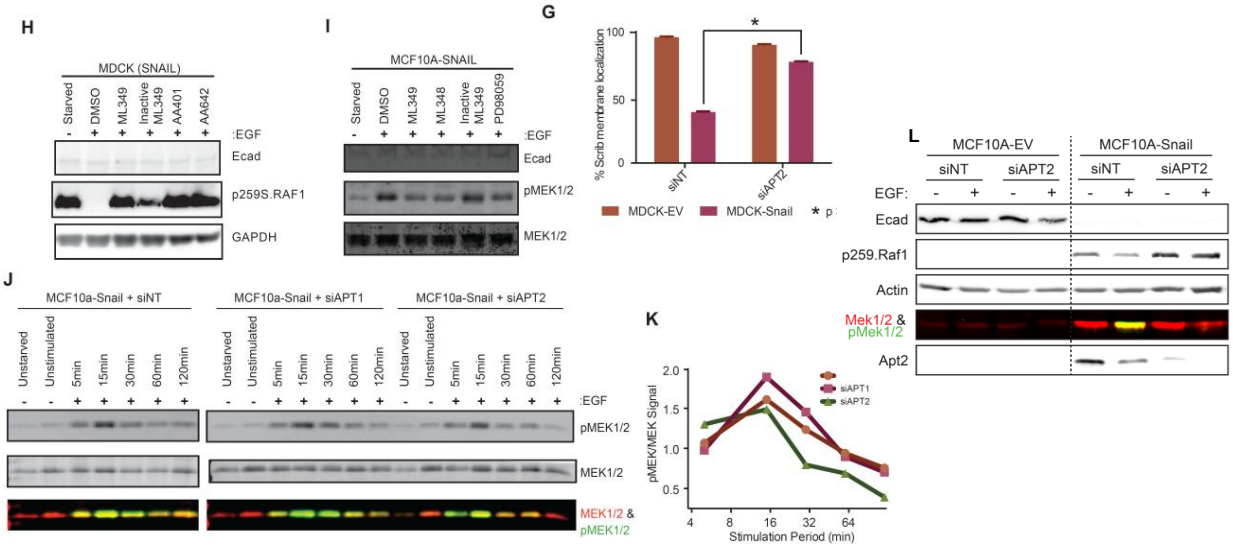

f. *siRNA mediated APT2 knockdown validated by immunoblotting in EV and Snail-derived MDCK cell lines.*
g. *APT2 knockdown in MDCK-Snail rescues Scrib palmitoylation.*
h. *APT2 inhibitor ablates RAF1 and MEK1/2 activation in MDCK-Snail.*
i. *APT2 inhibitor ablates RAF1 and MEK1/2 activation in MCF10a-Snail*
j. *APT2 knockdown attenuates MEK1/2 activation time course in MCF10a.*
k. *Quantitiation of (j) clearly showing shortened MEK1/2 activity duration with APT2 KD.*
l. *Validated APT2 knockdown in MCF10a-Snail attenuates RAF1 abrogates MEK1/2 activities.*

colocalized Scrib signal divided by the total Scrib signal per cell. Our typical workflow for each inhibitor concentration employed consisted of 3 well-replicates, each capturing 5 views per well with every image containing a thousand cell measurements on average. In turn, this systematic approach permits the accurate and precise measurement of Scrib membrane re-targeting by small-molecule inhibition of APTs in our EMT-model.

We then subjected EV and Snail-derived MDCK lines to our high-content analysis by culturing monolayers in 384-well plates in the presence of increasing inhibitor concentrations and measuring the percent membrane-localized Scrib by our custom-built workflow. Our analysis demonstrated that Scrib in MDCK-Snail cells was only about 70% membrane localized compared to MDCK-EV and that dose-dependent inhibition of APT2 and not APT1, restored membrane-Scrib levels back to that observed in EV lines (Figure 4-4E). The induced membrane-relocalization response EC_{50} for ML349 was measured around 2μM concentration of compound which was 10-fold

higher than its reported K_i towards APT2[69]. Given this drug's highly hydrophobic character, it is not unlikely for serum proteins to bind this compound and reduce its effective, free cellular concentrations. Nevertheless, to further validate and rule out non-specific drug interaction that could be associated with ML349 treatment, we chose to measure Scrib membrane re-targeting in the presence of siRNA-mediated APT2 knockdown as well. The knockdown data confirmed the involvement of APT2 in Scrib membrane dysregulation (Figure 4-4F and G), highlighting a novel role for this enzyme in metastatic transformation.

The metastatic transcriptional program induced by snail appears to boost APT2 activity, which consequently depalmitoylates and releases Scrib from the membrane. Given the anti-tumor propensities of membrane-localized Scrib, we speculated whether its membrane re-targeting via APT2 inhibition would inhibit the highly-excitable MAPK pathway seen in our Snail models. We therefore treated Snail-induced MDCK and MCF10a cells with either vehicle, ML348, ML349 or the two published dual APT1/2 triazole urea-based inhibitors that potently and irreversibly inhibit their targets and measured MAPK output in response to EGF stimulation as described previously. In both Snail lines, APT2 inhibition by the isoform-selective inhibitor ML349 resulted in a pronounced reductions in levels of both active RAF1 and MEK1/2, the downstream effectors of Ras. In contrast, the structurally-related ML349-null compound derivative showed no or negligible activity with either kinases in both Snail cell lines, suggesting that reductions in activated RAF1 and MEK1/2 were not due to off-target drug activities (Figure 4-4H and I). Interestingly, in MCF10a-Snail, the APT1-selective ML348 brought about similar attenuation in MEK activation in compare to ML349 treatment, suggesting a comparable contribution of APT1 to heightened MAPK activity in the MCF10a-Snail model. In more support to this mechanism, pretreatment of MDCK-Snail cells with the dual covalent APT1/2 inhibitors AA401 and AA642 both led to virtually complete inactivation of RAF1 as signified by the intense phosphorylated serine 259 inhibitory signal. Lastly, siRNA-mediated knockdown in MCF10a-Snail cells confirmed the role of APT2 in sustaining MAPK signal duration as reduced APT2 levels resulted in shorter signaling time frames for MEK1/2 and near complete attenuation in RAF1 activation (Figure 4-4J and K and L). Therefore, as corroborated by previous reports, small

molecule inhibitors of both APT1 and 2 lead to deactivation of certain MAPK proteins likely in both Ras-dependent and independent manners.

4.5 Discussion

MAPK transduction is frequently enhanced and exploited in the growth and invasion of metastatic cancer cells; however, the exact mechanism(s) that modulate its hypersensitivity in the absence of stimulus are still just partially understood. Within this context, scaffolding proteins may provide both a stimulatory *and* inhibitory platform upon which MAPK regulation can be achieved. The 175kDa tumor suppressor Scrib is the prime example of a contextually-defined, dual-acting regulator. Its localization at the plasma membrane enables it to control ERK1 expression through a direct interaction at two-conserved kinase interaction motifs, where ERK could conceivably dock in to Scrib and remain sequestered there through phosphorylation of Scrib at its second PDZ domain.[78] Scrib's position at the cortical (leading) edge during epithelial cell migration in MCF10a cells suggests that it localizes there to restore epithelial cell identity once a wound has fully closed; in its absence migrating cells fail to re-polarize.[103,104] C-terminal phosphorylation of Scrib was required for it to complex with Rho-kinase and Shroom2, an interaction that promoted contractility and therefore mobility at the cortical edge of keratinocytes.[105] We show in our EMT model that stimulation with EGF potentially causes a de-phosphorylation of cytosolic Scrib at its second PDZ domain, coinciding with an increase in phospho-MEK1/2 activity. While one set of phosphorylations by Rho-kinase enables Scrib to establish cell polarity in wound healing, another set of phosphorylations enables it to regulate MAPK - but these PTMs only work if Scrib is membrane-bound. Scrib is doing more than maintaining cell junctions; it appears to exquisitely orchestrate and fine-tune signaling cascades

Though still present and expressed in its genetically wild-type form in malignant cells, Scrib mis-localizes to the cytosol, suggesting either a now-missing protein-protein interaction or a disrupted PTM that ordinarily brings this large scaffold to the membrane. Given Scrib's homology with known palmitoylated LAP proteins Erbin and Densin and our recent identification of it by MS as being rapidly de-palmitoylated in a T-cell hybridoma line, we explored the latter hypothesis that Scrib could undergo palmitoylation in epithelial cells to keep it engaged at the membrane. We showed by acyl-biotin exchange on over-expressed Scrib variants, including a the cytosolic P305L mutant within the LRR domain, that Scrib does in fact undergo this modification. The

P305L mutant was significantly less palmitoylated than WT (Figure 5-3), while the N-terminal mutant showed no detectable palmitoylation through this method. Decreased palmitoylation of the Scrib and Erbin LRR mutants could be the result of a disrupted enzyme-substrate interaction; replacing the rigid proline residue with the larger hydrophobic side chain of leucine could create a significant change in protein structure and potential interactions, though this proline residue is not conserved in Lano or Densin. Other alterations in membrane-recruitment events, such as disrupted organization of ankyrin and spectrin proteins in EMT, may also play a role, though many of the observed changes are also intimately linked with palmitoylation.[44] We show the cysteines within Scrib's first twenty-two amino acids are required for its proper localization, as well, further suggesting a post-translational modification. Using mass spectrometry coupled with detection of the metabolically-incorporated fatty acid probe 17ODYA, we found that Scrib palmitoylation decreases by over 50% in Snail-driven EMT cell lines.

We explored a potential mechanism that could explain the loss of this modification on Scrib by examining the palmitoylation machinery in our EMT cell models. We discovered that upon EMT, the enzymatic palmitoylation machinery that catalyzes the cycling of this PTM is skewed two-fold in the direction of thioester hydrolysis. Our unpublished results also showed upregulation of other serine hydrolases like RBBP9 and seprase, which were elevated 16- and 30- fold respectively in the Snail lines and have been previously identified in similar cancer models.[102,106] We were surprised to find Snail-induced EMT down-regulated mRNA expression of nearly every protein acyltransferase we were able to detect by qPCR, including the PDZ binding motif-containing DHHC5 and DHHC14, the latter of which was recently identified as an oncogenic factor promoting metastasis of non small-cell lung cancer (NSCLC)[60]

We narrowed the focus of our investigation on the putative de-palmitoylating acyl protein thioesterases 1 and 2 (APT1 and APT2). Using both a pharmacological approach with various chemotypes and a genetic approach to reduce protein expression with siRNA, we found that blocking APT2 activity but not APT1 activity enhanced Scrib palmitoylation and membrane localization in Snail cells. APT2's elevated activity in many EMT models could account for the significant fraction of

cytosolic Scrib that has been observed by us and others[38,90]. The use of a high-content screen to test for compounds that modulate Scrib localization could lead to identifying other means of Scrib regulation through proteomic profiling of compound targets and Scrib interacting partners. The Z-factors, which have been estimated around 0.45 could be improved with a more reliable membrane marker other than Na^{+}/K^{++} ATPase, which was found to be heterogeneously expressed in Snail cell membranes.

Membrane association of Scrib is important in suppressing MAPK signaling and preventing activation of other oncogenic pathways. Together, our ABE and MAPK activation data suggest that as a scaffold that was previously shown to interact with MAPK players, Scrib is a leading candidate to linking its palmitoylation status with MAPK regulation. We observed that APT2, and not APT1 regulates MAPK activity possibly via Scrib localization in malignant cells, which supports earlier reports that APT1 may be working on Ras instead. The contribution of the Ras family of GTPases, all well-known substrates of palmitoylation, will need to be further addressed in the context of our EMT model in order to fully assign the unique contributions of palmitoylated small second-messengers vs. large scaffolds in MAPK signaling. Our results do demonstrate, however, that both APTs may coordinate pro-oncogenic effects on multiple regulatory components of the MAPK pathway, likely through disrupting the localization of membrane-tethered proteins. At the same time KRas4B is one isoform that is not palmitoylated, raising the possibility that APTs ought to extend their activities onto other non-core pathway regulators. Additionally, Scrib recruits and suppresses a RAF1 activating complex composed of the oncogenic LRR scaffold SHOC2, MRAS, RAF1 and PP1α.[24] The idea that two scaffolds with competing interests in MAPK activation would form a complex poses an interesting question. EMT-induced disruption in Scrib palmitoylation might partially explain how these two scaffolds lose their coordinated regulation of MAPK, with SHOC2 winning out. Indeed, the problem of elevated cellular growth through MAPK is further-complicated by other pathways changing in EMT and intersecting with Scrib, in particular the PI3-K/Akt and Hippo pathways.[35,90,107]

In summary, we demonstrate that Scrib palmitoylation is key to its normal localization and therefore function in epithelial cells before and after undergoing EMT.

The palmitoylation enzymes that play a direct role in modulating this important post-translational modification showed promising drug targets in APT1 and APT2, which in EMT displayed heightened expression and activity. Inhibition and knockdown of APT2 re-established palmitoylation of Scrib, but not Ras, while Scrib's localization returned to near wild-type proportions. This phenomenon correlated with reduced Raf1 and MEK1/2 activation, suggesting that palmitoylation-dependent changes in MAPK were mediated through Scrib, rather than increased membrane-bound Ras[59]. The contribution of scaffolding proteins to regulating MAPK activity is a rich area of investigation, and the mechanisms that dictate their proper function, localization and palmitoylation in cell polarity complexes and signal transduction is an untapped area of biomedical exploration.

4.6 Bibliography

1. Kolch, W. Meaningful relationships: the regulation of the Ras/Raf/MEK/ERK pathway by protein interactions. *Biochem. J.* **351 Pt 2,** 289–305 (2000).

2. Shaul, Y. D. & Seger, R. The MEK/ERK cascade: From signaling specificity to diverse functions. *Biochim. Biophys. Acta - Mol. Cell Res.* **1773,** 1213–1226 (2007).

3. Chang, F. *et al.* Signal transduction mediated by the Ras/Raf/MEK/ERK pathway from cytokine receptors to transcription factors: potential targeting for therapeutic intervention. *Leuk. Off. J. Leuk. Soc. Am. Leuk. Res. Fund, U.K* **17,** 1263–1293 (2003).

4. Cox, A. D., Fesik, S. W., Kimmelman, A. C., Luo, J. & Der, C. J. Drugging the undruggable RAS: Mission possible? *Nat. Rev. Drug Discov.* **13,** 828–51 (2014).

5. Martínez-Lacaci, I. *et al.* RAS transformation causes sustained activation of epidermal growth factor receptor and elevation of mitogen-activated protein kinase in human mammary epithelial cells. *Int. J. Cancer* **88,** 44–52 (2000).

6. Walker, F. *et al.* Activation of the Ras/mitogen-activated protein kinase pathway by kinase-defective epidermal growth factor receptors results in cell survival but not proliferation. *Mol. Cell. Biol.* **18,** 7192–7204 (1998).

7. Kang, E. S. *et al.* EGFR phosphorylation-dependent formation of cell-cell contacts by Ras/Erks cascade inhibition. *Biochim. Biophys. Acta - Mol. Cell Res.* **1773,** 833–843 (2007).

8. McKay, M. M. & Morrison, D. K. Integrating signals from RTKs to ERK/MAPK. *Oncogene* **26,** 3113–3121 (2007).

9. Nguyen, L. K., Kolch, W. & Kholodenko, B. N. When ubiquitination meets phosphorylation: a systems biology perspective of EGFR/MAPK signalling. *Cell Commun. Signal.* **11,** 52 (2013).

10. Anderson, D. H. Role of lipids in the MAPK signaling pathway. *Prog. Lipid Res.* **45,** 102–119 (2006).

11. Wang, Z. *et al.* Phosphatase-mediated crosstalk control of ERK and p38 MAPK signaling in corneal epithelial cells. *Investig. Ophthalmol. Vis. Sci.* **47,** 5267–5275 (2006).

12. Chapnick, D. a, Warner, L., Bernet, J., Rao, T. & Liu, X. Partners in crime: the TGFβ and MAPK pathways in cancer progression. *Cell Biosci.* **1,** 42 (2011).

13. González-Mariscal, L., Tapia, R. & Chamorro, D. Crosstalk of tight junction components with signaling pathways. *Biochim. Biophys. Acta - Biomembr.* **1778,** 729–756 (2008).

14. Witzel, F., Maddison, L. & Blüthgen, N. How scaffolds shape MAPK signaling: What we know and opportunities for systems approaches. *Front. Physiol.* **3 DEC,** 1–14 (2012).

15. Ferrell, J. E. & Cimprich, K. a. Enforced proximity in the function of a famous scaffold. *Mol. Cell* **11,** 289–291 (2003).

16. Malleshaiah, M. K., Shahrezaei, V., Swain, P. S. & Michnick, S. W. The scaffold protein Ste5 directly controls a switch-like mating decision in yeast. *Nature* **465,** 101–105 (2010).

17. Good, M. C. *et al.* The Ste5 Scaffold Allosterically Yeast Mating Pathway. **311,** 822–826 (2006).

18. Dhanasekaran, D. N., Kashef, K., Lee, C. M., Xu, H. & Reddy, E. P. Scaffold proteins of MAP-kinase modules. *Oncogene* **26,** 3185–3202 (2007).

19. Seeliger, M. a. & Kuriyan, J. A MAPK Scaffold Lends a Helping Hand. *Cell* **136,** 994–996 (2009).

20. Sacks, D. B. The role of scaffold proteins in MEK / ERK signalling. *Biochem. Soc. Trans.* **34,** 833–836 (2006).

21. Yoshioka, K. Scaffold proteins in mammalian MAP kinase cascades. *J. Biochem.* **135,** 657–661 (2004).

22. Matsunaga-Udagawa, R. *et al.* The scaffold protein Shoc2/SUR-8 accelerates the interaction of Ras and Raf. *J. Biol. Chem.* **285,** 7818–7826 (2010).

23. Rodriguez-Viciana, P., Oses-Prieto, J., Burlingame, A., Fried, M. & McCormick, F. A Phosphatase Holoenzyme Comprised of Shoc2/Sur8 and the Catalytic Subunit of PP1 Functions as an M-Ras Effector to Modulate Raf Activity. *Mol. Cell* **22,** 217–230 (2006).

24. Young, L. *et al.* An MRAS, SHOC2, and SCRIB complex coordinates erk pathway activation with polarity and tumorigenic growth. *Mol. Cell* **52,** 679–692 (2013).

25. Zeitler, J., Hsu, C. P., Dionne, H. & Bilder, D. Domains controlling cell polarity and proliferation in the Drosophila tumor suppressor scribble. *J. Cell Biol.* **167,** 1137–1146 (2004).

26. Martin-Belmonte, F. & Perez-Moreno, M. Epithelial cell polarity, stem cells and cancer. *Nat. Rev. Cancer* **12,** 23–38 (2011).

27. Pearson, H. B. *et al.* SCRIB expression is deregulated in human prostate cancer, and its deficiency in mice promotes prostate neoplasia. *J. Clin. Invest.* **121,** 4257–4267 (2011).

28. Zhan, L. *et al.* Deregulation of Scribble Promotes Mammary Tumorigenesis and Reveals a Role for Cell Polarity in Carcinoma. *Cell* **135,** 865–878 (2008).

29. Shook, D. & Keller, R. Mechanisms, mechanics and function of epithelial-mesenchymal transitions in early development. *Mech. Dev.* **120,** 1351–1383 (2003).

30. Lim, J. & Thiery, J. P. Epithelial-mesenchymal transitions: insights from development. *Development* **139,** 3471–3486 (2012).

31. Gout, S. & Huot, J. Role of cancer microenvironment in metastasis: Focus on colon cancer. *Cancer Microenviron.* **1,** 69–83 (2008).

32. Voulgari, A. & Pintzas, A. Epithelial-mesenchymal transition in cancer metastasis: Mechanisms, markers and strategies to overcome drug resistance in the clinic. *Biochim. Biophys. Acta - Rev. Cancer* **1796,** 75–90 (2009).

33. Pagliarini, R. A. & Xu, T. A genetic screen in Drosophila for metastatic behavior. *Science* **302,** 1227–1231 (2003).

34. Hawkins, E. D. *et al.* Scribble acts as an oncogene in Eμ-myc-driven lymphoma. *Oncogene* 1–5 (2015). doi:10.1038/onc.2015.167

35. Cordenonsi, M. *et al.* The hippo transducer TAZ confers cancer stem cell-related traits on breast cancer cells. *Cell* **147,** 759–772 (2011).

36. Feigin, M. E. *et al.* Mislocalization of the cell polarity protein scribble promotes mammary tumorigenesis and is associated with basal breast cancer. *Cancer Res.* **74,** 3180–3194 (2014).

37. Brumby, A. M. & Richardson, H. E. scribble mutants cooperate with oncogenic Ras or Notch to cause neoplastic overgrowth in Drosophila. *EMBO J.* **22,** 5769–5779 (2003).

38. Elsum, I. a. & Humbert, P. O. Localization, not important in all tumor-suppressing properties: A lesson learnt from scribble. *Cells Tissues Organs* **198,** 1–11 (2013).

39. Elsum, I. a *et al.* Scrib heterozygosity predisposes to lung cancer and cooperates with KRas hyperactivation to accelerate lung cancer progression in vivo. *Oncogene* 1–11 (2013). doi:10.1038/onc.2013.498

40. Resh, M. D. Targeting protein lipidation in disease. *Trends Mol. Med.* **18,** 206–214 (2012).

41. DiNitto, J. P. & Lambright, D. G. Membrane and juxtamembrane targeting by PH and PTB domains. *Biochim. Biophys. Acta - Mol. Cell Biol. Lipids* **1761,** 850–867 (2006).

42. Mulgrew-Nesbitt, A. *et al.* The role of electrostatics in protein-membrane interactions. *Biochim. Biophys. Acta - Mol. Cell Biol. Lipids* **1761,** 812–826 (2006).

43. Stahelin, R. V & Cho, W. Differential roles of ionic, aliphatic, and aromatic residues in membrane-protein interactions: a surface plasmon resonance study on phospholipases A2. *Biochemistry* **40,** 4672–4678 (2001).

44. Boëda, B. & Etienne-Manneville, S. Spectrin binding motifs regulate Scribble cortical dynamics and polarity function. *Elife* **4,** (2015).

45. Resh, M. D. Trafficking and signaling by fatty-acylated and prenylated proteins. *Nat. Chem. Biol.* **2,** 584–590 (2006).

46. Casey, P. J. Protein lipidation in cell signaling. *Science* **268,** 221–225 (1995).

47. Hancock, J. F., Magee, a I., Childs, J. E. & Marshall, C. J. All ras proteins are polyisoprenylated but only some are palmitoylated. *Cell* **57,** 1167–1177 (1989).

48. Topinka, J. R. & Bredt, D. S. N-terminal palmitoylation of PSD-95 regulates association with cell membranes and interaction with K+ channel K(v)1.4. *Neuron* **20,** 125–134 (1998).

49. Hernandez, J. L., Majmudar, J. D. & Martin, B. R. Profiling and inhibiting reversible palmitoylation. *Curr. Opin. Chem. Biol.* **17,** 20–26 (2013).

50. Baker, T. L., Zheng, H., Walker, J., Coloff, J. L. & Buss, J. E. Distinct rates of palmitate turnover on membrane-bound cellular and oncogenic H-Ras. *J. Biol. Chem.* **278,** 19292–19300 (2003).

51. Neve, K. a., Qanbar, R. & Bouvier, M. Role of palmitoylation/depalmitoylation reactions in G-protein-coupled receptor function. *Pharmacol. Ther.* **97,** 1–33 (2003).

52. Fukata, Y. & Fukata, M. Protein palmitoylation in neuronal development and synaptic plasticity. *Nat. Rev. Neurosci.* **11,** 161–175 (2010).

53. Yeste-Velasco, M., Linder, M. E. & Lu, Y.-J. Protein S-palmitoylation and cancer. *Biochim. Biophys. Acta - Rev. Cancer* **1856,** 107–120 (2015).

54. Greaves, J. & Chamberlain, L. H. S-acylation by the DHHC protein family. *Biochem. Soc. Trans.* **38,** 522–524 (2010).

55. Korycka, J. *et al.* Human DHHC proteins: A spotlight on the hidden player of palmitoylation. *Eur. J. Cell Biol.* **91,** 107–117 (2012).

56. Linder, M. E. & Jennings, B. C. Mechanism and function of DHHC S-acyltransferases. *Biochem. Soc. Trans.* **41,** 29–34 (2013).

57. Salaun, C., Greaves, J. & Chamberlain, L. H. The intracellular dynamic of protein palmitoylation. *J. Cell Biol.* **191,** 1229–1238 (2010).

58. Kong, E. *et al.* Dynamic palmitoylation links cytosol-membrane shuttling of acyl-protein thioesterase-1 and acyl-protein thioesterase-2 with that of proto-oncogene H-Ras product and growth-associated protein-43. *J. Biol. Chem.* **288,** 9112–9125 (2013).

59. Rocks, O. *et al.* The palmitoylation machinery is a spatially organizing system for peripheral membrane proteins. *Cell* **141,** 458–471 (2010).

60. Tian, H. *et al.* Systematic siRNA Screen Unmasks NSCLC Growth Dependence by Palmitoyltransferase DHHC5. *Mol. Cancer Res.* **13,** 784–794 (2015).

61. Mukai, J. *et al.* Molecular Substrates of Altered Axonal Growth and Brain Connectivity in a Mouse Model of Schizophrenia. *Neuron* 1–16 (2015). doi:10.1016/j.neuron.2015.04.003

62. Xu, J. *et al.* Inhibiting the palmitoylation/depalmitoylation cycle selectively reduces the growth of hematopoietic cells expressing oncogenic Nras. *Blood* **119,** 1032–1035 (2012).

63. Beronja, S. *et al.* RNAi screens in mice identify physiological regulators of oncogenic growth. *Nature* **501,** 185–190 (2013).

64. Dekker, F. J. *et al.* Small-molecule inhibition of APT1 affects Ras localization and signaling. *Nat. Chem. Biol.* **6,** 449–456 (2010).

65. Martin, B. R., Giepmans, B. N. G., Adams, S. R. & Tsien, R. Y. Mammalian cell-based optimization of the biarsenical-binding tetracysteine motif for improved fluorescence and affinity. *Nat. Biotechnol.* **23,** 1308–1314 (2005).

66. Laemmli, U. K. Cleavage of structural proteins during the assembly of the head of bacteriophage T4. *Nature* **227,** 680–685 (1970).

67. Henderson, C. J. & Wolf, C. R. Immunodetection of proteins by Western blotting. *Methods Mol. Biol.* **10,** 221–33 (1992).

68. Livak, K. J. & Schmittgen, T. D. Analysis of relative gene expression data using real-time quantitative PCR and the 2(-Delta Delta C(T)) Method. *Methods* **25,** 402–8 (2001).

69. Adibekian, A. *et al.* Confirming target engagement for reversible inhibitors in vivo by kinetically tuned activity-based probes. *J. Am. Chem. Soc.* **134,** 10345–10348 (2012).

70. Martin, B. R., Wang, C., Adibekian, A., Tully, S. E. & Cravatt, B. F. Global profiling of dynamic protein palmitoylation. *Nat. Methods* **9,** 84–89 (2011).

71. Wan, J., Roth, A. F., Bailey, A. O. & Davis, N. G. Palmitoylated proteins: purification and identification. *Nat. Protoc.* **2,** 1573–1584 (2007).

72. Le Bras, G. F., Taubenslag, K. J. & Andl, C. D. The regulation of cell-cell adhesion during epithelial-mesenchymal transition, motility and tumor progression. *Cell Adhes. Migr.* **6,** 365–373 (2012).

73. Hollestelle, A. *et al.* Loss of E-cadherin is not a necessity for epithelial to mesenchymal transition in human breast cancer. *Breast Cancer Res. Treat.* **138,** 47–57 (2013).

74. Lieber, M., Mazzetta, J. A., Nelson Rees, W., Kaplan, M. & Todaro, G. Establishment of a continuous tumor cell line (PANC-1) from a human carcinoma of the exocrine pancreas. *Int. J. Cancer* **15,** 741–747 (1975).

75. Zhou, B. P. *et al.* Dual regulation of Snail by GSK-3beta-mediated phosphorylation in control of epithelial-mesenchymal transition. *Nat. Cell Biol.* **6,** 931–940 (2004).

76. Barberà, M. J. *et al.* Regulation of Snail transcription during epithelial to mesenchymal transition of tumor cells. *Oncogene* **23,** 7345–7354 (2004).

77. Cano, a *et al.* The transcription factor snail controls epithelial-mesenchymal transitions by repressing E-cadherin expression. *Nat. Cell Biol.* **2,** 76–83 (2000).

78. Nagasaka, K. *et al.* The cell polarity regulator hScrib controls ERK activation through a KIM site-dependent interaction. *Oncogene* **29,** 5311–5321 (2010).

79. Nagasaka, K. *et al.* A Novel Interaction between hScrib and PP1γ Downregulates ERK Signaling and Suppresses Oncogene-Induced Cell Transformation. *PLoS One* **8,** 1–10 (2013).

80. Nagasaka, K. *et al.* The mechanism and implications of hScrib regulation of ERK. *Small GTPases* **1,** 108–112 (2010).

81. Lamouille, S., Xu, J. & Derynck, R. Molecular mechanisms of epithelial-mesenchymal transition. *Nat. Rev. Mol. Cell Biol.* **15,** 178–96 (2014).

82. Bilder, D. *et al.* Collective nomenclature for LAP proteins. *Nat. Cell Biol.* **2,** E114 (2000).

83. Bryant, P. J. & Huwe, a. LAP proteins: what's up with epithelia? *Nat. Cell Biol.* **2,** E141–E143 (2000).

84. Legouis, R. *et al.* Basolateral targeting by leucine-rich repeat domains in epithelial cells. *EMBO Rep.* **4,** 1096–1102 (2003).

85. Skelton, N. J. *et al.* Origins of PDZ domain ligand specificity. Structure determination and mutagenesis of the erbin PDZ domain. *J. Biol. Chem.* **278,** 7645–7654 (2003).

86. Izawa, I., Nishizawa, M., Hayashi, Y. & Inagaki, M. Palmitoylation of ERBIN is required for its plasma membrane localization. *Genes to Cells* **13,** 691–701 (2008).

87. Thalhammer, A., Trinidad, J. C., Burlingame, A. L. & Schoepfer, R. Densin-180: Revised membrane topology, domain structure and phosphorylation status. *J. Neurochem.* **109,** 297–302 (2009).

88. Kang, R. *et al.* Neural palmitoyl-proteomics reveals dynamic synaptic palmitoylation. *Nature* **456,** 904–909 (2008).

89. Zhan, L. *et al.* Deregulation of Scribble Promotes Mammary Tumorigenesis and Reveals a Role for Cell Polarity in Carcinoma. *Cell* **135,** 865–878 (2008).

90. Feigin, M. E. *et al. Mislocalization of the cell polarity protein scribble promotes mammary tumorigenesis and is associated with basal breast cancer*. *Cancer Research* **74,** (2014).

91. Li, X., Yang, H., Liu, J., Schmidt, M. D. & Gao, T. Scribble-mediated membrane targeting of PHLPP1 is required for its negative regulation of Akt. *EMBO Rep.* **12,** 818–824 (2011).

92. Zeng, X., Singh, S. R., Hou, D. & Hou, S. X. Tumor suppressors Sav/Scrib and oncogene ras regulate stem-cell transformation in adult Drosophila malpighian tubules. *J. Cell. Physiol.* **224,** 766–774 (2010).

93. Zhang, W., Trible, R. P. & Samelson, L. E. LAT palmitoylation: its essential role in membrane microdomain targeting and tyrosine phosphorylation during T cell activation. *Immunity* **9,** 239–246 (1998).

94. Webb, Y., Hermida-Matsumoto, L. & Resh, M. D. Inhibition of protein palmitoylation, raft localization, and T cell signaling by 2-bromopalmitate and polyunsaturated fatty acids. *J. Biol. Chem.* **275,** 261–270 (2000).

95. Krishnamurthy, K. *et al.* Depalmitoylation preferentially downregulates AMPA induced Ca2+ signaling and neurotoxicity in motor neurons. *Brain Res.* **1529,** 143–153 (2013).

96. Burgoyne, J. R. *et al.* Oxidation of HRas cysteine thiols by metabolic stress prevents palmitoylation in vivo and contributes to endothelial cell apoptosis. *FASEB J.* **26,** 832–841 (2012).

97. Lorentzen, A., Kinkhabwala, A., Rocks, O., Vartak, N. & Bastiaens, P. I. H. Regulation of Ras localization by acylation enables a mode of intracellular signal propagation. *Sci. Signal.* **3,** ra68 (2010).

98. Rocks, O. *et al.* An acylation cycle regulates localization and activity of palmitoylated Ras isoforms. *Science* **307,** 1746–1752 (2005).

99. Liu, Y., Patricelli, M. P. & Cravatt, B. F. Activity-based protein profiling: the serine hydrolases. *Proc. Natl. Acad. Sci. U. S. A.* **96,** 14694–14699 (1999).

100. Rusch, M. *et al.* Identification of acyl protein thioesterases 1 and 2 as the cellular targets of the ras-signaling modulators palmostatin B and M. *Angew. Chemie - Int. Ed.* **50,** 9838–9842 (2011).

101. Yao, T.-W. *et al.* A novel role of dipeptidyl peptidase 9 in epidermal growth factor signaling. *Mol. Cancer Res.* **9,** 948–959 (2011).

102. Shields, D. J. *et al.* RBBP9: a tumor-associated serine hydrolase activity required for pancreatic neoplasia. *Proc. Natl. Acad. Sci. U. S. A.* **107,** 2189–2194 (2010).

103. Dow, L. E. *et al.* The tumour-suppressor Scribble dictates cell polarity during directed epithelial migration: regulation of Rho GTPase recruitment to the leading edge. *Oncogene* **26,** 2272–2282 (2007).

104. Osmani, N., Vitale, N., Borg, J. P. & Etienne-Manneville, S. Scrib Controls Cdc42 Localization and Activity to Promote Cell Polarization during Astrocyte Migration. *Curr. Biol.* **16,** 2395–2405 (2006).

105. Amano, M. *et al.* Kinase-interacting substrate screening is a novel method to identify kinase substrates. *J. Cell Biol.* **209,** 895–912 (2015).

106. Goodman, J. D., Rozypal, T. L. & Kelly, T. Seprase, a membrane-bound protease, alleviates the serum growth requirement of human breast cancer cells. *Clin. Exp. Metastasis* **20,** 459–470 (2003).

107. Chatterjee, S. *et al.* Dysregulation of cell polarity proteins synergize with oncogenes or the microenvironment to induce invasive behavior in epithelial cells. *PLoS One* **7,** (2012).

Chapter 5:
Conclusions, Perspectives and Future Directions

5.1 Overall conclusions

Proteins are often regulated through the addition of chemical modifications to modulate their localization, activity, and interactions.[1–3] Protein *S*-palmitoylation describes the reversible attachment of long-chain fatty acids to cysteine residues in proteins to promote membrane association.[4–6] Altered palmitoylation contributes to the pathogenesis of cancer, neurological disorders and many other human diseases.[7–10] In fact, protein palmitoylation is involved in the regulation of essentially all cellular processes, yet the enzymes that catalyze lipid attachment (Protein Acyl Transferases, PATs) and removal (Acyl Protein Thioesterases, APTs) are poorly characterized. This work addresses this gap by focusing on the molecular mechanisms and biological roles of PATs and APTs in the regulation of palmitoylation. The research presented herein was divided into three chapters, each exploring a different aspect of protein *S*-palmitoylation.

The inhibitor 2-bromopalmitate (2BP) has been adopted over the past thirty years as a pan PAT inhibitor, widely used in hundreds of papers to interfere with palmitoylation. While not directly demonstrated, this inhibitor presumably modifies the active site of PAT enzymes, and potentially of a various unrelated enzymes involved in other biological pathways. In chapter two, novel 2BP derivatives were used to describe 2BP proteome reactivity, explore its mechanism of palmitoylation blockade and evaluate its general utility as a probe for assaying PAT enzyme activities in cells. To accomplish these goals, a functionalized 2BP analogue was synthesized that allowed for selective capture and mass spectrometric identification of inhibited proteins. Surprisingly, PAT enzymes were not the primary targets of 2BP. Furthermore, many of the targets identified were themselves palmitoylated proteins, suggesting that in addition to PAT inactivation, 2BP may inhibit protein palmitoylation by directly blocking palmitoylation

sites on target proteins. These findings highlighted the non-specific nature of 2BP, and suggested re-evaluation of the hundreds of publications that utilized 2BP for studying palmitoylation.

Two candidate protein depalmitoylases, APT1 and 2, have so-far been described in the literature, however their primary physiological roles are still incompletely defined. APT1 and 2 are serine hydrolases that show broad and possibly overlapping substrate specificities across diverse sets of biomolecules, further complicating the assignment of their primary cellular role(s). Indeed, isoform-selective pharmacological tools would aid in parsing out the specific contributions of these enzymes and defining their true biochemical functions. In chapter three, the molecular basis for the binding of two distinct, selective, reversible APT inhibitors was investigated from both a structural and chemical standpoint. To this end, the co-crystal structures for both APT1 and 2 with their corresponding selective inhibitors were solved and kinetic enzyme activity assays were used to confirm the structural determinants that give rise to the observed selectivity. The crystal structures reveal that APT1 and 2 share identical α/ß-hydrolase folds with nearly complete conservation of active-site residues. Interestingly, inhibitors occupied cognate active-site locations, yet retained relatively specific interactions with key residues in APT1 and 2. Taken together, the existence of discriminatory residues were invoked to gate access to the active-sites of APT1 and 2.

We previously identified the cell polarity regulator Scribble (Scrib) as a palmitoylated protein rapidly processed by APT enzymes. Epithelial cells normally exhibit a polarized structure that is lost when tumors undergo metastatic transformation. Scrib normally localizes to the basolateral membrane where it protects the cells against this transformation by scaffolding proteins that define polarity gradients, regulate cellular proliferation, and maintain cellular adhesion. Importantly, Scrib is often mislocalized in most malignant cancers, displaced from the plasma membrane, allowing cells to proliferate unchecked. Based on these observations, in chapter four, we explored the hypothesis that APT enzymes may remove Scrib palmitoylation, releasing it from the plasma membrane to promote malignancy. To this end, APT1 and 2 activities were inhibited with both pharmacological and genetic tools and Scrib palmitoylation and localization was measured in malignant cells. Indeed, incubating malignant cells with

these drugs largely rescues Scrib plasma membrane localization. Furthermore, APT2 inhibition also attenuated the mitogen activated protein kinase (MAPK) cascade, a growth signaling pathway that is known to be hyper-activated in metastatic cancers. Overall, we identified a new function for palmitoylation in suppressing cancer by regulating Scrib, a critical gatekeeper of cell polarity.

In summary, this thesis investigated novel biological activities of protein palmitoylation. Using a variety of biochemical methods and chemical biology techniques, I report preliminary data constituting an original contribution to the fields of chemistry, biochemistry, and cell biology. These findings provide new insights into the mechanistic role of PAT enzymes in mediating palmitoylation, describe the small-molecule selectivities of APT enzymes and characterize their biological role in regulating cell polarity and signaling complexes in cancer.

Most importantly, this thesis, throughout its chapters, continued to address the 'window of opportunity' concept of chemical biology, which is more often than not overlooked in studies of protein S-palmitoylation. Indeed, no chemical compound, or probe for this matter, is truly selective for its cellular target(s); instead, there is a useful range of concentrations and other assay conditions that allow for relatively specific probing of the desired on-target(s). This work along with many other valuable studies serve as cautionary tales for research communities, emphasizing that virtually all chemical biology techniques are prone to off-target effects. Therefore, these types of experiments should be performed within their known limits of specificity along with validated positive and negative controls to yield accurate and biologically relevant results.

5.2 Perspective and future directions for chapter 2

In the 2-bromopalmitate (2BP) study presented in the second chapter, we provided a proteomic and mechanistic view of this inhibitor's cellular targets by employing click-enabled derivatives (Figure 2-1A). Corroborating several earlier findings[11–13], we confirmed the promiscuity of this PAT inhibitor and demonstrated that despite its selective reaction with active DHHCs (Figure 2-7 and Figure 2-11), it largely targeted other classes of proteins of various function, the majority of which were membrane associated proteins (Table 2). Therefore, we concluded that 2BP lacked the pharmacological specificity necessary for correctly assigning the physiological roles and annotating the molecular substrates of PATs. Given the scarcity of PAT inhibitors however, it is understandable why many still resort to using 2BP for probing the palmitoylation effect *in vivo*. In this event, we highly recommend that investigators use multiple methods of inhibiting palmitoylation to clearly demonstrate its significance to the particular study. In addition to the pharmacological agents discussed in the first chapter, molecular biology approaches could also be applied to prevent acylation from taking place; these techniques include mutation of the exact palmitoylation site and genetic knockdowns of suspected PATs.

Despite the finding of 2BP's non-selective behavior, characterization of its reactivity did lead to several interesting findings that may support its use for the discovery of non-enzymatic palmitoylation events, also known as autoacylation[14–16]. Unexpectedly, a large number of 2BP targets were also validated palmitoylated proteins (Table 2 and Figure 2-13) which led us to theorize that 2BP reactivity can report on non-enzymatically, self plamitoylating proteins, here referred to as autopalmitoylated proteins. A number of proteins, including the GPCR rhodopsin[17], heterotrimeric G*α* subuits[14] and tubulin dimers[18], have been reported to undergo palmitoylation reactions *in vitro* when subjected to acyl-CoA donors. Perhaps, the intrinsic ability of these membrane proteins to self-install acyl chains is due to their harboring a heightened cysteine thiol nucleophile. This electronic argument is further supported by our experiments (Figure 2-7D) which show increased protein labeling observed for the more electrophilic 2BP coenzyme A variant in compare to the free fatty acid form. Since existence of this non-enzymatic process has yet to be confirmed *in vivo*, one would

need to demonstrate that a putative autopalmitoylated protein can undergo palmitoylation in the absence of any PATs, or their activities. Such an experiment could be performed in heterologous organism that lacks PAT enzymes but bears long chain acyl-CoA donors available to react with the exogenous protein.

Another aspect of chapter two that can be explored further is the mechanism by which 2BP blocks protein palmitoylation by direct competition for the palmitoylation site. We showed that FAM108B, a validated N-terminally palmitoylated protein, could no longer label with our 2BP probe when its N-terminus was deleted (Figure 2-14). This raised the possibility that 2BP modification site is likely coinciding with the native palmitoylated cysteine residue. However, it is unclear whether deleting the N-terminus of FAM10B prevents other cysteines, outside of the N-terminal portion, from reacting with 2BP resulting in the observed loss of labeling. One strategy to identify native palmitoylation sites that are directly competed by 2BP, is by performing a competitive-metabolic labeling experiment in which the 2BP probe is pre-incubated with cells and then a palmitoylation reporter (e.g. 17-ODYA, the ω-alkynylated stearic fatty acid analog, Figure 1-3) is used sequentially to measure the levels of both 2BP and palmitate incorporation into specific targets (Figure 5-1).

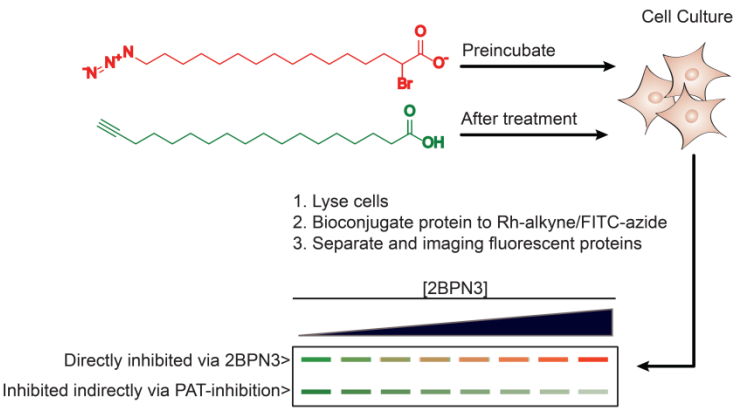

Figure 5-1 2BPN3/17ODYA competition experiment to resolve 2BP alkylated proteins from proteins that are truly depalmitoylated in the presence of this inhibitor.

In this manner, proteins that exhibit an inverse correlation between 2BP and 17ODYA incorporations are possibly 2BP-alkylated at the site(s) of their fatty acid attachment. An important caveat is that for some targets, 17ODYA-blockade may be achieved via both PAT inhibition and direct site alkylation, and therefore, in these cases, it is difficult to determine which mode is the primarily contributing to inhibition of acyl attachment.

5.3 Perspective and future directions for chapter 3

In chapter three, we explored the activities of the two homologous thioesterase enzymes, APT1 and 2[19], towards the isoform selective inhibitors, ML348 and ML349[20] respectively, in an effort to understand APT differential active-site ligand preferences. The co-crystal structures for each enzyme-inhibitor pair solved revealed the existence of residues that may confer active-site selectivity through both steric and electronic effects (Figure 3-11and Figure 3-12). These discriminatory amino acids, when mutated to their corresponding homologous residues, exhibited selective inhibitor affinities (K_i) and residency times (k_{off}) which mirrored those of wild type enzymes (Table 5 and Figure 3-15, respectively). Interestingly, the discriminating residue of APT1 had no effect when substituted into APT2 and *vice versa* (Table 5). These finding suggest that more than one amino acid contributes to inhibitor selectivity, and that inhibitor preference is possibly due to differences in the conformational dynamics about APT1 and 2 active-sites[21–24].

The most intriguing aspect of these reversible inhibitors was the different geometries in which they were docked into their respective active sites (Figure 3-6 and Figure 3-7). The more flexible ML348 was somewhat kinked when complexed to APT1 suggesting that the active site may have certain steric and or electronic requirements which scan for ligands that posses non-linear chemical structures. This could presumably be tested by designing and measuring the potency of ML348 analogs that have severely restricted rotational movement. In addition to ML348's unique conformation, the CF_3 substituent of the anilide structure appeared to block APT1 catalytic residues via strong hydrophobic interactions with residues lining the active site entry (Figure 3-6, Figure 3-7 and Figure 3-11). This finding was corroborated by the original SAR studies about ML348[20] which showed that substituting the trifluoromethyl group in any way, reduced the potency of the compound relative to the lead. Another important observation was made about guanidino group of R149 which appeared to be engaging, via a hydrogen bond, the carbonyl of the 2-furoyl amide group (Figure 3-10). Fortunately, a direct means of testing this hydrogen bond hypothesis is tractable as it would be to assay the affinity of ML348 towards an Arg mutant, such as an Ile, which lacks the ganidino group but still retains similar steric bulk. Alternatively, this

hypothetical hydrogen bond can be assessed by substituting the amide in question for the isosteric thioamide group (i.e. -(C=S)-NR_2), which should alter the potency if the aforementioned carbonyl was in fact H-bonding.

On the other hand, the ML349-APT2 interaction had defined planar contacts and yielded more direct structural information regarding the mechanism of ML349 binding (Figure 3-6 and Figure 3-7). While the sulfone moiety of ML349 was clearly engaging the nucleophilic hydroxyl of APT2 and resembling a transition-state analog, ML349 derivatives having the sulfone group swapped for aliphatic and sterically-demanding groups paralleled the activities of ML349 as reported in previous SAR studies[20]. This suggests that the sulfone may be serving both the role of a bulky group as well as a tetrahedral analog. This proposition is supported by the finding that the smaller sulfoxide derivative, representing a racemic mixture of diastereomers, lost marked potency compared to the lead compound (Figure 3-16). Thus, it should be evident that we cannot not directly assess the contribution of the serine hydroxyl-ML349 sulfone hydrogen bonds because isosterically modifying ML349 about its sulfone would be synthetically intractable. In addition, the thioether derivative could not be used to assess the H-bond contribution either because this variant lacks the steric bulk that was demonstrated to inhibit the enzyme as well. Therefore, the remaining approach to use for probing the transition state binding of the sulfone, would be to measure the binding of ML349 towards Ser122Ala mutant lacking the hydroxyl group altogether. Our Res-*O*-Ac substrate analog activity assay would not be applicable since this binding measurement relies on the enzyme possessing catalytic activity. Thus, one would need to perform binding experiments in an activity-independent manner, such a measurement could be acquired via thermodynamic binding experiments such as the well-known isothermal titration calorimetric method.[25]

The APT inhibitor studies also provided clues as to how these two thioesterase may have diverged in recognizing molecules at their active sites. Given that APT active sites must be different enough to discriminate between these reversible inhibitors, it is possible that the same residues that confer specificity towards small molecules may be involved in selection towards physiological substrates (Figure 3-17). One experiment that can establish this connection would be to measure the catalytic activities of these

mutants towards a variety of acyl substrates (i.e. *S*-palmitoylcysteine) and determine whether the residues in question confer substrate specificity as well. A faster way to achieve the same goal would be to perform product inhibition-like experiments in which enzyme activities are still assayed with Res-O-Ac except now in the presence of increasing concentrations of various fatty acids. These lipids represent the putative endogenous products of APTs and could therefore resemble acylated substrate binding the enzyme. In addition to point mutants, we also noted that flexibility of APT2's high mobility loop structure could exert some effects on the putative substrate channel of the enzyme, although we did not address its contribution towards ligand selectivity. Thus, one could generate APT1 and 2 loop-exchanged[24] mutants and assay their resulting inhibitor sensitivities to validate this claim. As a whole, thoroughly defining the scope of substrates efficiently hydrolyzed by APTs is expected to aid in future drug design attempts, which could then employ a substrate-guided approach in their medicinal chemistry efforts.

A comparison between the three-dimensional electrostatic maps of APT1 and 2 suggests that while both enzymes share hydrophobic residues inside their hydrophobic channels, it is APT2 which possess greater hydrophobic character bordering its active site (Figure 3-8). This fact, along with the high orthologous conservation of APT2 residues (Figure 3-17) suggest that it has evolved to engage and process specific sets of biomolecules that are hydrophobic in nature. To date, specific membrane affinity studies have focused on the role that fatty acylated residues play in APT membrane localization.[26–28] ; membrane affinity contributions from APT surface residues have not been addressed yet. Therefore, to measure the dependence of membrane association on surface character, surface point mutants can be designed which introduce residues that overwhelm the existing hydrophobic character of APT2. Membrane localization studies of GFP-tagged wild type and mutant constructs can then be assessed by microscopy techniques such as FRAP measurements[29–33] that were discussed in the first chapter.

Lastly, in light of the observed specificities of ML348 and ML349, we suggest these inhibitors could be utilized as probes to assay the exact contributions of each enzyme to depalmitoylation dynamics *in vivo*. For example, APTs have been implicated

in the deacylation and thus regulation of Ras isoforms[34–37], which are notorious cancer targets that have shown to promote uncontrolled growth and proliferation among other roles[38–42]. The current thinking is that Ras GTPases maintain imperative dynamic cycles of palmitoylation/depalmitoylation[34,43] which if altered, affect their signal transduction potential[36]. Therefore, the search for the bona fide Ras depalmitoylase(s) has been a recent focus in Ras biology studies. Specifically, APT1 has been suggested to deacylate HRas, whereas APT2 has shown to deacylate semi-synthetic NRas more efficiently than APT1. While these experiments are informative, they do not report on the physiological activities of APTs which would require further genetic knockout experiments to confirm APT *in vitro* activities. Instead of invoking these elaborate methods, we suggest to implement APT selective compounds to achieve these same goals. To this end, we used these inhibitors and some of their less potent derivatives in growth factor stimulation experiments and assessed the contributions of APTs to the activity of Ras isoforms. As can be seen in the active-Ras pulldown results[44,45] (Figure 5-2), treatment with ML349 led to a near-complete deactivation of Ras proteins, which were detected simultaneously with a pan-Ras antibody. This was in contrast to ML348 which only modestly reduced active Ras levels. Given that even selective-inhibitors may have unexpected yet relevant off-targets, we would need to confirm that the observed Ras deactivation was a result of inhibition of APT2 and not of a potential ML349 off-target. To conclude, APT-directed probes can be used as quick, inexpensive, preliminary tools for assessing their physiological contributions.

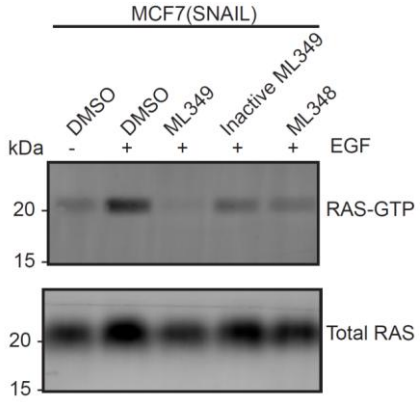

Figure 5-2 Active panRas pulldown from EGF-stimulated MCF7 breast cancer cells is dependent on APT2 but not on APT1 activity. MCF7 cells were pre-treated overnight with 5 µM of each inhibitor, serum starved briefly, and stimulated with EGF for 5 minutes. Inactive ML349 is the thioether-derivative presented in

5.4 Perspective and future directions for chapter 4

The Scrib palmitoylation and membrane localization studies that were conducted in chapter four demonstrated that dynamic palmitoylation played a central role in regulating the localization and activities of tumor-suppressor and oncogenes in cancer (Figure 4-2 and Figure 4-4). We specifically showed that the tumorigenic EMT program leads to the up-regulation of APT2 (Figure 4-3), which we revealed to be a bona fide Scrib depalmitoylase in epithelial cells (Figure 4-4). We suggested that APT2 activity would account for a significant fraction of cytosolic Scrib given the recent literature reports on LAP family membrane recruitment requirements. Namely, palmitoylation appears to be a unifying theme of LAP protein scaffolds as demonstrated by the close-relative LAP protein homologues Densin and Erbin, the latter of which has been shown to require palmitoylation for membrane targeting[46].

In this regard, we showed that deleting Scrib's first 22 N-terminal residues was enough to preclude its palmitoylation and membrane localization. We interpreted these findings to mean that Scrib's N-terminal cysteine residues were the sites of palmitoylation and that they were necessary for the protein's membrane association. As this is one way of perceiving these palmitoylation and membrane association results, there could be many other potential explanations such as deletion of N-terminus allosterically affects a distal palmitoylation site or protein interaction which is necessary for membrane recruitment. Thus, one would need to generate single and double point-mutants of the alleged N-cysteines (i. e. C4 and C10) and assay their palmitoylation levels and membrane localization. Nevertheless, these exact experiments were already performed on Scrib's close relative LAP member, Erbin, which showed that indeed the cysteine were the site of acyl attachment and that they led to loss of membrane Erbin.

Interestingly, the cytosolic Scrib P305L mutant, which corresponds to a P315L mutation in Erbin[46], showed a decrease in palmitoylation levels as well (Figure 5-3), but the origin of this reduction was not addressed. One likely explanation for why Pro-to-Leu mutation in Scrib, and likely other LAP members, exhibits decreased palmitoylation levels is that the substituted Leu residue alters the conformation of this domain affecting the engagement of the palmitoylation site to its corresponding palmitoylase (i.e. DHHC PAT). This disengagement could occur via two plausible mechanisms. In the first

scenario, the mutant Scrib is physically unable to reach the membrane in which the DHHC resides. In the alternative scenario, the mutant Scrib does reach the proper membrane but can no longer interact with the enzyme in a catalytically competent conformation. The latter would be more difficult to ascertain since the full-length Scrib structure is unknown and the proline mutation is distant in sequence to the palmitoylation site and therefore could exert its effects through a number of mechanisms.

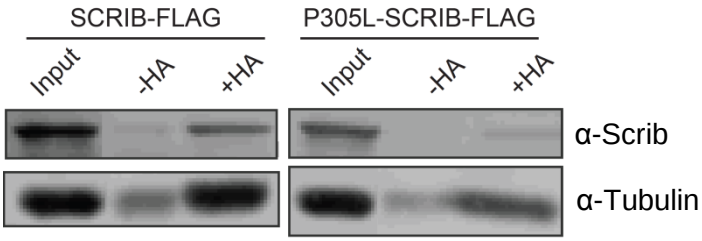

Figure 5-3 ABE of 293T cells overexpressing wild type or P305L Scrib mutant demonstrate a near-complete loss in Scrib P305L palmitoylation.

It is more likely that P305L mutant is just unable to engage the proper membrane and hence, does not get palmitoylated. As stated in chapter one, many proteins require a transitory membrane engagement before they can get stably palmitoylated by membrane-resident DHHCs[5,47]. Therefore it would not be surprising if the Scrib P305L mutant is lacking this transient interaction. Indeed, proteins can be weakly attracted to the membrane via either protein-protein interactions[48,49] or just by the sheer number of hydrophobic and basic residues present on their surface[50–52]. Thus, to clearly demonstrate that Pro305 mediates transient membrane association that is independent of prior N-terminal palmitoylation events, the membrane localization of a palmitoylation-deficient mutant should be compared with that of another palmitoylation-deficient mutant that also features the P305L substitution. This experiment would eliminate any contribution that may be conferred by the palmitoylation sites. It is possible that both constructs will exhibit the same localization properties given our data that suggests palmitoylation-deficient mutants do not bind membranes. In addition, mass-spectrometric analyses of wild type and P305L protein enrichments may reveal protein interactions that are lost in the mutant and thus could be contributing to transient membrane recruitment.

Another unexplored highlight of the Scrib chapter involved the high-content imaging analysis which demonstrated that inhibiting APT2 in MDCK-Snail cells seemed to retarget Scrib to membrane in a dose-dependent manner (Figure 4-4). Interesting enough, we did not observe reversion of MDCK-Snail's mesenchymal morphology upon drug treatment suggesting that we were not restoring the epithelial phenotype. This was a concern because Scrib membrane localization was shown to correlate with the epithelial identity of the cells[53,54], with the more polarized cells showing most signal at the cell membrane. It is possible, although highly unlikely, that morphological changes were induced in drug-treated MDCK-Snail cells and this could have affected the cells' physical shape which in turn would augment the our high-content calculations of Scrib membrane fractions. One way this could result in apparent membrane signal increase is if the membrane marker has now shifted into the cytosolic milieu of the cells. Thus, to limit membrane signal artifacts, we suggest to employ a supplementary membrane marker to aid in defining the membrane. Additionally, one may choose report more morphological features about the cells to be used in membrane fraction calculations; these include circularity and ellipticity measurements which can be used to filter abnormal-looking cells from the analysis.

A central finding in the Scrib chapter was that APT2 positively regulated the MAPK pathway during cancer transformation. We were able to demonstrate that inhibiting this APT2 in the oncogenic lines led to an attenuation of this signaling pathway (Figure 4-4). The main issue that was presented to us was determining through which protein(s) does APT2 exert effects that would lead to increased activation or relieved suppression of the MAPK cascade (Figure 5-4). Seeing that APT2 has been primarily characterized as a protein acyl thioesterase enzyme[19], our first guess was that MAPK-associated palmitoylated proteins were the direct targets of APT2. While numerous palmitoylated proteins have shown to indirectly affect this pathway in one way or another, to our knowledge, palmitoylatable Ras isoforms (i.e. H, N and K4b) are primary MAPK effectors which are thought to be physiological substrates of APTs. Thus we hypothesized that APT2 may exert its regulation on the MAPK though either appropriate Ras isoforms or Scrib which define to be another likely substrate of this enzyme.

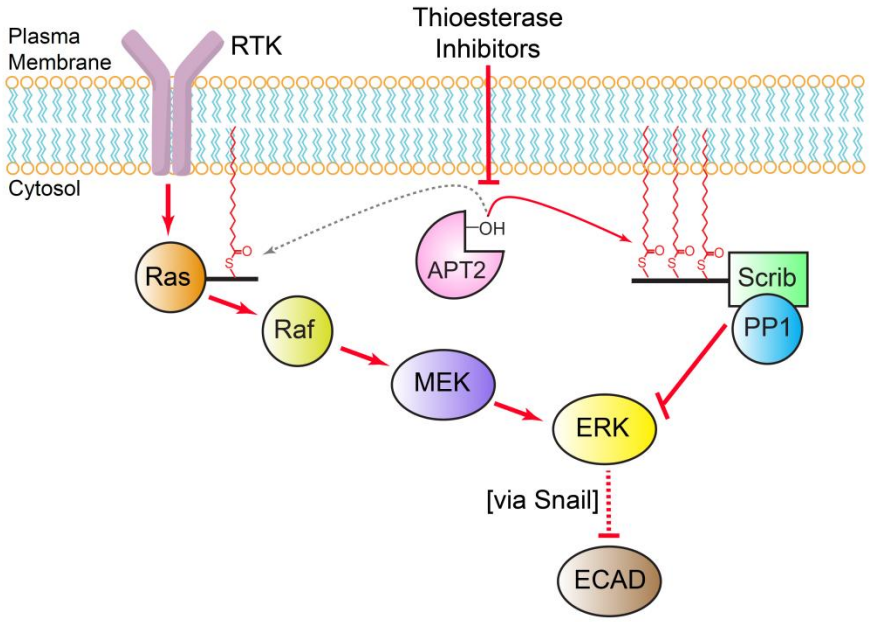

Figure 5-4 Determining the exact molecular node by which APT2 exerts its affects on MAPK. APT2 could active an oncogene or deactivate a tumor suppressor to bring about similar highly excitable MAPK pathway found in transformed fibroblastic cancer cells which show a loss of the epithelial marker ECAD.

To this end, we showed that APT2 does not affect the steady-state palmitoylation levels of Ras isoforms but does affect those of Scrib, with APT2 inhibition leading to a marked increase in steady-state Scrib palmitoylation. This result alone is not enough to suggest that APT2 could not exert effects through Ras; this is because we did not address APT2's contribution to Ras palmitoylation turnover dynamics, which has been shown to be essential to Ras transduction potential[43]. Another way to get at the question "is APT2 regulating Ras activity?" would be to assay the levels of active, GTP-bond Ras and determine if APT2 inhibition perturbs the activity of these GTPases. Regardless of the aforementioned experiment, Bastians and coworkers[37] have convincingly shown that inhibiting APTs may be detrimental to Ras activity as the acylated Ras proteins are allowed to equilibrate throughout all endo-membranes diluting their effective concentration at the plasma membrane[43].

Although it makes a lot of sense for the Scrib repressor to be the MAPK-node by which APT2 exerts its effects, it is still worth assaying Scrib's direct contribution to the attenuation of this signaling pathway. One would therefore need to knockdown or knockout Scrib in the Snail line, and determine whether inhibition of APT2 still leads to MAPK suppression. If Scrib was truly the palmitoylated MAPK effector responsible for

attenuation, then removal of Scrib from the equation would render a highly excitable cascade that cannot be suppressed by APT2 drug treatment.

Although we focused on APT contribution to Scrib palmitoylation, a decrease in steady-state palmitoylation may also result from a reduction in the levels or activity of its corresponding PAT enzyme(s). We showed by qRT-PCR experiments that inducing oncogenic transformation in MCF10a epithelial cells reduced the mRNA transcript levels across all DHHC PAT enzymes (Figure 4-3), suggesting that DHHC protein levels were reduced as well, however we did not validate this claim comprehensively in our study. Since our qRT-PCR data represented the fold-change between transcripts from the parent and oncogenic lines, we could not determine the definite mRNA levels of DHHCs between the tested lines, and to do so would required customized PCR standards for each DHHC. Therefore, it is inappropriate to compare and draw conclusion from the fold-change values between different DHHC transcripts, since low-level transcripts may still exhibit large fold changes if they are absent in one of the lines tested. Regardless, to draw meaningful conclusions, protein detection techniques, such as western blots, should be utilized to determine the levels of DHHCs between parent and oncogenic cell lines as mRNA transcript levels do not always correlate with protein levels although they did so perfectly for APTs (Figure 4-3).

In addition to describing changes in DHHCs, the qRT-PCR screen was also an effort to identify Scrib's palmitoyltransferase(s). Since Scrib featured reduced palmitoylation levels, we hypothesized that its DHHC PAT could be reduced in the oncogene line. However, changes in enzyme levels do not always reflect their catalytic outputs. Thus, to achieve this goal in a more direct manner, an elegant approach is offered which may accelerate the finding of Scrib's palmitoyltransferase. This method relies on the hypothesis that Scrib uses its PDZ interaction domains to engage its PAT and allow for concomitant palmitoylation; this is not a radical or novel proposition as several PATs have been shown to catalyze the palmitolyation of their substrate in a PDZ interaction-dependent manner.[55] Interestingly, there are 5 DHHC members (3, 5, 8, 14, 23) that contain the so-called PDZ interaction motif, a short C-terminal 4-peptide sequence which binds a cognate PDZ domain (Figure 1-7). Thus, if Scrib palmitoylation was dependent on PDZ interactions, one would expect that deleting or impairing the

alleged PDZ domain would hinder the palmitoylation of Scrib. If this were found to be the case, then it would be good grounds for employing the critical PDZ domain(s) as a bait to pulldown the associated DHHC PAT and assay its contribution directly.

5.5 Bibliography

1. Nadolski, M. J. & Linder, M. E. Protein lipidation. *FEBS J.* **274,** 5202–5210 (2007).

2. Casey, P. J. Protein lipidation in cell signaling. *Science* **268,** 221–225 (1995).

3. Triola, G., Waldmann, H. & Hedberg, C. Chemical biology of lipidated proteins. *ACS Chem. Biol.* **7,** 87–99 (2012).

4. Linder, M. & Deschenes, R. Protein palmitoylation. *Methods* **40,** 125–126 (2006).

5. Salaun, C., Greaves, J. & Chamberlain, L. H. The intracellular dynamic of protein palmitoylation. *J. Cell Biol.* **191,** 1229–1238 (2010).

6. Resh, M. D. Palmitoylation of ligands, receptors, and intracellular signaling molecules. *Sci. STKE* **2006,** re14 (2006).

7. Korycka, J. *et al.* Human DHHC proteins: A spotlight on the hidden player of palmitoylation. *Eur. J. Cell Biol.* **91,** 107–117 (2012).

8. Resh, M. D. Targeting protein lipidation in disease. *Trends Mol. Med.* **18,** 206–214 (2012).

9. Young, F. B., Butland, S. L., Sanders, S. S., Sutton, L. M. & Hayden, M. R. Putting proteins in their place: Palmitoylation in Huntington disease and other neuropsychiatric diseases. *Prog. Neurobiol.* **97,** 220–238 (2012).

10. Greaves, J. & Chamberlain, L. H. New links between S-acylation and cancer. *J. Pathol.* **233,** 4–6 (2014).

11. Coleman, R. A., Rao, P., Fogelsong, R. J. & Bardes, E. S. 2-Bromopalmitoyl-CoA and 2-bromopalmitate: promiscuous inhibitors of membrane-bound enzymes. *Biochim. Biophys. Acta* **1125,** 203–209 (1992).

12. Oku, H., Tokuda, M. & Umino, T. The effects of 2-bromopalmitate on the fatty acid composition in differentiating adipocytes of red sea bream (Pagrus major). *Comp. Biochem. Physiol. Part B Biochem. Mol. Biol.* **152,** 370–375 (2009).

13. Chase, J. F. & Tubbs, P. K. Specific inhibition of mitochondrial fatty acid oxidation by 2-bromopalmitate and its coenzyme A and carnitine esters. *Biochem. J.* **129,** 55–65 (1972).

14. Duncan, J. A. & Gilman, A. G. Autoacylation of G protein alpha subunits. *J. Biol. Chem.* **271,** 23594–23600 (1996).

15. Bizzozero, O. a., McGarry, J. F. & Lees, M. B. Autoacylation of myelin proteolipid protein with acyl coenzyme A. *J. Biol. Chem.* **262,** 13550–13557 (1987).

16. Dietrich, L. E. P. & Ungermann, C. On the mechanism of protein palmitoylation. *EMBO Rep.* **5,** 1053–1057 (2004).

17. O'Brien, P. J., St Jules, R. S., Reddy, T. S., Bazan, N. G. & Zatz, M. Acylation of disc membrane rhodopsin may be nonenzymatic. *J. Biol. Chem.* **262,** 5210–5215 (1987).

18. Wolff, J., Zambito, a M., Britto, P. J. & Knipling, L. Autopalmitoylation of tubulin. *Protein Sci.* **9,** 1357–1364 (2000).

19. Davda, D. & Martin, B. R. Acyl protein thioesterase inhibitors as probes of dynamic S-palmitoylation. *Medchemcomm* **5,** 268 (2014).

20. Adibekian, A. *et al.* Confirming target engagement for reversible inhibitors in vivo by kinetically tuned activity-based probes. *J. Am. Chem. Soc.* **134,** 10345–10348 (2012).

21. Kurth, T., Ullmann, D., Jakubke, H.-D. & Hedstrom, L. Converting Trypsin to Chymotrypsin: Structural Determinations of S1´ Specifity. *Biochemistry* **36,** 10098–10104 (1997).

22. Hedstrom, L., Szilagyi, L. & Rutter, W. J. Converting trypsin to chymotrypsin: the role of surface loops. *Science* **255,** 1249–1253 (1992).

23. Ma, W., Tang, C. & Lai, L. Specificity of trypsin and chymotrypsin: loop-motion-controlled dynamic correlation as a determinant. *Biophys. J.* **89,** 1183–1193 (2005).

24. Laskowski, M. & Qasim, M. a. What can the structures of enzyme-inhibitor complexes tell us about the structures of enzyme substrate complexes? *Biochim. Biophys. Acta - Protein Struct. Mol. Enzymol.* **1477,** 324–337 (2000).

25. Leavitt, S. & Freire, E. Direct measurement of protein binding energetics by isothermal titration calorimetry. *Curr. Opin. Struct. Biol.* **11,** 560–566 (2001).

26. Vartak, N. *et al.* The autodepalmitoylating activity of APT maintains the spatial organization of palmitoylated membrane proteins. *Biophys. J.* **106,** 93–105 (2014).

27. Tomatis, V. M., Trenchi, A., Gomez, G. a. & Daniotti, J. L. Acyl-protein thioesterase 2 catalizes the deacylation of peripheral membrane-associated GAP-43. *PLoS One* **5,** (2010).

28. Kong, E. *et al.* Dynamic palmitoylation links cytosol-membrane shuttling of acyl-protein thioesterase-1 and acyl-protein thioesterase-2 with that of proto-oncogene H-Ras product and growth-associated protein-43. *J. Biol. Chem.* **288,** 9112–9125 (2013).

29. Ishikawa-Ankerhold, H. C., Ankerhold, R. & Drummen, G. P. C. Advanced fluorescence microscopy techniques-FRAP, FLIP, FLAP, FRET and FLIM. *Molecules* **17,** 4047–4132 (2012).

30. Wu, J. *et al.* A coupled diffusion-kinetics model for analysis of contact-area FRAP experiment. *Biophys. J.* **95,** 910–919 (2008).

31. Sprague, B. L. & McNally, J. G. FRAP analysis of binding: Proper and fitting. *Trends Cell Biol.* **15,** 84–91 (2005).

32. Chen, Y., Lagerholm, B. C., Yang, B. & Jacobson, K. Methods to measure the lateral diffusion of membrane lipids and proteins. *Methods* **39,** 147–153 (2006).

33. Goodwin, J. S. & Kenworthy, A. K. Photobleaching approaches to investigate diffusional mobility and trafficking of Ras in living cells. *Methods* **37,** 154–164 (2005).

34. Dekker, F. J. *et al.* Small-molecule inhibition of APT1 affects Ras localization and signaling. *Nat. Chem. Biol.* **6,** 449–456 (2010).

35. Deck, P. *et al.* Development and biological evaluation of acyl protein thioesterase 1 (APT1) inhibitors. *Angew. Chemie - Int. Ed.* **44,** 4975–4980 (2005).

36. Rusch, M. *et al.* Identification of acyl protein thioesterases 1 and 2 as the cellular targets of the ras-signaling modulators palmostatin B and M. *Angew. Chemie - Int. Ed.* **50,** 9838–9842 (2011).

37. Dekker, F. J. & Hedberg, C. Small molecule inhibition of protein depalmitoylation as a new approach towards downregulation of oncogenic Ras signalling. *Bioorganic Med. Chem.* **19,** 1376–1380 (2011).

38. Hernández-Martín, a & Torrelo, a. Rasopathies: developmental disorders that predispose to cancer and skin manifestations. *Actas Dermosifiliogr.* **102,** 402–416 (2011).

39. Ji, Z., Flaherty, K. T. & Tsao, H. Targeting the RAS pathway in melanoma. *Trends Mol. Med.* **18,** 27–35 (2012).

40. Yuan, T. L. & McCormick, F. Killing Tumors by Keeping Ras and PI3’ Kinase Apart. *Cancer Cell* **24,** 562–563 (2013).

41. Horiguchi, K. *et al.* Role of Ras signaling in the induction of snail by transforming growth factor-?? *J. Biol. Chem.* **284,** 245–253 (2009).

42. Rajasekharan, S. K. & Raman, T. Ras and Ras mutations in cancer. *Cent. Eur. J. Biol.* **8,** 609–624 (2013).

43. Rocks, O. *et al.* The palmitoylation machinery is a spatially organizing system for peripheral membrane proteins. *Cell* **141,** 458–471 (2010).

44. Castro, A. F., Rebhun, J. F. & Quilliam, L. a. Measuring Ras-family GTP levels in vivo - Running hot and cold. *Methods* **37,** 190–196 (2005).

45. De Rooij, J. & Bos, J. L. Minimal Ras-binding domain of Raf1 can be used as an activation-specific probe for Ras. *Oncogene* **14,** 623–625 (1997).

46. Izawa, I., Nishizawa, M., Hayashi, Y. & Inagaki, M. Palmitoylation of ERBIN is required for its plasma membrane localization. *Genes to Cells* **13,** 691–701 (2008).

47. Smotrys, J. E. & Linder, M. E. Palmitoylation of intracellular signaling proteins: regulation and function. *Annu. Rev. Biochem.* **73,** 559–587 (2004).

48. Ernst, A. M., Contreras, F. X., Brügger, B. & Wieland, F. Determinants of specificity at the protein-lipid interface in membranes. *FEBS Lett.* **584,** 1713–1720 (2010).

49. Thalhammer, A., Trinidad, J. C., Burlingame, A. L. & Schoepfer, R. Densin-180: Revised membrane topology, domain structure and phosphorylation status. *J. Neurochem.* **109,** 297–302 (2009).

50. Rogaski, B. & Klauda, J. B. Membrane-binding mechanism of a peripheral membrane protein through microsecond molecular dynamics simulations. *J. Mol. Biol.* **423,** 847–861 (2012).

51. DiNitto, J. P. & Lambright, D. G. Membrane and juxtamembrane targeting by PH and PTB domains. *Biochim. Biophys. Acta - Mol. Cell Biol. Lipids* **1761,** 850–867 (2006).

52. Cowburn, D. Peptide recognition by PTB and PDZ domains. *Curr. Opin. Struct. Biol.* **7,** 835–838 (1997).

53. Pearson, H. B. *et al.* SCRIB expression is deregulated in human prostate cancer, and its deficiency in mice promotes prostate neoplasia. *J. Clin. Invest.* **121,** 4257–4267 (2011).

54. Feigin, M. E. *et al.* Mislocalization of the cell polarity protein scribble promotes mammary tumorigenesis and is associated with basal breast cancer. *Cancer Res.* **74,** 3180–3194 (2014).

55. Thomas, G., Hayashi, T., Chiu, S. L., Chen, C. M. & Huganir, R. Palmitoylation by DHHC5/8 Targets GRIP1 to Dendritic Endosomes to Regulate AMPA-R Trafficking. *Neuron* **73,** 482–496 (2012).

Appendix A

$2BPN_3$ Enriched 293T Proteomic Data Set

In the second chapter we presented label-free mass spectrometry-based proteomic data comparing the amounts of $2BPN_3$-enriched proteins relative to control enrichments in the presence of 2BP. In the tables below, we have included the entire data set for proteins enriched in both $2BPN_3$ and 2BP treated 293T cells. Relative abundance was measured by spectral counting, as previously described[86].

Table 6 Full-length 2BPN3 Enriched 293T Proteomic Data Set.

Number	IPI	Protein	Description	2BPN3-1	2BPN3-2	2BPN3-3	2BP-1	2BP-2	2BPN3-AVG	2BP-AVG
1	IPI00455531	VDAC2	Voltage-dependent anion channel 2	308	304	154	8	14	255	11
2	IPI00747443	ATP2A2	SERCA Ca(2+)-ATPase	195	151	156	1	4	167	3
3	IPI00026824	HMOX2	Heme oxygenase 2	143	179	81	0	0	134	0
4	IPI00141318	CKAP4	Cytoskeleton-associated protein 4	191	105	88	2	2	128	2
5	IPI00007188	SLC25A5	ADP/ATP translocase 2	95	77	95	12	22	89	17
6	IPI00639812	MGST3	Microsomal glutathione S-transferase 3	93	58	81	2	2	77	2
7	IPI00011284	COMT	Catechol O-methyltransferase	40	124	44	1	0	69	1
8	IPI00294779	VDAC3	Voltage-dependent anion-selective channel protein 3	86	63	57	6	6	69	6
9	IPI00303954	CYB5B	cytochrome b5	45	112	33	0	1	63	1
10	IPI00215790	RPL38	60S ribosomal protein L38	39	77	53	2	2	56	2
11	IPI00003833	MTCH2	Mitochondrial carrier homolog 2	45	87	29	0	1	54	1
12	IPI00012828	ACAA1	3-ketoacyl-CoA thiolase	64	54	21	2	3	46	3
13	IPI00748750	-	Adenine nucleotide translocator 2	38	31	65	0	0	45	0
14	IPI00016070	AGPAT6	1-acyl-sn-glycerol-3-phosphate acyltransferase zeta	32	63	32	0	0	42	0
15	IPI00021766	RTN4	Reticulon-4	57	27	41	4	1	42	3
16	IPI00171459	HSDL1	Hydroxysteroid dehydrogenase-like protein 1	45	46	29	0	2	40	1
17	IPI00827920	FAM62B	FAM62B	37	45	30	1	0	37	1
18	IPI00743293	RTN3	Reticulon-3	53	37	20	0	1	37	1
19	IPI00171626	AYTL2	1-acylglycerophosphocholine O-acyltransferase 1	51	37	17	1	1	35	1
20	IPI00026105	SCP2	sterol carrier protein 2	46	40	18	1	1	35	1
21	IPI00014053	TOMM40	mitochondrial import receptor subunit TOM40	37	33	32	1	2	34	2
22	IPI00024670	REEP5	Receptor expression-enhancing protein 5	28	31	34	0	0	31	0
23	IPI00177423	A8K3B9	Uncharacterized reticulon-like proetin	53	35	0	0	1	29	1
24	IPI00005677	GNPAT	Dihydroxyacetone phosphate acyltransferase	16	49	23	1	0	29	1
25	IPI00022891	SLC25A4	ADP/ATP translocase 1	34	28	25	0	0	29	0
26	IPI00026994	PRAF2	PRA1 family protein 2	46	22	16	0	0	28	0
27	IPI00328715	MTDH	Protein LYRIC	23	45	14	2	2	27	2
28	IPI00008998	PTPLAD1	Protein-tyrosine phosphatase-like A domain-containing protein 1	20	36	23	0	1	26	1
29	IPI00479205	SCAMP3	SCAMP3	34	30	11	0	2	25	1
30	IPI00022462	TFRC	Transferrin receptor protein 1	17	39	19	1	1	25	1
31	IPI00646889	C10orf57	Uncharacterized protein C10orf57	26	30	18	2	0	25	1
32	IPI00296190	C10orf58	Uncharacterized protein C10orf58	26	30	18	2	0	25	1
33	IPI00022202	SLC25A3	Phosphate carrier protein, mitochondrial	29	28	16	5	2	24	4
34	IPI00022793	HADHB	Trifunctional enzyme beta subunit, mitochondrial	30	28	12	1	2	23	2
35	IPI00002372	ABCD3	ATP-binding cassette sub-family D member 3	16	32	21	0	2	23	1
36	IPI00395887	TXNDC1	Thioredoxin domain-containing protein 1	32	27	9	1	2	23	2
37	IPI00328161	FKBP8	FK506-binding protein 8	19	29	16	1	0	21	1
38	IPI00396321	LRRC59	Leucine-rich repeat-containing protein 59	21	29	13	4	4	21	4
39	IPI00021978	PEX11B	Peroxisomal membrane protein 11B	37	17	9	0	0	21	0
40	IPI00031695	ELOVL6	Elongation of very long chain fatty acids protein 6	33	7	22	0	0	21	0
41	IPI00016670	C11orf59	UPF0404 protein C11orf59	30	16	15	0	0	20	0
42	IPI00465290	DNAJC11	DnaJ homolog subfamily C member 11	16	34	11	0	1	20	1
43	IPI00015713	CDKAL1	CDK5 regulatory subunit-associated protein 1-like 1	16	30	14	0	0	20	0
44	IPI00020944	FDFT1	Squalene synthetase	14	32	14	0	1	20	1
45	IPI00006663	ALDH2	Aldehyde dehydrogenase, mitochondrial	19	25	15	2	1	20	2
46	IPI00297492	STT3A	Dolichyl-diphosphooligosaccharide--protein glycosyltransferase subunit STT3A	21	32	6	1	2	20	2
47	IPI00549343	VAMP3	Vesicle-associated membrane protein 3	33	17	7	2	0	19	1
48	IPI00019472	SLC1A5	Neutral amino acid transporter B	13	30	13	3	4	19	4
49	IPI00020226	ACOX3	Acyl-coenzyme A oxidase 3, peroxisomal	18	22	14	0	0	18	0
50	IPI00026089	SF3B1	Splicing factor 3B subunit 1	17	27	10	1	3	18	2
51	IPI00180675	TUBA1A	Tubulin alpha-1A chain	24	30	0	0	0	18	0
52	IPI00218922	SEC63	Translocation protein SEC63 homolog	14	25	14	0	2	18	1
53	IPI00218343	TUBA1C	Tubulin alpha-1C chain	24	28	0	0	0	17	0
54	IPI00401147	UNC84A	91 kDa protein	13	30	8	0	0	17	0
55	IPI00549761	ALG1	Chitobiosyldiphosphodolichol beta-mannosyltransferase	14	22	13	1	0	16	1
56	IPI00554777	ASNS	Asparagine synthetase	12	30	7	0	0	16	0
57	IPI00745125	SOAT1	Uncharacterized protein SOAT1	20	16	12	1	0	16	1
58	IPI00604763	TMEM66	Transmembrane protein 66	20	17	11	0	0	16	0
59	IPI00003269	DKFZp686D0972	hypothetical protein LOC345651	27	13	7	4	0	16	2
60	IPI00305627	C16orf58	UPF0420 protein C16orf58	9	27	9	0	0	15	0
61	IPI00657752	CD81	Uncharacterized protein CD81	11	20	13	2	1	15	2
62	IPI00021147	DEGS1	degenerative spermatocyte homolog 1, lipid desaturase	14	21	8	2	0	14	1
63	IPI00644037	GPSN2	37 kDa protein	8	22	12	0	1	14	1
64	IPI00005719	RAB1A	Ras-related protein Rab-1A	11	23	8	3	0	14	2
65	IPI00009368	SFXN1	Sideroflexin-1	10	18	13	1	3	14	2
66	IPI00024642	CCDC47	Coiled-coil domain-containing protein 47	6	18	16	3	0	13	2
67	IPI00005737	SURF4	Surfeit locus protein 4	8	18	14	0	1	13	1
68	IPI00033075	BAT5	Protein BAT5	13	18	8	0	0	13	0
69	IPI00293336	LOC153364	similar to metallo-beta-lactamase superfamily protein	14	16	9	0	0	13	0
70	IPI00166865	CISD2	Zinc finger, CDGSH-type domain 2	26	6	6	0	0	13	0
71	IPI00007676	HSD17B12	Estradiol 17-beta-dehydrogenase 12	10	19	9	0	0	13	0
72	IPI00220739	PGRMC1	Membrane-associated progesterone receptor component 1	13	20	5	1	2	13	2
73	IPI00100674	REEP4	Receptor expression-enhancing protein 4	16	16	6	0	0	13	0
74	IPI00027728	SLC7A1	High affinity cationic amino acid transporter 1	12	17	8	1	0	12	1
75	IPI00295098	SRPRB	Signal recognition particle receptor subunit beta	10	18	9	2	1	12	2
76	IPI00298202	ACOT8	Acyl-coenzyme A thioesterase 8	10	15	11	0	0	12	0
77	IPI00001952	ENDOD1	Endonuclease domain-containing 1 protein	9	21	5	0	0	12	0
78	IPI00031458	ICMT	Protein-S-isoprenylcysteine O-methyltransferase	15	16	4	0	0	12	0
79	IPI00414168	MARCH5	E3 ubiquitin-protein ligase MARCH5	10	14	11	0	0	12	0
80	IPI00002230	AADACL1	arylacetamide deacetylase-like 1	4	16	14	0	0	11	0
81	IPI00032038	CPT1A	Carnitine O-palmitoyltransferase I	12	13	9	0	0	11	0
82	IPI00016405	OCIAD1	OCIA domain-containing protein 1	7	17	10	1	0	11	1
83	IPI00012512	RRAS2	Ras-related protein R-Ras2	9	16	9	0	0	11	0
84	IPI00099463	SGPL1	Sphingosine-1-phosphate lyase 1	14	5	15	0	0	11	0
85	IPI00030941	TSPAN3	Tetraspanin-3	8	18	8	0	0	11	0
86	IPI00470595	C1orf166	RING finger protein C1orf166	10	17	6	0	0	11	0
87	IPI00013068	EIF3E	Eukaryotic translation initiation factor 3 subunit 6	9	16	8	1	2	11	2
88	IPI00737518	RP13-15M17.2	similar to CG7744-PA	9	14	10	0	0	11	0

89	IPI00478410	ATP5C1	ATP synthase gamma chain, mitochondrial	5	14	13	2	1	11	2
90	IPI00025729	CAMLG	Calcium signal-modulating cyclophilin ligand	6	17	9	1	0	11	1
91	IPI00645518	CDIPT	CDP-diacylglycerol--inositol 3-phosphatidyltransferase	11	12	9	0	0	11	0
92	IPI00554481	SLC3A2	ute carrier family 3 (activators of dibasic and neutral amino acid transport), memb	8	19	5	1	1	11	1
93	IPI00019353	AGK	Acylglycerol kinase, mitochondrial	8	16	7	0	0	10	0
94	IPI00009896	EPHX1	Epoxide hydrolase 1	7	18	6	1	0	10	1
95	IPI00220578	GNAI3	Guanine nucleotide-binding protein G	10	12	9	2	2	10	2
96	IPI00140301	MAG1	1-acyl-sn-glycerol-3-phosphate acyltransferase theta	4	23	4	0	0	10	0
97	IPI00022275	SACM1L	SAC1 suppressor of actin mutations 1-like	8	17	6	1	1	10	1
98	IPI00027180	ZMPSTE24	CAAX prenyl protease 1 homolog	12	14	5	0	0	10	0
99	IPI00031397	ACSL3	Long-chain-fatty-acid--CoA ligase 3	4	16	10	0	0	10	0
100	IPI00745171	ATP2C1	Calcium-transporting ATPase type 2C member 1	4	19	7	0	0	10	0
101	IPI00479431	C20orf3	Uncharacterized protein C20orf3	5	17	8	0	0	10	0
102	IPI00010255	RHBDD2	Rhomboid domain-containing protein 2	8	12	10	0	0	10	0
103	IPI00172656	UBXD8	UBX domain-containing protein 8	8	13	9	2	0	10	1
104	IPI00294455	UGT8	2-hydroxyacylsphingosine 1-beta-galactosyltransferase	8	9	13	0	0	10	0
105	IPI00024143	AAAS	Aladin	12	12	5	0	1	10	1
106	IPI00009997	B3GNT1	N-acetyllactosaminide beta-1,3-N-acetylglucosaminyltransferase	8	11	9	0	0	9	0
107	IPI00030236	C1orf160	Uncharacterized protein C1orf160	10	12	6	0	0	9	0
108	IPI00171410	C3orf21	Uncharacterized protein C3orf21	5	18	5	0	0	9	0
109	IPI00550165	DHRS7B	dehydrogenase/reductase (SDR family) member 7B	15	8	5	1	0	9	1
110	IPI00784217	HRAS	29 kDa protein	12	12	4	0	0	9	0
111	IPI00028116	KDELR1	ER lumen protein retaining receptor 1	10	4	14	0	0	9	0
112	IPI00328921	PEMT	phosphatidylethanolamine N-methyltransferase	25	2	1	0	0	9	0
113	IPI00009976	TMED1	Transmembrane emp24 domain-containing protein 1	7	12	9	1	0	9	1
114	IPI00168284	UBAC2	UBA domain-containing protein PHGDHL1	11	10	7	0	0	9	0
115	IPI00478838	MLSTD2	Uncharacterized protein MLSTD2	6	15	6	0	0	9	0
116	IPI00782958	RDH11	Uncharacterized protein RDH11	10	10	7	0	1	9	1
117	IPI00412147	SLC27A4	Long-chain fatty acid transport protein 4	5	18	4	0	0	9	0
118	IPI00386760	TMEM48	Nucleoporin NDC1	10	10	7	0	0	9	0
119	IPI00295772	CYP51A1	cytochrome P450, family 51	4	15	7	1	0	9	1
120	IPI00472939	SPCS2	Signal peptidase complex subunit 2	4	16	6	0	0	9	0
121	IPI00301841	TMEM161A	Transmembrane protein 161A	7	9	10	0	0	9	0
122	IPI00008350	ZDHHC6	Probable palmitoyltransferase ZDHHC6	3	13	10	0	0	9	0
123	IPI00477729	ACOX1	Acyl-coenzyme A oxidase 1, peroxisomal	4	20	1	0	0	8	0
124	IPI00300971	ALG6	Asparagine-linked glycosylation 6 homolog	8	12	5	0	0	8	0
125	IPI00001891	AUP1	Ancient ubiquitous protein 1	5	12	8	0	0	8	0
126	IPI00844338	MTCH1	MTCH1 protein	8	12	5	0	0	8	0
127	IPI00016339	RAB5C	Ras-related protein Rab-5C	9	12	4	1	1	8	1
128	IPI00294159	SLC25A1	Tricarboxylate transport protein, mitochondrial	14	9	2	0	3	8	2
129	IPI00171421	C8orf55	Uncharacterized protein C8orf55	5	12	7	0	0	8	0
130	IPI00478208	hCG_2004593	hypothetical protein LOC645296	7	12	5	2	1	8	2
131	IPI00423568	KRAS	GTPase Kras	7	13	4	0	0	8	0
132	IPI00470649	NCLN	Nicalin	10	11	3	0	0	8	0
133	IPI00019407	NSDHL	Sterol-4-alpha-carboxylate 3-dehydrogenase, decarboxylating	10	9	5	1	0	8	1
134	IPI00031755	RCE1	CAAX prenyl protease 2	5	14	5	0	0	8	0
135	IPI00303214	TYSND1	Peroxisomal leader peptide-processing protease	8	8	8	0	0	8	0
136	IPI00034277	ATP13A1	Probable cation-transporting ATPase 13A1	3	12	8	0	0	8	0
137	IPI00477118	FLJ20254	Uncharacterized protein	5	13	5	0	0	8	0
138	IPI00029133	ATP5F1	ATP synthase B chain, mitochondrial	9	8	5	0	2	7	1
139	IPI00020510	CISD1	CDGSH iron sulfur domain-containing protein 1	14	6	2	0	0	7	0
140	IPI00009607	RAP2C	Ras-related protein Rap-2c	11	8	3	0	0	7	0
141	IPI00008351	SELT	Selenoprotein T	10	8	4	0	0	7	0
142	IPI00018415	TM9SF2	Transmembrane 9 superfamily protein member 2	4	13	5	1	0	7	1
143	IPI00328272	ZDHHC5	Probable palmitoyltransferase ZDHHC5	7	9	6	1	0	7	1
144	IPI00061777	CCDC97	Coiled-coil domain-containing protein 97	4	10	7	0	0	7	0
145	IPI00477518	EBAG9	Placenta derived apoptotic factor	4	12	5	0	0	7	0
146	IPI00418754	FLJ45032	CDNA FLJ45032 fis, clone BRAWH3018969	0	13	8	0	0	7	0
147	IPI00023406	HCCS	Cytochrome c-type heme lyase	6	11	4	0	2	7	1
148	IPI00220687	HM13	Isoform 2 of Minor histocompatibility antigen H13	5	14	2	0	0	7	0
149	IPI00413817	SERINC1	Serine incorporator 1	3	7	11	0	0	7	0
150	IPI00009225	STX8	Syntaxin-8	2	14	5	0	0	7	0
151	IPI00640630	-	Uncharacterized protein USMG5P1	11	6	3	1	1	7	1
152	IPI00639909	C1orf142	Uncharacterized protein C1orf142	6	8	6	0	0	7	0
153	IPI00005775	CEPT1	Choline/ethanolaminephosphotransferase 1	3	8	9	0	0	7	0
154	IPI00020124	PI4K2A	Phosphatidylinositol 4-kinase type 2-alpha	5	9	6	0	0	7	0
155	IPI00291007	SCARB1	Isoform 3 of Scavenger receptor class B member 1	3	10	7	0	0	7	0
156	IPI00063903	USMG5	Up-regulated during skeletal muscle growth protein 5	11	6	3	1	1	7	1
157	IPI00556385	ADPGK	ADP-dependent glucokinase	5	10	4	0	0	6	0
158	IPI00019141	AGPAT1	1-acyl-sn-glycerol-3-phosphate acyltransferase alpha	5	12	2	0	0	6	0
159	IPI00291695	LOC493869	Glutathione peroxidase	7	9	3	0	0	6	0
160	IPI00792395	POR	Putative uncharacterized protein DKFZp686G04235	5	11	3	0	2	6	1
161	IPI00549664	TEX10	Testis-expressed sequence 10 protein	4	11	4	0	0	6	0
162	IPI00032150	CDS2	Phosphatidate cytidylyltransferase 2	4	9	5	0	0	6	0
163	IPI00433284	GLCE	D-glucuronyl C5-epimerase	5	8	5	0	0	6	0
164	IPI00032355	PUM1	Pumilio homolog 1	4	11	3	0	0	6	0
165	IPI00478787	RAB18	RAB18, member RAS oncogene family	8	8	2	0	1	6	1
166	IPI00007755	RAB21	Ras-related protein Rab-21	7	7	4	1	0	6	1
167	IPI00005751	SPTLC2	Serine palmitoyltransferase 2	7	9	2	0	0	6	0
168	IPI00383684	C1orf121	UPF0326 protein C1orf121	4	8	5	0	0	6	0
169	IPI00299387	C3orf1	Uncharacterized protein C3orf1	4	9	4	0	0	6	0
170	IPI00032358	POM121	Nuclear envelope pore membrane protein POM 121	7	7	3	1	0	6	1
171	IPI00016513	RAB10	Ras-related protein Rab-10	6	8	3	0	1	6	1
172	IPI00016373	RAB13	Ras-related protein Rab-13	6	9	2	2	0	6	1
173	IPI00217536	RHOT1	Isoform 3 of Mitochondrial Rho GTPase 1	5	8	4	0	0	6	0
174	IPI00410034	SLC38A2	Solute carrier family 38 member 2	6	7	4	0	0	6	0
175	IPI00010438	SNAP23	SNAP-23a of Synaptosomal-associated protein 23	2	11	4	0	0	6	0
176	IPI00829865	TMTC3	Transmembrane and TPR repeat-containing protein 3	4	9	4	0	0	6	0
177	IPI00398974	ZDHHC20	Probable palmitoyltransferase ZDHHC20	7	5	5	0	0	6	0
178	IPI00830076	-	40 kDa protein	6	6	4	0	0	5	0
179	IPI00844526	ABHD12	Uncharacterized protein ABHD12	1	12	3	0	0	5	0
180	IPI00844092	APOOL	Putative uncharacterized protein DKFZp779P1227	3	11	2	0	0	5	0

181	IPI00215919	ARF5	ADP-ribosylation factor 5	0	11	5	0	0	5	0
182	IPI00157215	C19orf52	Uncharacterized protein C19orf52	1	7	8	1	0	5	1
183	IPI00290526	CCDC8	Coiled-coil domain-containing protein 8	4	9	3	0	0	5	0
184	IPI00010187	ELOVL1	Elongation of very long chain fatty acids protein 1	7	3	6	0	0	5	0
185	IPI00657706	LENG4	Leukocyte receptor cluster member 4	3	8	5	0	0	5	0
186	IPI00016610	PCBP1	Poly(rC)-binding protein 1	7	9	0	0	0	5	0
187	IPI00010232	PEX3	Peroxisomal biogenesis factor 3	3	11	2	0	0	5	0
188	IPI00291544	SQLE	Squalene monooxygenase	3	13	0	0	0	5	0
189	IPI00646625	TAP1	transporter 1, ATP-binding cassette, sub-family B	5	9	2	0	0	5	0
190	IPI00790248	VAMP2	13 kDa protein	0	11	5	1	0	5	1
191	IPI00006211	VAPB	Vesicle-associated membrane protein-associated protein B/C	6	7	3	1	1	5	1
192	IPI00738055	-	Uncharacterized protein	6	9	0	2	0	5	1
193	IPI00464993	AGPAT2	1-acylglycerol-3-phosphate O-acyltransferase 2	5	5	5	0	0	5	0
194	IPI00514471	AIG1	Androgen-induced protein 1	6	6	3	0	0	5	0
195	IPI00306048	ATAD3B	ATPase family AAA domain-containing protein 3B	6	7	2	0	0	5	0
196	IPI00022305	BZW2	Basic leucine zipper and W2 domain-containing protein 2	3	9	3	1	0	5	1
197	IPI00002478	ECE1	Endothelin-converting enzyme 1	3	9	3	0	0	5	0
198	IPI00556024	ELOVL5	35 kDa protein	4	6	5	0	0	5	0
199	IPI00480131	FLNB	Uncharacterized protein FLNB	4	7	4	0	0	5	0
200	IPI00789740	GEMIN4	Gem (Nuclear organelle) associated protein 4	4	9	2	0	0	5	0
201	IPI00472858	GPR89A	Uncharacterized protein GPR89B	2	13	0	0	0	5	0
202	IPI00410714	HBA2;HBA1	Hemoglobin subunit alpha	2	9	4	0	0	5	0
203	IPI00022300	METTL7A	Methyltransferase-like protein 7A	4	6	5	0	0	5	0
204	IPI00299468	SCD	Acyl-CoA desaturase	6	6	3	0	1	5	1
205	IPI00016968	SDHC	Succinate dehydrogenase cytochrome b560 subunit, mitochondrial	4	6	5	0	0	5	0
206	IPI00432425	SPTLC1	SPTLC1 protein	6	7	2	1	1	5	1
207	IPI00019004	TLOC1	Translocation protein SEC62	6	7	2	0	0	5	0
208	IPI00738677	-	Uncharacterized protein	8	0	6	0	0	5	0
209	IPI00102501	AGTRAP	Type-1 angiotensin II receptor-associated protein	5	7	2	0	1	5	1
210	IPI00294501	DHCR7	7-dehydrocholesterol reductase	4	8	2	0	0	5	0
211	IPI00644882	FAM69B	hypothetical protein LOC138311	4	6	4	0	0	5	0
212	IPI00001159	GCN1L1	GCN1-like protein 1	0	13	1	1	0	5	1
213	IPI00786874	GPR89C	G protein-coupled receptor 89C	1	10	3	0	0	5	0
214	IPI00329598	HSD17B11	Dehydrogenase/reductase SDR family member 8	1	5	8	0	0	5	0
215	IPI00554541	ILVBL	ilvB (bacterial acetolactate synthase)-like	2	10	2	0	0	5	0
216	IPI00009950	LMAN2	Vesicular integral-membrane protein VIP36	1	9	4	0	0	5	0
217	IPI00828198	MOSC1	MOSC domain-containing protein 1, mitochondrial	2	8	4	0	1	5	1
218	IPI00007909	RABAC1	Prenylated Rab acceptor protein 1	4	8	2	0	0	5	0
219	IPI00296157	RETSAT	All-trans-retinol 13,14-reductase	4	9	1	1	0	5	1
220	IPI00028635	RPN2	Ribophorin II	2	7	5	0	1	5	1
221	IPI00024650	SLC16A1	Monocarboxylate transporter 1	6	6	2	0	0	5	0
222	IPI00217277	SLC25A10	Mitochondrial dicarboxylate carrier	1	7	6	0	0	5	0
223	IPI00014440	SLC25A17	Peroxisomal membrane protein PMP34	3	6	5	0	0	5	0
224	IPI00013449	TSPAN6	Tetraspanin-6	4	6	4	0	0	5	0
225	IPI00298971	VTN	Vitronectin precursor	8	3	3	0	0	5	0
226	IPI00015826	ABCB10	ATP-binding cassette sub-family B member 10, mitochondrial	3	8	2	0	0	4	0
227	IPI00107357	CLPTM1	Cleft lip and palate transmembrane protein 1	3	7	3	0	0	4	0
228	IPI00166130	D15Wsu75e	DJ347H13.4 protein	11	1	1	0	0	4	0
229	IPI00174757	FBXL20	F-box/LRR-repeat protein 20	4	8	1	0	0	4	0
230	IPI00030634	GGTL3	Gamma-glutamyltransferase 4	2	5	6	0	0	4	0
231	IPI00023567	GHITM	Growth hormone-inducible transmembrane protein	6	6	1	0	0	4	0
232	IPI00465121	GNAI2	Galphai2 protein	0	10	3	0	0	4	0
233	IPI00419643	LYCAT	Lysocardiolipin acyltransferase	2	6	5	0	1	4	1
234	IPI00023974	PTTG1IP	Pituitary tumor-transforming gene 1 protein-interacting protein	4	6	3	0	0	4	0
235	IPI00550882	PYCR1	Pyrroline-5-carboxylate reductase 1	2	8	3	0	0	4	0
236	IPI00101186	RRP12	RRP12-like protein	0	7	6	0	1	4	1
237	IPI00218466	SEC61A1	Protein transport protein Sec61 subunit alpha	3	5	5	0	0	4	0
238	IPI00000948	TBL2	Transducin beta-like 2 protein	5	6	2	0	0	4	0
239	IPI00164949	TH1L	NELF-C of Negative elongation factor C/D	2	8	3	0	0	4	0
240	IPI00030847	TM9SF3	Transmembrane 9 superfamily protein member 3	5	4	4	0	0	4	0
241	IPI00061677	ALG14	UDP-N-acetylglucosamine transferase subunit ALG14 homolog	9	3	0	0	0	4	0
242	IPI00005163	ARL15	ADP-ribosylation factor-like protein 15	2	6	4	0	0	4	0
243	IPI00013466	ASNA1	Uncharacterized protein ASNA1	1	10	1	0	0	4	0
244	IPI00303401	C1orf75	Transmembrane protein C1orf75	3	8	1	0	0	4	0
245	IPI00102928	CYB5D2	Cytochrome b5 domain-containing protein 2	1	5	6	0	0	4	0
246	IPI00845461	DKFZP564J0863	Atlastin-3	1	9	2	0	0	4	0
247	IPI00029099	FAM69A	Protein FAM69A	2	9	1	0	0	4	0
248	IPI00642584	KIAA0090	Uncharacterized protein KIAA0090	2	6	4	0	0	4	0
249	IPI00642378	LASS2	LAG1 homolog, ceramide synthase 2	2	5	5	0	0	4	0
250	IPI00008511	MT-ND5	NADH-ubiquinone oxidoreductase chain 5	1	6	5	0	0	4	0
251	IPI00107753	OPA1	optic atrophy 1	0	9	3	0	0	4	0
252	IPI00329373	P117	Protein QIL1	6	3	3	0	0	4	0
253	IPI00240812	PDS5B	Androgen-induced proliferation inhibitor	2	7	3	0	0	4	0
254	IPI00293189	PERP	p53 apoptosis effector related to PMP-22	1	8	3	0	0	4	0
255	IPI00010746	PTDSS1	Phosphatidylserine synthase 1	1	8	3	0	0	4	0
256	IPI00217519	RALA	Ras-related protein Ral-A	6	4	2	0	1	4	1
257	IPI00329200	RANBP5	Importin-5	2	8	2	1	0	4	1
258	IPI00026627	RP2	Protein XRP2	2	8	2	0	0	4	0
259	IPI00218850	SCAMP2	Secretory carrier-associated membrane protein 2	6	4	2	0	0	4	0
260	IPI00217766	SCARB2	Lysosome membrane protein 2	3	7	2	0	0	4	0
261	IPI00031822	SLC5A6	Sodium-dependent multivitamin transporter	3	9	0	0	0	4	0
262	IPI00170517	TMEM115	Transmembrane protein 115	0	10	2	0	0	4	0
263	IPI00852851	TRABD	TraB Domain-Containing Protein	1	8	3	0	0	4	0
264	IPI00166079	VKORC1L1	Vitamin K epoxide reductase complex subunit 1-like protein 1	5	5	2	0	0	4	0
265	IPI00000115	CNIH4	Cornichon homolog 4	6	3	2	0	0	4	0
266	IPI00183603	DC2	DC2 protein	3	4	4	1	0	4	1
267	IPI00059955	DHRS13	dehydrogenase/reductase (SDR family) member 13	1	7	3	0	0	4	0
268	IPI00219678	EIF2S1	Eukaryotic translation initiation factor 2 subunit 1	4	7	0	0	1	4	1
269	IPI00216067	GK	Glycerol kinase	2	5	4	0	0	4	0
270	IPI00009747	LSS	Lanosterol synthase	4	5	2	0	0	4	0
271	IPI00470859	MAN1B1	Putative uncharacterized protein DKFZp686C04126	1	6	4	0	0	4	0
272	IPI00017510	MT-CO2	Cytochrome c oxidase subunit 2	3	6	2	0	1	4	1

273	IPI00787089	PELP1	Proline-, glutamic acid- and leucine-rich protein 1	4	6	1	1	0	4	1
274	IPI00217421	PIGO	GPI ethanolamine phosphate transferase 3	2	9	0	0	0	4	0
275	IPI00009447	PIGQ	Phosphatidylinositol N-acetylglucosaminyltransferase subunit Q	0	7	4	0	0	4	0
276	IPI00298731	PPP1R10	Serine/threonine-protein phosphatase 1 regulatory subunit 10	3	5	3	0	0	4	0
277	IPI00376394	QSOX2	Uncharacterized protein QSOX2	1	7	3	1	0	4	1
278	IPI00219833	TIMM17B	Mitochondrial import inner membrane translocase subunit Tim17-B	2	8	1	0	0	4	0
279	IPI00018237	TMEM38B	Transmembrane protein 38B	3	6	2	0	0	4	0
280	IPI00000735	TSPAN13	Tetraspanin-13	4	5	2	0	0	4	0
281	IPI00221179	ZDHHC7	Palmitoyltransferase ZDHHC7	6	3	2	0	0	4	0
282	IPI00295851	COPB1	Coatomer subunit beta	1	8	1	0	1	3	1
283	IPI00074870	DNAJC1	DnaJ homolog subfamily C member 1	2	7	1	0	0	3	0
284	IPI00007461	DPY19L1	dpy-19-like 1	0	6	4	0	0	3	0
285	IPI00025818	GALNT1	Polypeptide N-acetylgalactosaminyltransferase 1	3	6	1	0	0	3	0
286	IPI00305698	GGCX	Vitamin K-dependent gamma-carboxylase	3	5	2	0	0	3	0
287	IPI00410584	LONP2	Peroxisomal Lon protease homolog 2	0	8	2	0	0	3	0
288	IPI00719120	MRPL28	Mitochondrial ribosomal protein L28	2	8	0	0	0	3	0
289	IPI00013678	MTX1	metaxin 1	4	4	2	1	0	3	1
290	IPI00103059	NAT14	N-acetyltransferase 14	4	3	3	0	0	3	0
291	IPI00026044	PIGU	GPI transamidase component PIG-U	3	4	3	0	0	3	0
292	IPI00028481	RAB8A	Ras-related protein Rab-8A	3	7	0	0	0	3	0
293	IPI00018364	RAP2B	Ras-related protein Rap-2b precursor	0	9	1	0	0	3	0
294	IPI00337494	SLC25A24	solute carrier family 25 member 24	2	8	0	0	0	3	0
295	IPI00152377	STT3B	Dolichyl-diphosphooligosaccharide--protein glycosyltransferase subunit STT3B	2	7	1	0	0	3	0
296	IPI00013236	SYBL1	Synaptobrevin-like protein 1	2	4	4	0	1	3	1
297	IPI00026111	TMCO1	Transmembrane and coiled-coil domain-containing protein 1	6	0	4	0	0	3	0
298	IPI00385495	TMEM112B	Transmembrane protein 153	2	8	0	0	0	3	0
299	IPI00307572	TMEM165	Transmembrane protein 165	2	7	1	1	0	3	1
300	IPI00029705	TUBGCP2	Gamma-tubulin complex component 2	3	5	2	0	0	3	0
301	IPI00171445	ATAD1	ATPase family AAA domain-containing protein 1	2	4	3	1	0	3	1
302	IPI00025366	CS	Citrate synthase, mitochondrial	1	5	3	0	1	3	1
303	IPI00383704	DULLARD	Serine/threonine-protein phosphatase dullard	1	7	1	0	0	3	0
304	IPI00015952	EIF4G2	Eukaryotic translation initiation factor 4 gamma 2	2	6	1	0	0	3	0
305	IPI00784409	F2	70 kDa protein	1	6	2	0	0	3	0
306	IPI00013281	FKRP	Fukutin-related protein	3	4	2	0	0	3	0
307	IPI00328170	GCS1	Mannosyl-oligosaccharide glucosidase	2	6	1	0	1	3	1
308	IPI00030356	MCL1	Induced myeloid leukemia cell differentiation protein Mcl-1	1	7	1	0	0	3	0
309	IPI00410211	DPY19L3	Dpy-19-like protein 3	0	4	5	1	0	3	1
310	IPI00012315	NME3	Nucleoside diphosphate kinase 3	2	5	2	0	0	3	0
311	IPI00220987	PEX10	Isoform 2 of Peroxisome assembly protein 10	2	6	1	0	0	3	0
312	IPI00784216	PFKL	Liver phosphofructokinase	2	6	1	0	0	3	0
313	IPI00005263	PIGH	Phosphatidylinositol N-acetylglucosaminyltransferase subunit H	1	5	3	0	0	3	0
314	IPI00742852	PKMYT1	Uncharacterized protein PKMYT1	1	6	2	0	0	3	0
315	IPI00033349	PREB	Prolactin regulatory element-binding protein	2	6	1	0	1	3	1
316	IPI00005728	RER1	RER1 protein	3	5	1	0	0	3	0
317	IPI00219153	RPL22	60S ribosomal protein L22	1	6	2	1	0	3	1
318	IPI00182533	RPL28	60S ribosomal protein L28	4	1	4	1	0	3	1
319	IPI00028068	SLC25A19	Mitochondrial deoxynucleotide carrier	2	5	2	0	0	3	0
320	IPI00018071	SLC6A15	Orphan sodium- and chloride-dependent neurotransmitter transporter NTT73	3	5	1	0	0	3	0
321	IPI00030166	ST7	suppression of tumorigenicity 7	1	8	0	0	0	3	0
322	IPI00742851	TCTN2	Uncharacterized protein C12orf38	3	4	2	0	0	3	0
323	IPI00477734	YES1	YES1	3	5	1	0	0	3	0
324	IPI00748014	-	Uncharacterized protein	1	4	3	0	0	3	0
325	IPI00744964	-	HLA-C, HLA class I histocompatibility antigen	3	3	2	0	0	3	0
326	IPI00107039	ABHD6	Abhydrolase domain-containing protein 6	4	3	1	0	0	3	0
327	IPI00002506	ALG5	Dolichyl-phosphate beta-glucosyltransferase	2	5	1	0	0	3	0
328	IPI00298147	ANGEL1	Protein angel homolog 1	1	5	2	0	0	3	0
329	IPI00845436	ARF4	similar to ADP-ribosylation factor 4	1	5	2	1	0	3	1
330	IPI00479241	ARV1	Uncharacterized protein ARV1	2	5	1	0	0	3	0
331	IPI00645431	BAT3	HLA-B associated transcript 3	1	4	3	0	0	3	0
332	IPI00218200	BCAP31	B-cell receptor-associated protein 31	2	5	1	0	0	3	0
333	IPI00009922	C14orf156	SRA stem-loop-interacting RNA-binding protein, mitochondrial	2	5	1	0	0	3	0
334	IPI00006980	C14orf166	Protein C14orf166	1	6	1	0	1	3	1
335	IPI00374076	C20orf142	Uncharacterized protein C20orf142	0	7	1	0	0	3	0
336	IPI00418301	C3orf33	Uncharacterized protein C3orf33	1	5	2	0	0	3	0
337	IPI00032258	C4A	Complement C4-A	1	6	1	0	0	3	0
338	IPI00418163	C4B;C4A	complement component 4B preproprotein	1	6	1	0	0	3	0
339	IPI00019560	C6orf64	Uncharacterized protein C6orf64	0	6	2	0	0	3	0
340	IPI00642041	COMTD1	Catechol-O-methyltransferase domain-containing protein 1	1	5	2	0	0	3	0
341	IPI00012887	CTSL1	Cathepsin L precursor	3	5	0	1	0	3	1
342	IPI00291417	DCAKD	Dephospho-CoA kinase domain-containing protein	2	4	2	0	0	3	0
343	IPI00007165	DOLK	Transmembrane protein 15	5	1	2	0	0	3	0
344	IPI00640276	EFHA1	EF-hand domain-containing family member A1	0	6	2	0	0	3	0
345	IPI00472099	ERGIC3	Endoplasmic reticulum-Golgi intermediate compartment protein 3	0	6	2	0	0	3	0
346	IPI00015135	EXTL3	Exostosin-like 3	1	5	2	0	0	3	0
347	IPI00795979	FLOT2	Flotillin-2	1	5	2	0	0	3	0
348	IPI00031052	G6PC3	glucose-6-phosphatase catalytic subunit 3	3	2	3	0	0	3	0
349	IPI00384961	GPR177	Integral membrane protein GPR177	1	5	2	0	0	3	0
350	IPI00815882	HLA-A;HLA-B;	similar to HLA class I histocompatibility antigen, B-18 alpha chain	1	5	2	0	1	3	1
351	IPI00718879	HLA-E	Major histocompatibility complex, class I, E	3	3	2	0	0	3	0
352	IPI00656079	MIER1	Mesoderm induction early response protein 1	1	5	2	0	0	3	0
353	IPI00787791	NOC4L	similar to nucleolar complex associated 4 homolog	0	6	2	0	0	3	0
354	IPI00005107	NPC1	Niemann-Pick C1 protein precursor	1	5	2	0	0	3	0
355	IPI00291755	NUP210	Uncharacterized protein NUP210	1	5	2	0	0	3	0
356	IPI00384280	PCYOX1	Prenylcysteine oxidase 1	0	5	3	0	0	3	0
357	IPI00020042	PSMC4	26S protease regulatory subunit 6B	1	7	0	1	0	3	1
358	IPI00019346	RAP2A	Ras-related protein Rap-2a	4	4	0	0	0	3	0
359	IPI00099996	RG9MTD1	RNA (guanine-9-) methyltransferase domain-containing protein 1	2	6	0	0	0	3	0
360	IPI00029731	RPL35A	60S ribosomal protein L35a	1	5	2	0	1	3	1
361	IPI00329600	SCCPDH	Probable saccharopine dehydrogenase	1	4	3	0	0	3	0
362	IPI00642271	SLC35B2	Adenosine 3'-phospho 5'-phosphosulfate transporter 1	3	3	2	0	0	3	0
363	IPI00101952	SLC35E1	Solute carrier family 35 member E1	2	2	4	0	0	3	0
364	IPI00221393	SLC44A1	Isoform 1 of Choline transporter-like protein 1	2	3	3	0	0	3	0

365	IPI00217882	SORT1	Sortilin precursor	3	4	1	0	0	3	0
366	IPI00411628	STEAP3	Isoform 2 of Metalloreductase STEAP3	0	6	2	0	0	3	0
367	IPI00021985	TM9SF4	Transmembrane 9 superfamily protein member 4	1	7	0	0	0	3	0
368	IPI00470401	TMEM68	Transmembrane protein 68	1	4	3	0	0	3	0
369	IPI00789737	TMEM85	TMEM85	2	4	2	0	0	3	0
370	IPI00016676	TOMM20	Mitochondrial import receptor subunit TOM20 homolog	3	2	3	0	0	3	0
371	IPI00000736	TSPAN15	Tetraspanin-15	2	4	2	0	0	3	0
372	IPI00014149	TTC35	Tetratricopeptide repeat protein 35	1	3	4	0	1	3	1
373	IPI00004970	UTP20	Small subunit processome component 20 homolog	0	6	2	0	1	3	1
374	IPI00385128	AGPAT7	1-acyl-sn-glycerol-3-phosphate acyltransferase eta	2	4	1	0	0	2	0
375	IPI00386072	ALG2	Alpha-1,3-mannosyltransferase ALG2	2	4	1	0	0	2	0
376	IPI00217354	ARFGAP1	ADP-ribosylation factor GTPase-activating protein 1	2	4	1	0	0	2	0
377	IPI00169267	ARL6IP2	Atlastin-2	1	6	0	0	0	2	0
378	IPI00032423	DDX52	Probable ATP-dependent RNA helicase DDX52	2	5	0	0	0	2	0
379	IPI00470418	DHRS7	Putative uncharacterized protein DKFZp564H1664	1	4	2	0	0	2	0
380	IPI00376317	EDC4	Enhancer of mRNA-decapping protein 4	2	5	0	0	0	2	0
381	IPI00413930	ELOVL2	Elongation of very long chain fatty acids protein 2	3	4	0	0	0	2	0
382	IPI00029015	FVT1	3-ketodihydrosphingosine reductase	2	2	3	0	0	2	0
383	IPI00030811	GK;GK3P	Glycerol kinase, testis specific 1	2	5	0	0	0	2	0
384	IPI00004962	GOLIM4	Golgi integral membrane protein 4	2	3	2	0	0	2	0
385	IPI00749232	HACL1	Uncharacterized protein HACL1	1	4	2	0	0	2	0
386	IPI00830113	HBB	Delta-hemoglobin	2	3	2	0	0	2	0
387	IPI00293564	HMGCL	Hydroxymethylglutaryl-CoA lyase, mitochondrial	2	3	2	0	0	2	0
388	IPI00017283	IARS2	Isoleucyl-tRNA synthetase, mitochondrial	1	6	0	0	0	2	0
389	IPI00043598	IKIP	IKIP protein	1	5	1	0	0	2	0
390	IPI00008575	KHDRBS1	KH domain-containing, RNA-binding, signal transduction-associated protein 1	4	2	1	0	0	2	0
391	IPI00795030	LASS6	LASS6 protein	1	5	1	0	0	2	0
392	IPI00334453	LOC374395	Similar to RIKEN cDNA 1810059G22	2	3	2	0	0	2	0
393	IPI00293073	MFN1	Mitochondrial transmembrane GTPase FZO-2	2	5	0	0	0	2	0
394	IPI00021805	MGST1	Microsomal glutathione S-transferase 1	3	3	1	0	0	2	0
395	IPI00298235	POMT1	Protein O-mannosyl-transferase 1	1	3	3	0	0	2	0
396	IPI00305337	RFX1	MHC class II regulatory factor RFX1	1	3	3	0	0	2	0
397	IPI00412741	SFXN4	Isoform 1 of Sideroflexin-4	2	4	1	0	0	2	0
398	IPI00166484	SLC25A16	solute carrier family 25, member 16	2	5	0	0	0	2	0
399	IPI00003004	SLC25A22	Mitochondrial glutamate carrier 1	3	4	0	0	0	2	0
400	IPI00853224	STARD7	START domain containing 7	1	6	0	0	0	2	0
401	IPI00219682	STOM	Erythrocyte band 7 integral membrane protein	3	2	2	0	0	2	0
402	IPI00301280	TMEM43	Transmembrane protein 43	3	3	1	0	0	2	0
403	IPI00106966	TMEM70	Transmembrane protein 70	2	4	1	0	0	2	0
404	IPI00219111	TRAM1	Translocation-associated membrane protein 1	1	5	1	0	0	2	0
405	IPI00477161	TRIM13	ret finger protein 2 isoform 2	0	5	2	0	0	2	0
406	IPI00641933	TRIM59	109 kDa protein	2	5	0	0	0	2	0
407	IPI00455146	USP30	Ubiquitin carboxyl-terminal hydrolase 30	1	5	1	0	0	2	0
408	IPI00029954	VEZT	Vezatin	1	4	2	0	0	2	0
409	IPI00410067	ZC3HAV1	Zinc finger CCCH type antiviral protein 1	2	3	2	0	0	2	0
410	IPI00410687	ZDHHC17	Huntingtin interacting protein 14	0	6	1	0	0	2	0
411	IPI00001539	ACAA2	3-ketoacyl-CoA thiolase, mitochondrial	1	3	2	0	0	2	0
412	IPI00028491	AGPAT5	1-acyl-sn-glycerol-3-phosphate acyltransferase epsilon	1	5	0	0	0	2	0
413	IPI00014232	ARL6IP1	ARL-6-interacting protein 1	0	2	4	0	0	2	0
414	IPI00218919	ATP4A	Potassium-transporting ATPase alpha chain 1	0	4	2	0	0	2	0
415	IPI00002792	B4GALT7	Beta-1,4-galactosyltransferase 7	2	3	1	0	0	2	0
416	IPI00011420	BAK1	Putative uncharacterized protein DKFZp686D0345	1	4	1	0	0	2	0
417	IPI00607576	C9orf5	Uncharacterized protein C9orf5	2	4	0	0	0	2	0
418	IPI00166010	CNOT1	CCR4-NOT transcription complex, subunit 1 isoform a	2	3	1	0	0	2	0
419	IPI00025086	COX5A	Cytochrome c oxidase subunit 5A, mitochondrial	3	2	1	0	0	2	0
420	IPI00470674	CYB5R1	NADH-cytochrome b5 reductase 1	2	4	0	0	0	2	0
421	IPI00013271	DERL1	Derlin-1	1	4	1	0	0	2	0
422	IPI00796864	DPM1	Dolichyl-phosphate mannosyltransferase polypeptide 1, catalytic subunit	1	3	2	0	0	2	0
423	IPI00008599	EBP	3-beta-hydroxysteroid-Delta	2	2	2	0	0	2	0
424	IPI00398035	ELOVL7	34 kDa protein	0	5	1	0	0	2	0
425	IPI00643071	FAM108B1	Abhydrolase domain-containing protein FAM108B1	2	4	0	0	0	2	0
426	IPI00021594	GPAA1	Glycosylphosphatidylinositol anchor attachment 1 protein	2	2	2	0	0	2	0
427	IPI00031821	ITM2B	Integral membrane protein 2B	1	5	0	0	0	2	0
428	IPI00029046	KIAA0152	Uncharacterized protein KIAA0152 precursor	1	3	2	0	0	2	0
429	IPI00217966	LDHA	L-lactate dehydrogenase A chain	3	1	2	0	0	2	0
430	IPI00016334	MCAM	Cell surface glycoprotein MUC18	3	1	2	0	0	2	0
431	IPI00789529	MLSTD1	Fatty acyl-CoA reductase 2	1	5	0	0	0	2	0
432	IPI00103509	NDUFA10	NADH dehydrogenase ubiquinone 1 alpha subcomplex	1	5	0	0	0	2	0
433	IPI00061142	NUS1	Nogo-B receptor precursor	0	5	1	0	0	2	0
434	IPI00854642	PDS5A	Sister chromatid cohesion protein PDS5 homolog A	0	5	1	0	0	2	0
435	IPI00441867	PEX19	Isoform 1 of Peroxisomal biogenesis factor 19	1	4	1	0	0	2	0
436	IPI00643034	PLTP	Phospholipid transfer protein	0	5	1	0	0	2	0
437	IPI00028077	PSEN1	Presenilin-1	2	4	0	0	0	2	0
438	IPI00032808	RAB3D	Ras-related protein Rab-3D	0	4	2	0	0	2	0
439	IPI00023138	RAC3	Ras-related C3 botulinum toxin substrate 3	1	4	1	0	0	2	0
440	IPI00218086	RDH10	Retinol dehydrogenase 10	2	4	0	0	0	2	0
441	IPI00005129	SCAMP1	Secretory carrier-associated membrane protein 1	2	1	3	0	0	2	0
442	IPI00784117	SDHD	Uncharacterized protein SDHD	4	1	1	0	0	2	0
443	IPI00793181	SELS	25 kDa protein	1	4	1	0	0	2	0
444	IPI00032179	SERPINC1	Antithrombin III variant	2	3	1	0	0	2	0
445	IPI00217409	SLC37A4	Glucose-6-phosphate translocase	2	3	1	0	0	2	0
446	IPI00828125	SMPD4	Sphingomyelin phosphodiesterase 4	0	5	1	0	0	2	0
447	IPI00009507	SYPL1	Synaptophysin-like protein 1	1	4	1	0	0	2	0
448	IPI00002901	TEAD1	Transcriptional enhancer factor TEF-1	1	3	2	0	0	2	0
449	IPI00401264	TXNDC4	Thioredoxin domain-containing protein 4	1	5	0	0	0	2	0
450	IPI00171438	TXNDC5	Thioredoxin domain-containing protein 5	0	5	1	0	0	2	0

Appendix B

17ODYA Enriched MCF10a Proteomic Data Set

In Chapter four, we presented SILAC mass spectrometry-based proteomic data comparing 17ODYA-enriched proteins between MCF10a-EV and MCF10a-Snail cells. In the tables below, we have included the entire data set for the proteins enriched across these stable MCF10a lines. Mean SILAC ratios in each direction (i.e. $R_{EV/Snail}$ and $R_{Snail/EV}$) were computed based on the MS1 ion intensities of the precursor SILAC pairs. Proteins were first sorted by a directional consistency parameter referred to as $R \bullet R^{-1}$ and then by a fold-change parameter referred to as Δ. The value for $R \bullet R^{-1}$ is defined as the product of the mean ratios computed in each direction (i.e. $R_{EV/Snail} \times R_{Snail/EV}$) which, in the ideal case, would be inverses on one another. Thus, the closer this value is to unity the more consistent are the mean ratios between inverse experiments. The fold-change parameter Δ is defined as the sum of $R_{EV/Snail}$ and $1/R_{Snail/EV}$ divided by the sum of $1/R_{EV/Snail}$ and $R_{Snail/EV}$. This value represents the overall fold-change observed for EV over Snail. Lower values ($0<\Delta<1$) indicate proteins that were enriched more in the EV line compared to Snail, while larger values ($\Delta>1$) are associated with proteins enriched more in the Snail line compared to EV. Fold change values were not computed for proteins which only have a ratio in one direction. For more details regarding data analysis, see the methods section of chapter four.

Table 7 Full-length 17ODYA Enriched MCF10a Proteomic Data Set

			L(Snail) : H(EV)			L(EV) : H(Snail)				
UniProt Accession	**UniProt Entry Name**	**UniProt Protein Name**	**Mean**	**SD**	**SILAC Pairs**	**Mean**	**SD**	**SILAC Pairs**	**$R \bullet R^{-1}$**	**Δ**
Q9UMD9	COHA1_HUMAN	Collagen alpha-1(XVII) chain				28.57	6.71	10	0	
Q86X29	LSR_HUMAN	Lipolysis-stimulated lipoprotein receptor				12.22	1.302	4	0	
P09758	TACD2_HUMAN	Tumor-associated calcium signal transducer 2				14.55	0	2	0	
P12429	ANXA3_HUMAN	Annexin A3				7.582	5.643	7	0	
P22223	CADH3_HUMAN	Cadherin-3				7.78	0	2	0	
Q9Y446	PKP3_HUMAN	Plakophilin-3				9.053	1.037	6	0	
Q9Y624	JAM1_HUMAN	Junctional adhesion molecule A				9.692	0	2	0	
P22735	TGM1_HUMAN	Protein-glutamine gamma-glutamyltransferase K				9.946	3.39	12	0	
Q8WY22	BRI3B_HUMAN	BRI3-binding protein				3.23	1.713	4	0	
Q9UBC5	MYO1A_HUMAN	Unconventional myosin-Ia				4.15	2.579	6	0	
Q8TDN6	BRX1_HUMAN	Ribosome biogenesis protein BRX1 homolog				4.094	0	2	0	
O60437	PEPL_HUMAN	Periplakin				4.424	0.628	4	0	
Q8IYB8	SUV3_HUMAN	ATP-dependent RNA helicase SUPV3L1, mitochondrial				3.299	0	2	0	
Q9H0S4	DDX47_HUMAN	Probable ATP-dependent RNA helicase DDX47				4.82	0	2	0	
Q3SY69	AL1L2_HUMAN	Mitochondrial 10-formyltetrahydrofolate dehydrogenase				2.466	0	2	0	
P09622	DLDH_HUMAN	Dihydrolipoyl dehydrogenase, mitochondrial				2.421	0.348	12	0	
P18754	RCC1_HUMAN	Regulator of chromosome condensation				2.424	0.387	12	0	
Q96HS1	PGAM5_HUMAN	Serine/threonine-protein phosphatase PGAM5, mitochondrial				2.731	0.363	4	0	
O75380	NDUS6_HUMAN	NADH dehydrogenase [ubiquinone] iron-sulfur protein 6, mitochondrial				2.741	0.443	6	0	
Q02338	BDH_HUMAN	D-beta-hydroxybutyrate dehydrogenase, mitochondrial				3.039	0.008	4	0	

Q07021	C1QBP_HUMAN	Complement component 1 Q subcomponent-binding protein, mitochondrial				3.095	0.276	10	0	
Q14684	RRP1B_HUMAN	Ribosomal RNA processing protein 1 homolog B				2.508	0.19	6	0	
Q16531	DDB1_HUMAN	DNA damage-binding protein 1				3.226	0	2	0	
P08574	CY1_HUMAN	Cytochrome c1, heme protein, mitochondrial	0.25	0.01	6				0	
Q13428	TCOF_HUMAN	Treacle protein				4.032	0	2	0	
O00767	ACOD_HUMAN	Acyl-CoA desaturase				4.076	0.912	12	0	
P17480	UBF1_HUMAN	Nucleolar transcription factor 1				1.905	0.438	5	0	
O95140	MFN2_HUMAN	Mitofusin-2				1.905	0	2	0	
P10319	1B58_HUMAN	HLA class I histocompatibility antigen, B-58 alpha chain				2.518	0.628	4	0	
P18465	1B57_HUMAN	HLA class I histocompatibility antigen, B-57 alpha chain				2.518	0.628	4	0	
P30492	1B54_HUMAN	HLA class I histocompatibility antigen, B-54 alpha chain				2.518	0.628	4	0	
P07339	CATD_HUMAN	Cathepsin D				3.806	0	2	0	
Q9NQ55	SSF1_HUMAN	Suppressor of SWI4 1 homolog				3.816	1.179	4	0	
P49411	EFTU_HUMAN	Elongation factor Tu, mitochondrial				3.982	0.589	14	0	
Q9ULB1	NRX1A_HUMAN	Neurexin-1				4.194	0	2	0	
-	L_HRSVB	-	0.286	0	2				0	
P36957	ODO2_HUMAN	Dihydrolipoyllysine-residue succinyltransferase component of 2-oxoglutarate dehydrogenase complex, mitochondrial				1.7	0.161	12	0	
P08559	ODPA_HUMAN	Pyruvate dehydrogenase E1 component subunit alpha, somatic form, mitochondrial				1.988	0.152	7	0	
Q9Y5W8	SNX13_HUMAN	Sorting nexin-13				2.6	0	2	0	
Q96SI9	STRBP_HUMAN	Spermatid perinuclear RNA-binding protein				2.602	2.837	8	0	
O43615	TIM44_HUMAN	Mitochondrial import inner membrane translocase subunit TIM44				2.229	0.155	8	0	
Q9H7B2	RPF2_HUMAN	Ribosome production factor 2 homolog				2.17	0	2	0	
Q9BVP2	GNL3_HUMAN	Guanine nucleotide-binding protein-like 3				2.313	0.225	17	0	
Q9Y3T9	NOC2L_HUMAN	Nucleolar complex protein 2 homolog				2.328	0.271	8	0	

Q8IYB3	SRRM1_HUMAN	Serine/arginine repetitive matrix protein 1	0.31	0.08	8				0	
Q8TCS8	PNPT1_HUMAN	Polyribonucleotide nucleotidyltransferase 1, mitochondrial				3.323	0.504	6	0	
O95810	SDPR_HUMAN	Serum deprivation-response protein	0.312	0	2				0	
Q16134	ETFD_HUMAN	Electron transfer flavoprotein-ubiquinone oxidoreductase, mitochondrial	0.312	0.02	6				0	
Q9Y4K1	AIM1_HUMAN	Absent in melanoma 1 protein				1.236	0.092	10	0	
-	R1AB_CVHN5	-	0.316	0	2				0	
-	R1A_CVHN1	-	0.316	0	2				0	
-	R1AB_CVHN1	-	0.316	0	2				0	
-	R1A_CVHN5	-	0.316	0	2				0	
O15269	SPTC1_HUMAN	Serine palmitoyltransferase 1				1.086	0.117	4	0	
Q9NZN4	EHD2_HUMAN	EH domain-containing protein 2				1.087	0.118	12	0	
Q15643	TRIPB_HUMAN	Thyroid receptor-interacting protein 11	0.318	0.31	4				0	
Q14571	ITPR2_HUMAN	Inositol 1,4,5-trisphosphate receptor type 2	0.321	0.09	4				0	
O14684	PTGES_HUMAN	Prostaglandin E synthase				3.657	0.172	4	0	
P09211	GSTP1_HUMAN	Glutathione S-transferase P				2.689	0.702	16	0	
Q9NU22	MDN1_HUMAN	Midasin	0.337	0	2				0	
O95602	RPA1_HUMAN	DNA-directed RNA polymerase I subunit RPA1	0.337	0	2				0	
P30498	1B78_HUMAN	HLA class I histocompatibility antigen, B-78 alpha chain				2.179	0	2	0	
P18464	1B51_HUMAN	HLA class I histocompatibility antigen, B-51 alpha chain				2.179	0	2	0	
P30490	1B52_HUMAN	HLA class I histocompatibility antigen, B-52 alpha chain				2.179	0	2	0	
O95716	RAB3D_HUMAN	Ras-related protein Rab-3D				2.204	0.258	8	0	
Q5VTL8	PR38B_HUMAN	Pre-mRNA-splicing factor 38B				2.275	0.18	4	0	
Q15413	RYR3_HUMAN	Ryanodine receptor 3				2.647	0	2	0	
O00483	NDUA4_HUMAN	Cytochrome c oxidase subunit NDUFA4				1.993	0.092	8	0	
Q15424	SAFB1_HUMAN	Scaffold attachment factor B1				1.886	0.18	22	0	
Q9NP92	RT30_HUMAN	28S ribosomal protein S30, mitochondrial	0.365	0	2				0	

P82921	RT21_HUMAN	28S ribosomal protein S21, mitochondrial				2.441	0.528	8	0	
Q9NRC6	SPTN5_HUMAN	Spectrin beta chain, non-erythrocytic 5	0.366	0	2				0	
Q9Y6C9	MTCH2_HUMAN	Mitochondrial carrier homolog 2				1.895	0.071	4	0	
Q9H6R4	NOL6_HUMAN	Nucleolar protein 6				2.68	0.149	4	0	
Q3ZCQ8	TIM50_HUMAN	Mitochondrial import inner membrane translocase subunit TIM50	0.366	0	2				0	
Q92614	MY18A_HUMAN	Unconventional myosin-XVIIIa	0.372	0	2				0	
Q8N1A0	KT222_HUMAN	Keratin-like protein KRT222				6.625	0	2	0	
P35900	K1C20_HUMAN	Keratin, type I cytoskeletal 20				6.625	0	2	0	
Q9BRX8	F213A_HUMAN	Redox-regulatory protein FAM213A				6.748	0	2	0	
Q9UBX3	DIC_HUMAN	Mitochondrial dicarboxylate carrier	0.383	0	2				0	
Q6ZR08	DYH12_HUMAN	Dynein heavy chain 12, axonemal	0.384	0	2				0	
O14578	CTRO_HUMAN	Citron Rho-interacting kinase	0.386	0	2				0	
-	DHSB_HUMAN	-				2.114	0.314	16	0	
Q14151	SAFB2_HUMAN	Scaffold attachment factor B2				1.734	0.092	8	0	
P14678	RSMB_HUMAN	Small nuclear ribonucleoprotein-associated proteins B and B'				1.965	0.414	3	0	
P49756	RBM25_HUMAN	RNA-binding protein 25				1.966	0	2	0	
Q9UFH2	DYH17_HUMAN	Dynein heavy chain 17, axonemal				1.968	0	2	0	
P30510	1C14_HUMAN	HLA class I histocompatibility antigen, Cw-14 alpha chain				1.974	0	2	0	
Q29865	1C18_HUMAN	HLA class I histocompatibility antigen, Cw-18 alpha chain				1.974	0	2	0	
P30504	1C04_HUMAN	HLA class I histocompatibility antigen, Cw-4 alpha chain				1.974	0	2	0	
P17693	HLAG_HUMAN	HLA class I histocompatibility antigen, alpha chain G				1.974	0	2	0	
P78559	MAP1A_HUMAN	Microtubule-associated protein 1A	0.398	0	2				0	
Q6P1L8	RM14_HUMAN	39S ribosomal protein L14, mitochondrial				1.949	0	2	0	
Q13185	CBX3_HUMAN	Chromobox protein homolog 3				1.106	0	2	0	
P83916	CBX1_HUMAN	Chromobox protein homolog 1				1.106	0	2	0	
P12268	IMDH2_HUMAN	Inosine-5'-monophosphate dehydrogenase 2				1.107	0.162	14	0	

Q9H5Q4	TFB2M_HUMAN	Dimethyladenosine transferase 2, mitochondrial				1.642	0	2	0	
Q9Y6R7	FCGBP_HUMAN	IgGFc-binding protein				1.643	0	2	0	
P19404	NDUV2_HUMAN	NADH dehydrogenase [ubiquinone] flavoprotein 2, mitochondrial				2.065	0.146	3	0	
Q16718	NDUA5_HUMAN	NADH dehydrogenase [ubiquinone] 1 alpha subcomplex subunit 5				1.853	0	2	0	
Q9P015	RM15_HUMAN	39S ribosomal protein L15, mitochondrial				1.853	0	2	0	
Q5SY16	NOL9_HUMAN	Polynucleotide 5'-hydroxyl-kinase NOL9				1.84	0.219	12	0	
Q8NDA2	HMCN2_HUMAN	Hemicentin-2	0.697	0.32	4				0	
Q15006	EMC2_HUMAN	ER membrane protein complex subunit 2				1.401	0.18	10	0	
P55769	NH2L1_HUMAN	NHP2-like protein 1				2.241	0.155	6	0	
-	DEN_HHV11	-				2.141	0	2	0	
Q4G0P3	HYDIN_HUMAN	Hydrocephalus-inducing protein homolog	0.424	0	2				0	
P13646	K1C13_HUMAN	Keratin, type I cytoskeletal 13				3.737	1.784	8	0	
Q9Y230	RUVB2_HUMAN	RuvB-like 2				1.368	0.23	12	0	
Q7Z3Z0	K1C25_HUMAN	Keratin, type I cytoskeletal 25	0.445	0.03	4				0	
Q7Z3Y9	K1C26_HUMAN	Keratin, type I cytoskeletal 26	0.445	0.03	4				0	
Q7Z3Y8	K1C27_HUMAN	Keratin, type I cytoskeletal 27	0.445	0.03	4				0	
P11277	SPTB1_HUMAN	Spectrin beta chain, erythrocytic				1.634	0	2	0	
P52907	CAZA1_HUMAN	F-actin-capping protein subunit alpha-1				1.539	0.168	8	0	
P62314	SMD1_HUMAN	Small nuclear ribonucleoprotein Sm D1	0.451	0.02	6				0	
P25445	TNR6_HUMAN	Tumor necrosis factor receptor superfamily member 6				1.457	0.14	12	0	
Q29RF7	PDS5A_HUMAN	Sister chromatid cohesion protein PDS5 homolog A				1.459	0.093	6	0	
Q9BSD7	NTPCR_HUMAN	Cancer-related nucleoside-triphosphatase				1.423	0.345	4	0	
Q9NVI7	ATD3A_HUMAN	ATPase family AAA domain-containing protein 3A				1.744	0.573	12	0	
Q9UQE7	SMC3_HUMAN	Structural maintenance of chromosomes protein 3				1.66	0.402	12	0	
Q8IY95	TM192_HUMAN	Transmembrane protein 192				1.759	0.067	6	0	

Q92797	SYMPK_HUMAN	Symplekin				2.077	0.26	6	0	
Q8NI27	THOC2_HUMAN	THO complex subunit 2				1.775	0.097	5	0	
Q9Y512	SAM50_HUMAN	Sorting and assembly machinery component 50 homolog				1.785	0.093	4	0	
Q9Y4W6	AFG32_HUMAN	AFG3-like protein 2				1.787	0	2	0	
Q53H12	AGK_HUMAN	Acylglycerol kinase, mitochondrial	0.462	0	2				0	
Q8NBS9	TXND5_HUMAN	Thioredoxin domain-containing protein 5				1.219	0	2	0	
Q9H583	HEAT1_HUMAN	HEAT repeat-containing protein 1	0.466	0.42	28				0	
Q8NBM4	UBAC2_HUMAN	Ubiquitin-associated domain-containing protein 2				1.136	0	2	0	
Q9NSE4	SYIM_HUMAN	Isoleucine--tRNA ligase, mitochondrial				1.862	0.662	27	0	
P53804	TTC3_HUMAN	E3 ubiquitin-protein ligase TTC3				0.611	0	2	0	
Q9Y383	LC7L2_HUMAN	Putative RNA-binding protein Luc7-like 2				1.506	0.138	10	0	
Q9BZE1	RM37_HUMAN	39S ribosomal protein L37, mitochondrial				1.488	1.027	4	0	
Q7Z3Y7	K1C28_HUMAN	Keratin, type I cytoskeletal 28	0.477	0.19	10				0	
Q8N684	CPSF7_HUMAN	Cleavage and polyadenylation specificity factor subunit 7	0.478	0.02	6				0	
Q5JTV8	TOIP1_HUMAN	Torsin-1A-interacting protein 1				2.566	1.072	4	0	
Q9BQ67	GRWD1_HUMAN	Glutamate-rich WD repeat-containing protein 1				1.683	0	2	0	
O94906	PRP6_HUMAN	Pre-mRNA-processing factor 6				1.684	0.325	14	0	
Q8NAT2	TDRD5_HUMAN	Tudor domain-containing protein 5	0.48	0	2				0	
Q96RL7	VP13A_HUMAN	Vacuolar protein sorting-associated protein 13A	0.48	0	2				0	
Q9P225	DYH2_HUMAN	Dynein heavy chain 2, axonemal	0.481	0	2				0	
Q8WXX0	DYH7_HUMAN	Dynein heavy chain 7, axonemal	0.483	0	2				0	
-	R1AB_CVHOC	-				1.266	0.518	6	0	
-	R1A_CVHOC	-				1.266	0.518	6	0	
P30040	ERP29_HUMAN	Endoplasmic reticulum resident protein 29				1.425	0	2	0	
Q16850	CP51A_HUMAN	Lanosterol 14-alpha demethylase				1.418	0	2	0	
P42765	THIM_HUMAN	3-ketoacyl-CoA thiolase, mitochondrial				1.636	0.329	10	0	

Q9NW13	RBM28_HUMAN	RNA-binding protein 28	0.501	0.15	12				0	
Q9Y6M5	ZNT1_HUMAN	Zinc transporter 1				1.315	0	2	0	
Q9UHX1	PUF60_HUMAN	Poly(U)-binding-splicing factor PUF60				1.578	0.52	6	0	
Q9Y2L1	RRP44_HUMAN	Exosome complex exonuclease RRP44				1.359	0	2	0	
P04156	PRIO_HUMAN	Major prion protein				1.361	0.014	8	0	
O60508	PRP17_HUMAN	Pre-mRNA-processing factor 17				1.361	0	2	0	
Q9Y320	TMX2_HUMAN	Thioredoxin-related transmembrane protein 2				1.361	0	2	0	
O94901	SUN1_HUMAN	SUN domain-containing protein 1	0.506	0	4				0	
Q8IUE6	H2A2B_HUMAN	Histone H2A type 2-B	0.511	0.13	4				0	
Q14674	ESPL1_HUMAN	Separin	0.513		1				0	
Q16787	LAMA3_HUMAN	Laminin subunit alpha-3	0.521	0	2				0	
O95071	UBR5_HUMAN	E3 ubiquitin-protein ligase UBR5	0.527	0	2				0	
O14936	CSKP_HUMAN	Peripheral plasma membrane protein CASK	0.528	0	2				0	
O95292	VAPB_HUMAN	Vesicle-associated membrane protein-associated protein B/C				1.767	0.115	4	0	
Q01081	U2AF1_HUMAN	Splicing factor U2AF 35 kDa subunit				1.678	0.025	4	0	
P21817	RYR1_HUMAN	Ryanodine receptor 1	0.537	0.45	4				0	
O75251	NDUS7_HUMAN	NADH dehydrogenase [ubiquinone] iron-sulfur protein 7, mitochondrial				1.957	0.091	6	0	
Q6NZI2	PTRF_HUMAN	Polymerase I and transcript release factor				1.265	0.269	4	0	
Q587I9	SFT2C_HUMAN	Vesicle transport protein SFT2C				1.464	0.051	3	0	
Q9NQA5	TRPV5_HUMAN	Transient receptor potential cation channel subfamily V member 5				1.292	0	2	0	
Q9BX66	SRBS1_HUMAN	Sorbin and SH3 domain-containing protein 1				1.293	0	2	0	
Q9Y394	DHRS7_HUMAN	Dehydrogenase/reductase SDR family member 7				1.339	0.257	4	0	
Q9BXP5	SRRT_HUMAN	Serrate RNA effector molecule homolog				1.341	0	2	0	
P38159	RBMX_HUMAN	RNA-binding motif protein, X chromosome				1.342	0	2	0	
Q96E39	RMXL1_HUMAN	RNA binding motif protein, X-linked-like-1				1.342	0	2	0	
Q96QV6	H2A1A_HUMAN	Histone H2A type 1-A	0.55	0.09	10				0	
P16104	H2AX_HUMAN	Histone H2AX	0.55	0.09	10				0	

Q12873	CHD3_HUMAN	Chromodomain-helicase-DNA-binding protein 3				1.24	0	2	0	
Q8TDI0	CHD5_HUMAN	Chromodomain-helicase-DNA-binding protein 5				1.24	0	2	0	
Q99798	ACON_HUMAN	Aconitate hydratase, mitochondrial				2.574	0	2	0	
O60763	USO1_HUMAN	General vesicular transport factor p115				1.146	0.069	4	0	
Q6DRA6	H2B2D_HUMAN	Putative histone H2B type 2-D				1.322	0	2	0	
O75915	PRAF3_HUMAN	PRA1 family protein 3				1.297	0.116	6	0	
Q8WUM0	NU133_HUMAN	Nuclear pore complex protein Nup133				1.298	0	2	0	
Q9C0F0	ASXL3_HUMAN	Putative Polycomb group protein ASXL3	0.578	0.03	4				0	
Q8WXF1	PSPC1_HUMAN	Paraspeckle component 1				1.531	0.415	6	0	
Q6ZRV2	FA83H_HUMAN	Protein FAM83H				1.481	0.294	4	0	
P54753	EPHB3_HUMAN	Ephrin type-B receptor 3				1.28	0	2	0	
Q13283	G3BP1_HUMAN	Ras GTPase-activating protein-binding protein 1	0.59	0.1	18				0	
Q15751	HERC1_HUMAN	Probable E3 ubiquitin-protein ligase HERC1	0.594	0.5	4				0	
P28288	ABCD3_HUMAN	ATP-binding cassette sub-family D member 3	0.601	0.13	22				0	
Q9UKA9	PTBP2_HUMAN	Polypyrimidine tract-binding protein 2				1.316	0	2	0	
Q149N8	SHPRH_HUMAN	E3 ubiquitin-protein ligase SHPRH				2.019	0	2	0	
P0C0S5	H2AZ_HUMAN	Histone H2A.Z	0.608	0.02	6				0	
Q71UI9	H2AV_HUMAN	Histone H2A.V	0.608	0.02	6				0	
P54886	P5CS_HUMAN	Delta-1-pyrroline-5-carboxylate synthase				1.417	0.443	12	0	
P11532	DMD_HUMAN	Dystrophin				1.077	0.544	4	0	
Q8WUD1	RAB2B_HUMAN	Ras-related protein Rab-2B				1.077	0.346	8	0	
P11498	PYC_HUMAN	Pyruvate carboxylase, mitochondrial				1.228	1.739	22	0	
-	K1967_HUMAN	-				1.23	0.104	12	0	
Q5JRX3	PREP_HUMAN	Presequence protease, mitochondrial				1.232	0	2	0	
Q9P2P6	STAR9_HUMAN	StAR-related lipid transfer protein 9	0.628	0	2				0	
Q9Y305	ACOT9_HUMAN	Acyl-coenzyme A thioesterase 9, mitochondrial				1.33	0.241	12	0	
Q9H2J7	S6A15_HUMAN	Sodium-dependent neutral amino acid	0.632	0	2				0	

		transporter B(0)AT2								
Q6NUK1	SCMC1_HUMAN	Calcium-binding mitochondrial carrier protein SCaMC-1	0.635	0.13	4				0	
P02549	SPTA1_HUMAN	Spectrin alpha chain, erythrocytic 1	0.64	0	2				0	
P37108	SRP14_HUMAN	Signal recognition particle 14 kDa protein				0.939	0.026	8	0	
Q9NXF1	TEX10_HUMAN	Testis-expressed sequence 10 protein	0.658	0.16	6				0	
Q12923	PTN13_HUMAN	Tyrosine-protein phosphatase non-receptor type 13	0.666	0	2				0	
P20674	COX5A_HUMAN	Cytochrome c oxidase subunit 5A, mitochondrial	0.668	0.52	6				0	
Q4VXU2	PAP1L_HUMAN	Polyadenylate-binding protein 1-like				0.888	0.227	4	0	
Q9Y4L1	HYOU1_HUMAN	Hypoxia up-regulated protein 1	0.672	0.09	16				0	
Q96A33	CCD47_HUMAN	Coiled-coil domain-containing protein 47	0.673	0.4	20				0	
Q8TDW7	FAT3_HUMAN	Protocadherin Fat 3	0.675	0	2				0	
Q9H2M9	RBGPR_HUMAN	Rab3 GTPase-activating protein non-catalytic subunit	0.681	0	2				0	
Q9Y2H5	PKHA6_HUMAN	Pleckstrin homology domain-containing family A member 6				1.018	0.111	4	0	
Q8WVM8	SCFD1_HUMAN	Sec1 family domain-containing protein 1				1.024	0.165	12	0	
O95714	HERC2_HUMAN	E3 ubiquitin-protein ligase HERC2	0.693		1				0	
Q86UQ4	ABCAD_HUMAN	ATP-binding cassette sub-family A member 13	0.694	0	2				0	
Q460N5	PAR14_HUMAN	Poly [ADP-ribose] polymerase 14	0.695	0.3	6				0	
Q12830	BPTF_HUMAN	Nucleosome-remodeling factor subunit BPTF	0.701	0	2				0	
P51587	BRCA2_HUMAN	Breast cancer type 2 susceptibility protein	0.704	0	2				0	
-	ENV_FOAMV	-	0.717	0.01	3				0	
P08F94	PKHD1_HUMAN	Fibrocystin	0.718	0.54	4				0	
P30876	RPB2_HUMAN	DNA-directed RNA polymerase II subunit RPB2				1.234	0.003	4	0	
P50395	GDIB_HUMAN	Rab GDP dissociation inhibitor beta	0.734	0.3	4				0	
Q92736	RYR2_HUMAN	Ryanodine receptor 2	0.737	0	2				0	
Q92526	TCPW_HUMAN	T-complex protein 1 subunit zeta-2				0.944	0	2	0	

Q9BZZ5	API5_HUMAN	Apoptosis inhibitor 5	0.738	0.08	4				0	
Q9P003	CNIH4_HUMAN	Protein cornichon homolog 4	0.739	0.13	6				0	
Q9Y221	NIP7_HUMAN	60S ribosome subunit biogenesis protein NIP7 homolog	0.743	0	2				0	
Q13905	RPGF1_HUMAN	Rap guanine nucleotide exchange factor 1	0.75	0.54	4				0	
-	R1A_CVHSA	-				1.032	0	2	0	
O15027	SC16A_HUMAN	Protein transport protein Sec16A	0.809	0.18	8				0	
P05026	AT1B1_HUMAN	Sodium/potassium-transporting ATPase subunit beta-1				1.148	0.082	8	0	
P33527	MRP1_HUMAN	Multidrug resistance-associated protein 1	0.786	0.03	6				0	
O75165	DJC13_HUMAN	DnaJ homolog subfamily C member 13	0.787	0.18	14				0	
Q14517	FAT1_HUMAN	Protocadherin Fat 1	0.789	0.77	8				0	
Q58FF7	H90B3_HUMAN	Putative heat shock protein HSP 90-beta-3				0.974	0.042	5	0	
P13667	PDIA4_HUMAN	Protein disulfide-isomerase A4				1.604	0.946	12	0	
Q8N4Y2	EFC4A_HUMAN	EF-hand calcium-binding domain-containing protein 4A				1.217	0	2	0	
P55884	EIF3B_HUMAN	Eukaryotic translation initiation factor 3 subunit B				0.753	0.021	10	0	
A6NNZ2	TBB8L_HUMAN	Tubulin beta-8 chain-like protein LOC260334				0.754	0.048	4	0	
Q9H254	SPTN4_HUMAN	Spectrin beta chain, non-erythrocytic 4	0.817	0.79	4				0	
Q13501	SQSTM_HUMAN	Sequestosome-1				1.14	0.219	10	0	
Q8NF37	PCAT1_HUMAN	Lysophosphatidylcholine acyltransferase 1	0.822	0	2				0	
O95425	SVIL_HUMAN	Supervillin				1.306	0	2	0	
Q12802	AKP13_HUMAN	A-kinase anchor protein 13	0.824	0	2				0	
P34932	HSP74_HUMAN	Heat shock 70 kDa protein 4	0.826	0	2				0	
Q01518	CAP1_HUMAN	Adenylyl cyclase-associated protein 1				0.849	0.238	8	0	
Q86WV6	STING_HUMAN	Stimulator of interferon genes protein	0.834	0.03	8				0	
Q8IXB1	DJC10_HUMAN	DnaJ homolog subfamily C member 10	0.838	0.06	4				0	
Q9HC07	TM165_HUMAN	Transmembrane protein 165				0.764	0.591	4	0	
Q9Y6E2	BZW2_HUMAN	Basic leucine zipper and W2 domain-containing protein 2				0.788	0	2	0	

P14868	SYDC_HUMAN	Aspartate--tRNA ligase, cytoplasmic				0.788	0.051	4	0	
O60568	PLOD3_HUMAN	Procollagen-lysine,2-oxoglutarate 5-dioxygenase 3				1.257	0	2	0	
P54707	AT12A_HUMAN	Potassium-transporting ATPase alpha chain 2				1.258	0	2	0	
P0CG08	GPHRB_HUMAN	Golgi pH regulator B				0.96	0.2	4	0	
A6NKF9	GPHRC_HUMAN	Putative Golgi pH regulator C				0.96	0.2	4	0	
B7ZAQ6	GPHRA_HUMAN	Golgi pH regulator A				0.96	0.2	4	0	
O75592	MYCB2_HUMAN	E3 ubiquitin-protein ligase MYCBP2				0.962	0	2	0	
P30508	1C12_HUMAN	HLA class I histocompatibility antigen, Cw-12 alpha chain				0.99	0.608	8	0	
Q29960	1C16_HUMAN	HLA class I histocompatibility antigen, Cw-16 alpha chain				0.99	0.608	8	0	
P30505	1C08_HUMAN	HLA class I histocompatibility antigen, Cw-8 alpha chain				0.99	0.608	8	0	
Q29963	1C06_HUMAN	HLA class I histocompatibility antigen, Cw-6 alpha chain				0.99	0.608	8	0	
Q07000	1C15_HUMAN	HLA class I histocompatibility antigen, Cw-15 alpha chain				0.99	0.608	8	0	
P30501	1C02_HUMAN	HLA class I histocompatibility antigen, Cw-2 alpha chain				0.99	0.608	8	0	
Q9TNN7	1C05_HUMAN	HLA class I histocompatibility antigen, Cw-5 alpha chain				0.99	0.608	8	0	
Q8IZA0	K319L_HUMAN	Dyslexia-associated protein KIAA0319-like protein				0.99	0.262	4	0	
P30455	1A36_HUMAN	HLA class I histocompatibility antigen, A-36 alpha chain				0.99	0.608	8	0	
P16188	1A30_HUMAN	HLA class I histocompatibility antigen, A-30 alpha chain				0.99	0.608	8	0	
P05534	1A24_HUMAN	HLA class I histocompatibility antigen, A-24 alpha chain				0.99	0.608	8	0	
P30447	1A23_HUMAN	HLA class I histocompatibility antigen, A-23 alpha chain				0.99	0.608	8	0	
P13746	1A11_HUMAN	HLA class I histocompatibility antigen, A-11 alpha chain				0.99	0.608	8	0	
P04439	1A03_HUMAN	HLA class I histocompatibility antigen, A-3 alpha chain				0.99	0.608	8	0	

P30443	1A01_HUMAN	HLA class I histocompatibility antigen, A-1 alpha chain				0.99	0.608	8	0	
P01893	HLAH_HUMAN	Putative HLA class I histocompatibility antigen, alpha chain H				0.99	0.608	8	0	
O95674	CDS2_HUMAN	Phosphatidate cytidylyltransferase 2				0.991	0	2	0	
P20042	IF2B_HUMAN	Eukaryotic translation initiation factor 2 subunit 2				1.083	0.187	6	0	
Q9UBF2	COPG2_HUMAN	Coatomer subunit gamma-2	0.852	0.39	4				0	
O94973	AP2A2_HUMAN	AP-2 complex subunit alpha-2	0.887	0.13	26				0	
P07195	LDHB_HUMAN	L-lactate dehydrogenase B chain				0.815	0.044	8	0	
P51809	VAMP7_HUMAN	Vesicle-associated membrane protein 7	0.884	0.08	20				0	
P04114	APOB_HUMAN	Apolipoprotein B-100	0.866	0.48	10				0	
P46776	RL27A_HUMAN	60S ribosomal protein L27a				0.904	0.069	12	0	
P42167	LAP2B_HUMAN	Lamina-associated polypeptide 2, isoforms beta/gamma				0.905	0.141	20	0	
Q58FG1	HS904_HUMAN	Putative heat shock protein HSP 90-alpha A4	0.878	0	2				0	
Q9BZF1	OSBL8_HUMAN	Oxysterol-binding protein-related protein 8	0.882	0.3	8				0	
P39019	RS19_HUMAN	40S ribosomal protein S19				0.856	0.175	6	0	
-	CHCH3_HUMAN	-				1.35	0.062	4	0	
P46783	RS10_HUMAN	40S ribosomal protein S10	0.893	0.01	4				0	
P10620	MGST1_HUMAN	Microsomal glutathione S-transferase 1	0.895	0.02	6				0	
Q9NZJ4	SACS_HUMAN	Sacsin	0.895	0	2				0	
Q01844	EWS_HUMAN	RNA-binding protein EWS				1.039	0.535	6	0	
Q9Y5S2	MRCKB_HUMAN	Serine/threonine-protein kinase MRCK beta	0.898	0	2				0	
P57088	TMM33_HUMAN	Transmembrane protein 33	0.9	0	2				0	
Q969V3	NCLN_HUMAN	Nicalin				0.798	0.001	4	0	
Q9UBV2	SE1L1_HUMAN	Protein sel-1 homolog 1	0.925	0.54	8				0	
Q5T890	ER6L2_HUMAN	DNA excision repair protein ERCC-6-like 2	0.926	0	2				0	
Q99698	LYST_HUMAN	Lysosomal-trafficking regulator				0.87	0	2	0	
A4UGR9	XIRP2_HUMAN	Xin actin-binding repeat-containing protein 2	0.929	0.25	5				0	
Q68DK2	ZFY26_HUMAN	Zinc finger FYVE domain-containing protein	0.936	0	2				0	

		26								
Q6ZMW3	EMAL6_HUMAN	Echinoderm microtubule-associated protein-like 6				1.016	0	2	0	
Q5SZK8	FREM2_HUMAN	FRAS1-related extracellular matrix protein 2	0.947	0	2				0	
Q8WXG9	GPR98_HUMAN	G-protein coupled receptor 98				0.828	0	2	0	
Q9H490	PIGU_HUMAN	Phosphatidylinositol glycan anchor biosynthesis class U protein	0.955	0.01	4				0	
Q5JNZ5	RS26L_HUMAN	Putative 40S ribosomal protein S26-like 1	0.958	0.04	4				0	
Q12907	LMAN2_HUMAN	Vesicular integral-membrane protein VIP36	0.962	0	2				0	
Q08722	CD47_HUMAN	Leukocyte surface antigen CD47				0.901	0.043	4	0	
Q6NUM9	RETST_HUMAN	All-trans-retinol 13,14-reductase	0.967	0.15	4				0	
O95864	FADS2_HUMAN	Fatty acid desaturase 2				1.097	0.156	8	0	
Q9Y6M1	IF2B2_HUMAN	Insulin-like growth factor 2 mRNA-binding protein 2				0.774	0.222	8	0	
P16401	H15_HUMAN	Histone H1.5				1.309	0.155	10	0	
Q15041	AR6P1_HUMAN	ADP-ribosylation factor-like protein 6-interacting protein 1	0.972	0	2				0	
P27695	APEX1_HUMAN	DNA-(apurinic or apyrimidinic site) lyase				0.928	0.273	6	0	
Q8TCU4	ALMS1_HUMAN	Alstrom syndrome protein 1				0.661	0	2	0	
P31150	GDIA_HUMAN	Rab GDP dissociation inhibitor alpha	1.004	0.02	4				0	
P53992	SC24C_HUMAN	Protein transport protein Sec24C				0.518	0	2	0	
-	L_SABVB	-	1.03	0	2				0	
Q9Y673	ALG5_HUMAN	Dolichyl-phosphate beta-glucosyltransferase				1.454	0	2	0	
P22307	NLTP_HUMAN	Non-specific lipid-transfer protein				1.455	0	2	0	
Q9UBM7	DHCR7_HUMAN	7-dehydrocholesterol reductase				1.455	0	2	0	
P63000	RAC1_HUMAN	Ras-related C3 botulinum toxin substrate 1				0.921	0.376	4	0	
Q5ZPR3	CD276_HUMAN	CD276 antigen				0.622	0	2	0	
Q9Y6V0	PCLO_HUMAN	Protein piccolo				0.624	0	2	0	
Q9H0X9	OSBL5_HUMAN	Oxysterol-binding protein-related protein 5	1.054	0.46	9				0	
Q9Y4P3	TBL2_HUMAN	Transducin beta-like protein 2				0.725	0.005	4	0	

P11717	MPRI_HUMAN	Cation-independent mannose-6-phosphate receptor	1.042	0.47	8				0	
Q9H4B7	TBB1_HUMAN	Tubulin beta-1 chain				0.791	0.038	2	0	
-	YI016_HUMAN	-				0.791	0.038	2	0	
P11217	PYGM_HUMAN	Glycogen phosphorylase, muscle form	1.052	0	2				0	
P56539	CAV3_HUMAN	Caveolin-3				0.53	0	2	0	
Q04826	1B40_HUMAN	HLA class I histocompatibility antigen, B-40 alpha chain				2.405	0.517	6	0	
P30483	1B45_HUMAN	HLA class I histocompatibility antigen, B-45 alpha chain				2.405	0.517	6	0	
P30480	1B42_HUMAN	HLA class I histocompatibility antigen, B-42 alpha chain				2.405	0.517	6	0	
P30485	1B47_HUMAN	HLA class I histocompatibility antigen, B-47 alpha chain				2.405	0.517	6	0	
P30487	1B49_HUMAN	HLA class I histocompatibility antigen, B-49 alpha chain				2.405	0.517	6	0	
P30481	1B44_HUMAN	HLA class I histocompatibility antigen, B-44 alpha chain				2.405	0.517	6	0	
P30475	1B39_HUMAN	HLA class I histocompatibility antigen, B-39 alpha chain				2.405	0.517	6	0	
Q95365	1B38_HUMAN	HLA class I histocompatibility antigen, B-38 alpha chain				2.405	0.517	6	0	
Q29836	1B67_HUMAN	HLA class I histocompatibility antigen, B-67 alpha chain				2.405	0.517	6	0	
P18463	1B37_HUMAN	HLA class I histocompatibility antigen, B-37 alpha chain				2.405	0.517	6	0	
Q29718	1B82_HUMAN	HLA class I histocompatibility antigen, B-82 alpha chain				2.405	0.517	6	0	
P03989	1B27_HUMAN	HLA class I histocompatibility antigen, B-27 alpha chain				2.405	0.517	6	0	
P30466	1B18_HUMAN	HLA class I histocompatibility antigen, B-18 alpha chain				2.405	0.517	6	0	
P01891	1A68_HUMAN	HLA class I histocompatibility antigen, A-68 alpha chain	1.054	0.49	6				0	
P30457	1A66_HUMAN	HLA class I histocompatibility antigen, A-66 alpha chain	1.054	0.49	6				0	
P30453	1A34_HUMAN	HLA class I histocompatibility antigen, A-34 alpha chain	1.054	0.49	6				0	

P30450	1A26_HUMAN	HLA class I histocompatibility antigen, A-26 alpha chain	1.054	0.49	6				0	
P18462	1A25_HUMAN	HLA class I histocompatibility antigen, A-25 alpha chain	1.054	0.49	6				0	
P30479	1B41_HUMAN	HLA class I histocompatibility antigen, B-41 alpha chain				2.405	0.517	6	0	
P30488	1B50_HUMAN	HLA class I histocompatibility antigen, B-50 alpha chain				2.405	0.517	6	0	
P01889	1B07_HUMAN	HLA class I histocompatibility antigen, B-7 alpha chain				2.405	0.517	6	0	
P30460	1B08_HUMAN	HLA class I histocompatibility antigen, B-8 alpha chain				2.405	0.517	6	0	
P30461	1B13_HUMAN	HLA class I histocompatibility antigen, B-13 alpha chain				2.405	0.517	6	0	
P30462	1B14_HUMAN	HLA class I histocompatibility antigen, B-14 alpha chain				2.405	0.517	6	0	
Q9BVG9	PTSS2_HUMAN	Phosphatidylserine synthase 2				0.797		1	0	
O00487	PSDE_HUMAN	26S proteasome non-ATPase regulatory subunit 14				0.664	0.024	6	0	
Q9UG63	ABCF2_HUMAN	ATP-binding cassette sub-family F member 2				0.668	0.297	4	0	
P27348	1433T_HUMAN	14-3-3 protein theta				0.95		1	0	
P59190	RAB15_HUMAN	Ras-related protein Rab-15				0.986	0.028	6	0	
Q92930	RAB8B_HUMAN	Ras-related protein Rab-8B				0.986	0.028	6	0	
P61006	RAB8A_HUMAN	Ras-related protein Rab-8A				0.986	0.028	6	0	
Q709C8	VP13C_HUMAN	Vacuolar protein sorting-associated protein 13C	1.082	1.49	3				0	
Q6P2E9	EDC4_HUMAN	Enhancer of mRNA-decapping protein 4				0.778	0	2	0	
P18206	VINC_HUMAN	Vinculin	1.094	0	2				0	
Q3V6T2	GRDN_HUMAN	Girdin	1.102	0	2				0	
-	R1AB_CVHNL	-	1.103	0	2				0	
-	R1A_CVHNL	-	1.103	0	2				0	
Q96P70	IPO9_HUMAN	Importin-9	1.105	0	2				0	
O14672	ADA10_HUMAN	Disintegrin and metalloproteinase domain-containing protein 10				1.165	0.422	6	0	
P10321	1C07_HUMAN	HLA class I histocompatibility antigen, Cw-7				0.658	0	2	0	

		alpha chain								
P31947	1433S_HUMAN	14-3-3 protein sigma				1	0.071	2	0	
Q8N3C0	ASCC3_HUMAN	Activating signal cointegrator 1 complex subunit 3	1.121	0.06	4				0	
Q13200	PSMD2_HUMAN	26S proteasome non-ATPase regulatory subunit 2	1.128	0.21	8				0	
Q7Z401	MYCPP_HUMAN	C-myc promoter-binding protein	1.141	1.08	4				0	
-	K6PP_HUMAN	-				0.64	0	2	0	
A1L0T0	ILVBL_HUMAN	Acetolactate synthase-like protein	1.165	0.07	16				0	
P22090	RS4Y1_HUMAN	40S ribosomal protein S4, Y isoform 1				0.643	0.208	4	0	
Q8TD47	RS4Y2_HUMAN	40S ribosomal protein S4, Y isoform 2				0.643	0.208	4	0	
Q6UB99	ANR11_HUMAN	Ankyrin repeat domain-containing protein 11				1.173	0	2	0	
Q96AE4	FUBP1_HUMAN	Far upstream element-binding protein 1				1.178	0.043	6	0	
Q9UIG0	BAZ1B_HUMAN	Tyrosine-protein kinase BAZ1B				1.179		1	0	
O00232	PSD12_HUMAN	26S proteasome non-ATPase regulatory subunit 12	1.176	0	2				0	
Q9UH99	SUN2_HUMAN	SUN domain-containing protein 2	1.179	0.24	8				0	
Q9BT22	ALG1_HUMAN	Chitobiosyldiphosphodolichol beta-mannosyltransferase	1.182	0.4	4				0	
Q9UHB9	SRP68_HUMAN	Signal recognition particle subunit SRP68				1.081	0.426	4	0	
P35241	RADI_HUMAN	Radixin	1.193	0	2				0	
P61619	S61A1_HUMAN	Protein transport protein Sec61 subunit alpha isoform 1	1.201	0	2				0	
Q96RQ1	ERGI2_HUMAN	Endoplasmic reticulum-Golgi intermediate compartment protein 2				0.826	0.056	4	0	
Q9H5V8	CDCP1_HUMAN	CUB domain-containing protein 1				6.047	0.109	4	0	
Q9C075	K1C23_HUMAN	Keratin, type I cytoskeletal 23				6.09	0	2	0	
Q6DN03	H2B2C_HUMAN	Putative histone H2B type 2-C				1.322	0	2	0	
P42285	SK2L2_HUMAN	Superkiller viralicidic activity 2-like 2				1.813	0.011	4	0	
Q5THJ4	VP13D_HUMAN	Vacuolar protein sorting-associated protein 13D	1.276	0	2				0	
Q15392	DHC24_HUMAN	Delta(24)-sterol reductase				0.685		1	0	
Q9NYC9	DYH9_HUMAN	Dynein heavy chain 9, axonemal				0.714	0.803	4	0	

P35610	SOAT1_HUMAN	Sterol O-acyltransferase 1	1.331	0.03	4				0	
Q5W111	SPRY7_HUMAN	SPRY domain-containing protein 7	1.662	0.51	8				0	
Q9P035	HACD3_HUMAN	Very-long-chain (3R)-3-hydroxyacyl-CoA dehydratase 3	1.341	0.07	12				0	
Q9Y2Q3	GSTK1_HUMAN	Glutathione S-transferase kappa 1				1.071	0.506	10	0	
P25398	RS12_HUMAN	40S ribosomal protein S12				0.625	0.095	6	0	
P23528	COF1_HUMAN	Cofilin-1				0.625	0.061	4	0	
Q9Y3F4	STRAP_HUMAN	Serine-threonine kinase receptor-associated protein				0.627	0	2	0	
Q15046	SYK_HUMAN	Lysine--tRNA ligase				0.629	0.049	12	0	
O76094	SRP72_HUMAN	Signal recognition particle subunit SRP72				0.913	0.482	8	0	
P15151	PVR_HUMAN	Poliovirus receptor				0.653	0	2	0	
Q08J23	NSUN2_HUMAN	tRNA (cytosine(34)-C(5))-methyltransferase				0.653	0.053	4	0	
O75489	NDUS3_HUMAN	NADH dehydrogenase [ubiquinone] iron-sulfur protein 3, mitochondrial				0.605	0.005	4	0	
Q99536	VAT1_HUMAN	Synaptic vesicle membrane protein VAT-1 homolog				0.707	0.155	12	0	
P50281	MMP14_HUMAN	Matrix metalloproteinase-14				0.616	0	2	0	
P20929	NEBU_HUMAN	Nebulin	1.374	1.02	12				0	
Q96TA1	NIBL1_HUMAN	Niban-like protein 1	1.388	0.4	14				0	
P56192	SYMC_HUMAN	Methionine--tRNA ligase, cytoplasmic	1.398	0.35	12				0	
O15371	EIF3D_HUMAN	Eukaryotic translation initiation factor 3 subunit D				0.671	0.168	12	0	
Q15012	LAP4A_HUMAN	Lysosomal-associated transmembrane protein 4A				0.571	0	2	0	
Q5VT25	MRCKA_HUMAN	Serine/threonine-protein kinase MRCK alpha				0.709	0	2	0	
O00429	DNM1L_HUMAN	Dynamin-1-like protein	1.845	1.46	10				0	
Q9BRR6	ADPGK_HUMAN	ADP-dependent glucokinase	1.494	0.27	4				0	
Q99943	PLCA_HUMAN	1-acyl-sn-glycerol-3-phosphate acyltransferase alpha	1.525	0	2				0	
Q9Y281	COF2_HUMAN	Cofilin-2				0.678	0	2	0	
Q13724	MOGS_HUMAN	Mannosyl-oligosaccharide glucosidase	1.556	0.08	4				0	
Q9UNK0	STX8_HUMAN	Syntaxin-8	1.558	0.09	4				0	

O96005	CLPT1_HUMAN	Cleft lip and palate transmembrane protein 1				0.696	0.196	6	0	
P09543	CN37_HUMAN	2',3'-cyclic-nucleotide 3'-phosphodiesterase				1.251	0.324	18	0	
Q9UHG3	PCYOX_HUMAN	Prenylcysteine oxidase 1	1.632	1.38	20				0	
Q7Z2W4	ZCCHV_HUMAN	Zinc finger CCCH-type antiviral protein 1				1.335	0.211	10	0	
-	APOOL_HUMAN	-				2.862	0	2	0	
Q2TB90	HKDC1_HUMAN	Putative hexokinase HKDC1				2.866	0.03	4	0	
P62888	RL30_HUMAN	60S ribosomal protein L30				0.847	0.057	8	0	
P00558	PGK1_HUMAN	Phosphoglycerate kinase 1				0.848	0.247	6	0	
Q96N66	MBOA7_HUMAN	Lysophospholipid acyltransferase 7				0.881	0.113	10	0	
P29144	TPP2_HUMAN	Tripeptidyl-peptidase 2				0.914	0.174	6	0	
Q8NCM8	DYHC2_HUMAN	Cytoplasmic dynein 2 heavy chain 1	1.695	0	2				0	
Q9UBI6	GBG12_HUMAN	Guanine nucleotide-binding protein G(I)/G(S)/G(O) subunit gamma-12				0.881		1	0	
O15438	MRP3_HUMAN	Canalicular multispecific organic anion transporter 2	1.76	0.21	6				0	
O00299	CLIC1_HUMAN	Chloride intracellular channel protein 1				0.225	0.207	4	0	
Q13421	MSLN_HUMAN	Mesothelin				0.254	0	2	0	
O00220	TR10A_HUMAN	Tumor necrosis factor receptor superfamily member 10A	1.799	0.77	14				0	
P30613	KPYR_HUMAN	Pyruvate kinase PKLR				0.583	0.04	6	0	
Q96RT1	LAP2_HUMAN	Protein LAP2	1.838	0.2	4				0	
Q9NRQ2	PLS4_HUMAN	Phospholipid scramblase 4				0.45	0	2	0	
P60174	TPIS_HUMAN	Triosephosphate isomerase				0.457	0.209	6	0	
Q8TF72	SHRM3_HUMAN	Protein Shroom3	1.888	0	2				0	
Q04917	1433F_HUMAN	14-3-3 protein eta				0.95		1	0	
Q7Z3J3	RGPD4_HUMAN	RanBP2-like and GRIP domain-containing protein 4				1.194	0	2	0	
A6NKT7	RGPD3_HUMAN	RanBP2-like and GRIP domain-containing protein 3				1.194	0	2	0	
-	R1AB_CVH22	-	2.115	0.21	4				0	
O75396	SC22B_HUMAN	Vesicle-trafficking protein SEC22b	2.206	0.09	4				0	

Q02809	PLOD1_HUMAN	Procollagen-lysine,2-oxoglutarate 5-dioxygenase 1				0.377	0.001	6	0	
Q8TED1	GPX8_HUMAN	Probable glutathione peroxidase 8				0.291	0.001	3	0	
-	POLG_HPE2W	-	2.308	0	2				0	
Q9Y4A5	TRRAP_HUMAN	Transformation/transcription domain-associated protein	2.395	2.47	4				0	
Q9NZI8	IF2B1_HUMAN	Insulin-like growth factor 2 mRNA-binding protein 1				0.582	0	2	0	
O00425	IF2B3_HUMAN	Insulin-like growth factor 2 mRNA-binding protein 3				0.582	0.022	4	0	
P55209	NP1L1_HUMAN	Nucleosome assembly protein 1-like 1	2.52	0.41	4				0	
Q86UW6	N4BP2_HUMAN	NEDD4-binding protein 2				0.595	0	2	0	
O94874	UFL1_HUMAN	E3 UFM1-protein ligase 1				0.595	0	2	0	
Q92626	PXDN_HUMAN	Peroxidasin homolog				0.596	0.039	4	0	
Q8TC12	RDH11_HUMAN	Retinol dehydrogenase 11				0.7	0.209	10	0	
Q8NEV8	EXPH5_HUMAN	Exophilin-5	2.674	0	2				0	
Q6NUQ4	TM214_HUMAN	Transmembrane protein 214	2.833	0	2				0	
Q9NV31	IMP3_HUMAN	U3 small nucleolar ribonucleoprotein protein IMP3				0.363	0	2	0	
Q10472	GALT1_HUMAN	Polypeptide N-acetylgalactosaminyltransferase 1	3.348	1.19	16				0	
P15529	MCP_HUMAN	Membrane cofactor protein				0.459	0	2	0	
Q5T4S7	UBR4_HUMAN	E3 ubiquitin-protein ligase UBR4	3.607	1.94	10				0	
Q9NRR3	C42S2_HUMAN	CDC42 small effector protein 2	3.652	0.79	4				0	
Q14118	DAG1_HUMAN	Dystroglycan	4.043	0	2				0	
Q86WI1	PKHL1_HUMAN	Fibrocystin-L	4.069	4.08	4				0	
O00469	PLOD2_HUMAN	Procollagen-lysine,2-oxoglutarate 5-dioxygenase 2				0.098	0.011	22	0	
Q03252	LMNB2_HUMAN	Lamin-B2				0.133	0	2	0	
Q9NYQ8	FAT2_HUMAN	Protocadherin Fat 2	4.239	0.83	6				0	
O60831	PRAF2_HUMAN	PRA1 family protein 2	4.325	0.08	4				0	
Q8TD57	DYH3_HUMAN	Dynein heavy chain 3, axonemal	5.992	11.1	10				0	
P04264	K2C1_HUMAN	Keratin, type II cytoskeletal 1	9.458	0	2				0	

-	MLL1_HUMAN	-	30.97	0	2				0	
O15230	LAMA5_HUMAN	Laminin subunit alpha-5	41.75	0	2				0	
Q6R327	RICTR_HUMAN	Rapamycin-insensitive companion of mTOR	66.61	0	2				0	
O60664	PLIN3_HUMAN	Perilipin-3	0.639	0.37	8	0.446	0.116	14	0.28	1.433
O75531	BAF_HUMAN	Barrier-to-autointegration factor	0.473	0.09	10	0.611	0.059	4	0.29	0.774
-	MLL3_HUMAN	-	0.695	0	2	0.492	0	2	0.34	1.413
Q14978	NOLC1_HUMAN	Nucleolar and coiled-body phosphoprotein 1	0.325	0.04	12	1.088	0.106	10	0.35	0.299
O95613	PCNT_HUMAN	Pericentrin	0.373	0	2	0.964	0	2	0.36	0.387
P13639	EF2_HUMAN	Elongation factor 2	0.596	0.08	34	0.648	0.055	38	0.39	0.92
Q5SRD1	TI23B_HUMAN	Putative mitochondrial import inner membrane translocase subunit Tim23B	0.315	0	2	1.236	0	2	0.39	0.255
O14925	TIM23_HUMAN	Mitochondrial import inner membrane translocase subunit Tim23	0.315	0	2	1.236	0	2	0.39	0.255
O15121	DEGS1_HUMAN	Sphingolipid delta(4)-desaturase DES1	2.078	0	2	0.202	0	2	0.42	10.29
Q14533	KRT81_HUMAN	Keratin, type II cuticular Hb1	0.248	0	6	1.695	0.745	6	0.42	0.146
O43790	KRT86_HUMAN	Keratin, type II cuticular Hb6	0.248	0	6	1.695	0.745	6	0.42	0.146
P78385	KRT83_HUMAN	Keratin, type II cuticular Hb3	0.248	0	6	1.695	0.745	6	0.42	0.146
P35222	CTNB1_HUMAN	Catenin beta-1	0.192	0.03	8	2.19	0.384	19	0.42	0.088
P02751	FINC_HUMAN	Fibronectin	5.895	2.66	4	0.072	0.035	6	0.42	81.88
Q99714	HCD2_HUMAN	3-hydroxyacyl-CoA dehydrogenase type-2	0.173	0.03	6	2.497	0.34	10	0.43	0.069
Q7Z794	K2C1B_HUMAN	Keratin, type II cytoskeletal 1b	0.086	0	4	5.115	1.216	8	0.44	0.017
Q3SY84	K2C71_HUMAN	Keratin, type II cytoskeletal 71	0.086	0	4	5.115	1.216	8	0.44	0.017
Q7RTS7	K2C74_HUMAN	Keratin, type II cytoskeletal 74	0.086	0	4	5.158	1.076	10	0.44	0.017
O75071	EFC14_HUMAN	EF-hand calcium-binding domain-containing protein 14	0.895	0.02	4	0.496	0	2	0.44	1.804
P57721	PCBP3_HUMAN	Poly(rC)-binding protein 3	0.636	0	2	0.698	0.208	8	0.44	0.911
Q99456	K1C12_HUMAN	Keratin, type I cytoskeletal 12	0.128	0.01	4	3.473	0	2	0.44	0.037
P41091	IF2G_HUMAN	Eukaryotic translation initiation factor 2 subunit 3	0.738	0.13	22	0.603	0.25	12	0.45	1.224
Q15365	PCBP1_HUMAN	Poly(rC)-binding protein 1	0.636	0	2	0.714	0.243	6	0.45	0.891
P53999	TCP4_HUMAN	Activated RNA polymerase II transcriptional	0.6	0.02	4	0.758	0.084	16	0.45	0.792

		coactivator p15								
P35527	K1C9_HUMAN	Keratin, type I cytoskeletal 9	0.131	0.01	6	3.473	0	2	0.45	0.038
P02533	K1C14_HUMAN	Keratin, type I cytoskeletal 14	0.141	0.11	58	3.251	0.948	82	0.46	0.043
Q2VIR3	IF2GL_HUMAN	Putative eukaryotic translation initiation factor 2 subunit 3-like protein	0.765	0.14	16	0.603	0.31	12	0.46	1.269
Q9H8H3	MET7A_HUMAN	Methyltransferase-like protein 7A	0.195	0.05	10	2.427	0.131	10	0.47	0.08
P07942	LAMB1_HUMAN	Laminin subunit beta-1	0.541	0.03	14	0.879	0.081	14	0.48	0.615
Q14764	MVP_HUMAN	Major vault protein	1.775	0.88	38	0.269	0.012	10	0.48	6.599
P10412	H14_HUMAN	Histone H1.4	0.283	0.03	16	1.696	0.174	12	0.48	0.167
P16402	H13_HUMAN	Histone H1.3	0.283	0.03	16	1.696	0.174	12	0.48	0.167
P16403	H12_HUMAN	Histone H1.2	0.283	0.03	16	1.696	0.174	12	0.48	0.167
P21397	AOFA_HUMAN	Amine oxidase [flavin-containing] A	1.382	0.05	6	0.356	0.106	13	0.49	3.882
O75477	ERLN1_HUMAN	Erlin-1	0.726	0.07	6	0.684	0.099	16	0.5	1.061
P26038	MOES_HUMAN	Moesin	1.193	0	2	0.418	0.102	6	0.5	2.854
Q01628	IFM3_HUMAN	Interferon-induced transmembrane protein 3	0.984	0.39	8	0.51	0.09	20	0.5	1.929
P08133	ANXA6_HUMAN	Annexin A6	11.43	8.5	6	0.044	0	2	0.5	259.7
Q31612	1B73_HUMAN	HLA class I histocompatibility antigen, B-73 alpha chain	0.774	0	2	0.658	0	2	0.51	1.176
P62258	1433E_HUMAN	14-3-3 protein epsilon	0.558	0.12	13	0.913	0.063	8	0.51	0.611
P48047	ATPO_HUMAN	ATP synthase subunit O, mitochondrial	0.268	0.11	6	1.907	0.297	9	0.51	0.141
Q15366	PCBP2_HUMAN	Poly(rC)-binding protein 2	0.643	0.02	8	0.795	0.194	14	0.51	0.809
P07737	PROF1_HUMAN	Profilin-1	0.731	0.09	10	0.7	0.043	22	0.51	1.044
P35637	FUS_HUMAN	RNA-binding protein FUS	0.773	0.25	34	0.668	0.158	36	0.52	1.157
P62937	PPIA_HUMAN	Peptidyl-prolyl cis-trans isomerase A	0.442	0.1	32	1.169	0.253	28	0.52	0.378
P22492	H1T_HUMAN	Histone H1t	0.297	0	2	1.74	0.012	4	0.52	0.171
Q02539	H11_HUMAN	Histone H1.1	0.297	0	2	1.74	0.012	4	0.52	0.171
Q7Z406	MYH14_HUMAN	Myosin-14	0.47	0.01	8	1.1	0.521	16	0.52	0.427
Q99623	PHB2_HUMAN	Prohibitin-2	0.287	0.14	8	1.805	0.266	20	0.52	0.159
P08729	K2C7_HUMAN	Keratin, type II cytoskeletal 7	0.157	0.08	47	3.308	1.313	78	0.52	0.047
O43776	SYNC_HUMAN	Asparagine--tRNA ligase, cytoplasmic	0.764	0.09	6	0.693	0.106	4	0.53	1.102

Q9H0D6	XRN2_HUMAN	5'-3' exoribonuclease 2	0.36	0.15	18	1.482	0.35	6	0.53	0.243
P31949	S10AB_HUMAN	Protein S100-A11	0.682	0	6	0.783	0.158	17	0.53	0.871
Q92621	NU205_HUMAN	Nuclear pore complex protein Nup205	0.364	0.07	18	1.47	0.43	16	0.54	0.248
Q9Y4G6	TLN2_HUMAN	Talin-2	1.026	0	2	0.522	0	2	0.54	1.966
O95299	NDUAA_HUMAN	NADH dehydrogenase [ubiquinone] 1 alpha subcomplex subunit 10, mitochondrial	0.28	0.1	6	1.923	0	2	0.54	0.146
Q16795	NDUA9_HUMAN	NADH dehydrogenase [ubiquinone] 1 alpha subcomplex subunit 9, mitochondrial	0.399	0	4	1.35	0	2	0.54	0.296
P04083	ANXA1_HUMAN	Annexin A1	0.583	0.14	72	0.924	0.28	66	0.54	0.631
P78386	KRT85_HUMAN	Keratin, type II cuticular Hb5	0.248	0	6	2.175	0.036	4	0.54	0.114
Q8WUM4	PDC6I_HUMAN	Programmed cell death 6-interacting protein	0.946	0.04	6	0.577	0.101	4	0.55	1.64
Q92804	RBP56_HUMAN	TATA-binding protein-associated factor 2N	0.582	0.14	18	0.938	0.27	20	0.55	0.62
O75746	CMC1_HUMAN	Calcium-binding mitochondrial carrier protein Aralar1	0.205	0	2	2.667	0.34	10	0.55	0.077
O94905	ERLN2_HUMAN	Erlin-2	0.787	0.09	16	0.699	0.095	20	0.55	1.126
O75131	CPNE3_HUMAN	Copine-3	0.651	0.07	10	0.847	0.109	20	0.55	0.769
-	R1AB_CVHSA	-	0.539	0.5	4	1.032	0	2	0.56	0.522
Q58FF8	H90B2_HUMAN	Putative heat shock protein HSP 90-beta 2	0.791	0.03	8	0.706	0.055	12	0.56	1.12
Q14568	HS902_HUMAN	Heat shock protein HSP 90-alpha A2	0.791	0.03	8	0.706	0.055	12	0.56	1.12
P63104	1433Z_HUMAN	14-3-3 protein zeta/delta	0.634	0.1	21	0.885	0.13	16	0.56	0.716
P30153	2AAA_HUMAN	Serine/threonine-protein phosphatase 2A 65 kDa regulatory subunit A alpha isoform	0.462	0	2	1.221	0.664	6	0.56	0.378
P60660	MYL6_HUMAN	Myosin light polypeptide 6	0.635	0.05	8	0.89	0.015	4	0.57	0.713
P04406	G3P_HUMAN	Glyceraldehyde-3-phosphate dehydrogenase	0.609	0.07	53	0.934	0.059	36	0.57	0.652
Q9BUJ2	HNRL1_HUMAN	Heterogeneous nuclear ribonucleoprotein U-like protein 1	0.451	0.08	4	1.262	0.146	8	0.57	0.357
P13647	K2C5_HUMAN	Keratin, type II cytoskeletal 5	0.114	0.06	80	5.003	2.053	123	0.57	0.023
O95782	AP2A1_HUMAN	AP-2 complex subunit alpha-1	1.053	0.19	24	0.546	0.086	8	0.57	1.929
P52789	HXK2_HUMAN	Hexokinase-2	0.272	0.08	8	2.117	0.321	10	0.58	0.128
Q09666	AHNK_HUMAN	Neuroblast differentiation-associated protein AHNAK	0.934	1.81	650	0.618	0.186	594	0.58	1.511

P23786	CPT2_HUMAN	Carnitine O-palmitoyltransferase 2, mitochondrial	0.211	0.03	10	2.748	0.473	6	0.58	0.077
Q96PK6	RBM14_HUMAN	RNA-binding protein 14	0.332	0	2	1.754	0.234	12	0.58	0.189
Q04695	K1C17_HUMAN	Keratin, type I cytoskeletal 17	0.081	0.06	42	7.19	2.829	62	0.58	0.011
P35579	MYH9_HUMAN	Myosin-9	0.419	0.11	158	1.41	0.335	158	0.59	0.297
O94826	TOM70_HUMAN	Mitochondrial import receptor subunit TOM70	0.376	0.06	45	1.575	0.213	31	0.59	0.239
Q53EL6	PDCD4_HUMAN	Programmed cell death protein 4	0.472	0.02	4	1.255	0.243	7	0.59	0.376
P05783	K1C18_HUMAN	Keratin, type I cytoskeletal 18	0.142	0.05	11	4.179	1.653	12	0.59	0.034
Q9NYF8	BCLF1_HUMAN	Bcl-2-associated transcription factor 1	0.297	0.07	24	2.002	0.353	20	0.59	0.148
P08758	ANXA5_HUMAN	Annexin A5	2.874	0.88	32	0.207	0.039	29	0.59	13.88
P11216	PYGB_HUMAN	Glycogen phosphorylase, brain form	1.09	0.15	28	0.548	0.07	20	0.6	1.989
Q03701	CEBPZ_HUMAN	CCAAT/enhancer-binding protein zeta	0.3	0.04	24	1.992	0.089	6	0.6	0.151
P14649	MYL6B_HUMAN	Myosin light chain 6B	0.672	0.05	4	0.89	0.015	4	0.6	0.755
P31946	1433B_HUMAN	14-3-3 protein beta/alpha	0.732	0.23	5	0.822	0.137	10	0.6	0.891
Q14498	RBM39_HUMAN	RNA-binding protein 39	0.477	0.04	30	1.264	0.408	22	0.6	0.377
Q12905	ILF2_HUMAN	Interleukin enhancer-binding factor 2	0.499	0.13	54	1.211	0.187	48	0.6	0.412
P07900	HS90A_HUMAN	Heat shock protein HSP 90-alpha	0.92	0.25	34	0.657	0.158	30	0.6	1.4
P35221	CTNA1_HUMAN	Catenin alpha-1	0.188	0.04	78	3.221	0.499	58	0.61	0.058
Q8NC51	PAIRB_HUMAN	Plasminogen activator inhibitor 1 RNA-binding protein	0.841	0.05	8	0.721	0.157	6	0.61	1.166
P09874	PARP1_HUMAN	Poly [ADP-ribose] polymerase 1	0.443	0.16	50	1.376	0.159	44	0.61	0.322
P19012	K1C15_HUMAN	Keratin, type I cytoskeletal 15	0.166	0.22	24	3.684	1.578	10	0.61	0.045
P62318	SMD3_HUMAN	Small nuclear ribonucleoprotein Sm D3	0.391	0	4	1.574	0.097	6	0.62	0.248
P46940	IQGA1_HUMAN	Ras GTPase-activating-like protein IQGAP1	0.815	0.16	110	0.756	0.122	118	0.62	1.078
P49448	DHE4_HUMAN	Glutamate dehydrogenase 2, mitochondrial	0.486	0.07	12	1.268	0.127	32	0.62	0.383
P06733	ENOA_HUMAN	Alpha-enolase	0.974	0.18	46	0.635	0.128	52	0.62	1.534
Q9Y2W1	TR150_HUMAN	Thyroid hormone receptor-associated protein 3	0.345	0.04	15	1.802	0.172	12	0.62	0.191
P62851	RS25_HUMAN	40S ribosomal protein S25	0.812	0.13	8	0.766	0.061	8	0.62	1.06
P19338	NUCL_HUMAN	Nucleolin	0.6	0.08	128	1.047	0.145	124	0.63	0.573

Q9BW60	ELOV1_HUMAN	Elongation of very long chain fatty acids protein 1	0.787	0	2	0.8	0.025	6	0.63	0.984
P30048	PRDX3_HUMAN	Thioredoxin-dependent peroxide reductase, mitochondrial	0.202	0	2	3.131	0.007	4	0.63	0.065
Q9NSB2	KRT84_HUMAN	Keratin, type II cuticular Hb4	0.153	0.09	14	4.135	1.742	12	0.63	0.037
P13010	XRCC5_HUMAN	X-ray repair cross-complementing protein 5	0.514	0.06	110	1.237	0.221	51	0.64	0.416
P16520	GBB3_HUMAN	Guanine nucleotide-binding protein G(I)/G(S)/G(T) subunit beta-3	0.82	0	2	0.776	0.024	6	0.64	1.057
P20700	LMNB1_HUMAN	Lamin-B1	0.445	0.09	38	1.434	0.359	56	0.64	0.31
Q13423	NNTM_HUMAN	NAD(P) transhydrogenase, mitochondrial	0.391	0.07	52	1.633	0.465	51	0.64	0.239
P62879	GBB2_HUMAN	Guanine nucleotide-binding protein G(I)/G(S)/G(T) subunit beta-2	0.77	0.24	14	0.833	0.086	11	0.64	0.924
O60264	SMCA5_HUMAN	SWI/SNF-related matrix-associated actin-dependent regulator of chromatin subfamily A member 5	0.405	0	2	1.597	0.386	28	0.65	0.254
Q13247	SRSF6_HUMAN	Serine/arginine-rich splicing factor 6	0.507	0.1	22	1.276	0.204	20	0.65	0.397
P18031	PTN1_HUMAN	Tyrosine-protein phosphatase non-receptor type 1	0.608	0.15	6	1.065	0.143	14	0.65	0.571
P09104	ENOG_HUMAN	Gamma-enolase	1.038	0.02	6	0.624	0.011	6	0.65	1.663
Q9BUF5	TBB6_HUMAN	Tubulin beta-6 chain	0.922	0.15	12	0.703	0.047	14	0.65	1.312
Q9C0G6	DYH6_HUMAN	Dynein heavy chain 6, axonemal	1.299	0	2	0.501	0	2	0.65	2.593
P55084	ECHB_HUMAN	Trifunctional enzyme subunit beta, mitochondrial	0.427	0.07	36	1.525	0.212	52	0.65	0.28
Q01082	SPTB2_HUMAN	Spectrin beta chain, non-erythrocytic 1	0.629	0.18	150	1.036	0.32	195	0.65	0.607
Q9H307	PININ_HUMAN	Pinin	0.245	0.03	10	2.66	0.498	10	0.65	0.092
P13929	ENOB_HUMAN	Beta-enolase	1.048	0.02	6	0.624	0.011	6	0.65	1.679
P49748	ACADV_HUMAN	Very long-chain specific acyl-CoA dehydrogenase, mitochondrial	0.485	0.12	24	1.349	0.134	38	0.65	0.36
P21333	FLNA_HUMAN	Filamin-A	1.292	0.33	183	0.507	0.147	162	0.66	2.548
P50990	TCPQ_HUMAN	T-complex protein 1 subunit theta	0.757	0.19	36	0.866	0.097	47	0.66	0.874
P62995	TRA2B_HUMAN	Transformer-2 protein homolog beta	0.415	0.06	15	1.589	0.236	18	0.66	0.261
O00159	MYO1C_HUMAN	Unconventional myosin-Ic	0.87	0.1	56	0.759	0.114	44	0.66	1.146
P52272	HNRPM_HUMAN	Heterogeneous nuclear ribonucleoprotein M	0.503	0.1	58	1.315	0.297	60	0.66	0.383
Q00610	CLH1_HUMAN	Clathrin heavy chain 1	0.998	0.25	146	0.663	0.148	126	0.66	1.505

Q15287	RNPS1_HUMAN	RNA-binding protein with serine-rich domain 1	0.356	0.01	12	1.86	0.045	6	0.66	0.191
Q16698	DECR_HUMAN	2,4-dienoyl-CoA reductase, mitochondrial	0.615	0.1	34	1.077	0.058	30	0.66	0.571
Q99613	EIF3C_HUMAN	Eukaryotic translation initiation factor 3 subunit C	1.013	0.16	38	0.655	0.099	14	0.66	1.547
P24539	AT5F1_HUMAN	ATP synthase F(0) complex subunit B1, mitochondrial	0.376	0.03	26	1.766	0.128	16	0.66	0.213
P42166	LAP2A_HUMAN	Lamina-associated polypeptide 2, isoform alpha	0.696	0.31	6	0.959	0.298	20	0.67	0.726
Q96EY7	PTCD3_HUMAN	Pentatricopeptide repeat domain-containing protein 3, mitochondrial	0.31	0.08	10	2.155	0.452	18	0.67	0.144
P63010	AP2B1_HUMAN	AP-2 complex subunit beta	1.004	0.17	30	0.666	0.026	12	0.67	1.508
P08779	K1C16_HUMAN	Keratin, type I cytoskeletal 16	0.215	0.14	24	3.111	1.054	28	0.67	0.069
Q99729	ROAA_HUMAN	Heterogeneous nuclear ribonucleoprotein A/B	0.406	0.1	18	1.648	0.103	16	0.67	0.246
O75947	ATP5H_HUMAN	ATP synthase subunit d, mitochondrial	0.349	0.1	20	1.918	0.351	16	0.67	0.182
Q9UJZ1	STML2_HUMAN	Stomatin-like protein 2, mitochondrial	0.308	0.03	34	2.174	0.487	30	0.67	0.142
P53675	CLH2_HUMAN	Clathrin heavy chain 2	1.02	0.14	34	0.657	0.15	32	0.67	1.553
P13164	IFM1_HUMAN	Interferon-induced transmembrane protein 1	1.194	0.01	6	0.562	0.046	14	0.67	2.125
Q01629	IFM2_HUMAN	Interferon-induced transmembrane protein 2	1.194	0.01	6	0.562	0.046	14	0.67	2.125
P61981	1433G_HUMAN	14-3-3 protein gamma	0.564	0.03	3	1.191	0.287	8	0.67	0.474
P00338	LDHA_HUMAN	L-lactate dehydrogenase A chain	0.845	0.21	22	0.795	0.072	27	0.67	1.063
Q01814	AT2B2_HUMAN	Plasma membrane calcium-transporting ATPase 2	0.945	0.1	12	0.711	0.054	14	0.67	1.329
Q9Y6N5	SQRD_HUMAN	Sulfide:quinone oxidoreductase, mitochondrial	0.072	0.02	16	9.335	1.625	28	0.67	0.008
Q9Y3U8	RL36_HUMAN	60S ribosomal protein L36	0.968	0.15	6	0.695	0.06	6	0.67	1.393
P62857	RS28_HUMAN	40S ribosomal protein S28	0.865	0.02	6	0.779	0.102	10	0.67	1.11
P60842	IF4A1_HUMAN	Eukaryotic initiation factor 4A-I	0.718	0.21	34	0.939	0.247	24	0.67	0.765
Q9NY65	TBA8_HUMAN	Tubulin alpha-8 chain	1.049	0.25	22	0.645	0.098	29	0.68	1.626
Q14574	DSC3_HUMAN	Desmocollin-3	0.044	0	2	15.39	17.09	4	0.68	0.003
P62873	GBB1_HUMAN	Guanine nucleotide-binding protein G(I)/G(S)/G(T) subunit beta-1	0.788	0.23	16	0.86	0.104	15	0.68	0.916
O15042	SR140_HUMAN	U2 snRNP-associated SURP motif-containing	0.452	0.05	4	1.504	0.463	26	0.68	0.301

		protein								
Q9H9B4	SFXN1_HUMAN	Sideroflexin-1	0.355	0.13	28	1.915	0.374	28	0.68	0.185
Q8WXA9	SREK1_HUMAN	Splicing regulatory glutamine/lysine-rich protein 1	0.45	0.04	6	1.511	0	2	0.68	0.298
P62269	RS18_HUMAN	40S ribosomal protein S18	0.792	0.21	4	0.859	0.038	6	0.68	0.922
Q15149	PLEC_HUMAN	Plectin	0.703	0.2	852	0.97	0.229	859	0.68	0.725
P26232	CTNA2_HUMAN	Catenin alpha-2	0.187	0	2	3.656	1.302	6	0.68	0.051
Q9Y490	TLN1_HUMAN	Talin-1	1.621	0.97	95	0.422	0.144	48	0.68	3.841
P51991	ROA3_HUMAN	Heterogeneous nuclear ribonucleoprotein A3	0.394	0.11	40	1.737	0.452	40	0.68	0.227
Q14980	NUMA1_HUMAN	Nuclear mitotic apparatus protein 1	0.441	0.13	18	1.552	0.346	12	0.68	0.284
P51648	AL3A2_HUMAN	Fatty aldehyde dehydrogenase	0.307	0.08	24	2.23	0.291	28	0.68	0.138
Q13733	AT1A4_HUMAN	Sodium/potassium-transporting ATPase subunit alpha-4	0.485	0.09	22	1.414	0.198	23	0.69	0.343
P49792	RBP2_HUMAN	E3 SUMO-protein ligase RanBP2	0.359	0.06	8	1.913	0.477	16	0.69	0.188
P50993	AT1A2_HUMAN	Sodium/potassium-transporting ATPase subunit alpha-2	0.505	0.07	46	1.364	0.223	51	0.69	0.37
Q14103	HNRPD_HUMAN	Heterogeneous nuclear ribonucleoprotein D0	0.497	0.08	26	1.388	0.426	14	0.69	0.358
O14979	HNRDL_HUMAN	Heterogeneous nuclear ribonucleoprotein D-like	0.499	0.06	28	1.384	0.522	20	0.69	0.361
-	R1AB_CVHN2	-	0.316	0	2	2.19	0	2	0.69	0.144
Q13148	TADBP_HUMAN	TAR DNA-binding protein 43	0.524	0.08	16	1.321	0.285	14	0.69	0.397
Q02543	RL18A_HUMAN	60S ribosomal protein L18a	0.914	0.11	14	0.758	0.046	12	0.69	1.206
Q9UQ80	PA2G4_HUMAN	Proliferation-associated protein 2G4	0.652	0.11	20	1.064	0.164	22	0.69	0.613
Q13740	CD166_HUMAN	CD166 antigen	2.307	1.46	10	0.301	0.039	8	0.69	7.664
Q13084	RM28_HUMAN	39S ribosomal protein L28, mitochondrial	0.366	0	4	1.898	0	2	0.69	0.193
Q8IY81	SPB1_HUMAN	pre-rRNA processing protein FTSJ3	0.377	0.1	32	1.844	0.262	36	0.7	0.204
P13637	AT1A3_HUMAN	Sodium/potassium-transporting ATPase subunit alpha-3	0.502	0.07	53	1.385	0.206	63	0.7	0.362
P00367	DHE3_HUMAN	Glutamate dehydrogenase 1, mitochondrial	0.545	0.29	34	1.276	0.167	66	0.7	0.427
Q96IX5	USMG5_HUMAN	Up-regulated during skeletal muscle growth protein 5	0.309	0	2	2.251	0.31	4	0.7	0.137
P42677	RS27_HUMAN	40S ribosomal protein S27	0.854	0.07	6	0.815	0.075	10	0.7	1.048

P0CW22	RS17L_HUMAN	40S ribosomal protein S17-like	0.955	0.31	30	0.729	0.043	18	0.7	1.31
P08708	RS17_HUMAN	40S ribosomal protein S17	0.955	0.31	30	0.729	0.043	18	0.7	1.31
Q08945	SSRP1_HUMAN	FACT complex subunit SSRP1	0.737	0.2	32	0.945	0.152	30	0.7	0.78
Q14974	IMB1_HUMAN	Importin subunit beta-1	0.552	0.08	20	1.262	0.121	23	0.7	0.437
P22087	FBRL_HUMAN	rRNA 2'-O-methyltransferase fibrillarin	0.317	0.03	12	2.198	0.278	18	0.7	0.144
Q9NTI5	PDS5B_HUMAN	Sister chromatid cohesion protein PDS5 homolog B	0.562	0.15	10	1.241	0.317	10	0.7	0.453
P78527	PRKDC_HUMAN	DNA-dependent protein kinase catalytic subunit	0.452	0.1	194	1.547	0.325	203	0.7	0.292
O15523	DDX3Y_HUMAN	ATP-dependent RNA helicase DDX3Y	0.681	0.17	24	1.029	0.135	19	0.7	0.662
P05198	IF2A_HUMAN	Eukaryotic translation initiation factor 2 subunit 1	0.744	0.22	24	0.942	0.057	16	0.7	0.79
P32969	RL9_HUMAN	60S ribosomal protein L9	0.959	0.1	34	0.734	0.092	26	0.7	1.307
Q16695	H31T_HUMAN	Histone H3.1t	0.496	0.06	12	1.42	0.078	13	0.7	0.349
P68431	H31_HUMAN	Histone H3.1	0.496	0.06	12	1.42	0.078	13	0.7	0.349
Q71DI3	H32_HUMAN	Histone H3.2	0.496	0.06	12	1.42	0.078	13	0.7	0.349
P84243	H33_HUMAN	Histone H3.3	0.496	0.06	12	1.42	0.078	13	0.7	0.349
P12956	XRCC6_HUMAN	X-ray repair cross-complementing protein 6	0.549	0.1	68	1.285	0.185	70	0.71	0.427
P48668	K2C6C_HUMAN	Keratin, type II cytoskeletal 6C	0.114	0.07	62	6.193	2.678	92	0.71	0.018
Q14254	FLOT2_HUMAN	Flotillin-2	1.637	0.27	47	0.432	0.075	32	0.71	3.789
P28331	NDUS1_HUMAN	NADH-ubiquinone oxidoreductase 75 kDa subunit, mitochondrial	0.367	0.05	48	1.928	0.273	65	0.71	0.19
P48643	TCPE_HUMAN	T-complex protein 1 subunit epsilon	0.833	0.1	58	0.85	0.124	44	0.71	0.98
Q13509	TBB3_HUMAN	Tubulin beta-3 chain	0.974	0.14	34	0.727	0.128	42	0.71	1.34
-	HSP71_HUMAN	-	0.522	0.19	30	1.357	0.291	24	0.71	0.385
Q9HAV0	GBB4_HUMAN	Guanine nucleotide-binding protein subunit beta-4	0.913	0.13	8	0.777	0.022	7	0.71	1.175
P22695	QCR2_HUMAN	Cytochrome b-c1 complex subunit 2, mitochondrial	0.355	0.05	52	1.999	0.469	32	0.71	0.178
P49368	TCPG_HUMAN	T-complex protein 1 subunit gamma	0.789	0.1	46	0.9	0.072	52	0.71	0.877
Q9UGP8	SEC63_HUMAN	Translocation protein SEC63 homolog	0.643	0.18	18	1.105	0.185	8	0.71	0.582
P31943	HNRH1_HUMAN	Heterogeneous nuclear ribonucleoprotein H	0.477	0.13	52	1.49	0.2	48	0.71	0.32

P05787	K2C8_HUMAN	Keratin, type II cytoskeletal 8	0.153	0.09	14	4.653	2.402	16	0.71	0.033
Q8WTT2	NOC3L_HUMAN	Nucleolar complex protein 3 homolog	0.324	0.06	16	2.199	0.304	12	0.71	0.147
Q9BVA1	TBB2B_HUMAN	Tubulin beta-2B chain	1.035	0.09	44	0.689	0.12	52	0.71	1.502
Q13885	TBB2A_HUMAN	Tubulin beta-2A chain	1.035	0.09	44	0.689	0.12	52	0.71	1.502
P04259	K2C6B_HUMAN	Keratin, type II cytoskeletal 6B	0.115	0.08	56	6.204	2.768	85	0.71	0.019
P46781	RS9_HUMAN	40S ribosomal protein S9	0.879	0.33	21	0.812	0.044	6	0.71	1.083
Q9UJS0	CMC2_HUMAN	Calcium-binding mitochondrial carrier protein Aralar2	0.245	0.02	22	2.914	0.136	16	0.71	0.084
P61313	RL15_HUMAN	60S ribosomal protein L15	0.921	0.27	28	0.776	0.158	24	0.71	1.187
Q96A08	H2B1A_HUMAN	Histone H2B type 1-A	0.508	0.1	14	1.41	0.15	13	0.72	0.36
Q99460	PSMD1_HUMAN	26S proteasome non-ATPase regulatory subunit 1	1.073	0.29	14	0.668	0.118	14	0.72	1.606
-	DHSA_HUMAN	-	0.308	0.16	28	2.329	0.904	19	0.72	0.132
P61247	RS3A_HUMAN	40S ribosomal protein S3a	0.929	0.11	36	0.773	0.09	28	0.72	1.202
Q6PEY2	TBA3E_HUMAN	Tubulin alpha-3E chain	1.107	0.22	24	0.649	0.05	33	0.72	1.706
P62750	RL23A_HUMAN	60S ribosomal protein L23a	1.026	0	2	0.701	0.137	9	0.72	1.464
O75367	H2AY_HUMAN	Core histone macro-H2A.1	0.29	0.11	18	2.481	0.469	22	0.72	0.117
P34931	HS71L_HUMAN	Heat shock 70 kDa protein 1-like	0.555	0.19	24	1.297	0.26	30	0.72	0.428
O75533	SF3B1_HUMAN	Splicing factor 3B subunit 1	0.518	0.14	59	1.394	0.31	46	0.72	0.372
P23246	SFPQ_HUMAN	Splicing factor, proline- and glutamine-rich	0.51	0.06	48	1.416	0.172	46	0.72	0.36
O60841	IF2P_HUMAN	Eukaryotic translation initiation factor 5B	0.904	0.17	14	0.799	0.211	24	0.72	1.131
P60903	S10AA_HUMAN	Protein S100-A10	0.88	0.2	26	0.825	0.047	20	0.73	1.067
P12236	ADT3_HUMAN	ADP/ATP translocase 3	0.445	0.11	42	1.636	0.376	34	0.73	0.272
P43243	MATR3_HUMAN	Matrin-3	0.509	0.11	54	1.432	0.155	52	0.73	0.355
P62266	RS23_HUMAN	40S ribosomal protein S23	0.925	0.12	12	0.788	0.097	15	0.73	1.174
P02538	K2C6A_HUMAN	Keratin, type II cytoskeletal 6A	0.118	0.07	60	6.189	2.764	87	0.73	0.019
P62854	RS26_HUMAN	40S ribosomal protein S26	1.021	0.07	10	0.716	0.021	6	0.73	1.426
P0C7P4	UCRIL_HUMAN	Putative cytochrome b-c1 complex subunit Rieske-like protein 1	0.303	0.06	10	2.413	0.522	14	0.73	0.126
Q00839	HNRPU_HUMAN	Heterogeneous nuclear ribonucleoprotein U	0.519	0.11	80	1.409	0.149	80	0.73	0.368

P62249	RS16_HUMAN	40S ribosomal protein S16	0.814	0.12	13	0.899	0.042	6	0.73	0.905
P17987	TCPA_HUMAN	T-complex protein 1 subunit alpha	0.817	0.1	42	0.896	0.101	52	0.73	0.912
P11142	HSP7C_HUMAN	Heat shock cognate 71 kDa protein	0.659	0.11	98	1.111	0.094	84	0.73	0.593
Q13523	PRP4B_HUMAN	Serine/threonine-protein kinase PRP4 homolog	0.314	0.01	4	2.334	0	2	0.73	0.135
Q71U36	TBA1A_HUMAN	Tubulin alpha-1A chain	1.114	0.13	40	0.659	0.089	47	0.73	1.69
P68363	TBA1B_HUMAN	Tubulin alpha-1B chain	1.114	0.12	42	0.659	0.089	47	0.73	1.69
P23396	RS3_HUMAN	40S ribosomal protein S3	0.964	0.08	53	0.763	0.08	61	0.74	1.263
P49821	NDUV1_HUMAN	NADH dehydrogenase [ubiquinone] flavoprotein 1, mitochondrial	0.378	0.1	10	1.946	0.14	12	0.74	0.194
P62081	RS7_HUMAN	40S ribosomal protein S7	0.941	0.14	16	0.782	0.043	12	0.74	1.203
Q9BQE3	TBA1C_HUMAN	Tubulin alpha-1C chain	1.114	0.12	42	0.661	0.092	43	0.74	1.685
P07437	TBB5_HUMAN	Tubulin beta chain	1.069	0.1	60	0.689	0.139	72	0.74	1.552
P42704	LPPRC_HUMAN	Leucine-rich PPR motif-containing protein, mitochondrial	0.369	0.08	99	2	0.309	103	0.74	0.185
P47985	UCRI_HUMAN	Cytochrome b-c1 complex subunit Rieske, mitochondrial	0.303	0.06	10	2.436	0.49	16	0.74	0.124
O96008	TOM40_HUMAN	Mitochondrial import receptor subunit TOM40 homolog	0.328	0.06	12	2.252	0.224	20	0.74	0.146
O00571	DDX3X_HUMAN	ATP-dependent RNA helicase DDX3X	0.752	0.13	52	0.985	0.154	39	0.74	0.763
-	IMMT_HUMAN	-	0.442	0.15	50	1.676	0.245	50	0.74	0.264
Q13243	SRSF5_HUMAN	Serine/arginine-rich splicing factor 5	0.694	0.19	6	1.068	0.126	12	0.74	0.65
P83731	RL24_HUMAN	60S ribosomal protein L24	0.954	0.02	14	0.777	0.115	16	0.74	1.228
A6NIZ1	RP1BL_HUMAN	Ras-related protein Rap-1b-like protein	0.58	0.09	8	1.279	0.101	4	0.74	0.453
P04350	TBB4A_HUMAN	Tubulin beta-4A chain	0.974	0.1	32	0.762	0.146	32	0.74	1.278
P54652	HSP72_HUMAN	Heat shock-related 70 kDa protein 2	0.662	0.11	42	1.124	0.056	34	0.74	0.589
Q15165	PON2_HUMAN	Serum paraoxonase/arylesterase 2	2.305	0.14	12	0.323	0.002	4	0.74	7.136
P62847	RS24_HUMAN	40S ribosomal protein S24	0.951	0	2	0.783	0.017	6	0.74	1.215
Q14839	CHD4_HUMAN	Chromodomain-helicase-DNA-binding protein 4	0.48	0.09	14	1.552	0.279	30	0.74	0.309
P07355	ANXA2_HUMAN	Annexin A2	1.163	0.13	144	0.641	0.092	133	0.75	1.814
P63241	IF5A1_HUMAN	Eukaryotic translation initiation factor 5A-1	0.7	0.09	4	1.065	0.142	8	0.75	0.657

Q12846	STX4_HUMAN	Syntaxin-4	1.059	0.19	8	0.704	0.101	20	0.75	1.504
-	R13AX_HUMAN	-	0.901	0.08	6	0.828	0.077	6	0.75	1.088
Q6S8J3	POTEE_HUMAN	POTE ankyrin domain family member E	0.576	0.1	32	1.298	0.07	18	0.75	0.444
P68371	TBB4B_HUMAN	Tubulin beta-4B chain	1.01	0.11	50	0.741	0.151	60	0.75	1.363
P35659	DEK_HUMAN	Protein DEK	0.407	0.12	15	1.839	0.107	14	0.75	0.221
O75844	FACE1_HUMAN	CAAX prenyl protease 1 homolog	0.683	0.11	22	1.096	0.136	18	0.75	0.623
Q01130	SRSF2_HUMAN	Serine/arginine-rich splicing factor 2	0.456	0.01	6	1.642	0.026	6	0.75	0.278
P52790	HXK3_HUMAN	Hexokinase-3	0.317	0.01	6	2.363	0.063	6	0.75	0.134
P0CG38	POTEI_HUMAN	POTE ankyrin domain family member I	0.574	0.07	20	1.306	0.016	6	0.75	0.44
P0CG39	POTEJ_HUMAN	POTE ankyrin domain family member J	0.574	0.07	20	1.306	0.016	6	0.75	0.44
P63244	GBLP_HUMAN	Guanine nucleotide-binding protein subunit beta-2-like 1	0.945	0.08	26	0.794	0.107	34	0.75	1.19
P46777	RL5_HUMAN	60S ribosomal protein L5	0.96	0.07	38	0.782	0.076	40	0.75	1.228
O95831	AIFM1_HUMAN	Apoptosis-inducing factor 1, mitochondrial	0.398	0.1	38	1.891	0.423	36	0.75	0.21
P62917	RL8_HUMAN	60S ribosomal protein L8	0.935	0.21	15	0.805	0.066	12	0.75	1.161
P14866	HNRPL_HUMAN	Heterogeneous nuclear ribonucleoprotein L	0.474	0.09	72	1.588	0.284	74	0.75	0.298
P62906	RL10A_HUMAN	60S ribosomal protein L10a	0.924	0.1	34	0.815	0.2	26	0.75	1.134
P68032	ACTC_HUMAN	Actin, alpha cardiac muscle 1	0.568	0.09	74	1.327	0.086	72	0.75	0.428
P68133	ACTS_HUMAN	Actin, alpha skeletal muscle	0.568	0.09	74	1.327	0.086	72	0.75	0.428
Q02878	RL6_HUMAN	60S ribosomal protein L6	1.011	0.11	58	0.746	0.07	43	0.75	1.355
P56537	IF6_HUMAN	Eukaryotic translation initiation factor 6	0.449	0.04	10	1.68	0.059	6	0.75	0.267
P08238	HS90B_HUMAN	Heat shock protein HSP 90-beta	0.969	0.22	54	0.779	0.152	56	0.75	1.244
Q9BZE4	NOG1_HUMAN	Nucleolar GTP-binding protein 1	0.379	0.01	12	1.992	0.225	18	0.75	0.19
Q05639	EF1A2_HUMAN	Elongation factor 1-alpha 2	1.04	0.24	23	0.726	0.036	30	0.76	1.433
A6NMY6	AXA2L_HUMAN	Putative annexin A2-like protein	1.173	0.14	114	0.644	0.087	103	0.76	1.821
P10809	CH60_HUMAN	60 kDa heat shock protein, mitochondrial	0.299	0.04	77	2.528	0.471	69	0.76	0.118
-	HNRCL_HUMAN	-	0.396	0.07	10	1.909	0.472	12	0.76	0.207
P46782	RS5_HUMAN	40S ribosomal protein S5	0.883	0.04	12	0.857	0.256	14	0.76	1.03
P18085	ARF4_HUMAN	ADP-ribosylation factor 4	1.74	0	2	0.435	0.025	4	0.76	4

O43707	ACTN4_HUMAN	Alpha-actinin-4	1.139	0.21	167	0.665	0.089	178	0.76	1.713
Q14204	DYHC1_HUMAN	Cytoplasmic dynein 1 heavy chain 1	1.134	0.26	147	0.668	0.125	106	0.76	1.698
P51572	BAP31_HUMAN	B-cell receptor-associated protein 31	0.59	0.09	10	1.284	0.463	12	0.76	0.46
P18621	RL17_HUMAN	60S ribosomal protein L17	0.98	0.06	48	0.774	0.079	36	0.76	1.266
P50991	TCPD_HUMAN	T-complex protein 1 subunit delta	0.877	0.09	50	0.865	0.112	43	0.76	1.014
Q09161	NCBP1_HUMAN	Nuclear cap-binding protein subunit 1	0.505	0.08	8	1.509	0.068	8	0.76	0.335
Q15233	NONO_HUMAN	Non-POU domain-containing octamer-binding protein	0.584	0.13	42	1.305	0.514	32	0.76	0.448
Q13748	TBA3C_HUMAN	Tubulin alpha-3C/D chain	1.149	0.21	36	0.664	0.086	41	0.76	1.73
Q99877	H2B1N_HUMAN	Histone H2B type 1-N	0.518	0.1	26	1.473	0.153	41	0.76	0.352
Q99880	H2B1L_HUMAN	Histone H2B type 1-L	0.518	0.1	26	1.473	0.153	41	0.76	0.352
O60814	H2B1K_HUMAN	Histone H2B type 1-K	0.518	0.1	26	1.473	0.153	41	0.76	0.352
Q93079	H2B1H_HUMAN	Histone H2B type 1-H	0.518	0.1	26	1.473	0.153	41	0.76	0.352
Q99879	H2B1M_HUMAN	Histone H2B type 1-M	0.518	0.1	26	1.473	0.153	41	0.76	0.352
Q5QNW6	H2B2F_HUMAN	Histone H2B type 2-F	0.518	0.1	26	1.473	0.153	41	0.76	0.352
P57053	H2BFS_HUMAN	Histone H2B type F-S	0.518	0.1	26	1.473	0.153	41	0.76	0.352
P62807	H2B1C_HUMAN	Histone H2B type 1-C/E/F/G/I	0.518	0.1	26	1.473	0.153	41	0.76	0.352
P58876	H2B1D_HUMAN	Histone H2B type 1-D	0.518	0.1	26	1.473	0.153	41	0.76	0.352
P35908	K22E_HUMAN	Keratin, type II cytoskeletal 2 epidermal	0.159	0.07	18	4.805	1.939	20	0.76	0.033
P63267	ACTH_HUMAN	Actin, gamma-enteric smooth muscle	0.576	0.1	68	1.327	0.09	72	0.76	0.434
P62736	ACTA_HUMAN	Actin, aortic smooth muscle	0.576	0.09	68	1.327	0.086	72	0.76	0.434
Q02880	TOP2B_HUMAN	DNA topoisomerase 2-beta	0.62	0.06	4	1.233	0.294	12	0.76	0.503
Q6NXT2	H3C_HUMAN	Histone H3.3C	0.551	0.04	2	1.388		1	0.76	0.397
Q14240	IF4A2_HUMAN	Eukaryotic initiation factor 4A-II	0.812	0.12	16	0.942	0.203	20	0.76	0.862
Q14137	BOP1_HUMAN	Ribosome biogenesis protein BOP1	0.359	0.07	12	2.132	0.276	26	0.77	0.168
Q08170	SRSF4_HUMAN	Serine/arginine-rich splicing factor 4	0.48	0.09	18	1.596	0.407	20	0.77	0.301
O60506	HNRPQ_HUMAN	Heterogeneous nuclear ribonucleoprotein Q	0.57	0.1	74	1.344	0.236	93	0.77	0.424
Q92945	FUBP2_HUMAN	Far upstream element-binding protein 2	0.636	0.19	27	1.206	0.179	27	0.77	0.527
P62805	H4_HUMAN	Histone H4	0.493	0.08	20	1.556	0.174	22	0.77	0.317
P63261	ACTG_HUMAN	Actin, cytoplasmic 2	0.571	0.09	124	1.344	0.102	116	0.77	0.425

P60709	ACTB_HUMAN	Actin, cytoplasmic 1	0.571	0.09	124	1.344	0.102	116	0.77	0.425
P08727	K1C19_HUMAN	Keratin, type I cytoskeletal 19	0.152	0.05	14	5.049	1.82	4	0.77	0.03
P12814	ACTN1_HUMAN	Alpha-actinin-1	1.321	0.25	177	0.581	0.108	134	0.77	2.274
P43304	GPDM_HUMAN	Glycerol-3-phosphate dehydrogenase, mitochondrial	0.434	0.05	38	1.769	0.603	16	0.77	0.245
Q95604	1C17_HUMAN	HLA class I histocompatibility antigen, Cw-17 alpha chain	1.167	0.34	6	0.658	0	2	0.77	1.774
Q5SSJ5	HP1B3_HUMAN	Heterochromatin protein 1-binding protein 3	0.671	0.24	18	1.146	0.231	8	0.77	0.586
Q9BYX7	ACTBM_HUMAN	Putative beta-actin-like protein 3	0.606	0.1	20	1.269	0.06	12	0.77	0.478
Q14683	SMC1A_HUMAN	Structural maintenance of chromosomes protein 1A	0.418	0.23	5	1.84	0.045	6	0.77	0.227
Q14692	BMS1_HUMAN	Ribosome biogenesis protein BMS1 homolog	0.336	0.03	4	2.291	0.349	12	0.77	0.147
A5A3E0	POTEF_HUMAN	POTE ankyrin domain family member F	0.607	0.09	26	1.269	0.06	12	0.77	0.478
P22314	UBA1_HUMAN	Ubiquitin-like modifier-activating enzyme 1	0.913	0.14	6	0.847	0	2	0.77	1.078
Q8N257	H2B3B_HUMAN	Histone H2B type 3-B	0.519	0.1	24	1.492	0.141	36	0.77	0.348
P61106	RAB14_HUMAN	Ras-related protein Rab-14	0.823	0.01	4	0.941	0.14	12	0.77	0.875
P01892	1A02_HUMAN	HLA class I histocompatibility antigen, A-2 alpha chain	1.177	0.41	10	0.658	0	2	0.77	1.789
P07954	FUMH_HUMAN	Fumarate hydratase, mitochondrial	0.343	0.09	18	2.259	0.236	10	0.77	0.152
Q15029	U5S1_HUMAN	116 kDa U5 small nuclear ribonucleoprotein component	0.446	0.1	56	1.741	0.288	55	0.78	0.256
O75923	DYSF_HUMAN	Dysferlin	1.592	0.02	6	0.488	0.009	8	0.78	3.262
O60832	DKC1_HUMAN	H/ACA ribonucleoprotein complex subunit 4	0.351	0.06	26	2.214	0.42	10	0.78	0.159
P17066	HSP76_HUMAN	Heat shock 70 kDa protein 6	0.656	0.16	20	1.185	0.018	12	0.78	0.554
P23527	H2B1O_HUMAN	Histone H2B type 1-O	0.518	0.1	26	1.501	0.139	39	0.78	0.345
P06899	H2B1J_HUMAN	Histone H2B type 1-J	0.518	0.1	26	1.501	0.139	39	0.78	0.345
Q16778	H2B2E_HUMAN	Histone H2B type 2-E	0.518	0.1	26	1.501	0.139	39	0.78	0.345
P33778	H2B1B_HUMAN	Histone H2B type 1-B	0.518	0.1	26	1.501	0.139	39	0.78	0.345
Q14739	LBR_HUMAN	Lamin-B receptor	0.755	0.16	12	1.032	0.182	14	0.78	0.732
O95202	LETM1_HUMAN	LETM1 and EF-hand domain-containing protein 1, mitochondrial	0.366	0.04	36	2.129	0.275	40	0.78	0.172
P01111	RASN_HUMAN	GTPase NRas	0.8	0.16	6	0.975	0.225	7	0.78	0.821

P54819	KAD2_HUMAN	Adenylate kinase 2, mitochondrial	0.401	0.09	8	1.946	0.085	10	0.78	0.206
Q5VTE0	EF1A3_HUMAN	Putative elongation factor 1-alpha-like 3	1.107	0.22	73	0.706	0.063	62	0.78	1.568
P68104	EF1A1_HUMAN	Elongation factor 1-alpha 1	1.107	0.22	73	0.706	0.063	62	0.78	1.568
P08754	GNAI3_HUMAN	Guanine nucleotide-binding protein G(k) subunit alpha	0.794	0.28	36	0.985	0.226	36	0.78	0.806
Q9UNX4	WDR3_HUMAN	WD repeat-containing protein 3	0.347	0.01	4	2.259	0.356	4	0.78	0.154
Q9BQ39	DDX50_HUMAN	ATP-dependent RNA helicase DDX50	0.325	0.01	6	2.412	0.305	7	0.78	0.135
P68366	TBA4A_HUMAN	Tubulin alpha-4A chain	1.094	0.16	22	0.717	0.319	35	0.78	1.526
P40939	ECHA_HUMAN	Trifunctional enzyme subunit alpha, mitochondrial	0.397	0.1	122	1.976	0.335	143	0.78	0.201
P31930	QCR1_HUMAN	Cytochrome b-c1 complex subunit 1, mitochondrial	0.316	0.06	45	2.483	0.908	55	0.78	0.127
O43390	HNRPR_HUMAN	Heterogeneous nuclear ribonucleoprotein R	0.501	0.13	68	1.568	0.342	87	0.79	0.32
P39023	RL3_HUMAN	60S ribosomal protein L3	1.001	0.22	94	0.785	0.101	78	0.79	1.275
Q99832	TCPH_HUMAN	T-complex protein 1 subunit eta	0.815	0.12	22	0.966	0.17	44	0.79	0.844
P46778	RL21_HUMAN	60S ribosomal protein L21	1.064	0.11	18	0.74	0.059	20	0.79	1.438
P40429	RL13A_HUMAN	60S ribosomal protein L13a	0.953	0.08	14	0.828	0.077	6	0.79	1.151
P34897	GLYM_HUMAN	Serine hydroxymethyltransferase, mitochondrial	0.285	0.07	21	2.772	0.078	10	0.79	0.103
P35609	ACTN2_HUMAN	Alpha-actinin-2	1.221	0.14	41	0.648	0.062	41	0.79	1.884
P46939	UTRO_HUMAN	Utrophin	1.117	0.32	26	0.71	0.348	6	0.79	1.573
O15162	PLS1_HUMAN	Phospholipid scramblase 1	4.118	0.1	4	0.193	0.01	6	0.79	21.34
P12035	K2C3_HUMAN	Keratin, type II cytoskeletal 3	0.153	0.09	14	5.196	2.039	20	0.79	0.029
Q96EP5	DAZP1_HUMAN	DAZ-associated protein 1	0.504	0	2	1.578	0.154	8	0.8	0.319
P09471	GNAO_HUMAN	Guanine nucleotide-binding protein G(o) subunit alpha	1.082	0.1	8	0.736	0.09	12	0.8	1.47
Q562R1	ACTBL_HUMAN	Beta-actin-like protein 2	0.605	0.1	18	1.318	0.099	32	0.8	0.459
Q14152	EIF3A_HUMAN	Eukaryotic translation initiation factor 3 subunit A	1.103	0.25	54	0.723	0.14	52	0.8	1.526
P55265	DSRAD_HUMAN	Double-stranded RNA-specific adenosine deaminase	0.483	0.09	50	1.653	0.263	44	0.8	0.292
O95758	PTBP3_HUMAN	Polypyrimidine tract-binding protein 3	0.532	0.03	6	1.501	0.388	6	0.8	0.354
P15880	RS2_HUMAN	40S ribosomal protein S2	1.113	0.58	26	0.718	0.183	11	0.8	1.55

Q8N1N4	K2C78_HUMAN	Keratin, type II cytoskeletal 78	0.248	0	6	3.227	1.629	6	0.8	0.077
Q9BVK6	TMED9_HUMAN	Transmembrane emp24 domain-containing protein 9	0.953	0.08	8	0.84	0.012	6	0.8	1.135
Q27J81	INF2_HUMAN	Inverted formin-2	0.431	0.11	24	1.859	0.336	6	0.8	0.232
P19367	HXK1_HUMAN	Hexokinase-1	0.347	0.06	66	2.31	0.364	74	0.8	0.15
P60866	RS20_HUMAN	40S ribosomal protein S20	0.995	0.13	6	0.807	0.088	12	0.8	1.233
P50454	SERPH_HUMAN	Serpin H1	0.925	0.06	22	0.869	0.069	16	0.8	1.064
Q9P2E9	RRBP1_HUMAN	Ribosome-binding protein 1	2.31	0.3	40	0.348	0.175	16	0.8	6.638
P12235	ADT1_HUMAN	ADP/ATP translocase 1	0.454	0.09	32	1.772	0.245	28	0.8	0.256
P41252	SYIC_HUMAN	Isoleucine--tRNA ligase, cytoplasmic	0.927	0.25	12	0.87	0.342	25	0.81	1.066
Q14789	GOGB1_HUMAN	Golgin subfamily B member 1	1.158	0.5	8	0.697	0	2	0.81	1.661
Q92901	RL3L_HUMAN	60S ribosomal protein L3-like	0.937	0.04	4	0.862	0.049	4	0.81	1.087
P55795	HNRH2_HUMAN	Heterogeneous nuclear ribonucleoprotein H2	0.551	0.07	18	1.466	0.202	38	0.81	0.376
Q05519	SRS11_HUMAN	Serine/arginine-rich splicing factor 11	0.511	0.27	6	1.582	0.066	6	0.81	0.323
Q15269	PWP2_HUMAN	Periodic tryptophan protein 2 homolog	0.313	0.05	10	2.583	0.139	10	0.81	0.121
P62834	RAP1A_HUMAN	Ras-related protein Rap-1A	0.58	0.09	8	1.394	0.117	14	0.81	0.416
Q9ULV4	COR1C_HUMAN	Coronin-1C	0.669	0.06	18	1.209	0.139	20	0.81	0.553
Q8WXH0	SYNE2_HUMAN	Nesprin-2	0.457	0.21	59	1.771	0.366	46	0.81	0.258
P40227	TCPZ_HUMAN	T-complex protein 1 subunit zeta	0.875	0.13	48	0.925	0.228	42	0.81	0.946
P36776	LONM_HUMAN	Lon protease homolog, mitochondrial	0.387	0	2	2.094	0	2	0.81	0.185
O15427	MOT4_HUMAN	Monocarboxylate transporter 4	0.897	0.13	16	0.904	0.077	16	0.81	0.992
P26641	EF1G_HUMAN	Elongation factor 1-gamma	1.366	0.18	12	0.594	0	2	0.81	2.3
Q15717	ELAV1_HUMAN	ELAV-like protein 1	0.583	0.03	11	1.393	0.35	18	0.81	0.419
P60953	CDC42_HUMAN	Cell division control protein 42 homolog	0.553	0.03	8	1.47	0.315	4	0.81	0.376
Q9Y2X3	NOP58_HUMAN	Nucleolar protein 58	0.383	0.12	42	2.123	0.684	40	0.81	0.18
P78371	TCPB_HUMAN	T-complex protein 1 subunit beta	0.897	0.3	74	0.907	0.098	62	0.81	0.989
P22626	ROA2_HUMAN	Heterogeneous nuclear ribonucleoproteins A2/B1	0.465	0.12	65	1.751	0.39	73	0.81	0.266
Q96CS3	FAF2_HUMAN	FAS-associated factor 2	0.767	0.05	12	1.063	0.099	18	0.82	0.722

P10515	ODP2_HUMAN	Dihydrolipoyllysine-residue acetyltransferase component of pyruvate dehydrogenase complex, mitochondrial	0.259	0.02	8	3.148	0.286	20	0.82	0.082
P61978	HNRPK_HUMAN	Heterogeneous nuclear ribonucleoprotein K	0.557	0.1	48	1.464	0.267	31	0.82	0.38
P40926	MDHM_HUMAN	Malate dehydrogenase, mitochondrial	0.34	0.1	8	2.403	0.475	28	0.82	0.141
Q969X5	ERGI1_HUMAN	Endoplasmic reticulum-Golgi intermediate compartment protein 1	1.711	0.44	26	0.478	0.042	26	0.82	3.579
P06576	ATPB_HUMAN	ATP synthase subunit beta, mitochondrial	0.387	0.15	100	2.117	0.36	98	0.82	0.183
P05386	RLA1_HUMAN	60S acidic ribosomal protein P1	0.793	0.37	14	1.034	0.322	14	0.82	0.767
P02545	LMNA_HUMAN	Prelamin-A/C	0.739	0.12	48	1.111	0.25	69	0.82	0.665
Q6P2Q9	PRP8_HUMAN	Pre-mRNA-processing-splicing factor 8	0.448	0.13	104	1.837	0.655	65	0.82	0.244
P05023	AT1A1_HUMAN	Sodium/potassium-transporting ATPase subunit alpha-1	0.552	0.1	110	1.491	0.194	119	0.82	0.37
O95678	K2C75_HUMAN	Keratin, type II cytoskeletal 75	0.151	0.08	24	5.456	3.471	26	0.82	0.028
P52597	HNRPF_HUMAN	Heterogeneous nuclear ribonucleoprotein F	0.466	0.09	34	1.768	0.282	40	0.82	0.264
Q08211	DHX9_HUMAN	ATP-dependent RNA helicase A	0.543	0.12	116	1.518	0.231	108	0.82	0.358
O43143	DHX15_HUMAN	Pre-mRNA-splicing factor ATP-dependent RNA helicase DHX15	0.428	0.09	26	1.926	0.218	31	0.82	0.222
P49207	RL34_HUMAN	60S ribosomal protein L34	1.016	0.12	18	0.812	0.061	12	0.82	1.251
P48741	HSP77_HUMAN	Putative heat shock 70 kDa protein 7	0.698	0.16	12	1.182	0.015	6	0.83	0.591
P26373	RL13_HUMAN	60S ribosomal protein L13	0.961	0.17	8	0.859	0.071	4	0.83	1.119
Q9BWM7	SFXN3_HUMAN	Sideroflexin-3	0.461	0.02	8	1.792	0.238	10	0.83	0.257
P07910	HNRPC_HUMAN	Heterogeneous nuclear ribonucleoproteins C1/C2	0.433	0.07	26	1.909	0.472	36	0.83	0.227
P08240	SRPR_HUMAN	Signal recognition particle receptor subunit alpha	1.365	0.28	14	0.606	0.047	8	0.83	2.252
Q16720	AT2B3_HUMAN	Plasma membrane calcium-transporting ATPase 3	1.442	0.75	14	0.574	0.199	20	0.83	2.512
Q07666	KHDR1_HUMAN	KH domain-containing, RNA-binding, signal transduction-associated protein 1	0.491	0.08	24	1.686	0.556	36	0.83	0.291
P61224	RAP1B_HUMAN	Ras-related protein Rap-1b	0.58	0.09	8	1.428	0.117	14	0.83	0.406
Q9NP72	RAB18_HUMAN	Ras-related protein Rab-18	1.048	0.29	9	0.791	0.115	8	0.83	1.325
Q99959	PKP2_HUMAN	Plakophilin-2	0.035	0.02	14	23.71	4.104	20	0.83	0.001

P35232	PHB_HUMAN	Prohibitin	0.449	0.12	35	1.852	0.191	25	0.83	0.242
P15311	EZRI_HUMAN	Ezrin	1.092	0.12	4	0.762	0.261	4	0.83	1.433
P26640	SYVC_HUMAN	Valine--tRNA ligase	1.123	0.41	22	0.741	0.14	14	0.83	1.516
P50416	CPT1A_HUMAN	Carnitine O-palmitoyltransferase 1, liver isoform	0.76	0.05	16	1.096	0.231	20	0.83	0.693
P16144	ITB4_HUMAN	Integrin beta-4	0.163	0.06	126	5.111	1.454	142	0.83	0.032
P23634	AT2B4_HUMAN	Plasma membrane calcium-transporting ATPase 4	1.101	0.6	32	0.757	0.487	37	0.83	1.454
P84103	SRSF3_HUMAN	Serine/arginine-rich splicing factor 3	0.576	0.06	28	1.447	0.046	21	0.83	0.398
P19013	K2C4_HUMAN	Keratin, type II cytoskeletal 4	0.162	0.08	8	5.15	1.075	10	0.83	0.031
P15924	DESP_HUMAN	Desmoplakin	0.038	0.02	58	21.98	7.269	84	0.84	0.002
P38919	IF4A3_HUMAN	Eukaryotic initiation factor 4A-III	0.406	0.11	18	2.057	0.986	20	0.84	0.197
P53985	MOT1_HUMAN	Monocarboxylate transporter 1	0.629	0.25	14	1.332	0.166	18	0.84	0.472
Q14318	FKBP8_HUMAN	Peptidyl-prolyl cis-trans isomerase FKBP8	0.804	0.12	12	1.043	0.038	6	0.84	0.771
P29401	TKT_HUMAN	Transketolase	1.043	0.11	18	0.804	0.068	8	0.84	1.297
O95470	SGPL1_HUMAN	Sphingosine-1-phosphate lyase 1	0.406	0	2	2.067	0.1	4	0.84	0.196
Q6FI13	H2A2A_HUMAN	Histone H2A type 2-A	0.555	0.06	12	1.516	0.053	6	0.84	0.366
Q93077	H2A1C_HUMAN	Histone H2A type 1-C	0.555	0.06	12	1.516	0.053	6	0.84	0.366
P04908	H2A1B_HUMAN	Histone H2A type 1-B/E	0.555	0.06	12	1.516	0.053	6	0.84	0.366
P20671	H2A1D_HUMAN	Histone H2A type 1-D	0.555	0.06	12	1.516	0.053	6	0.84	0.366
Q96KK5	H2A1H_HUMAN	Histone H2A type 1-H	0.555	0.06	12	1.516	0.053	6	0.84	0.366
Q7L7L0	H2A3_HUMAN	Histone H2A type 3	0.555	0.06	12	1.516	0.053	6	0.84	0.366
P0C0S8	H2A1_HUMAN	Histone H2A type 1	0.555	0.06	12	1.516	0.053	6	0.84	0.366
Q99878	H2A1J_HUMAN	Histone H2A type 1-J	0.555	0.06	12	1.516	0.053	6	0.84	0.366
Q16777	H2A2C_HUMAN	Histone H2A type 2-C	0.555	0.06	12	1.516	0.053	6	0.84	0.366
P62424	RL7A_HUMAN	60S ribosomal protein L7a	1.02	0.13	48	0.826	0.063	32	0.84	1.235
P46977	STT3A_HUMAN	Dolichyl-diphosphooligosaccharide--protein glycosyltransferase subunit STT3A	1.082	0.5	20	0.779	0.354	7	0.84	1.389
A8MTJ3	GNAT3_HUMAN	Guanine nucleotide-binding protein G(t) subunit alpha-3	1.041	0	4	0.81	0.074	10	0.84	1.285
P19087	GNAT2_HUMAN	Guanine nucleotide-binding protein G(t) subunit alpha-2	1.041	0	4	0.81	0.074	10	0.84	1.285

P11488	GNAT1_HUMAN	Guanine nucleotide-binding protein G(t) subunit alpha-1	1.041	0	4	0.81	0.074	10	0.84	1.285
P27635	RL10_HUMAN	60S ribosomal protein L10	1.058	0.05	22	0.798	0.075	18	0.84	1.326
Q9UMS4	PRP19_HUMAN	Pre-mRNA-processing factor 19	0.553	0.13	28	1.529	0.558	30	0.85	0.362
P09651	ROA1_HUMAN	Heterogeneous nuclear ribonucleoprotein A1	0.587	0.18	40	1.441	0.051	32	0.85	0.407
Q01546	K22O_HUMAN	Keratin, type II cytoskeletal 2 oral	0.172	0.08	18	4.918	2.067	18	0.85	0.035
P62913	RL11_HUMAN	60S ribosomal protein L11	1.043	0.08	18	0.812	0.073	18	0.85	1.284
P09382	LEG1_HUMAN	Galectin-1	1.372	0.12	36	0.618	0.056	26	0.85	2.22
Q9Y678	COPG1_HUMAN	Coatomer subunit gamma-1	1.322	0.25	24	0.642	0.135	12	0.85	2.059
P62244	RS15A_HUMAN	40S ribosomal protein S15a	1.028	0.07	12	0.827	0.01	4	0.85	1.243
Q8NHW5	RLA0L_HUMAN	60S acidic ribosomal protein P0-like	1.193	0.11	34	0.713	0.058	28	0.85	1.673
Q9GZL7	WDR12_HUMAN	Ribosome biogenesis protein WDR12	0.362	0.07	12	2.351	0.72	9	0.85	0.154
P23284	PPIB_HUMAN	Peptidyl-prolyl cis-trans isomerase B	0.88	0.07	14	0.969	0.21	16	0.85	0.908
Q08043	ACTN3_HUMAN	Alpha-actinin-3	1.172	0.15	23	0.728	0.201	26	0.85	1.61
P46779	RL28_HUMAN	60S ribosomal protein L28	1.167	0.11	20	0.732	0.089	16	0.85	1.594
P38405	GNAL_HUMAN	Guanine nucleotide-binding protein G(olf) subunit alpha	1.038	0	2	0.823	0.003	6	0.85	1.261
O75369	FLNB_HUMAN	Filamin-B	0.339	0.19	142	2.52	0.689	156	0.85	0.135
Q8N1F7	NUP93_HUMAN	Nuclear pore complex protein Nup93	0.424	0.16	12	2.016	0.666	18	0.85	0.21
P05387	RLA2_HUMAN	60S acidic ribosomal protein P2	1.14	0.65	16	0.75	0.381	14	0.86	1.52
P24752	THIL_HUMAN	Acetyl-CoA acetyltransferase, mitochondrial	0.258	0.08	10	3.316	0.535	12	0.86	0.078
Q9Y3I0	RTCB_HUMAN	tRNA-splicing ligase RtcB homolog	1.057	0.11	12	0.812	0.209	20	0.86	1.302
P04844	RPN2_HUMAN	Dolichyl-diphosphooligosaccharide--protein glycosyltransferase subunit 2	1.159	0.16	47	0.741	0.116	36	0.86	1.564
P18124	RL7_HUMAN	60S ribosomal protein L7	1.026	0.16	21	0.838	0.136	31	0.86	1.224
Q8IWA0	WDR75_HUMAN	WD repeat-containing protein 75	0.364	0.08	16	2.363	0.022	5	0.86	0.154
O75694	NU155_HUMAN	Nuclear pore complex protein Nup155	0.495	0.07	26	1.739	0.337	23	0.86	0.285
O76021	RL1D1_HUMAN	Ribosomal L1 domain-containing protein 1	0.302	0.06	28	2.853	0.342	38	0.86	0.106
Q03135	CAV1_HUMAN	Caveolin-1	1.664	0.24	36	0.518	0.073	34	0.86	3.212
P05388	RLA0_HUMAN	60S acidic ribosomal protein P0	1.228	0.22	52	0.704	0.055	40	0.86	1.744

O60716	CTND1_HUMAN	Catenin delta-1	0.331	0.09	52	2.612	0.741	52	0.86	0.127
P15144	AMPN_HUMAN	Aminopeptidase N	3.163	0.66	154	0.274	0.052	159	0.87	11.54
Q9Y5B9	SP16H_HUMAN	FACT complex subunit SPT16	0.807	0.13	30	1.074	0.131	44	0.87	0.751
P62277	RS13_HUMAN	40S ribosomal protein S13	0.963	0.04	6	0.902	0.062	10	0.87	1.068
Q9Y5M8	SRPRB_HUMAN	Signal recognition particle receptor subunit beta	0.67	0.17	14	1.299	0.122	18	0.87	0.516
Q3ZCM7	TBB8_HUMAN	Tubulin beta-8 chain	1.062	0.02	6	0.824	0.067	10	0.88	1.289
P49755	TMEDA_HUMAN	Transmembrane emp24 domain-containing protein 10	0.826	0.1	28	1.063	0.218	30	0.88	0.777
P36578	RL4_HUMAN	60S ribosomal protein L4	1.033	0.41	58	0.85	0.057	32	0.88	1.215
Q15436	SC23A_HUMAN	Protein transport protein Sec23A	2.296	0.43	28	0.383	0.088	6	0.88	5.995
P45880	VDAC2_HUMAN	Voltage-dependent anion-selective channel protein 2	0.545	0.09	41	1.615	0.254	37	0.88	0.337
P54709	AT1B3_HUMAN	Sodium/potassium-transporting ATPase subunit beta-3	0.377	0.05	14	2.338	0.401	24	0.88	0.161
P16435	NCPR_HUMAN	NADPH--cytochrome P450 reductase	0.756	0.12	38	1.167	0.163	8	0.88	0.648
P05141	ADT2_HUMAN	ADP/ATP translocase 2	0.409	0.09	41	2.164	0.351	34	0.89	0.189
P21796	VDAC1_HUMAN	Voltage-dependent anion-selective channel protein 1	0.472	0.07	56	1.876	0.988	66	0.89	0.252
P26599	PTBP1_HUMAN	Polypyrimidine tract-binding protein 1	0.771	1.23	64	1.149	0.473	48	0.89	0.671
P39656	OST48_HUMAN	Dolichyl-diphosphooligosaccharide--protein glycosyltransferase 48 kDa subunit	1.208	0.13	26	0.734	0.067	20	0.89	1.646
Q92542	NICA_HUMAN	Nicastrin	0.718	0.03	14	1.235	0.145	9	0.89	0.581
Q9HDC9	APMAP_HUMAN	Adipocyte plasma membrane-associated protein	0.557	0.04	8	1.593	0.111	18	0.89	0.35
P14618	KPYM_HUMAN	Pyruvate kinase PKM	1.528	1.59	36	0.581	0.061	40	0.89	2.63
Q9P2J5	SYLC_HUMAN	Leucine--tRNA ligase, cytoplasmic	1.291	0.16	44	0.688	0.194	28	0.89	1.876
Q96I24	FUBP3_HUMAN	Far upstream element-binding protein 3	0.605	0.22	12	1.469	0.173	14	0.89	0.412
P53007	TXTP_HUMAN	Tricarboxylate transport protein, mitochondrial	0.69	0.05	6	1.292	0.108	12	0.89	0.534
P27105	STOM_HUMAN	Erythrocyte band 7 integral membrane protein	0.603	0.09	72	1.481	0.64	53	0.89	0.407
Q99575	POP1_HUMAN	Ribonucleases P/MRP protein subunit POP1	0.421	0	2	2.124	0.236	4	0.89	0.198
Q16629	SRSF7_HUMAN	Serine/arginine-rich splicing factor 7	0.533	0.1	14	1.678	0.223	14	0.89	0.318

O75955	FLOT1_HUMAN	Flotillin-1	2.626	0.61	46	0.341	0.078	51	0.9	7.701
P33121	ACSL1_HUMAN	Long-chain-fatty-acid--CoA ligase 1	0.583	0.1	60	1.539	0.212	65	0.9	0.379
P12532	KCRU_HUMAN	Creatine kinase U-type, mitochondrial	0.041	0.01	12	21.89	3.507	22	0.9	0.002
Q9UKV3	ACINU_HUMAN	Apoptotic chromatin condensation inducer in the nucleus	0.366	0	2	2.454	0.29	14	0.9	0.149
Q15738	NSDHL_HUMAN	Sterol-4-alpha-carboxylate 3-dehydrogenase, decarboxylating	0.809	0.18	12	1.112	0.029	6	0.9	0.728
P62701	RS4X_HUMAN	40S ribosomal protein S4, X isoform	1.034	0.44	37	0.871	0.159	32	0.9	1.187
Q03113	GNA12_HUMAN	Guanine nucleotide-binding protein subunit alpha-12	1.218	0.36	6	0.741	0.04	4	0.9	1.644
P11387	TOP1_HUMAN	DNA topoisomerase 1	0.533	0.18	44	1.699	0.554	38	0.91	0.314
Q13838	DX39B_HUMAN	Spliceosome RNA helicase DDX39B	0.898	0.06	16	1.01	0.249	22	0.91	0.889
P17844	DDX5_HUMAN	Probable ATP-dependent RNA helicase DDX5	0.604	0.12	46	1.503	0.263	51	0.91	0.402
Q12788	TBL3_HUMAN	Transducin beta-like protein 3	0.337	0.01	4	2.697	0.433	18	0.91	0.125
P25705	ATPA_HUMAN	ATP synthase subunit alpha, mitochondrial	0.434	0.12	94	2.096	0.642	88	0.91	0.207
P56134	ATPK_HUMAN	ATP synthase subunit f, mitochondrial	0.424	0.01	6	2.146	0	2	0.91	0.198
Q9NYU2	UGGG1_HUMAN	UDP-glucose:glycoprotein glucosyltransferase 1	0.768	0.16	70	1.187	0.15	86	0.91	0.647
Q01780	EXOSX_HUMAN	Exosome component 10	0.531	0.17	6	1.72	0.226	12	0.91	0.309
P61026	RAB10_HUMAN	Ras-related protein Rab-10	0.786	0.08	7	1.164	0.207	11	0.91	0.675
Q07020	RL18_HUMAN	60S ribosomal protein L18	0.982	0.06	12	0.932	0.11	18	0.92	1.054
P07196	NFL_HUMAN	Neurofilament light polypeptide	1.776	0.7	6	0.516	0.039	6	0.92	3.442
P01116	RASK_HUMAN	GTPase KRas	0.834	0.19	4	1.101	0.083	5	0.92	0.757
P08195	4F2_HUMAN	4F2 cell-surface antigen heavy chain	0.192	0.2	90	4.787	1.161	84	0.92	0.04
Q9BTM1	H2AJ_HUMAN	Histone H2A.J	0.608	0.06	12	1.516	0.053	6	0.92	0.401
P36542	ATPG_HUMAN	ATP synthase subunit gamma, mitochondrial	0.485	0.29	18	1.904	0.159	8	0.92	0.255
Q9BSJ8	ESYT1_HUMAN	Extended synaptotagmin-1	0.602	0.14	60	1.535	0.275	51	0.92	0.392
Q71UM5	RS27L_HUMAN	40S ribosomal protein S27-like	1.144	0.26	8	0.808	0.07	12	0.92	1.416
Q00765	REEP5_HUMAN	Receptor expression-enhancing protein 5	1.036	0.06	6	0.893	0.046	6	0.93	1.16
P84095	RHOG_HUMAN	Rho-related GTP-binding protein RhoG	0.799	0.08	8	1.159	0.314	10	0.93	0.689

P35606	COPB2_HUMAN	Coatomer subunit beta'	1.297	0.18	25	0.714	0.17	12	0.93	1.817
Q16630	CPSF6_HUMAN	Cleavage and polyadenylation specificity factor subunit 6	0.816	0.58	12	1.136	0.019	8	0.93	0.718
P06748	NPM_HUMAN	Nucleophosmin	0.556	0.49	71	1.669	0.225	70	0.93	0.333
P00403	COX2_HUMAN	Cytochrome c oxidase subunit 2	0.351	0.06	20	2.65	0.4	19	0.93	0.132
Q9NR30	DDX21_HUMAN	Nucleolar RNA helicase 2	0.31	0.04	52	3.008	0.598	65	0.93	0.103
O15260	SURF4_HUMAN	Surfeit locus protein 4	1.842	0.64	20	0.508	0.043	8	0.94	3.626
P61019	RAB2A_HUMAN	Ras-related protein Rab-2A	0.922	0.06	14	1.015	0.216	22	0.94	0.908
P01112	RASH_HUMAN	GTPase HRas	0.82	0.15	6	1.142	0.076	7	0.94	0.718
Q9BQG0	MBB1A_HUMAN	Myb-binding protein 1A	0.366	0.08	62	2.56	0.455	45	0.94	0.143
P62753	RS6_HUMAN	40S ribosomal protein S6	0.978	0.22	28	0.959	0.201	20	0.94	1.02
P51149	RAB7A_HUMAN	Ras-related protein Rab-7a	0.824	0.2	26	1.139	0.202	35	0.94	0.723
P20020	AT2B1_HUMAN	Plasma membrane calcium-transporting ATPase 1	1.407	0.54	48	0.672	0.444	48	0.95	2.094
P62280	RS11_HUMAN	40S ribosomal protein S11	1.278	1.25	22	0.742	0.084	24	0.95	1.722
Q9H0C2	ADT4_HUMAN	ADP/ATP translocase 4	0.472	0.05	10	2.01	0.088	7	0.95	0.235
Q02218	ODO1_HUMAN	2-oxoglutarate dehydrogenase, mitochondrial	0.417	0.28	36	2.283	0.691	22	0.95	0.183
P30050	RL12_HUMAN	60S ribosomal protein L12	1.186	0.31	18	0.803	0.126	16	0.95	1.477
P30101	PDIA3_HUMAN	Protein disulfide-isomerase A3	0.801	0.09	54	1.189	0.204	50	0.95	0.674
Q92616	GCN1L_HUMAN	Translational activator GCN1	1.033	0.18	15	0.922	0.361	9	0.95	1.12
P31942	HNRH3_HUMAN	Heterogeneous nuclear ribonucleoprotein H3	0.498	0.06	12	1.913	0.304	22	0.95	0.26
Q9NZB2	F120A_HUMAN	Constitutive coactivator of PPAR-gamma-like protein 1	1.461	0.69	22	0.653	0.081	18	0.95	2.237
P05556	ITB1_HUMAN	Integrin beta-1	0.953	0.22	44	1.002	0.143	44	0.95	0.951
Q8WYP5	ELYS_HUMAN	Protein ELYS	0.65	0.11	6	1.471	0.172	4	0.96	0.442
Q9Y277	VDAC3_HUMAN	Voltage-dependent anion-selective channel protein 3	0.48	0.24	20	1.992	0.517	34	0.96	0.241
P35268	RL22_HUMAN	60S ribosomal protein L22	0.94		1	1.018	0	2	0.96	0.923
Q14728	MFS10_HUMAN	Major facilitator superfamily domain-containing protein 10	0.461	0	2	2.076	0.165	5	0.96	0.222
O75643	U520_HUMAN	U5 small nuclear ribonucleoprotein 200 kDa helicase	0.516	0.39	50	1.857	0.39	50	0.96	0.278

Q7L014	DDX46_HUMAN	Probable ATP-dependent RNA helicase DDX46	0.496	0.41	6	1.933	0.246	18	0.96	0.257
P04899	GNAI2_HUMAN	Guanine nucleotide-binding protein G(i) subunit alpha-2	1.601	0.42	50	0.599	0.143	42	0.96	2.673
P07237	PDIA1_HUMAN	Protein disulfide-isomerase	1.387	0.46	66	0.692	0.124	76	0.96	2.004
P18583	SON_HUMAN	Protein SON	0.424	0.18	12	2.268	0.302	14	0.96	0.187
Q7KZF4	SND1_HUMAN	Staphylococcal nuclease domain-containing protein 1	1.343	0.82	107	0.722	0.085	106	0.97	1.86
P84098	RL19_HUMAN	60S ribosomal protein L19	0.998	0.04	12	0.972	0.297	8	0.97	1.027
A0FGR8	ESYT2_HUMAN	Extended synaptotagmin-2	0.858	0.23	14	1.131	0.032	6	0.97	0.759
O14980	XPO1_HUMAN	Exportin-1	0.858	0.58	18	1.131	0.448	8	0.97	0.759
Q9BTT6	LRRC1_HUMAN	Leucine-rich repeat-containing protein 1	0.49	0.05	8	1.982	0.196	7	0.97	0.247
Q00325	MPCP_HUMAN	Phosphate carrier protein, mitochondrial	0.676	0.1	34	1.439	0.191	33	0.97	0.47
O15020	SPTN2_HUMAN	Spectrin beta chain, non-erythrocytic 2	0.446	0.73	8	2.198	0	2	0.98	0.203
P55072	TERA_HUMAN	Transitional endoplasmic reticulum ATPase	1.718	0.39	76	0.571	0.09	38	0.98	3.009
Q9UNL2	SSRG_HUMAN	Translocon-associated protein subunit gamma	1.271	0.03	4	0.772	0.034	6	0.98	1.646
Q92841	DDX17_HUMAN	Probable ATP-dependent RNA helicase DDX17	0.874	0.25	32	1.124	0.411	44	0.98	0.778
O00567	NOP56_HUMAN	Nucleolar protein 56	0.47	0.23	34	2.091	0.217	37	0.98	0.225
P62829	RL23_HUMAN	60S ribosomal protein L23	0.903	0.23	30	1.089	0.282	18	0.98	0.829
O75494	SRS10_HUMAN	Serine/arginine-rich splicing factor 10	0.59	0.16	8	1.668	0.103	16	0.98	0.354
Q9NRY6	PLS3_HUMAN	Phospholipid scramblase 3	2.461	0.15	6	0.4	0.019	6	0.98	6.153
P51659	DHB4_HUMAN	Peroxisomal multifunctional enzyme type 2	0.895	0.18	52	1.102	0.206	49	0.99	0.812
P51148	RAB5C_HUMAN	Ras-related protein Rab-5C	0.582	0.12	6	1.696	0.296	16	0.99	0.343
P08621	RU17_HUMAN	U1 small nuclear ribonucleoprotein 70 kDa	0.631	0.02	8	1.566	0.173	4	0.99	0.403
Q9BTV4	TMM43_HUMAN	Transmembrane protein 43	1.299	0.47	29	0.761	0.069	22	0.99	1.707
Q01650	LAT1_HUMAN	Large neutral amino acids transporter small subunit 1	0.159	0	6	6.225	0.402	6	0.99	0.026
Q8TCJ2	STT3B_HUMAN	Dolichyl-diphosphooligosaccharide--protein glycosyltransferase subunit STT3B	1.418	0.06	6	0.7	0.046	8	0.99	2.026
P20645	MPRD_HUMAN	Cation-dependent mannose-6-phosphate receptor	1.405	0.21	12	0.709	0.002	4	1	1.982

P50914	RL14_HUMAN	60S ribosomal protein L14	1.064	0.04	11	0.941	0.109	18	1	1.131
P04843	RPN1_HUMAN	Dolichyl-diphosphooligosaccharide--protein glycosyltransferase subunit 1	1.214	0.21	81	0.826	0.154	69	1	1.47
Q07955	SRSF1_HUMAN	Serine/arginine-rich splicing factor 1	0.554	0.1	36	1.816	0.509	29	1.01	0.305
Q63HN8	RN213_HUMAN	E3 ubiquitin-protein ligase RNF213	1.196	0.5	8	0.843	0.481	4	1.01	1.419
Q9BY44	EIF2A_HUMAN	Eukaryotic translation initiation factor 2A	0.936	0	2	1.082	0.187	12	1.01	0.865
Q96AG4	LRC59_HUMAN	Leucine-rich repeat-containing protein 59	0.983	0.06	16	1.031	0.051	25	1.01	0.953
P27708	PYR1_HUMAN	CAD protein	1.038	0.34	15	0.978	0.064	7	1.02	1.061
Q7L2E3	DHX30_HUMAN	Putative ATP-dependent RNA helicase DHX30	0.635	0.08	11	1.601	0.116	11	1.02	0.397
P51153	RAB13_HUMAN	Ras-related protein Rab-13	1.381	0.61	4	0.738	0.225	14	1.02	1.871
P61353	RL27_HUMAN	60S ribosomal protein L27	1.073	0.32	10	0.95	0.156	9	1.02	1.129
Q00341	VIGLN_HUMAN	Vigilin	2.427	1.92	48	0.421	0.078	22	1.02	5.765
P60228	EIF3E_HUMAN	Eukaryotic translation initiation factor 3 subunit E	1.083	0.32	22	0.944	0.296	22	1.02	1.147
P08670	VIME_HUMAN	Vimentin	2.008	0.52	131	0.51	0.338	117	1.02	3.937
O75976	CBPD_HUMAN	Carboxypeptidase D	0.979	0.76	66	1.05	0.483	41	1.03	0.932
Q9Y265	RUVB1_HUMAN	RuvB-like 1	0.627	0.14	20	1.641	0.319	16	1.03	0.382
P11177	ODPB_HUMAN	Pyruvate dehydrogenase E1 component subunit beta, mitochondrial	0.435	0.18	8	2.367	0.613	24	1.03	0.184
O00763	ACACB_HUMAN	Acetyl-CoA carboxylase 2	1.016	0.31	4	1.014	0.051	2	1.03	1.002
P23229	ITA6_HUMAN	Integrin alpha-6	0.097	0.06	9	10.7	10.61	9	1.04	0.009
Q12931	TRAP1_HUMAN	Heat shock protein 75 kDa, mitochondrial	0.311	0.33	10	3.339	1.49	18	1.04	0.093
O00161	SNP23_HUMAN	Synaptosomal-associated protein 23	1.428	0.33	52	0.728	0.131	49	1.04	1.962
Q5JTH9	RRP12_HUMAN	RRP12-like protein	0.455	0.16	13	2.29	0.444	22	1.04	0.199
Q15155	NOMO1_HUMAN	Nodal modulator 1	0.985	0.22	26	1.058	0.208	28	1.04	0.931
O15127	SCAM2_HUMAN	Secretory carrier-associated membrane protein 2	1.189	0.23	8	0.877	0.021	6	1.04	1.356
O15126	SCAM1_HUMAN	Secretory carrier-associated membrane protein 1	0.922	0.08	22	1.135	0.108	18	1.05	0.812
O94919	ENDD1_HUMAN	Endonuclease domain-containing 1 protein	2.584	0.42	6	0.405	0	2	1.05	6.38
Q9UQ35	SRRM2_HUMAN	Serine/arginine repetitive matrix protein 2	0.425	0.23	36	2.475	0.774	28	1.05	0.172

Q9H0A0	NAT10_HUMAN	N-acetyltransferase 10	0.372	0.08	48	2.829	3.644	43	1.05	0.131
Q6DD88	ATLA3_HUMAN	Atlastin-3	1.411	0.22	28	0.746	0.329	26	1.05	1.891
Q1KMD3	HNRL2_HUMAN	Heterogeneous nuclear ribonucleoprotein U-like protein 2	0.633	0.07	10	1.664	0.223	20	1.05	0.38
Q96GQ7	DDX27_HUMAN	Probable ATP-dependent RNA helicase DDX27	0.538	0.34	8	1.962	0.185	10	1.06	0.274
Q92499	DDX1_HUMAN	ATP-dependent RNA helicase DDX1	1.549	0.73	32	0.682	0.115	14	1.06	2.271
Q04637	IF4G1_HUMAN	Eukaryotic translation initiation factor 4 gamma 1	1.762	0.35	14	0.6	0.298	20	1.06	2.937
Q9BUQ8	DDX23_HUMAN	Probable ATP-dependent RNA helicase DDX23	0.671	0.43	4	1.576	0.499	7	1.06	0.426
Q93050	VPP1_HUMAN	V-type proton ATPase 116 kDa subunit a isoform 1	0.625	0.17	21	1.693	0.382	18	1.06	0.369
Q15758	AAAT_HUMAN	Neutral amino acid transporter B(0)	0.967	0.11	20	1.098	0.278	26	1.06	0.881
Q9Y3L5	RAP2C_HUMAN	Ras-related protein Rap-2c	1.08	0.45	18	0.987	0.234	36	1.07	1.094
P11940	PABP1_HUMAN	Polyadenylate-binding protein 1	1.344	0.33	12	0.794	0.151	14	1.07	1.693
P20648	ATP4A_HUMAN	Potassium-transporting ATPase alpha chain 1	0.846	0.83	12	1.262	0.027	8	1.07	0.67
P69849	NOMO3_HUMAN	Nodal modulator 3	1.016	0.19	24	1.061	0.216	26	1.08	0.958
Q5JPE7	NOMO2_HUMAN	Nodal modulator 2	1.016	0.19	24	1.061	0.216	26	1.08	0.958
P00387	NB5R3_HUMAN	NADH-cytochrome b5 reductase 3	1.481	0.13	20	0.728	0.118	22	1.08	2.034
P07814	SYEP_HUMAN	Bifunctional glutamate/proline--tRNA ligase	1.334	0.79	76	0.81	0.161	90	1.08	1.647
Q5XKE5	K2C79_HUMAN	Keratin, type II cytoskeletal 79	0.265	0.31	22	4.087	1.917	26	1.08	0.065
O00148	DX39A_HUMAN	ATP-dependent RNA helicase DDX39A	1.078	0.25	12	1.008	0.394	14	1.09	1.069
P63096	GNAI1_HUMAN	Guanine nucleotide-binding protein G(i) subunit alpha-1	0.808	0.34	26	1.346	0.864	22	1.09	0.6
Q13310	PABP4_HUMAN	Polyadenylate-binding protein 4	1.351	0.14	8	0.806	0.139	4	1.09	1.676
P60033	CD81_HUMAN	CD81 antigen	1.834	0.04	6	0.594	0.053	8	1.09	3.088
O60488	ACSL4_HUMAN	Long-chain-fatty-acid--CoA ligase 4	0.72	0.4	34	1.514	0.638	27	1.09	0.476
Q14697	GANAB_HUMAN	Neutral alpha-glucosidase AB	0.66	0.11	32	1.653	0.338	35	1.09	0.399
Q969E2	SCAM4_HUMAN	Secretory carrier-associated membrane protein 4	1.57	0	2	0.697	0.001	4	1.09	2.253
P14923	PLAK_HUMAN	Junction plakoglobin	0.11	0.03	12	10.04	3.095	22	1.1	0.011

O14828	SCAM3_HUMAN	Secretory carrier-associated membrane protein 3	1.365	0.19	44	0.81	0.344	42	1.11	1.685
Q14160	SCRIB_HUMAN	Protein scribble homolog	0.544	0.15	26	2.033	0.582	13	1.11	0.268
P54136	SYRC_HUMAN	Arginine--tRNA ligase, cytoplasmic	1.475	0.45	20	0.752	0.276	16	1.11	1.961
P63092	GNAS2_HUMAN	Guanine nucleotide-binding protein G(s) subunit alpha isoforms short	1.435	0.46	4	0.773	0.091	8	1.11	1.856
Q5JWF2	GNAS1_HUMAN	Guanine nucleotide-binding protein G(s) subunit alpha isoforms XLas	1.435	0.46	4	0.773	0.091	8	1.11	1.856
P02786	TFR1_HUMAN	Transferrin receptor protein 1	3.059	0.77	124	0.363	0.074	101	1.11	8.427
Q92928	RAB1C_HUMAN	Putative Ras-related protein Rab-1C	1.002	0.68	20	1.111	0.103	20	1.11	0.902
P46087	NOP2_HUMAN	Probable 28S rRNA (cytosine(4447)-C(5))-methyltransferase	0.416	0.07	28	2.681	0.477	24	1.12	0.155
P07099	HYEP_HUMAN	Epoxide hydrolase 1	1.275	0.75	28	0.876	0.173	33	1.12	1.455
Q9H0U4	RAB1B_HUMAN	Ras-related protein Rab-1B	1.117	0.64	26	1.001	0.274	24	1.12	1.116
P61204	ARF3_HUMAN	ADP-ribosylation factor 3	1.392	0.31	10	0.804	0.32	6	1.12	1.731
P84077	ARF1_HUMAN	ADP-ribosylation factor 1	1.392	0.31	10	0.804	0.32	6	1.12	1.731
Q10471	GALT2_HUMAN	Polypeptide N-acetylgalactosaminyltransferase 2	2.609	0.46	24	0.429	0.038	24	1.12	6.082
Q9ULC5	ACSL5_HUMAN	Long-chain-fatty-acid--CoA ligase 5	0.712	0.11	6	1.574	0.146	8	1.12	0.452
Q9P0L0	VAPA_HUMAN	Vesicle-associated membrane protein-associated protein A	0.815	0.4	10	1.385	0.1	10	1.13	0.588
Q9H3P7	GCP60_HUMAN	Golgi resident protein GCP60	1.054	0.08	12	1.082	0.04	4	1.14	0.974
P62820	RAB1A_HUMAN	Ras-related protein Rab-1A	1.052	0.36	26	1.085	0.272	28	1.14	0.97
P17661	DESM_HUMAN	Desmin	2.252	0.19	16	0.507	0.034	13	1.14	4.442
Q9P2B2	FPRP_HUMAN	Prostaglandin F2 receptor negative regulator	0.519	0.2	49	2.202	0.549	49	1.14	0.236
P07197	NFM_HUMAN	Neurofilament medium polypeptide	2.227	0.1	4	0.516	0.039	6	1.15	4.316
P14625	ENPL_HUMAN	Endoplasmin	0.73	0.25	20	1.579	0.397	30	1.15	0.462
P51571	SSRD_HUMAN	Translocon-associated protein subunit delta	1.634	1.05	14	0.706	0.193	10	1.15	2.314
Q12906	ILF3_HUMAN	Interleukin enhancer-binding factor 3	0.886	1.22	77	1.306	0.97	86	1.16	0.678
Q53GQ0	DHB12_HUMAN	Very-long-chain 3-oxoacyl-CoA reductase	1.18	0.07	16	0.981	0.015	10	1.16	1.203
Q13308	PTK7_HUMAN	Inactive tyrosine-protein kinase 7	2.316	0.72	35	0.503	0.143	31	1.16	4.604
Q32P51	RA1L2_HUMAN	Heterogeneous nuclear ribonucleoprotein A1-like 2	0.814	0.69	24	1.434	0.039	18	1.17	0.568

P61225	RAP2B_HUMAN	Ras-related protein Rap-2b	1.08	0.37	26	1.086	0.227	28	1.17	0.994
Q86Y82	STX12_HUMAN	Syntaxin-12	1.679	0.14	40	0.701	0.034	30	1.18	2.395
Q6IAA8	LTOR1_HUMAN	Ragulator complex protein LAMTOR1	0.993	0.1	36	1.19	0.051	27	1.18	0.834
P11021	GRP78_HUMAN	78 kDa glucose-regulated protein	1.082	0.18	72	1.093	0.403	72	1.18	0.99
Q16666	IF16_HUMAN	Gamma-interferon-inducible protein 16	0.279	0.19	17	4.239	2.833	28	1.18	0.066
P48449	ERG7_HUMAN	Lanosterol synthase	0.876	0.08	26	1.354	0.252	34	1.19	0.647
P49327	FAS_HUMAN	Fatty acid synthase	0.931	0.16	96	1.278	0.188	76	1.19	0.728
P13987	CD59_HUMAN	CD59 glycoprotein	2.539	0.87	12	0.469	0.027	14	1.19	5.414
O43795	MYO1B_HUMAN	Unconventional myosin-Ib	0.182	0.13	34	6.544	1.187	34	1.19	0.028
Q8WVX9	FACR1_HUMAN	Fatty acyl-CoA reductase 1	0.426	0.18	12	2.805	0.324	10	1.19	0.152
Q9BXY0	MAK16_HUMAN	Protein MAK16 homolog	0.326	0.04	20	3.672	0.146	4	1.2	0.089
Q9UKD2	MRT4_HUMAN	mRNA turnover protein 4 homolog	0.439	0.01	8	2.75	0.015	4	1.21	0.16
Q8TDD1	DDX54_HUMAN	ATP-dependent RNA helicase DDX54	0.446	0.15	6	2.711	0.039	4	1.21	0.165
P54760	EPHB4_HUMAN	Ephrin type-B receptor 4	0.91	0.15	4	1.333	0.062	4	1.21	0.683
P61513	RL37A_HUMAN	60S ribosomal protein L37a	1.206	0.01	6	1.015	0.011	4	1.22	1.188
Q9NVP1	DDX18_HUMAN	ATP-dependent RNA helicase DDX18	0.456	0.27	4	2.685	0.562	23	1.22	0.17
Q9H3Z4	DNJC5_HUMAN	DnaJ homolog subfamily C member 5	0.755	0.03	6	1.623	0.18	14	1.23	0.465
O00116	ADAS_HUMAN	Alkyldihydroxyacetonephosphate synthase, peroxisomal	0.78	0.53	24	1.575	0.409	24	1.23	0.495
Q14344	GNA13_HUMAN	Guanine nucleotide-binding protein subunit alpha-13	1.433	0.26	33	0.858	0.136	28	1.23	1.67
Q14573	ITPR3_HUMAN	Inositol 1,4,5-trisphosphate receptor type 3	0.479	0.17	16	2.573	0.411	20	1.23	0.186
P62263	RS14_HUMAN	40S ribosomal protein S14	0.915	0.1	12	1.354	0.631	14	1.24	0.676
Q12797	ASPH_HUMAN	Aspartyl/asparaginyl beta-hydroxylase	1.476	0.27	52	0.844	0.575	42	1.25	1.749
Q13085	ACACA_HUMAN	Acetyl-CoA carboxylase 1	0.616	0.17	12	2.028	0.946	8	1.25	0.304
P37268	FDFT_HUMAN	Squalene synthase	1.041	0.1	17	1.201	0.191	26	1.25	0.867
O75691	UTP20_HUMAN	Small subunit processome component 20 homolog	0.427	0.19	14	2.941	0.66	8	1.26	0.145
Q8TCT9	HM13_HUMAN	Minor histocompatibility antigen H13	1.673	0.09	12	0.752	0.064	14	1.26	2.225
Q96FQ6	S10AG_HUMAN	Protein S100-A16	0.12	0.04	16	10.49	0.826	14	1.26	0.011
Q86UP2	KTN1_HUMAN	Kinectin	0.941	1.6	38	1.352	0.188	32	1.27	0.696

Q969X1	LFG3_HUMAN	Protein lifeguard 3	1.07	0	2	1.19	0	2	1.27	0.899
O00559	RCAS1_HUMAN	Receptor-binding cancer antigen expressed on SiSo cells	0.972	0.08	4	1.311	0.09	12	1.27	0.741
O60313	OPA1_HUMAN	Dynamin-like 120 kDa protein, mitochondrial	0.495	0.5	28	2.583	0.466	14	1.28	0.192
P62241	RS8_HUMAN	40S ribosomal protein S8	1.32	0.72	28	0.973	0.507	32	1.28	1.357
O95573	ACSL3_HUMAN	Long-chain-fatty-acid--CoA ligase 3	1.615	0.42	74	0.796	0.133	50	1.29	2.029
O15400	STX7_HUMAN	Syntaxin-7	0.871	0.15	30	1.477	0.154	20	1.29	0.59
Q9BTU6	P4K2A_HUMAN	Phosphatidylinositol 4-kinase type 2-alpha	1.283	0.28	46	1.005	0.217	32	1.29	1.277
P10316	1A69_HUMAN	HLA class I histocompatibility antigen, A-69 alpha chain	1.11	0.41	12	1.167	0.784	6	1.3	0.951
O75400	PR40A_HUMAN	Pre-mRNA-processing factor 40 homolog A	0.415	0.07	10	3.123	2.814	16	1.3	0.133
Q99848	EBP2_HUMAN	Probable rRNA-processing protein EBP2	0.481	0.57	7	2.7	0	2	1.3	0.178
P62987	RL40_HUMAN	Ubiquitin-60S ribosomal protein L40	1.55	0.65	17	0.841	0.155	11	1.3	1.843
P62979	RS27A_HUMAN	Ubiquitin-40S ribosomal protein S27a	1.55	0.65	17	0.841	0.155	11	1.3	1.843
Q9H3N1	TMX1_HUMAN	Thioredoxin-related transmembrane protein 1	1.031	0.07	14	1.269	0.14	22	1.31	0.812
Q14126	DSG2_HUMAN	Desmoglein-2	0.303	0.18	94	4.324	1.698	78	1.31	0.07
P09525	ANXA4_HUMAN	Annexin A4	2.059	3.53	19	0.639	0.053	16	1.32	3.222
P32926	DSG3_HUMAN	Desmoglein-3	0.04	0.02	4	32.95	0	2	1.32	0.001
Q9Y262	EIF3L_HUMAN	Eukaryotic translation initiation factor 3 subunit L	1.092	1	30	1.224	1.558	26	1.34	0.892
Q7Z5G4	GOGA7_HUMAN	Golgin subfamily A member 7	1.251	0	2	1.071	0.08	4	1.34	1.168
Q14690	RRP5_HUMAN	Protein RRP5 homolog	0.532	0.5	36	2.524	0.253	24	1.34	0.211
P50148	GNAQ_HUMAN	Guanine nucleotide-binding protein G(q) subunit alpha	1.868	0.29	28	0.722	0.067	18	1.35	2.587
Q9NTJ5	SAC1_HUMAN	Phosphatidylinositide phosphatase SAC1	0.811	0.23	13	1.682	0.607	14	1.36	0.482
Q6UW68	TM205_HUMAN	Transmembrane protein 205	1.175	0.4	8	1.181	0.053	12	1.39	0.995
Q8WXF0	SRS12_HUMAN	Serine/arginine-rich splicing factor 12	0.854	0	2	1.648	0.096	10	1.41	0.518
P63027	VAMP2_HUMAN	Vesicle-associated membrane protein 2	2.152	0.3	12	0.654	0.045	12	1.41	3.291
P29992	GNA11_HUMAN	Guanine nucleotide-binding protein subunit alpha-11	2.513	0.6	36	0.564	0.104	15	1.42	4.456
O00560	SDCB1_HUMAN	Syntenin-1	1.407	0.9	18	1.009	0.41	10	1.42	1.394

P30519	HMOX2_HUMAN	Heme oxygenase 2	0.757	0.16	32	1.904	0.396	22	1.44	0.398
Q96JJ7	TMX3_HUMAN	Protein disulfide-isomerase TMX3	1.341	0.23	28	1.075	0.118	20	1.44	1.247
O00461	GOLI4_HUMAN	Golgi integral membrane protein 4	1.561	0.29	14	0.927	0.198	16	1.45	1.684
Q68D91	MBLC2_HUMAN	Metallo-beta-lactamase domain-containing protein 2	0.671	0	2	2.204	0.564	8	1.48	0.304
O15270	SPTC2_HUMAN	Serine palmitoyltransferase 2	0.723	0	2	2.052	0	2	1.48	0.352
O15381	NVL_HUMAN	Nuclear valosin-containing protein-like	0.646	0	2	2.305	0	2	1.49	0.28
P27797	CALR_HUMAN	Calreticulin	1.032	0.23	20	1.456	0.367	24	1.5	0.709
P16070	CD44_HUMAN	CD44 antigen	1.234	0.4	44	1.218	0.157	33	1.5	1.013
P10301	RRAS_HUMAN	Ras-related protein R-Ras	3.892	1.28	14	0.388	0.15	14	1.51	10.03
Q6PIU2	NCEH1_HUMAN	Neutral cholesterol ester hydrolase 1	2.275	0.23	14	0.664	0.051	6	1.51	3.426
Q14165	MLEC_HUMAN	Malectin	2.34	0.31	38	0.648	0.116	38	1.52	3.611
Q15393	SF3B3_HUMAN	Splicing factor 3B subunit 3	0.622	0.18	36	2.439	2.427	51	1.52	0.255
P15291	B4GT1_HUMAN	Beta-1,4-galactosyltransferase 1	3.027	0.67	14	0.502	0.137	12	1.52	6.03
Q07065	CKAP4_HUMAN	Cytoskeleton-associated protein 4	3.242	0.4	123	0.469	0.062	122	1.52	6.913
A3KMH1	VWA8_HUMAN	von Willebrand factor A domain-containing protein 8	0.448	0	2	3.404	0.322	4	1.52	0.132
P84085	ARF5_HUMAN	ADP-ribosylation factor 5	1.74	0	2	0.881	0	2	1.53	1.975
P53618	COPB_HUMAN	Coatomer subunit beta	1.604	0	2	0.965	0.731	18	1.55	1.662
Q15836	VAMP3_HUMAN	Vesicle-associated membrane protein 3	2.07	0.27	19	0.748	0.153	18	1.55	2.767
P10114	RAP2A_HUMAN	Ras-related protein Rap-2a	1.69	0.44	18	0.919	0.161	26	1.55	1.839
P08962	CD63_HUMAN	CD63 antigen	3.377	0.92	9	0.46	0.021	4	1.55	7.341
P35613	BASI_HUMAN	Basigin	0.457	0.11	14	3.437	3.274	16	1.57	0.133
Q6YHK3	CD109_HUMAN	CD109 antigen	0.61	0.15	38	2.576	1.927	40	1.57	0.237
Q5CZC0	FSIP2_HUMAN	Fibrous sheath-interacting protein 2	1.47	1.6	6	1.071	0.307	6	1.57	1.373
Q15084	PDIA6_HUMAN	Protein disulfide-isomerase A6	0.948	0.56	30	1.675	1.053	26	1.59	0.566
Q92896	GSLG1_HUMAN	Golgi apparatus protein 1	2.062	0.63	11	0.773	0.124	8	1.59	2.668
P49257	LMAN1_HUMAN	Protein ERGIC-53	1.466	0.75	8	1.096	0.834	6	1.61	1.338
Q03001	DYST_HUMAN	Dystonin	0.451	0.51	16	3.57	1.322	8	1.61	0.126
O95837	GNA14_HUMAN	Guanine nucleotide-binding protein subunit alpha-14	2.565	0.47	18	0.634	0.018	6	1.63	4.046

P27824	CALX_HUMAN	Calnexin	1.692	0.56	143	0.97	0.135	120	1.64	1.744
P11388	TOP2A_HUMAN	DNA topoisomerase 2-alpha	1.647	0	2	0.998	0.155	6	1.64	1.65
Q14008	CKAP5_HUMAN	Cytoskeleton-associated protein 5	1.248	0.5	20	1.322	0.131	4	1.65	0.944
Q8WZ42	TITIN_HUMAN	Titin	0.916	0.42	6	1.823	0.404	6	1.67	0.502
P26006	ITA3_HUMAN	Integrin alpha-3	2.3	0.56	17	0.729	0.271	19	1.68	3.155
Q16352	AINX_HUMAN	Alpha-internexin	2.227	0.1	4	0.768	0.467	8	1.71	2.9
Q8IVF2	AHNK2_HUMAN	Protein AHNAK2	0.754	0.33	8	2.284	0	2	1.72	0.33
Q8N766	EMC1_HUMAN	ER membrane protein complex subunit 1	1.07	0.68	19	1.614	0.557	14	1.73	0.663
P43121	MUC18_HUMAN	Cell surface glycoprotein MUC18	67.1	11.5	6	0.026	0	2	1.74	2581
P16615	AT2A2_HUMAN	Sarcoplasmic/endoplasmic reticulum calcium ATPase 2	1.205	3.21	80	1.461	0.246	75	1.76	0.825
Q14315	FLNC_HUMAN	Filamin-C	1.146	1	14	1.563	0.956	16	1.79	0.733
P35749	MYH11_HUMAN	Myosin-11	1.353	2.23	16	1.328	0.158	28	1.8	1.019
P47914	RL29_HUMAN	60S ribosomal protein L29	2.245	2.21	8	0.818	0.069	12	1.84	2.744
O43169	CYB5B_HUMAN	Cytochrome b5 type B	1.557	0.08	10	1.185	0.028	6	1.85	1.314
P53396	ACLY_HUMAN	ATP-citrate synthase	2.002	0.45	12	0.956	0.315	11	1.91	2.094
Q14108	SCRB2_HUMAN	Lysosome membrane protein 2	1.704	0.19	32	1.131	1.13	28	1.93	1.507
O75306	NDUS2_HUMAN	NADH dehydrogenase [ubiquinone] iron-sulfur protein 2, mitochondrial	0.862	0.94	10	2.249	0.106	6	1.94	0.383
Q9Y3E5	PTH2_HUMAN	Peptidyl-tRNA hydrolase 2, mitochondrial	1.403	0.97	16	1.397	0.18	10	1.96	1.004
Q9H078	CLPB_HUMAN	Caseinolytic peptidase B protein homolog	0.832	0.46	8	2.399	0.784	8	2	0.347
Q86UE4	LYRIC_HUMAN	Protein LYRIC	1.603	0.55	26	1.253	0.286	32	2.01	1.279
Q9NQC3	RTN4_HUMAN	Reticulon-4	1.775	0.39	36	1.156	1.363	38	2.05	1.535
O14786	NRP1_HUMAN	Neuropilin-1	22.18	2.16	6	0.094	0	2	2.08	235.9
Q96QD8	S38A2_HUMAN	Sodium-coupled neutral amino acid transporter 2	5.181	0.74	16	0.414	0.094	16	2.14	12.51
P08865	RSSA_HUMAN	40S ribosomal protein SA	2.516	4.27	16	0.858	0.086	12	2.16	2.932
Q13151	ROA0_HUMAN	Heterogeneous nuclear ribonucleoprotein A0	1.225	1.15	5	1.794	0.303	30	2.2	0.683
P55290	CAD13_HUMAN	Cadherin-13	1.478	0.72	20	1.544	0.398	9	2.28	0.957
P53621	COPA_HUMAN	Coatomer subunit alpha	1.271	0.26	38	1.814	4.565	42	2.31	0.701

Q13813	SPTN1_HUMAN	Spectrin alpha chain, non-erythrocytic 1	1.912	9.74	92	1.209	0.291	114	2.31	1.581
P14136	GFAP_HUMAN	Glial fibrillary acidic protein	1.073	1.53	8	2.175	0.036	4	2.33	0.493
Q8WTV0	SCRB1_HUMAN	Scavenger receptor class B member 1	3.04	1.4	28	0.827	0.132	12	2.51	3.676
P30493	1B55_HUMAN	HLA class I histocompatibility antigen, B-55 alpha chain	1.054	0.49	6	2.405	0.517	6	2.53	0.438
P30491	1B53_HUMAN	HLA class I histocompatibility antigen, B-53 alpha chain	1.054	0.49	6	2.405	0.517	6	2.53	0.438
Q29940	1B59_HUMAN	HLA class I histocompatibility antigen, B-59 alpha chain	1.054	0.49	6	2.405	0.517	6	2.53	0.438
P30685	1B35_HUMAN	HLA class I histocompatibility antigen, B-35 alpha chain	1.054	0.49	6	2.405	0.517	6	2.53	0.438
P30464	1B15_HUMAN	HLA class I histocompatibility antigen, B-15 alpha chain	1.054	0.49	6	2.405	0.517	6	2.53	0.438
P30495	1B56_HUMAN	HLA class I histocompatibility antigen, B-56 alpha chain	1.054	0.49	6	2.405	0.517	6	2.53	0.438
P30484	1B46_HUMAN	HLA class I histocompatibility antigen, B-46 alpha chain	1.054	0.49	6	2.405	0.517	6	2.53	0.438
P35580	MYH10_HUMAN	Myosin-10	1.961	7.49	50	1.301	0.223	48	2.55	1.507
O15031	PLXB2_HUMAN	Plexin-B2	1.743	0.81	16	1.464	0.766	4	2.55	1.191
P62070	RRAS2_HUMAN	Ras-related protein R-Ras2	3.258	0.98	18	0.786	0.153	18	2.56	4.145
P58107	EPIPL_HUMAN	Epiplakin	0.374	0.28	44	6.882	9.524	42	2.57	0.054
Q14534	ERG1_HUMAN	Squalene monooxygenase	3.552	1.14	26	0.735	0.082	20	2.61	4.833
P26368	U2AF2_HUMAN	Splicing factor U2AF 65 kDa subunit	1.819	4.38	24	1.469	0.093	14	2.67	1.238
Q70UQ0	IKIP_HUMAN	Inhibitor of nuclear factor kappa-B kinase-interacting protein	2.622	0.61	12	1.196	1.106	10	3.14	2.192
P00533	EGFR_HUMAN	Epidermal growth factor receptor	0.586	0.09	14	5.386	1.771	8	3.16	0.109
P38646	GRP75_HUMAN	Stress-70 protein, mitochondrial	1.187	5	58	2.772	0.416	91	3.29	0.428
O14983	AT2A1_HUMAN	Sarcoplasmic/endoplasmic reticulum calcium ATPase 1	2.297	5.46	24	1.46	0.147	29	3.35	1.573
Q9HCY8	S10AE_HUMAN	Protein S100-A14	0.073	0.06	6	48.96	11.86	8	3.57	0.001
P21589	5NTD_HUMAN	5'-nucleotidase	11.03	15	62	0.336	0.403	38	3.7	32.82
P12036	NFH_HUMAN	Neurofilament heavy polypeptide	2.227	0.1	4	1.72	2.228	8	3.83	1.295
Q8NI36	WDR36_HUMAN	WD repeat-containing protein 36	1.181	0.93	4	4.328	1.334	6	5.11	0.273
Q86Y46	K2C73_HUMAN	Keratin, type II cytoskeletal 73	1.123	1.61	6	5.158	1.216	10	5.79	0.218

Q9NZM1	MYOF_HUMAN	Myoferlin	1.832	0.65	157	3.388	10.74	123	6.21	0.541
P15941	MUC1_HUMAN	Mucin-1	16.4	27.1	8	0.42	0.055	8	6.89	39.05
Q14CN4	K2C72_HUMAN	Keratin, type II cytoskeletal 72	1.417	2.06	6	4.964	1.7	20	7.03	0.285
Q9UPN3	MACF1_HUMAN	Microtubule-actin cross-linking factor 1, isoforms 1/2/3/5	3.927	9.27	20	1.85	0.531	8	7.26	2.123
P17301	ITA2_HUMAN	Integrin alpha-2	1.228	1.4	16	6.14	1.088	8	7.54	0.2
Q13751	LAMB3_HUMAN	Laminin subunit beta-3	0.839	1.62	10	11.24	2.635	8	9.43	0.075
Q93084	AT2A3_HUMAN	Sarcoplasmic/endoplasmic reticulum calcium ATPase 3	7.151	9.98	6	1.579	0.094	9	11.3	4.529
P13645	K1C10_HUMAN	Keratin, type I cytoskeletal 10	4.328	4.17	46	4.953	3.108	10	21.4	0.874